DOCTORAL THESIS

Data Analytics and Control for Stability and Resilience of Future Smart Grids

Submitted by Deepak Kumar Panda to the University of Exeter
as a thesis for the degree of
Doctor of Philosophy in Mathematics
In March 2022

I certify that all material in this thesis, which is not, my own work has been identified and that no material has previously been submitted and approved for the award of a degree by this or any other University.

Signature: ……..

Abstract

With the increased deployment of renewable energy sources and digitization, the evolution from the traditional grid to the smart grid has become an urgent priority. As the grid becomes increasingly complex with increased functionalities and embedded intelligence, its stability and resilience become essential to provide secure and dependable services to the end-user. Moreover, the smart grid operations incorporate the end-users in demand response and EV management, thus giving rise to the concept of prosumers. Previous studies have focused primarily on a single aspect of the smart grid. However, to realize the futuristic grid vision, a fundamental study is required to analyze operations while incorporating most aspects. The comprehensive analysis must be performed at generation, transmission and distribution levels spanning geographical regions and time scales. This thesis provides a framework for this analysis by studying the system stability and resilience at various time and spatial scales.

Firstly, grid stability has been analyzed at a smaller scale by framing it as a frequency control problem while incorporating the cyber-physical aspects with uncontrollable and controllable decentralized energy sources. A framework has also been developed to study the grid resilience to communication packet drop rates and cyber-attacks. Then, the role of consumer response and market price elasticity has been explored in relation to grid stability.

Secondly, the operations of the energy storage devices have been analyzed with non-parametric test statistic, with hourly generation scheduling under stochastic wind and contingency scenarios.

Thirdly, the grid stability and resilience analysis are performed at a larger scale by statistical and machine learning methods. The aim was to determine the relationship between the topological features and nodal voltage stability index for various power networks. The eigen-spectrum of the power networks has been utilized along with real-time voltage measurement using spectral filters to find a critical community of nodes to improve the power network resilience to nodal attacks.

Hence, the work in this thesis provides a generalized analysis framework at all levels of smart grids utilizing the concept of control theory, optimization and data science for stability and resilience.

Acknowledgement

Firstly, I would like to thank my parents for their blessing and support throughout my PhD journey. It would have been impossible without them to deal with the tough time in research far away from home.

I would like to express my gratitude to my PhD supervisor, Dr. Saptarshi Das, for his guidance, inspiration, and supervision, as it helped me stay focused and motivated throughout my PhD journey. I really feel proud being his first PhD student. I am grateful to him for providing the mentorship and overall direction during the whole journey, which helped me grow into an able and competent researcher. Due to his motivation, I was able to stay focused throughout the entire period while challenging myself in every situation, as it helped me grow. I am also grateful to my collaborators Dr. Kaushik Halder, Dr. Soumyajit Ghosh and Sourav Das for their inputs, hope to collaborate on exciting research topics in the future. I am thankful to the College of Engineering, Mathematics and Physical sciences for the funding provided during the given period.

I am also grateful to Professor Stuart Townley for his valuable input whenever I needed him. In addition to this, I am thankful to Professor Mohammad Abusara, as he provided practical inputs to improve my research work as my PhD assessor. In addition to it, I am also grateful to him for employing me in the Cornwall New Energy project for added research experience. I am really obliged by the support provided by the Environmental Mathematics Penryn group, from the start till the end. I am thankful to the colleagues, Lamiya, Ahmed, Ernst and Mofareh, and I wish them all the best in their PhD journey.

The PhD journey is always difficult away from home and amidst the pandemic. Luckily, I got amazing peers and friends who helped me face these challenging times. I am grateful to Mitch, my first housemate in the UK, who helped me settle down initially when I arrived here. During the pandemic period, I am also thankful to Ed and Dan, housemates, for the movie nights and long walks along the beach. It has been an amazing post-pandemic cricket journey with St. Gluvias cricket club. I enjoyed playing cricket at scenic places in the summer while making amazing friends. I am super thankful to Ananya, Faith,

Kanchan for being a fantastic company in the pub quizzes and trips around Cornwall and helping me overcome final stressful phases in my PhD journey.

Finally, yet importantly, I am super thankful to friends who have always been there for me, even though they were at different time zones. I am grateful to my best friend Sumita in India, who has always been a rock for me ever since I am here and has always been available whenever I needed her. I am grateful to my pandemic friend Ruble in the US, a fantastic friend during the tough pandemic times. She was also there to support especially during the midnight research stress.

I also want to thank my internal examiner Prof. Richard Everson and external examiner Prof. Subhash Lakshminarayana, for providing extremely helpful inputs to improve my thesis immensely.

I feel lucky to be surrounded by supportive supervisors, peers, friends throughout my journey, which helped me grow as a complete individual.

Contents

List of Figures

List of Tables

Author Declaration

I, Deepak Kumar Panda, declare that the some part of Chapter 1 is published in *Journal of Cleaner Production* 301 (2021). The full citation of the publication is as follows:

Deepak Kumar Panda, and Saptarshi Das. "Smart grid architecture model for control, optimization and data analytics of future power networks with more renewable energy." *Journal of Cleaner Production* 301 (2021): 126877. (DOI: https://doi.org/10.1016/j.jclepro.2021.126877)

Entire chapter 3.1 is published in *IEEE Transactions on Automation Science and Engineering* (2020), whose full citation is:

Deepak Kumar Panda, Saptarshi Das, and Stuart Townley. "Toward a More Renewable Energy-Based LFC Under Random Packet Transmissions and Delays With Stochastic Generation and Demand." *IEEE Transactions on Automation Science and Engineering* (2020), vol. 19, no. 2, pp. 1217-1232. (DOI: https://doi.org/10.1109/TASE.2020.3042570).

Robust control theory from Chapter 3.2 is taken from the following work,

Halder, Kaushik, **Deepak Kumar Panda**, Saptarshi Das, Sourav Das, and Amitava Gupta. "Specified QoS based networked observer and PI controller design with disturbance and noise rejection under random packet dropout." *Physica A: Statistical Mechanics and its Applications* 604 (2022): 127965. (DOI: https://doi.org/10.1016/j.physa.2022.127965).

Entire Chapter 3.3, is adapted from my conference paper work, which is cited as:

Deepak Kumar Panda, and Saptarshi Das. "Regression analysis of grid stability under decentralized control." In *2019 International Conference on Engineering, Science, and Industrial Applications (ICESI)*, *pp. 1-6. IEEE, 2019.* (DOI: https://doi.org/10.1109/ICESI.2019.8863027).

Entire Chapter Chapter 4 is adapted from my published work, whose citation is:

Deepak Kumar Panda, and Saptarshi Das. "Economic operational analytics for energy storage placement at different grid locations and contingency scenarios with stochastic wind profiles." *Renewable and Sustainable Energy Reviews* 137 (2021): 110474. (DOI: https://doi.org/10.1016/j.rser.2020.110474).

Part of Chapter 5.1, is taken from my conference publication, whose citation is given as:

Deepak Kumar Panda, and Saptarshi Das. "Robust Bayesian Regression Model of Centrality and Voltage Stability Index for Power Networks under Nodal Attack." In *2021 3rd International Youth Conference on Radio Electronics, Electrical and Power Engineering (REEPE)*, pp. 1-7. IEEE, 2021. (DOI: https://doi.org/10.1109/REEPE51337.2021.9388045).

Chapter 1 Introduction

1.1 Motivation

The smart grid is an enhanced version of the traditional power grid, which provides secure and dependable electrical services while incorporating a two-way communication between the utility and the electrical consumer. The smart grid features allow the monitoring of the grid-connected systems, incorporating consumer usage of electricity, and real-time availability of all the events. Real-time data availability using massively deployed sensors will collect weather data, equipment condition and operational status data to enhance the grid intelligence to handle the faults with minimal damage. Moreover, the availability of the data also improves the control paradigm of the smart grid as it can take the best action from numerous possibilities. Smart grids also have unique features such as wide-area measurement systems deploying phasor measurement units (PMUs), special protection schemes, and wide-area situational awareness for healing applications. Smart restoration involves decision support tools that must be highly flexible and adaptive for the ever-changing power grid conditions to be reflected. Restoration should have the black start capability. MW generation capacity of the generators will determine the number of loads that can be energized. Electrical islands can be combined to minimize the frequency difference of the islands involved to control the synchronizing angle.

Smart grid also allows energy integration from diverse sources to fulfil consumers' needs while minimizing the environmental impact and maximizing sustainability. It also incorporates the widespread deployment of numerous energy storage centres to buffer the enormous scale impact of sudden load changes and fluctuation of renewable energy sources. In addition to that, the breakthroughs in battery technology are increasing the viability of plug-in electric vehicles (EV). The EVs are mobile loads and energy sources. The sophisticated communication protocols in the smart grid will enable the charge and discharge of EVs, which can neutralize the load and RES fluctuations in a decentralized manner. The smart grid concept is also utilized to incorporate the active involvement of the end-users, who can schedule their appliance usage based on real-time pricing. A smart grid integrates all the players involved in energy

generation and consumption to address the following limitations of the traditional grid [1] is, given as

- Centralized generation.
- One way power distribution.
- Limited sensing capabilities.
- One-way communication.
- Manual monitoring and restoration of faults.
- Low diversification of energy sources.
- Frequent failures and blackouts.
- Centralized control.
- Limited consumer involvement.

In addition to that, the traditional power grid cannot meet the rising power demand while addressing environmental concerns. However, the concept of smart grid resolves the limitations of traditional power can be addressed by considering the interoperability of different players as shown in the following Figure 1-1. Various aspects of the smart grid have been previously described e.g. peer to peer energy trading [2], integration of distributed energy resources [3], distributed control in laboratory environment [4], e-mobility for electric cars [5], security management [6], distributed automation for distribution networks [7], advanced metering infrastructure [8], energy management in traction systems [9], virtual power plant [10], substation automation [11], wireless communication [12], software-defined networking [13] etc. In a smart grid environment, all these aspects are needed to be integrated along with cyber-physical systems for enhancing operational capacity, reliability and efficiency [14]. The fusion opens up many vulnerabilities, hence making cyber-security of future smart grids a challenging task. Therefore, it is important to use mathematical and statistical models for cyber-attack analysis, security and privacy concerns [15].

As we observe in Figure 1-1, the consumers and producers will interact with each other, along giving rise to the concept of prosumers. A smart grid will help the world manage demand growth, conserve energy, maximize asset utilization, improve grid security and reliability. Advanced metering infrastructure can help the utilities to eliminate barriers to demand response especially with time-of-use

meters would encourage natural demand-side control. NIST/Gridwise Architecture Council efforts have defined Home-to-Grid (H2G), Building-to-Grid (B2G), and Industry-to-Grid (I2G) interoperability requirements [16], will enable the integration of demand-side resources with distribution and transmission operations.

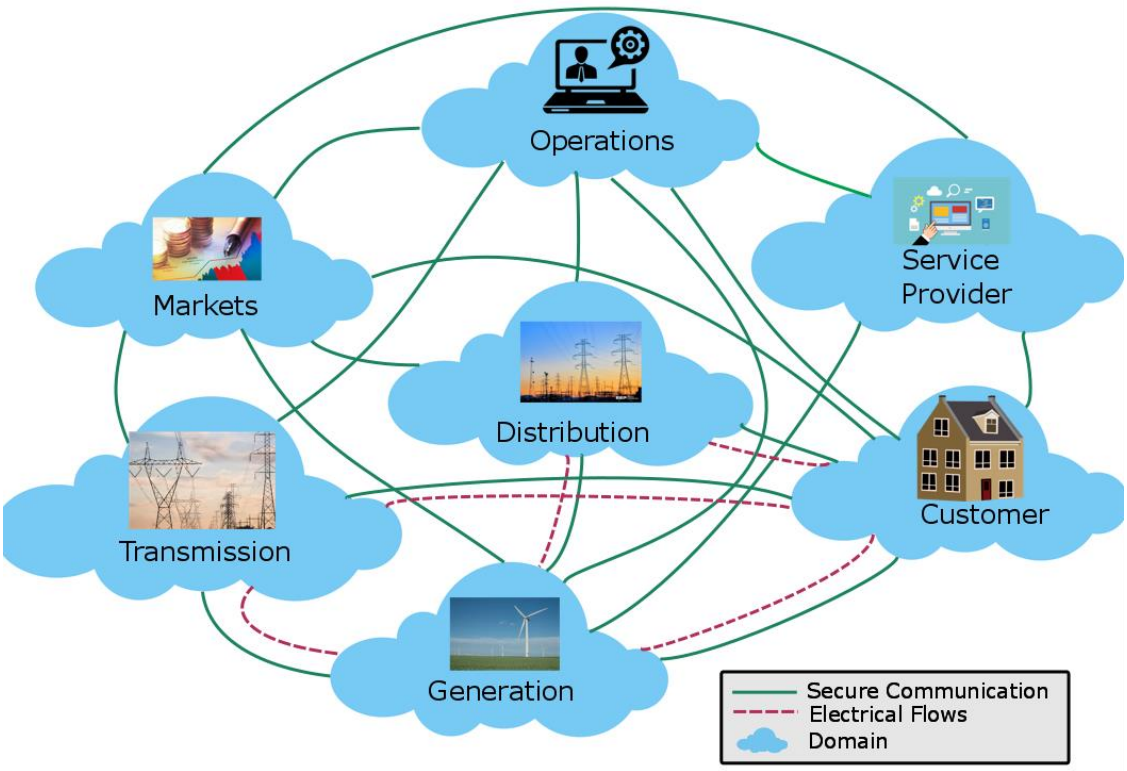

Figure 1-1: Smart grid conceptual model NIST [17], [18].

The operational flexibility will enable the grid to move from the traditional load following operating strategy to a load-shaping strategy. Incorporating a lot of demand response replacing the transmission systems. Advanced metering infrastructure to provide a wealth of information, and it will eliminate the needs for labor intensive business process, with the pricing signal communication between the utilities and the consumers. Real time pricing will aid the consumer to manage their energy usage efficiently. The energy pricing can also be utilized to manage the appliances. The smart meters are to be connected to a central unit, where the data is to be sent to the central server. AMI have low reliability and connectivity requirements from the communication network.

However, in order to study the various functionalities of smart grid, it has to be analysed through an integrated framework which is known as SGAM (Smart Grid Architectural Model) as shown in Figure 1-2.

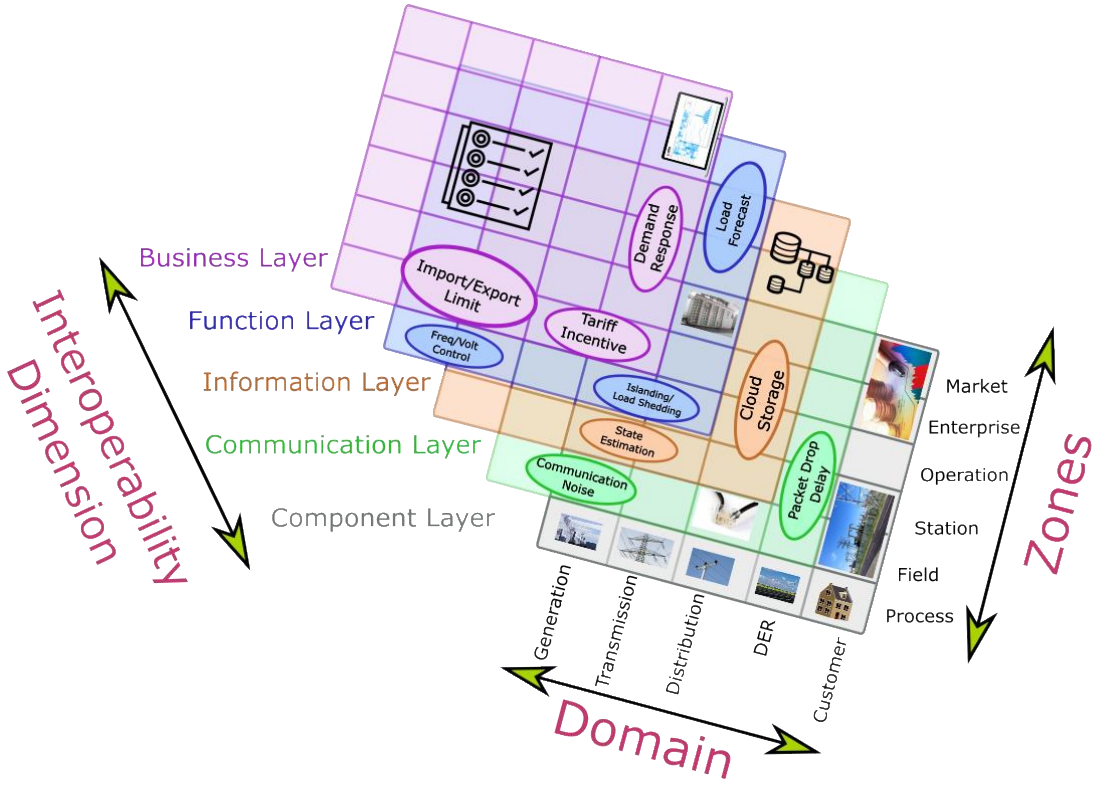

Figure 1-2: Five interoperability layers, domains and zones of the SGAM model

There have been several designs and operational standardization attempts for futuristic smart grid technologies. Amongst various philosophies of smart grid design, mainly three standardized models are widely accepted viz.

- The NIST (National Institute of Standards and Technology) smart grid conceptual model [17], [18].

- IEEE 2030 standard [19] and IEEE grid vision 2050 [20].

- The smart grid architecture model or SGAM (CEN-CENELEC-ETSI Smart Grid Coordination Group, 2012) [21].

The SGAM is developed by three leading European Standardization Organizations – CEN (European Committee for Standardization), CENELEC (European Committee for Electrotechnical Standardization) and ETSI (European

Telecommunication Standards Institute). In response to the European Commission's standardization mandate M/490, these three organizations have developed the SGAM through the SG-CG (smart grid coordination group). The taxonomy for smart grid development from a systems' engineering perspective has been compared using these widely used models in [12] and the usefulness of architectural standards [22]. Previous studies have shown that the SGAM [23] is one of the most prominent ones among these conceptual models for systematic smart grid architecture development due to its clarity of use case management, visualization, and interoperable systems being explicit for modelling, analysis and design [24].

The SGAM is a cube-like structure, as shown in Figure 1, consisting of five different interoperability layers (component, communication, information, function, and business). The layers significantly interplay between the information and communication technologies (ICT), energy informatics and business perspectives within the modern and future smart grid technologies [25]. Each layer is further divided into domains and zones [23]. The domains span over the full energy conversion chains starting from bulk generation, transmission, distribution, distributed energy resources (DER) and customer premises or loads. The zones are divided according to hierarchical levels of power systems management viz. process, field, station, operation, enterprise, and market. Most of the physical energy conversion devices are categorized within the process zone. The field zone includes the protection, control and monitoring devices, whereas the station zone holds the data concentration and functional aggregation modules. In the operation zone, the microgrid energy and distribution management modules are held. The conceptual SGAM model consisting of five interoperability layers, each comprising six domains and five zones, is shown in Figure 1-2.

In the SGAM inspired mathematical models, each component (physical hardware, communication channel, data, software, functionality, and constraints) needs to be mapped into the 6 × 5 matrix, and their inter-connections need to be investigated. The zonal component placement is interpreted based on their respective application. The process zone contains major components that exchange power and cables, loads, sensors and actuators [23] while the field

zone contains the equipment for control, protection, and monitoring. The data concentrators, functional aggregators, substation automation and supervision modules and devices are placed within the station zone while the energy management and distribution modules of a microgrid are incorporated in the operation zone. This matrix is replicated in the five different layers with a vertical interaction between the functional and business objectives via the data models and communication medium. The SGAM is developed to describe large-scale power systems, substation automation [26] and distribution networks. However, the use of SGAM for integrated complex systems modelling for simulation studies and control design purposes has not been explored, which is the primary motivation of this paper. The models need to be developed by encompassing the inadvertent compromises of the electrical and communication infrastructure.

1.2 Challenges

The requirement of smart grid brings about many stability and reliability challenges as shown in Figure 1-3. The stability and resiliency challenges have emerged due to the increased reliance on the stochastic distributed generation

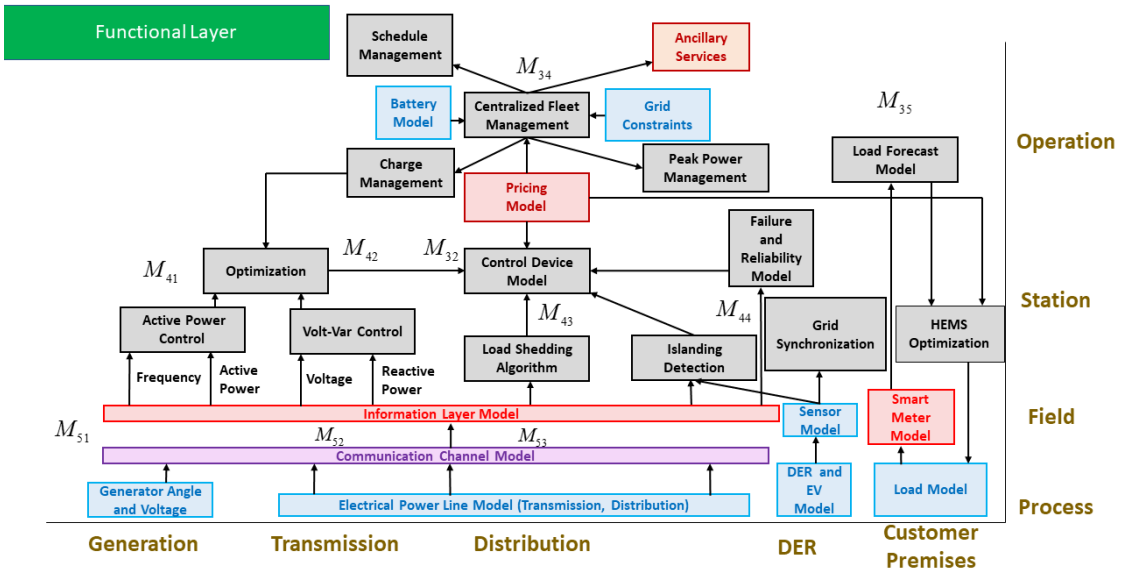

Figure 1-3: The operational challenges in Smart Grid as visualized from the functional layer in SGAM

, along with the grid vulnerability to both cyber and topological attacks. Moreover, the widespread availability of the consumer consumption data also poses an

additional challenge to formulate policies based on their pattern and respective location while interacting with the real-time markets. Hence the challenges in the smart grid can be summarized as follows:

- The intermittent nature of wind and solar generation poses operational challenges for the grid, including ramping of generator reserves, operational regulation requirements and system stability to disturbances.
- The reliable supply of electric power is a critical element of any economy. The new operating strategies for environmental compliance challenge the electric power supply security, reliability, and quality. Upgradation in the consumer load pattern and level, higher loading in the facility transformer, congestion in the lines. The utilization of energy storage devices to manage congestion due to contingencies in the power grids with stochastic renewable energy sources.
- Transmission system issues good sites for wind or large-scale solar plants (greater than 100 MW) may be located in areas distant from any existing transmission lines. These capacity limits are the most fundamental constraint. Hence the role of topology in the stability of complex power networks along with investigation of its resiliency is essential.
- Integration of data and capabilities from multiple, diverse energy sources for decentralized communication protocol-driven control strategies exposes communication systems to potential cyber-physical attacks like Denial of Service (DoS), False Data Injection (FDI) or topology attacks. Furthermore, the communication channels should be two-way while incorporating the consumers and utility providers.
- Energy and information infrastructures have reached a level of complexity interconnection which has made them vulnerable to outages. Interdependency analysis should be conducted for resisting attacks is one of the crucial functions of the smart grid.

1.3 Research Contribution

The contribution of the thesis along the lines of the above research problems are:

- Frequency stability of smaller area power grid with base-load power generation and stochastic renewable energy under communication

constraints. The work in the thesis tackles both the non-linear and linear aspects of the grid components. Swarm based optimization strategies are used for the non-linear model, while robust control theory is used to derive guaranteed stability conditions under communication constraints like time delay and packet drop rate. Decentralized energy sources like EV, battery energy and demand response techniques are also incorporated in the smart grid model.

- Regression techniques to analyze demand response patterns and market price elasticity with the grid stability.
- The use of non-parametric statistics to analyse the multi-period optimal power flow-based battery operations at different locations in the grid while considering the stochastic load demand wind power and component contingencies. The locations considered are renewable energy sources, residential systems and controllable generation sources.
- The dependence of the power network steady-state voltage stability and resiliency with topological features. Moreover, along with dependency, the predictive power of the centrality measures to identify the voltage stability margin is utilized. Bayesian methods are used to predict the mean and uncertainty associated with the stability margin.
- Real-time voltage signals from phasor measurement units (PMU) and eigen-spectrum using graph signal processing to identify the critical nodal community in the power network. Critical communities can be utilized for preventive strategies to avoid a blackout when a node is attacked.

1.4 Research Publications (Accepted/Submitted/To Be Submitted)

1.4.1 Accepted

1. **Deepak Kumar Panda**, and Saptarshi Das. "Smart grid architecture model for control, optimization and data analytics of future power networks with more renewable energy." *Journal of Cleaner Production* 301 (2021): 126877. (DOI: https://doi.org/10.1016/j.jclepro.2021.126877).
2. **Deepak Kumar Panda**, and Saptarshi Das. "Economic operational analytics for energy storage placement at different grid locations and contingency scenarios with stochastic wind profiles." *Renewable and*

Sustainable Energy Reviews 137 (2021): 110474. (DOI: https://doi.org/10.1016/j.rser.2020.110474).

3. **Deepak Kumar Panda**, Saptarshi Das, and Stuart Townley. "Toward a More Renewable Energy-Based LFC Under Random Packet Transmissions and Delays With Stochastic Generation and Demand." *IEEE Transactions on Automation Science and Engineering* (2020), vol. 19, no. 2, pp. 1217-1232. (DOI: https://doi.org/10.1109/TASE.2020.3042570).
4. **Deepak Kumar Panda**, and Saptarshi Das. "Robust Bayesian Regression Model of Centrality and Voltage Stability Index for Power Networks under Nodal Attack." In *2021 3rd International Youth Conference on Radio Electronics, Electrical and Power Engineering (REEPE)*, pp. 1-7. IEEE, 2021. (DOI: https://doi.org/10.1109/REEPE51337.2021.9388045).
5. **Deepak Kumar Panda**, and Saptarshi Das. "Regression analysis of grid stability under decentralized control." In *2019 International Conference on Engineering, Science, and Industrial Applications (ICESI)*, pp. 1-6. IEEE, 2019. (DOI: https://doi.org/10.1109/ICESI.2019.8863027).
6. Halder, Kaushik, **Deepak Kumar Panda**, Saptarshi Das, Sourav Das, and Amitava Gupta. "Specified QoS based networked observer and PI controller design with disturbance and noise rejection under random packet dropout." *Physica A: Statistical Mechanics and its Applications* 604 (2022): 127965. (DOI: https://doi.org/10.1016/j.physa.2022.127965).

1.4.2 Submitted/Revision

1. **Deepak Kumar Panda**, Kaushik Halder, Saptarshi Das, and Stuart Townley "Decentralized LFC and State Estimation with Demand Response and EV with FDI Attack for Specified QoS and Delay ". *Information Sciences (Submitted)*.
2. **Deepak Kumar Panda**, Saptarshi Das, "Critical nodes community identification using spectral filters in complex power networks" *Physica A. (Submitted).*
3. **Deepak Kumar Panda**, Saptarshi Das, "Gaussian Process Digital Twin for Voltage Stability Analysis of Complex Power Networks Under Perturbation" *IEEE Transactions on Reliability (Submitted).*

1.4.3 Accepted (Not/Partial Part of Thesis)

1. Kaushik Halder, Saptarshi Das, **Deepak Kumar Panda**, Sourav Das, and Amitava Gupta. "QoS aware joint observer and networked PI/PID controller design using LMIs under specified rate of packet dropouts." Applied Mathematics and Computation 401 (2021): 126125. (DOI: https://doi.org/10.1016/j.amc.2021.126125).
2. Soumyajit Ghosh, **Deepak Kumar Panda**, Saptarshi Das, and Debashis Chatterjee. "Cross-Correlation Based Classification of Electrical Appliances for Non-Intrusive Load Monitoring." *In 2021 International Conference on Sustainable Energy and Future Electric Transportation (SEFET), pp. 1-6. IEEE, 2021.* (DOI: https://doi.org/10.1109/SeFet48154.2021.9375687).

1.4.4 Submitted/Revision (Not Part of Thesis)

1. **Deepak Kumar Panda**, Saptarshi Das, and Stuart Townley," Hyperparameter Optimized Classification Pipeline for Handling Unbalanced Urban and Rural Energy Consumption Patterns", *Expert Systems with Applications. (Revision Submitted)*
2. **Deepak Kumar Panda**, Saptarshi Das, and Mohammed Abusara, "Parametric Study of Adaptive Reinforcement Learning for Energy Management of Grid-Connected Residential Microgrids" *IEEE Transactions on Control Systems Technology.*
3. **Deepak Kumar Panda**, Ollie Turner, Saptarshi Das, and Mohammad Abusara, "Prioritized Experience Replay Based Deep Distributional Reinforcement Learning for Data-Driven Battery Operation in PV-Microgrid" *Renewable and Sustainable Energy Reviews.*

Chapter 2 Literature and Thesis Overview

This chapter reviews the necessary background behind the current state of the art techniques in smart grid resiliency and stability on smaller and larger power grids and residential management.

Firstly, on a dynamic time-scale and geographical region, the study of smart grid stability and resiliency is based on generation-demand balance by analyzing grid frequency. The load frequency control (LFC) technique is used to study the frequency stability of the smart grid. The primary task is to design a controller for smart grid under cyber-physical constraints like communication delay, packet drop rate and false data injection. The controller has been designed for linear and non-linear models of smart grid components while incorporating the stochastic fluctuation of renewable energy sources (RES). Non-linear models have been utilized, which mimic the actual physics of the components involved. However, it is very challenging to design a controller. Hence, swarm, a based optimization strategy, fulfils the desired objective. We can approximate the dynamics of the load frequency control loop at the operating point while considering linear state space models. Robust H_∞ control theory is used to design the controller and observer gains from the state-space model of the smart grid. The resiliency study analyses the frequency stability at packet drop rates and communication delays. Decentralized energy sources like EV, energy storage and demand response techniques are also incorporated in the non-linear and state-space models. In the second subchapter, we investigate the role of market elasticity and consumer response to the angular stability of the grid.

In the next chapter, a statistical analysis of energy storage operations is conducted for various contingencies and at different grid locations. Multi-period optimal power flow is solved under stochastic wind power and contingency scenarios, resulting in battery storage operations. Non-parametric multivariate hypothesis testing is conducted, and the resultant test statistic is used to compare energy storage operations for various probabilistic inter-hour contingencies and locations in the grid for stochastic load demand and wind power generations.

Then, on a large transmission scale, the resiliency and voltage stability of the grid is studied from the centrality and topological features. A resilience index is derived, and its dependency on the critical centrality measures is examined. Moreover, the analysis is extended for a wide variety of centrality measures for the stability of the large-area spatial network under various perturbations. The spectral filters, utilizing the stability measure from real-time PMU signals and the eigen-spectrum of the weighted power network, are used to find the critical nodes of the power network. Statistical and machine learning methods are used for the analysis.

2.1 Dynamics and Control for Smart Grid Frequency Stability

The utility industries are now facing several operational challenges with the increasing usage of RES. With the focus on reducing the dependence on fossil fuels, several technical and economic feasibility studies have been conducted on 100% renewable usage taking the case of New Zealand [27], Nordic Countries [28], Caribbean island [29], Macedonia [30], Denmark [31], [32], Ireland [33], Japan [34], United States [35] and United Kingdom [36], with the optimal usage of hydro, wind, geothermal and energy storage devices. In [35], an analysis is performed concerning the country's economy and global climate cost reduction per person.

The increasing roles of inverters, highly distributed VRE generation, storage, and DERs bring a complex control challenge unlike anything seen before in the bulk power system [37]. The control room can be considered the core centre to maintain system stability for complex scenarios. As the grid becomes more dynamic and stochastic, the control room must be equipped to collect process data. Dealing with RES uncertainty is the fundamental supply-demand challenge in the smart grid. Moreover, grid planning should consider the extreme events which can be detrimental to routine operations. With the increasing integration of RES, studying the implications on the smart grid dynamics using various LFC schemes is becoming essential. The ICT system performance can be categorized into 1) Full QoS: all connected nodes receive the information they require to work as expected on time. 2) Reduced QoS: information and control signals arrive late or are lost when ICT is not fully available. The ICT system that

is explicitly used to provide beneficial services for the power system itself could be corrupted, thus affecting the resilience of the grid-balancing services.

Responsive loads can be utilized as a part of the demand response (DR) strategy to balance the generation and demand. Moreover, it also helps avoid the traditional load following schemes that lower operational costs and greenhouse gas emissions. The load demands are met by balancing mechanisms (BM) with units operating at different time scales. Non-BM units typically involve the loads participating in DR. As per the report by National Grid [38], £105.6M was spent on the generation side for the balancing mechanism. DR techniques can reduce the costs incurred in the balancing mechanism. DR strategies are implemented with real-time consumer participation by regulating the electricity market price [39]. The price adjustment for DR techniques by the load aggregators incurs a delay in the consumer response, which can cause grid stability issues [40].

Load frequency control problem provides a robust framework to incorporate decentralized energy sources in a cyber-physical smart grid. The grid frequency fluctuation can be utilized to characterize the stability and resilience of the system. In the existing works, the studies are conducted mainly while considering distinct aspects. However, it becomes challenging to conduct a study about stability and resilience integrating all the aspects of the smart grid, which is primarily missing in the previous literature.

2.2 Statistical characterization of energy storage operations in the smart grid under contingencies

The smart grid generation and demand balance problem has been characterized on an hourly scale by solving a DC-optimal power flow (DC-OPF) problem. The resilience analysis is conducted by studying the behaviour of energy storage operations obtained after solving DC-OPF.

ESS deployment in modern power systems and smart grids has been experiencing rapid growth. It provides a solution to mitigate volatility and intermittency in wind energy, meeting real-time demands, thus improving its reliability and economy, as discussed in [41]. Many successful deployments of bulk energy storage have been completed in smart power grids [42], [43]. As shown in [44], energy storage can benefit the power grids. These include robustness of the network sizing during peak periods and eliminating grid

reinforcements with renewable energy integration, thus improving the stability of the power system. Several examples of battery storage deployments with wind energy systems have been discussed in [45]. ESS is operated as a generator and a load in grid under-voltage and over-voltage conditions. Thus, ESS operations involve different stakeholders based on its benefits to the whole electricity system, as discussed in [46], [47]. However, the placement of energy storage devices in the correct location of the grid is essential as it provides several market and operational benefits.

However, in the previous works, the problem of energy storage placement has been conducted, framing it as an optimization problem. The solution strategy fails to account for the nature of energy storage operation, even though the framework is applicable for the large size of the power grid. Moreover, the characterization of energy storage operations has not been conducted for different contingencies.

2.3 Statistics and Machine Learning for Stability and Resilience in Complex Transmission Power Network

Stability and resilience have been explained in the previous subsections on a dynamic and hourly scale and in smaller regions. However, to envision the goal of smart grids on a grand scale, it is essential to characterize the concept of stability and resilience in the power network. Moreover, it is beneficial to analyze the operations in a steady state to test the concept from small to large networks. Even if the generation and demand are balanced, as per previous subsections, the resilience and stability of the power network are not guaranteed as voltage levels play a crucial role.

Power networks are critical infrastructure in modern society. Extreme events or component failure can cause a widespread blackout or a massive area interruption having severe economic consequences [48]. The resiliency techniques primarily combine the top-down and bottom-up approaches while coordinating with the transmission and generation operators. Transmission system states can be classified into normal, alert, emergency, blackout, or restorative. Resilience deals with high impact and low probability events. The critical challenge is to find the right balance between investment in network reinforcements and reducing high-impact/low-probability events. Resilience is an

open-ended optimization goal because it can never be ultimately achieved. Such high-impact, low-frequency threats on the power network include extreme weather ad physical attacks. In order to prevent a wide-scale blackout, it is essential to identify critical nodes and branches in the power network where network centrality measures with electrical and topological features are mainly used.

System resilience is a crucial consideration in the evaluation of solution alternatives. Metrics are required to assign a resilience score to every transmission network facility. However, the impact of recent extreme events on power systems, e.g., bushfires in Australia, flooding events in the United Kingdom, storms in the Americas, and earthquakes in countries located at the edge of the Pacific Ocean, highlights the need for rethinking current planning practices.

Due to the move towards net-zero by 2050, transmission systems in several regions in Great Britain require reinforcements, including upgrading the existing circuits and building new substations [49], [50]. The new low carbon generations will be built around northern England and Scotland with abundant wind resources but low local demands. A similar argument can also be made for South Wales, which has a high RES generation, and the supply has to be provided to regions with higher load demand like midlands and south England [51]. Hence due to the mismatch in the low carbon generation and the load demand centre, and the ambitions of meeting the net-zero target, significant investment in the transmission sector is expected. The investment in the transmission sector improves the transferability of the surplus power from the generator region to the region of high load demand; it also improves the grid's flexibility and reduces the curtailment of RES. However, steady-state voltage stability is critical while upgrading existing power networks.

Voltage stability is getting massive attention with the penetration of renewable energy resources. Due to voltage instability, grid blackouts have created significant losses with an unpredictable socioeconomic impact [52]. As defined in [53], voltage stability is the ability of the power system to maintain its voltage such that, with the increase in load, both power and voltage are controllable. It can maintain steady-state voltage after being subjected to a

disturbance. As given in [54], weak buses or lines need to be improved by distributed generation or voltage supporting equipment to avoid voltage instability. The voltage stability index (VSI) helps in finding the weak nodes/links in the power networks [55], [56].

It is essential to characterize VSI with the topological features incomplete so far in previous literature. It is cumbersome to monitor the voltage at every bus or run continuation power flow (CPF), to study the voltage stability of the grid. Hence, a detailed study has to be conducted concerning centrality measures to ascertain the role of topology in power network stability and resilience. Secondly, it is also essential to identify the critical nodes utilizing the node and edge property of the network to improve the resilience concerning node removals.

2.4 Literature Gap and Thesis Contribution

As described in Section 2.1, there have been works on LFC with stochastic RES and cyber-physical constraints; however, work considering both aspects has not been covered significantly in previous literature. The system characteristics have not been analyzed considering the stochastic nature of packet drops and RES. Moreover, the smart grid state estimator and controller design aspect are also missing while considering stochastic aspects of packet drops and FDI attacks. Hence in this chapter, a heuristic controller is designed for the load frequency control problem comprising the detailed physical model of the components with non-linearities. Secondly, the joint state estimator and controller have been designed for an approximate linear model which guarantees system stability under prescribed parametric bounds. The stable system is then tested for resiliency with various stochastic communication packet drop rates, time delays, false data injection attacks and stochastic RES and load demand. The system response is characterized primarily using frequency fluctuation behaviour.

As discussed in Section 2.2, the role of energy storage operations has not been analyzed in detail for different stochastic contingencies and placement, wind power and load demand. The analysis has been conducted by comparing the similarities of the battery operations using non-parametric hypothesis test statistic.

As discussed in Section 2.3, centrality measures have been mainly used to study the power network intentional attack strategies. However, its role in voltage stability has not been analyzed before. Moreover, the eigenvector corresponding to the highest eigenvalue has been studied for community detection in a complex power network. However, the utilization of the eigenvectors across the eigen spectrum to study the critical nodes of power networks has not been conducted. Hence, the statistical model is used to characterize the importance of centrality measures with the stability and resilience of the power network. Secondly, features are generated using a graph spectral filter incorporating nodal stability index and edge weights to find the community of critical and non-critical nodes to improve the resilience of the power network.

2.5 Thesis Organization

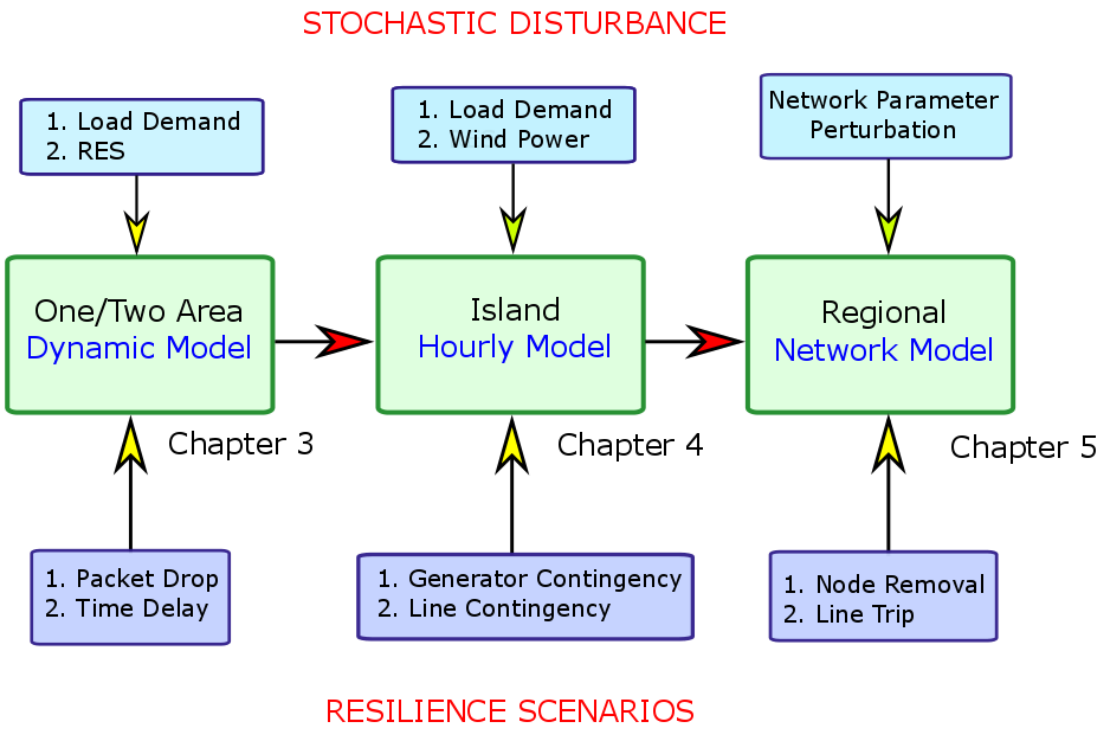

Figure 2-1: The thesis overview block diagram and the resilience and stochastic scenarios for each model.

As per the schematic in Figure 2-1, we see the thesis organization based on the gaps identified from the literature in Section 2.4. As we move from left to right, the analysis is being considered on the larger area along with increasing time scales. Moreover, it also signifies that the conditions from the preceding chapter is satisfied as the analysis is conducted. We also observe the resilience scenarios

for different models in consideration. A brief overview of the remaining chapters in the thesis is given as follows:

Chapter 3

The first subchapter introduces the small-scale dynamic smart grid model as a load frequency control problem incorporating energy storage devices, demand response, and renewable energy. The stability of the cyber-physical system is analyzed with various packet drop, delay, and FDI attacks. The component linear and non-linear models are described, and the controller design and analysis are performed accordingly. As given in Figure 2-1, the controlled system is tested for resilience at different random packet drop rates and delays. The system is tested with various ensembles of stochastic renewable energy and load demand. Secondly, we also analyse the stability behaviour from the market elasticity and consumer response time. In this chapter, we consider single or a two-area for analysis.

Chapter 4

Assuming the frequency is stable on a dynamic scale from the previous chapter, we move on to generation demand balance by statistical analysis of the energy storage operations on an hourly scale. The problem is framed as DC-optimal power flow (DC-OPF) while incorporating energy storage, stochastic wind power, and load demand. As observed in Figure 2-1, the system resilience is analyzed at the line and generator contingencies. The statistical analysis is conducted on energy storage operations obtained after solving DC-OPF with wind power and load demand ensembles. In this chapter, the analysis is considered on a small island-based system consisting of 3 bus incorporating both controllable generation and RES.

Chapter 5

As we scale the analysis on a larger geographical region, we assume that the frequency is stable at the local level, and the generators are optimally scheduled. Here the topological features are considered for analysing the power networks to the stability and resilience index. As given in Figure 2-1, the contingencies

considered here are node removal and line trips. In addition, the voltage stability index is derived with realistic assumptions, which is dependent on the open circuit voltage of the network. The analysis is considered on a large scale national and continental grids.

Chapter 6

This chapter draws the conclusion and presents several new research directions for future work.

Chapter 3 Dynamics and Control for Smart Grid Frequency Stability

In this chapter, they key focus will be on the scheduling the controllable generation sources to meet the load demand at different time scales. In the first subchapter the load is met using a controller at various decentralized location, and the time scale is in seconds.

3.1 Networked Load Frequency Control with Stochastic Communication Constraints and Renewable Energy for Linear and Non-Linear Models

As we have reviewed the necessary literature behind the frequency stability in Section 2.1, this chapter focuses on the control aspects of the decentralized smart grid while considering the stochastic nature of packet drops in communication channel and RES. The non-linear model is considered for a two-area system consisting of energy storage elements and different RES models. The controller is designed for the non-linear model using swarm-based optimization technique. The system response with the tuned controller is checked with various time-delay, packet drop rates. Then the stabilized frequency fluctuations are analyzed for different stochastic models of RES and load demand. The analysis is performed on the norm of frequency fluctuations and the fluctuations are compared with the real-world RES and load demand data.

3.1.1 Previous Works

The solar and wind power generation along with load demands have been considered as stochastic models in the LFC models in [57], [58], [59] where the stochastic nature of the inputs are described using synthetic profiles as filtered random numbers with drifts and jumps. However, in these cases, the system consists of RES acting as stochastic input variables and the storage devices as actuators to damp out the grid oscillations. Filtered white noise is used to model the wind velocities in [60] to control the pitch angle of the wind turbine system. Electric vehicles (EVs) as storage devices with nonlinear functionality have been used within LFC in [61], [62]. EV is introduced in the LFC problem in [63] while coordinating with other household appliances as controllable loads. EVs are utilized along with microgrids having a renewable energy source [64].

When we see networked control system for LFC, event-triggered methods are used in [65]–[67] for LFC. According to this scheme, the information is transmitted if the control signals meet a specific criterion. In [65]–[67], the event triggering strategy has been modified for LFC to make the communication system robust to the interrupted data transmission induced by the DoS attacks. Several other methods have been discussed to mitigate the cyber-attacks in the networked control system (NCS) using evolutionary optimization technique [68], hierarchical games [69], delay estimator and decision making unit [70], zero-input actuator policy using an additional loop [71].

3.1.2 Contribution in this sub-chapter

This subchapter combines the whole system complexities posed by the controller communication network like the DoS attacks modelled by random interruption of data packets and random time delays due to its decentralized nature of the operation. So far the existing works have incorporated either DoS cyberattacks or time delays in the control loops except in [72] where analytical stability is obtained for a less complicated LFC scheme. The DoS attacks modelled in the existing works are bounded by duration and frequency. The work done in this paper eliminates the need for a predictor and an estimator for the lost data packets. Moreover, it does not need a change in the existing communication networks to handle these complexities of random time delays or DoS cyberattacks as dropped out control signal packets. Performance robustness is obtained by tuning the PID controllers in each area using particle swarm optimization (PSO) considering the presence of time delay and cyberattack in the simulation model as an adversarial tuning mechanism for resilient control design. The robustness of the controller in the cyber-physical system is tested using the stochastic profiles including stationary (i.e. Gaussian) and nonstationary inputs, e.g. geometric Brownian motion (gBm) and fractional Brownian motion (fBm), which are simulated by solving stochastic differential equations (SDEs) as discussed in [73]. The results are also validated with the real profiles of solar, wind and load demand. Several energy storage elements are also added in the hybrid power system, as shown in Figure 3-1, as per the schemes in [74] and [57].

The main contributions of this paper are as follows:

• Tuning the filtered PID controllers for two-area LFC with energy storage devices using PSO on a more realistic and complex smart grid model considering random time delays and DoS cyberattacks in the form of high data packet interruptions from the controllers to the actuators. Also, higher system complexities involve different types of nonlinearities (rate constraints and output saturations) in the storage elements and the control loops. Post-hoc analysis of the control performance of the tuned LFC system and convergence characteristics of the optimization-based controller design is also investigated.

• Comparison of the frequency and rate of change of frequency (ROCOF) fluctuations for varying random packet transmission rate and random time delays. The control performances are also compared with stationary, nonstationary and real input profiles as per the IEEE grid standards [75] recommended for connecting distributed energy resources to the grid.

• Comparison of other important grid operational measures in case of different RES and load profiles, e.g. storage operations and RES penetration level into the smart grid as well as visualizing the uncertainties on these grid performance measures using Monte Carlo simulations.

• Insights into the LFC system operations using bivariate statistical analysis of the smart grid operational variables. Also, carrying out nonparametric hypothesis tests on the signal norms of the grid frequency fluctuations for two areas and tie-line power using Monte Carlo simulations.

3.1.3 Two-Area Load Frequency Control Scheme with Non-Linear Components

The multi-area LFC maintains grid frequency of different areas within certain tolerance limits by controlling the generation rates and the power exchanges between them, as shown in Figure 3-1. The LFC also ensures the load sharing between the sub-systems, keeping the frequency deviation within limits. The area control error ACE_i for each area *i* is generated as a weighted summation of the

frequency deviation error $(\Delta f)_i$ and the tie-line power exchange (ΔP_{Tie}) between the two areas is kept to the minimum possible level using the controllers employed in the respective areas.

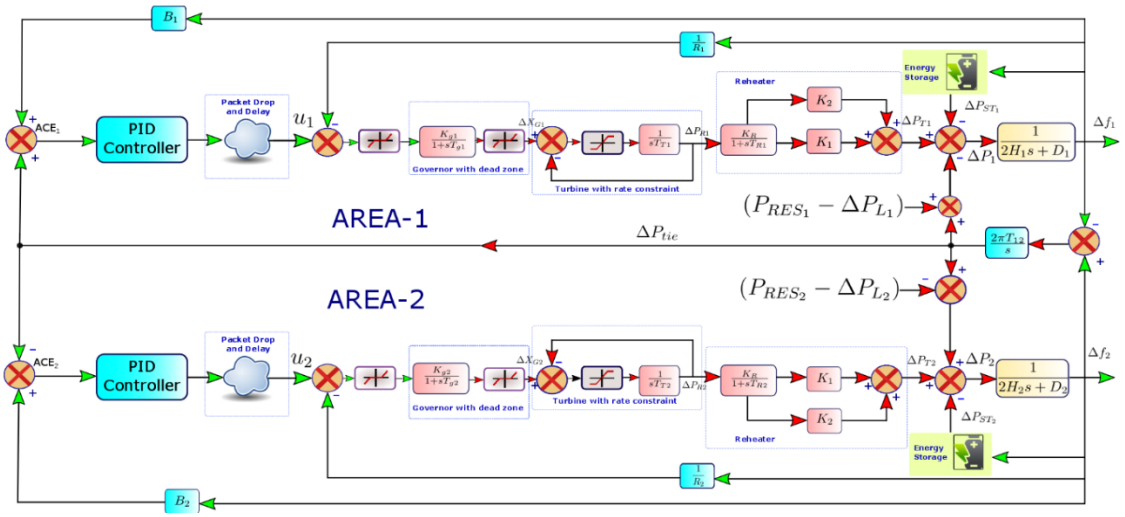

Figure 3-1: Schematic of the two-area LFC scheme with RES and energy storage with filtered PID controllers. The dead zones between the controller and governor increase the RES utilization in the smart grid.

3.1.3.1 LFC in Conventional Fossil Fuel Power Plant Units

The thermal power plant model in each area consists of the steam governor with dead-zone, a steam turbine with the rate constraints and a reheater system, as shown in Figure 3-1. The first-order dynamic models, along with their associated nonlinearities, are modelled as per the scheme in [57]. The coefficients $1/R_i$ in the i^{th} area are the primary control gain and the droop constant of the governor which act upon to reduce the immediate frequency fluctuations. The coefficients Bi act upon the longer fluctuations which act as a bias to the inter-area fluctuations. The PID controller used in the scheme in Figure 3-1 minimizes the area control error (ACE) comprising of the frequency deviations and the inter-area tie-line power oscillations. As given in [76], the frequency deviation due to load change in one area is not corrected by the controller in the other areas in case of primary frequency control. While in the secondary frequency control, the deviations due to the load changes are generally corrected using the tie-line power exchange between the two areas. This deviation is reflected in the system using $(\mathrm{ACE})_i$ for each area *i* which is defined as:

$$\mathrm{ACE}_i = \sum_{j=1}^{M} \Delta P_{ij} + B_i \Delta f_i, \quad (1)$$

where, ΔP_{ij} represents tie-line power flow from the i^{th} area to the j^{th} area, Δf_i is the frequency deviation in the i^{th} area, and M is the number of areas connected to the i^{th} area. The bias factor due to frequency (B_i) is generally expressed as a combination of speed regulation (R_i) and damping coefficient (D_i) which is given in (1) as:

$$B_i = (1/R_i) + D_i. \quad (2)$$

The nonlinearity in the system is represented by a generation rate constraint (GRC) and the dead zone for the governor and the turbine, respectively. A reheater is also considered in the thermal power plant as a first-order model, which is shown in Figure 3-1. It increases the steam quality at the turbine exhaust and improves the thermodynamic efficiency of the power plant. Several realistic modelling aspects like nonlinearities, e.g. GRC in turbines in the LFC loops have been studied in [77], [78], dead-zone in [79] along with reheat turbine [80]. Due to the regulations to increase the usage of the RES, in the proposed scheme, the increase in the conventional thermal power plant outputs for each area *i* are only activated when the RES generation is unable to meet the increased load demand, with the control input $\tilde{u}_i$ to the governor given as:

$$\tilde{u}_i = \max\left[\hat{u}_i - (\Delta f_i / R_i), 0\right], \quad (3)$$

where, $\hat{u}_i$ signifies the controller output after the communication network with DoS attacks and random delays.

3.1.3.2 Nonlinear Models of Energy Storage Devices

The energy storage devices are connected to the grid as per the scheme in [74]. In [81], the stochastic nature of RES is incorporated in the battery energy operation instead of direct solar power output. However in this work, first-order models for the energy storage elements are used viz. ultra-capacitors (UCs) [82], electric vehicles (EVs) [62], battery storage, flywheel [74], fuel cell (FC) and the solar power output is separately modelled so that the aggregated power of a bus is obtained. The energy storage devices have been used to damp out the grid

frequency fluctuations due to load disturbances instead as a control device in [57], [58], [83], [59]. The detailed energy storage scheme is shown in Figure 3-2.

First-order model of the EVs has been used without any nonlinearity constraint [62]. The diesel generator has a rate constraint nonlinearity, but its operation is limited to restrain the harmful emissions from the fuel combustion. Hence it is scheduled to start only when the frequency deviations are beyond 0.05 p.u. The GRCs for the energy storage components are given as $\left|\dot{P}_{fw}\right| < 0.9$, $\left|\dot{P}_{bat}\right| < 0.05$, $\left|\dot{P}_{uc}\right| < 1.2$, $\left|\dot{P}_{DG}\right| < 0.5$, $\left|\dot{P}_{fc}\right| < 0.1$. The rate constraints account for the electro-mechanical constraints of the storage devices. The overall dynamics of the storage devices are governed by the relative values of its gains and time constants. This property of energy storage devices influences the overall response of the LFC system as it consists of a combination of fast and slow dynamics of various components.

3.1.3.3 DoS Cyberattack and Stochastic Time Delay Models

In networked control system (NCS), packet drops and time delays are usually considered from sensor to controller and controller to actuator paths [84]. In the context of load frequency control, the feedback and the forward path is analogous to the data transmitted from the remote terminal units (RTU) to the control center and from control center to the generation companies where the governor set-point is transmitted. As given in [85], the application layer in the communication system is responsible for the transmission of data packets within a given bandwidth from the control center to the generation company (GENCO) which makes it vulnerable to DoS cyber-attack [86]. Time delay is considered due to the transmission of the data from the control center to the governor control system. The packet drops and delays are considered negligible in the feedback path and significant in the forward path.

The DoS attack in the form of random packet drops is modelled in cascade with a random time delay model, as addressed in [87]. The random time delay model considered here detains the PID controller output by random amount following a Gaussian distribution. The distribution parameters μ_d and σ_d are,

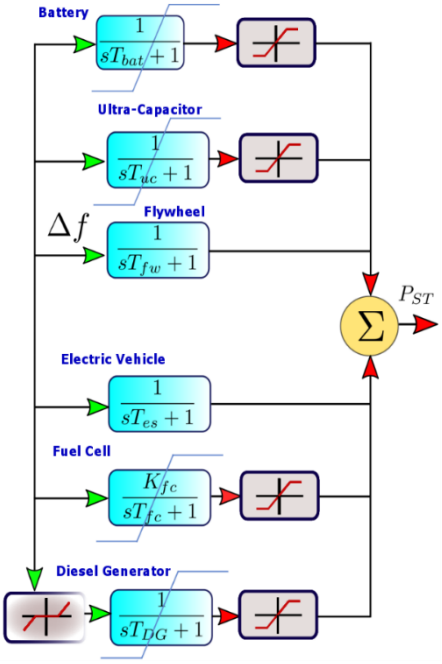

Figure 3-2: First order storage device models with nonlinearities like dead bands, output saturations and generation rate constraints.

considered as 1.5 and 0.1, respectively, for the simulation of random time delays. Let us now consider the total time interval for consideration is T seconds. The packet transmission occurs when certain criteria, as in [65]–[67], is satisfied, which is given as:

$$\mathsf{P}_{\text{Trans}} = \mathbb{P}\left(a_{\text{DoS}} > p_{\text{drop}}\right), \tag{4}$$

where, $a_{\text{DoS}} \sim \mathcal{U}[0,1]$ is uniformly distributed and p_{drop} governs the packet transmission rate by regulating the number of packets to be dropped. The control packet is held over the interval till the next event (4) is satisfied, and the next packet is transmitted. The controller output after interrupted transmission of the packets can be modelled using the following logic. Let us consider the sampling time for the controller output be given as T_s, and the discrete-time instants are expressed as:

$$\varsigma = \{0,1,\ldots,(N-1)\mathsf{T}_s, N\mathsf{T}_s\}, \tag{5}$$

where $N = \mathsf{T}/\mathsf{T}_s$ and T represents total simulation time. Now we consider the time instants $\varsigma_{\text{Trans}} \subset \varsigma = \{t_0,\ldots,t_N\}$ where (4) is satisfied and the control packets are

transmitted. Here, N represents the time instants where (4) is satisfied. Let us consider H be the Heaviside step function defined by:

$$H(t)=\begin{cases}1 & t\geq 0\\ 0 & t<0.\end{cases} \tag{6}$$

When the packets are not transmitted from the controller, the packet at previous instant goes to the actuator. Hence, we can model this using a zero-order hold (ZOH) which is represented using the difference between the Heaviside unit step function H between two instants. We denote the delayed control signal as $\hat{u}(t)=u(t-\tau_d)$. Hence, the control output from the communication network can be expressed as:

$$\begin{aligned}\hat{u}_i(t) &= \hat{u}(t_0)+\left[\hat{u}(t_1)-\hat{u}(t_0)\right]\cdot H(t_1-t_0)\\ &\quad+\left[\hat{u}(t_2)-\hat{u}(t_1)\right]\cdot H(t_2-t_1)+\ldots\\ &\quad+\left[\hat{u}(t)-\hat{u}(t_{-1})\right]\cdot H(t_N-t_{N-1})\\ &= \hat{u}(t_0)+\sum_{i=1}^{N}\left[\hat{u}(t_i)-\hat{u}(t_{i-1})\right]\cdot H(t_i-t_{i-1}).\end{aligned} \tag{7}$$

Here, $\{t_0,\ldots,t_N\}\in\varsigma_{\text{Trans}}$ be the time instants when (4) is satisfied and i be the instant of the sample when the signal is transmitted. Substituting the value of $\hat{u}_i(t)$ in (7), the governor input is represented as:

$$\begin{aligned}\tilde{u}_i(t) &= \max\left\{\hat{u}_i(t)-(\Delta f_i/R_i),0\right\}\\ &= \max\left\{\hat{u}(t_0)+\sum_{i=1}^{N}\left[\hat{u}(t_i)-\hat{u}(t_{i-1})\right]\cdot H(t_i-t_{i-1})-(\Delta f_i/R_i),0\right\}.\end{aligned} \tag{8}$$

As per (4), a higher p_{drop} makes P_{Trans} quite small, thus transmitting a lower number of packets inside the LFC loop. Furthermore, it reduces the value of N thus limiting the number of time instants in ς_{Trans}.

3.1.4 Swarm Optimization Based Controller Design for Non-Linear LFC

PID controllers with derivative filters are used in both the areas of the LFC loops to reduce the effect of noise and stochastic disturbances. The controllers are tuned considering the nonlinearities and stochasticity in the system due to

random delays and cyberattack models. Previous studies in [87], [88] have shown that tuning PID controllers considering the upper limit of the stochastic delays and packet dropout probability rate as an adversarial tuning method by including the stochastic cyberattack models in the tuning phase, helps to improve the control performances as compared to controller tuning using static lumped delay assumption without considering the intrinsic stochasticity in the system. Hence the value of p_{drop} considered to be 0.99 during the PID controller tuning phase. The load disturbances in the form of step inputs are unequal for the two areas and have been considered as active while tuning the PID controllers using constrained single objective global optimization. The controller is tuned by minimizing the Integral of Squared Error (ISE) criterion which aims to minimize sustained frequency fluctuations as compared to other time-weighted criteria like the integral of time multiplied squared error (ITSE). The former penalizes large oscillations as opposed to small-sustained oscillations later and helps to prevent the damage to the connected components to the grid. The weighted sum of the ACEs and the squared deviations of the control signals in two areas are considered as the objective function to be minimized for controller tuning as:

$$J = \sum_{i=1}^{2} \int_0^{\infty} \left(w_1 \left(B_i \Delta f_i + \Delta P_{Tie} \right)^2 + w_2 \left(\Delta u_i \right)^2 \right) dt$$

$$= \sum_{i=1}^{2} \int_0^{\infty} \left(w_1 \left(\text{ACE}_i \right)^2 + w_2 \left(\Delta u_i \right)^2 \right) dt, \tag{9}$$

where, $w_1 = w_2 = 0.5$ indicating equal weightage on both the objectives – ACE and the control effort and *i* represents each area. The four tuning parameters of the PID controller with the derivative filter i.e. $\{K_p, K_i, K_d, N\}$ as shown in Figure 3-1 for each area, are tuned using the global optimizer PSO by minimizing the weighted objective function (9). PSO has been widely utilized for handling linear and nonlinear systems with optimal PID controllers in [89]–[91] where the performance of the tuned PID controllers are shown to be acceptable under various operating conditions. The research in [92], [93] requires the system to have dual loops for minimizing the energy consumption, thus keeping the parameters within a specific limit. However, in this study, an expected minimum of the stochastic objective function (9) is achieved using PSO, satisfying the given

objectives. Our study shows that the system tends to be more stable when high communication packet drops and random time delays are considered in the tuning phase with PSO as an adversarial mechanism. Most of the earlier works have tuned controllers by optimizing static objective function without the stochastic components in such complex systems. Due to the presence of random packet drops for simulating DoS attack and stochastic delays in the NCS, the cost function also becomes stochastic, even for a deterministic step load disturbance in both the areas. Global optimization-based controller design approaches for such NCS problems have been previously studied in [87], [88], [94], [95]. These approaches of optimizing dynamic and stochastic objective function have been shown to outperform deterministic objective function-based controller design methods for NCS applications, which have also been adopted in this work.

The PSO algorithm consists of the swarm of particles $x_i \ \forall i \in \{1,2,\ldots,n_p\}$ where n_p is given by the user. The position and the velocity of each particle is updated in each iteration as given by [96]:

$$\begin{aligned} x_i^{k+1} &= x_i^k + v_i^{k+1}, \\ v_i^{k+1} &= \bar{\alpha} v_i^k + \bar{\beta}_1 \theta_{1,i}^k \left(x_i^{\text{best},k} - x_i^k \right) + \bar{\beta}_2 \theta_{2,i}^k \left(x_{\text{swarm}}^{\text{best},k} - x_i^k \right), \end{aligned} \tag{10}$$

where, $\bar{\alpha}$ represents the inertia factor, $\bar{\beta}_1$ is the cognitive learning rate and $\bar{\beta}_2$ is the social learning rate which influences the exploration and exploitation nature of the particles. The values $\theta_{1,i}^k$ and $\theta_{2,i}^k$ represent random numbers uniformly distributed in the interval $\mathcal{U}[0,1]$. The variable $x_i^{\text{best},k}$ represents the previously obtained best value while $x_{\text{swarm}}^{\text{best},k}$ denotes the best position of the swarm at iteration *k* and expressed as:

$$\begin{aligned} x_i^{\text{best},k} &:= \underset{x_i^j}{\text{argmin}} \left\{ f\left(x_i^j\right), 0 \le j < k \right\}, \\ x_{\text{swarm}}^{\text{best},k} &:= \underset{x_i^k}{\text{argmin}} \left\{ f\left(x_i^k\right), \forall i \right\}. \end{aligned} \tag{11}$$

The PID controllers in the LFC system are tuned with a deterministic step load disturbance but random NCS components. The system with the designed

controller is then tested against various stationary and nonstationary input profiles of load and RES for testing its robustness.

3.1.5 Mathematical Model of the Stochastic Load Demand and Renewable Energy Generation

The power produced due to solar and wind energy depends on the power electronic energy conversion devices, as shown in Figure 3-3 to integrate into the smart grid. The solar power needs a DC-DC converter interconnection and an inverter which has a time constant of T_{IN} and $T_{I/C}$ respectively as described in [97]. Since the induction generator dynamics of a wind generator is faster than the turbine, it is ignored, and the latter is considered as a first-order model using gain K_{WTG} and time constant T_{WTG}.

The uncertainty of the RES generation has been considered in different stochastic profiles used for modelling. The maximum solar and wind power output in each area is limited to 0.01 pu and 0.02 pu, respectively using appropriate bias and gain as analogous to the maximum rating of the solar and wind power installed in each area. The maximum load demand in area 1 is limited to 0.03 pu and 0.025 pu as analogous to the maximum demand contracted by the consumer with the utilities. The mathematical models of various stochastic input profiles are described in the next subsections.

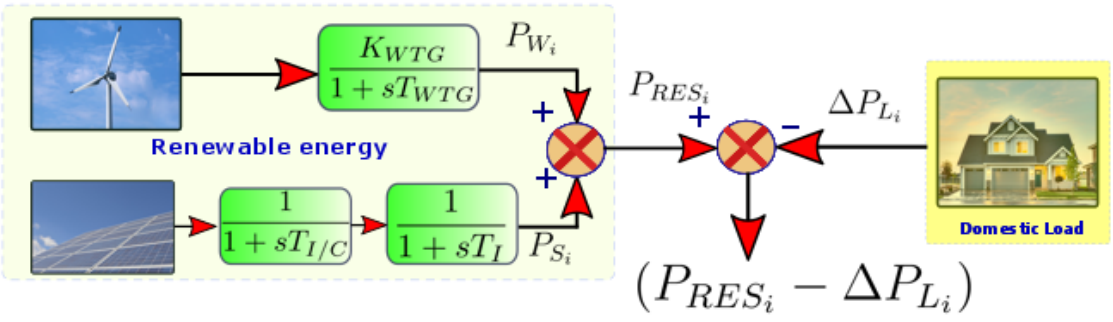

Figure 3-3: RES generation and load model used in the LFC scheme.

3.1.5.1 Filtered White Gaussian Noise (wGn) Profile

The system is tested considering the input profile as wGn as given in [60]. The generated white noise is filtered using a bandpass filter which yields a correlated noise. The transfer function of the bandpass filter used is given by:

$$\tilde{\mathcal{B}}_{bp}(s) = \frac{1}{1800s+1} + \frac{300s}{300s+1}. \tag{12}$$

The random number generated from the wGn generator which has equal intensities at all frequencies is represented by:

$$p_G(z) = \frac{1}{\sigma\sqrt{2\pi}} \exp\left(-\frac{(z-\mu)^2}{2\sigma^2}\right), \tag{13}$$

where, μ represents the mean and σ represents the standard deviation of the signal. For this case, we assume, $\mu = 0$ and $\sigma = 1$. The power generated in (13) is passed through the bandpass filter in (12) to produce a correlated noisy signal which is further conditioned to keep the load demand, solar power and wind power within the given bounds.

3.1.5.2 Nonstationary Synthetic Input Profiles

The wind velocity and solar irradiation can be modelled using various other random number generators (RNGs) e.g. fractional Brownian motion [98]–[100] and geometric Brownian motion [101]–[103]. The wind speed needs to be modelled such that it represents the spatial dependencies of the wind flow. The power production due to wind is highly dependent on the fluctuation of the wind speed, especially at higher values due to the turbulent behaviour. The output of wind power varies with the wind velocity as [104]:

$$P_W(t) = \begin{cases} 130 - 63v(t) + 9.1v^2(t) - 0.3v^3(t) & ;\ 4 < v(t) < 15 \text{ m/s} \\ 140 + 11v(t) - 0.36v^2(t) & ;\ 15 \le v(t) < 26 \text{ m/s} \\ 0 & ;\ v(t) > 26 \text{ m/s}. \end{cases} \tag{14}$$

Here, $v(t)$ is considered as the stochastic variable and $P_W(t)$ is the wind power generated due to the random variable v in (14). Similarly, for solar power, the

solar irradiance Φ is considered as the random variable, which is related to the production of solar PV power as given in [105]:

$$P_{PV} = \eta S \Phi(t)\{1 - 0.005(\mathsf{T}_a + 25)\}, \quad (15)$$

where, the parameter $\eta = 10\%$ is the conversion efficiency of the PV cells, $S = 4084\,\text{m}^2$ is the measured area of the PV array, Φ is measured in kW/m^2 which is the solar radiation of the PV cells and $\mathsf{T}_a = 25^o C$ is considered as the ambient temperature. The nonstationary signals used to model $v(t)$ and $\Phi(t)$ are given as the following two RNGs – fBm and gBm.

3.1.5.3 Fractional Brownian Motion (fBm) Profile

The wind velocity has been modelled as an fBm in [100]. As given in [106], Brownian Motion is defined as $\mathcal{B}$, having the following properties:

- $\mathcal{B}_0 = 0$,
- For $n \geq 1$ and $0 < t_0 < t_1 < .. < t_n$, the increments $\delta\mathcal{B}_{t_0 t_1}, \delta\mathcal{B}_{t_1 t_2}, \ldots, \delta\mathcal{B}_{t_{n-1} t_n}$ are independent,
- For $0 \leq \tilde{s} < t$ we have $\delta\mathcal{B}_{\tilde{s}t} \sim \mathcal{N}(0, t - \tilde{s})$.

For fractional Brownian motion, if $\mathcal{B}(t)$ is the ordinary Brownian motion and H is the Hurst parameter. The parameter has the property satisfying $0 < H < 1$ then, the fBm is defined as the moving average (MA) of Brownian motion $\mathcal{B}(t)$, in which past increments of $\mathcal{B}(t)$ are weighted by $(t - \tilde{s})^{H-1/2}$ [107]. Defining t as the time such that $-\infty < t < \infty$ and ω belonging to the samples space Ω, one can write the Brownian motion as $\mathcal{B}(t, \omega)$. Hence random function $\mathcal{B}_H(t, \omega)$ is defined considering b_0 as the arbitrary real number such that:

$$\mathcal{B}_H(0,\omega) = b_0$$

$$\mathcal{B}_H(t,\omega) - \mathcal{B}_H(0,\omega) = \frac{1}{\Gamma\left(H+\frac{1}{2}\right)}\left\{\int_{-\infty}^{0}\left[(t-\tilde{s})^{H-1/2} - (-\tilde{s})^{H-1/2}\right] d\mathcal{B}(\tilde{s},\omega) + \int_{0}^{t}(t-\tilde{s})^{H-1/2}\, d\mathcal{B}(\tilde{s},\omega)\right\}. \tag{16}$$

For $H = 1/2$, $\mathcal{B}_H(t,\omega)$ represents a Brownian motion. For other value of H, it represents fractional derivative or integral of Brownian motion as defined in [108]. $\Gamma(\cdot)$ represents the Gamma function or generalized factorial. For $H > 1/2$, there is a positive autocorrelation and for $H < 1/2$ there is a negative auto-correlation. The expectation of the function is given by:

$$\mathbb{E}\left[\mathcal{B}_H(t,\omega)\mathcal{B}_H(\tilde{s},\omega)\right] = \tfrac{1}{2}\left(|t|^{2H} + |\tilde{s}|^{2H} - |t-\tilde{s}|^{2H}\right). \tag{17}$$

Solar irradiation is highly nonstationary; hence the analysis does not give the correct value of H, but better trends have been obtained using the detrended fluctuation analysis (DFA) in [99]. The Hurst exponent $H = 0.7$ is obtained for solar irradiation which proves that the signals have a persistent long-range correlation. Considering the homogeneous turbulence of the wind speed as given in [100], Hurst exponent $H = 1/3$ has been considered to model the wind speed. For area 1, the wind speed (v) is considered from 4-15 m/s and in area 2, the wind speed is considered from 0-30 m/s. The wind and solar power are calculated from the wind speed and solar irradiation values from (14) and (15) respectively. The load demand fluctuations as the probabilistic forecast have been tackled in [98] using fBm, as it depends on the range and length of the Hurst exponent. Hence the value of $H = 0.185$ in this work to model the randomness in load demand. The fBm has been simulated in MATLAB using the function `fbm()` from the Wavelet Toolbox [109].

3.1.5.4 Geometric Brownian Motion (gBm) Profile

Next, the stochastic process S_t is considered to follow a gBm as described in [110] if it satisfies the SDE defined as:

$$dS_t = \mu S_t dt + \sigma S_t d\mathcal{B}_t, \tag{18}$$

where, μ is the percentage drift and σ represents the volatility rate where the former models the deterministic trends while the latter explains the unpredictability in the motion. Under Ito's representation, the SDE defined in (18) has the solution:

$$S_t = S_0 \exp\left(\left(\mu - \left(\sigma^2/2\right)\right)t + \sigma\mathcal{B}_t\right), \tag{19}$$

where, S_0 is the initial condition. The nonstationary nature of the process is inferred from the expectation and covariance defined as:

$$\begin{aligned} &\mathbb{E}\left[S_t\right] = S_0 e^{\mu t}, \\ &\mathrm{Var}\left[S_t\right] = S_0^2 e^{2\mu t}\left(e^{\sigma^2 t} - 1\right). \end{aligned} \tag{20}$$

The distributed lag model has been used to predict the local levels of the incoming solar radiation in [103] where it was found that it follows a gBm. Time-varying rate parameter has been used to model the stochastic nature of the RES in [81]. However, as per [103], a constant value also captures the stochasticity of monthly solar irradiation variation. The rate $\left(\mu = 0.014\right)$ and the drift $\left(\sigma^2 = 0.019\right)$ are obtained from [103] to generate the random input profiles for solar irradiation. The solar PV power from the RNG is obtained from (15) using the gBm profile. The gBm has been simulated in MATLAB using the function `gbm()` in the Financial Toolbox [111].

The stochastic behaviour of the energy consumption and wind speed has been discussed in [101], [102] using Ornstein-Uhlenbeck (OU) Brownian motion model. The physical model is based on the motion of the particles of Brownian motion under friction, and it tends to drift towards its long-term mean. It is defined as the solution of the SDE $\left(\varkappa_t\right)$ as:

$$d\varkappa_t = -\theta\varkappa_t dt + \acute{o}d\beta_t, \tag{21}$$

where, $\theta > 0$ and $\acute{o} > 0$. Considering $\varkappa_0$ as constant, we can define the mean and covariance as:

$$\begin{aligned} &\mathbb{E}\left[\varkappa_t\right] = \varkappa_0 e^{-\theta t} + \mu\left(1 - e^{-\theta t}\right), \\ &\operatorname{cov}\left(\varkappa_{\bar{s}}, \varkappa_t\right) = \frac{\acute{o}^2}{2\theta}\left(e^{-\theta|t-\bar{s}|} - e^{-\theta\left(t+\bar{s}\right)}\right). \end{aligned} \tag{22}$$

The SDE (21) is used to model the energy consumption of the multi-area power system in [102]. The OU gBm model has been used in continuous time to represent the wind speed as it models its long term daily cycle in [101], for energy system balancing. Numerical solution of the SDE is defined in [112]. Here, the OU process is defined as the univariate Markov process X that evolves with time *t* as per the Langevin equation with its update formula given as:

$$X\left(t + \Delta t\right) \approx X\left(t\right) - \frac{1}{\tau}X\left(t\right)\Delta t + c^{1/2}\backsim\left(\Delta t\right)^{1/2}, \tag{23}$$

where, $\backsim$ represents the sample value of the unit normal random variable with mean zero and variance 1, τ represents relaxation time and *c* represents diffusion constant. Based on the Langevin equation, the constants τ and *c* can be defined to represent the parameters of the SDE defined as:

$$\tau = 1/\theta, c = \acute{o}^2. \tag{24}$$

The values of $\left\{\theta, \acute{o}\right\}$ for the load demand and wind velocity are obtained in [101], [102]. The wind velocity is converted into equivalent wind power using the model in (14).

3.1.5.5 Real Datasets as the Input Profiles

Beside synthetic profiles as described above, real data is used from the Dalrymple ESCRI battery energy project [113] where the load demand, solar irradiation and wind power values are obtained at 4-sec, 1 min and 4-sec interval respectively. One-month data has been used for our analysis. The per-second values are generated using a higher-order interpolation algorithm `interp1( )` in Matlab with modified Akima method as described in [114], although other

interpolators could have been used as well. After the data is read and partitioned as per 5 mins interval, it is conditioned (by adjusting the gain and bias) so that the output value is within the given prescribed limits. Randomly selected 1000 samples (out of ~8350) are used in the simulations. The solar power is obtained from the solar irradiance values using (15). Since in the real data, for some instants, the solar and wind power are not available, care has been taken that the data is normalized and cleaned before using in the LFC simulations.

3.1.6 Controller Tuning Results

3.1.6.1 Tuning of Swarm Optimization Based Controller

The PSO algorithm, as described in (59), is used to minimize the stochastic objective function in (9) for tuning the two PID controllers simultaneously through a random search and optimization process. Simulations were run on a Windows PC Intel Xeon E5-2687W CPU, 3 GHz processor with 12 parallel cores. The LFC model in Simulink is run with the `ode8( )` Dormand Prince solver with a fixed step size of 0.1 sec. The default recommended values $\overline{\alpha}, \overline{\beta_1}, \overline{\beta_2}, \theta_{1,i}^{k}, \theta_{2,i}^{k}$ has been considered in the PSO algorithm as in [115], using the function `particleswarm()` from the Global Optimization Toolbox in MATLAB [116]. Objective function tolerance value of 10^{-6} has been used for convergence of the PSO algorithm. The search range for the three controller gains is $\{K_p, K_i, K_d\}_i \in \mathcal{U}[-1,1]$ for both the areas and the filter constants $N_i \in \mathcal{U}[0,1]$, using 80 particles to navigate the 8D controller parameter space for both the areas. The search ranges were limited to ensure faster convergence of the optimizer. The optimum PID controller parameters are obtained considering a 0.01 pu step load change in area 1 and a 0.02 pu step load change in area 2. Tuning both areas with different magnitude of step input makes the LFC scheme more robust to other disturbances. The PSO algorithm has been run 10 times independently with the convergence characteristics shown in Figure 3-4, with the best solution found in each iteration from a stack of all datapoints visited in the random search process. It is observed that in some cases the PSO algorithm converges quickly, while in some others, it converges after a larger number of iterations which is due to the high complexity of the proposed LFC with NCS considerations. The best controller parameters for the LFC system is considered in the run, which yielded

the lowest objective function value. Average time for convergence of the 10 PSO runs is 3500 seconds $\approx$ 58.33 minutes, as shown in Figure 3-4.

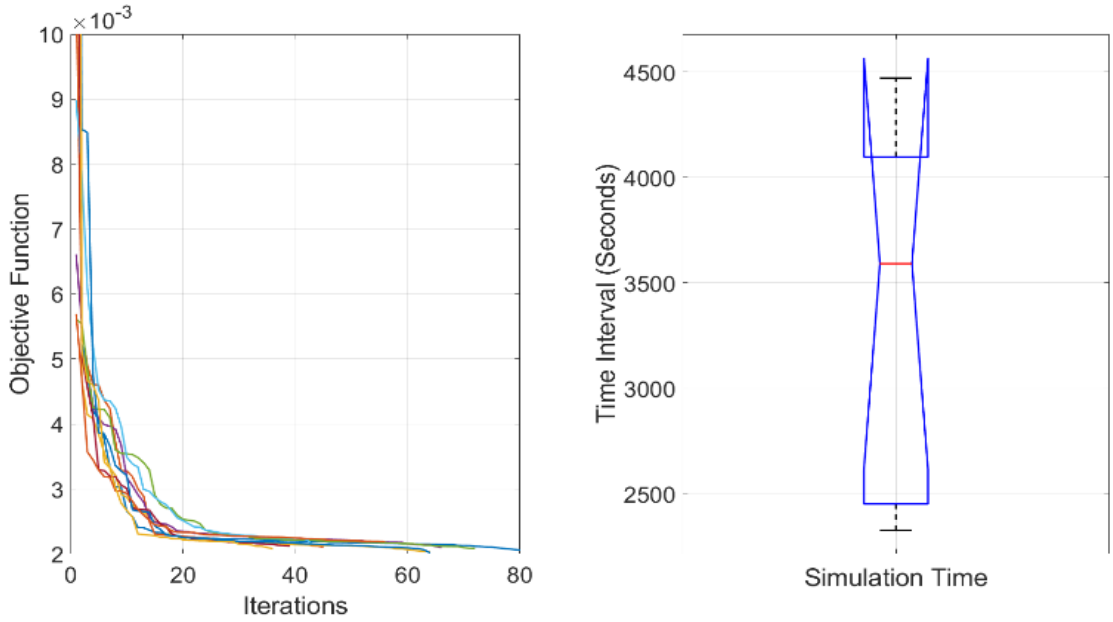

Figure 3-4: (left) 10 independent simulation runs of PSO and its convergence characteristics, (right) total time taken for PSO to converge.

The objective function values traversed by the particles in the successive PSO iterations are stacked together to visualize the exploration characteristics. Moreover, in the search process, the feasible or stabilizable region are also obtained in the controller parameter space [117]. The J_{best} obtained from $x_{\text{swarm}}^{\text{best},k}$ is plotted in Figure 3-5. It shows the pairwise approximate bivariate distribution of the objective function as a function of the PID controller parameters in both the areas. The sampled data points shown in Figure 3-5 correspond to a threshold of $J_{\text{best}} < 0.01$. The colorbar represents the objective function values which converge towards the expected global minima of the stochastic objective function. The graph shows a nonconvex pattern revealing the need of meta-heuristic optimization and the trajectory of the particles moving towards the expected minima after randomly navigating the objective function space. We observe a thicker blue patch for area 1 as compared to area 2, which suggests that the particles moved towards the minima faster in area 1 as compared to area 2, which can be primarily accounted due to smaller magnitude of the load

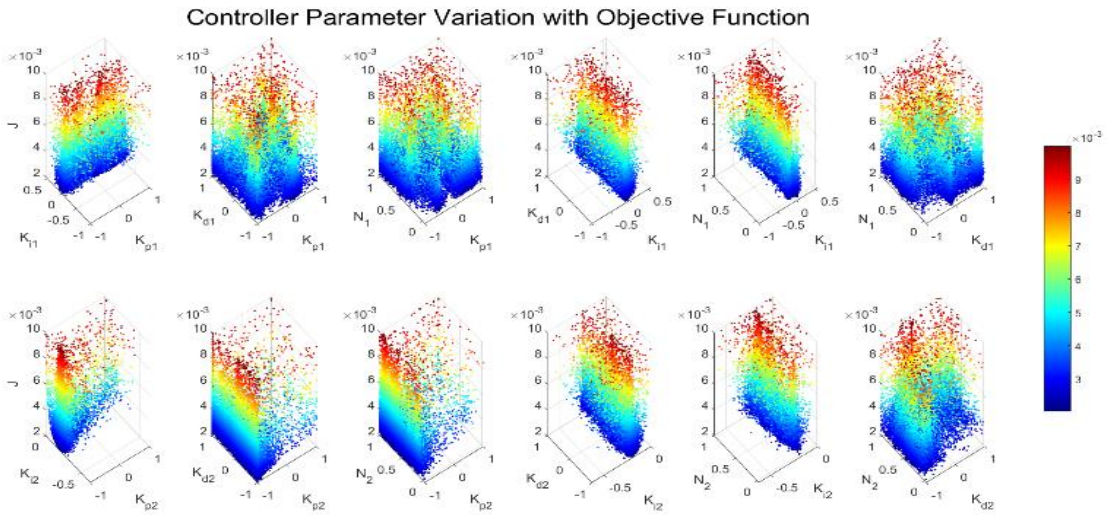

Figure 3-5: Convergence/bivariate distribution of the objective functions in terms of the PID controller parameters; (top panels) area 1, (bottom panels) area 2.

disturbance in area 1 as compared to in area 2. The exploration of the particles in the joint controller parameter space is shown in Figure 3-6. It reveals the stabilizable region in the controller parameter space. The cluster of particles around the optima is thicker for area 1 as compared to the one in area 2, which indicates that the convergence for area 2 is slower than area 1.

3.1.7 System Response with Step Load Disturbance on Non-Linear LFC

Deterministic step inputs of 0.01 pu and 0.02 pu are now applied in two areas, and the responses are analyzed. Since the parameters in the NCS like a_{DoS} and τ_d are sampled from the respective stochastic processes, the grid frequency fluctuations are analyzed considering 100 Monte Carlo system simulations and shown in Figure 3-7 for three different packet dropout levels. The controller tuning was done considering 99% packet drop probability. The random delay parameter has been considered as per the works in [57], [87], [88] .

The maximum frequency fluctuations $\left(\Delta f_i\right)_{\max}$ obtained in our case are lesser than as it was obtained in benchmarks results by Nanda et al. [118] and also for similar step load responses, albeit being tested on a much complex LFC model. The response is also better than the complex LFC model considering the time delay in [119] with a PID controller. Our results are also better in terms of

maximum deviation $(\Delta f_i)_{\max}$ for the LFC problem with time delays reported in [120], [121], [122] where $(\Delta f_i)_{\max}$ *is* $5\times10^{-3}, 5\times10^{-3}$ and 0.1 pu, respectively.

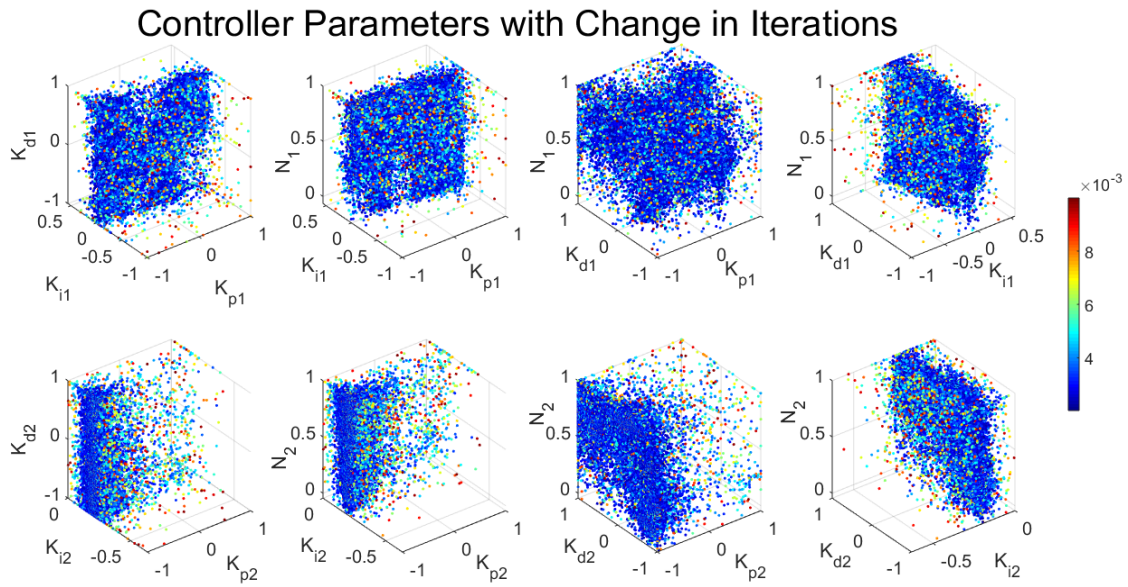

Figure 3-6: Multivariate distribution or feasible/stabilizable region in the PID controller parameters $\{K_p, K_i, K_d, N\}$. Colorbar represents ISE values.

Similarly, event-triggered problems with cyber-attack for LFC solved in [65], [66], [123] have $(\Delta f_i)_{\max}$ as 0.05 ,0.06 and 0.04 pu respectively. Combination of cyber-attack and time delay was studied in [72], which resulted $(\Delta f_i)_{\max}$ as 2×10^{-5} pu, but the time delay (τ) was considered to be quite small. The cyber-attack considered in [72] is limited by frequency and time duration, unlike this work, where a much higher packet drop rate is considered.

Moreover, previous analyses were conducted mostly on simpler LFC models without considering any nonlinearities in the energy storage components. The control performance is superior in our work as compared to these because they mostly used some variants of convex optimizers like linear matrix inequalities (LMIs), semi-definite programming on simpler linear LFC models. These methods can ensure guaranteed convergence to global optima, considering the objective function being convex. However, in the present work, the models contain significant nonlinearities along with stochastic network induced delays and packet drops which makes the problem nonconvex. These realistic effects make the

optimization problem intractable using the traditional convex optimization algorithms. It is better solved by meta-heuristic global optimizers involving nonconvex multi-agent search like PSO, which gives an improved performance.

The oscillations in the grid frequency can be compared to the results reported in [124] where the controller was tuned using computational intelligence techniques for a complex LFC with similar load changes in both the areas. The stochastic simulations conducted for different cases of packet drops and random delays are shown in Figure 3-8 and Figure *3-9*. It is evident in Figure 3-8 that since the controller was tuned for 99% packet drop, the control input moving towards the steady-state value even though only fewer packets are successfully transmitted. However, when the packet transmission rate is even lower, the delayed control signal starts oscillating. The control signals transmitted at an average 0.5% rate makes it oscillatory. However, when the packet transmission rate is reduced to 0.1%, the delayed control signals get unbounded and makes the LFC system unstable. Hence, we observe that with sparse packet transmission, control inputs work on a lesser amount of discrete levels exposing the system with a higher switch in control input magnitude. The effect of the control signal at several discrete levels is seen in Figure 3-8 and Figure *3-9*. Figure 3-9 shows the comparison of having and not having random delays in the NCS as the delay makes the control signal larger and more oscillatory.

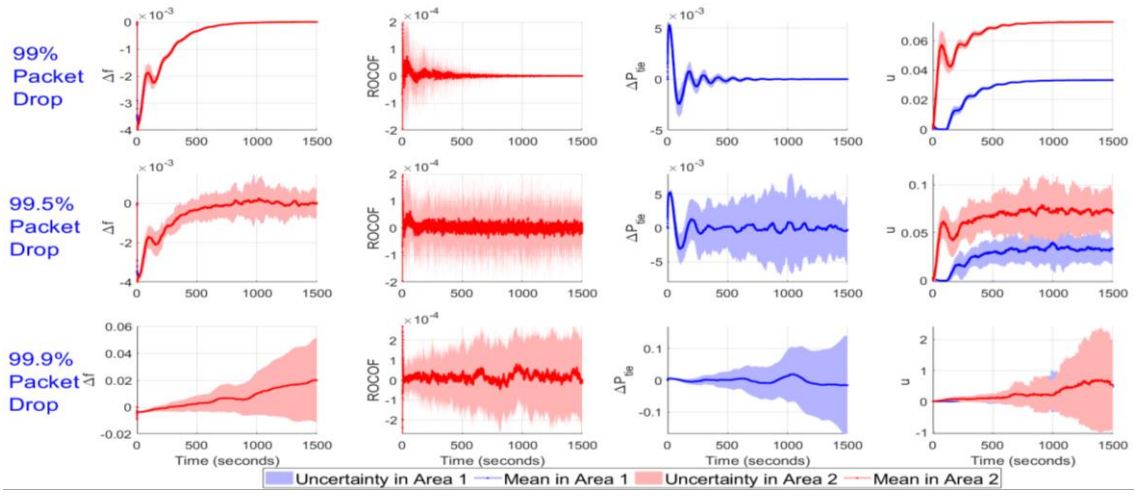

Figure 3-7: Step response of proposed LFC with 99%, 99.5% and 99.9% packet drops as the DoS attack on both the areas with 100 Monte Carlo simulations.

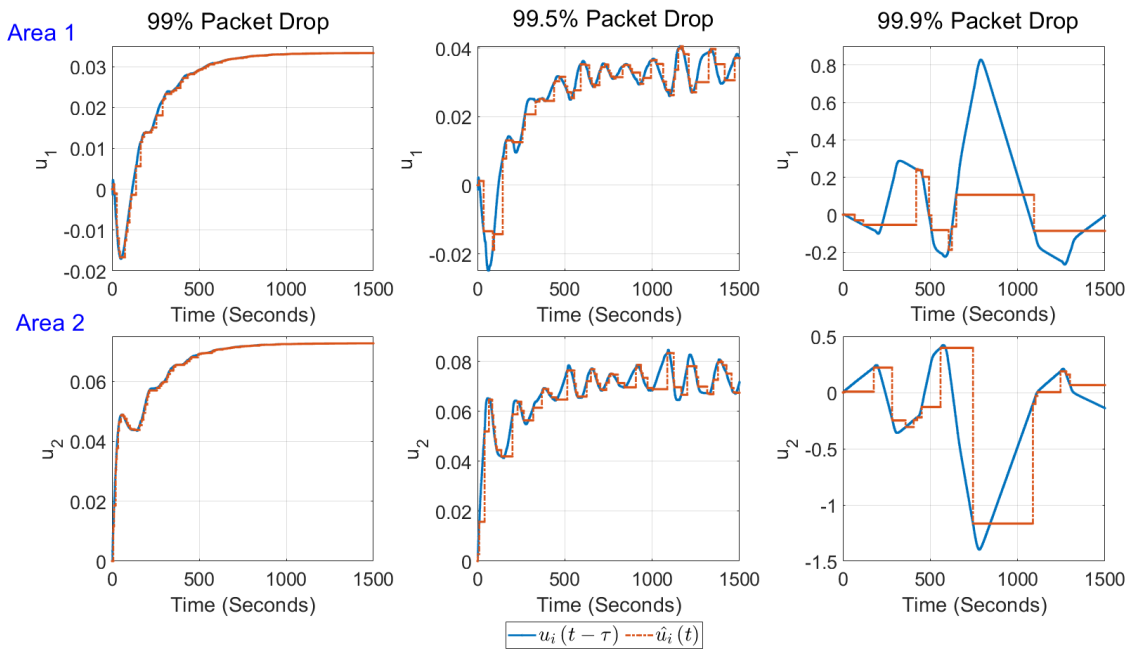

(a)

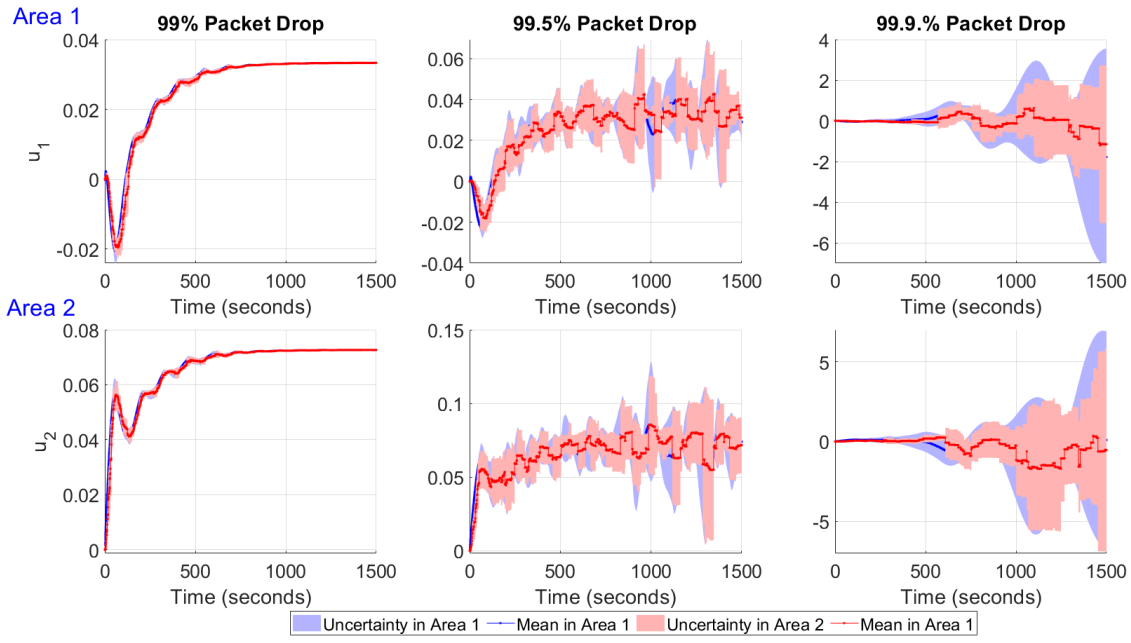

(b)

Figure 3-8: (a) Simulations of the delay-free and randomly delayed control signal for two areas with 99%, 99.5% and 99.9% packet drop. (blue)-randomly delayed control signal (red)-control signal with random delay and dropout. (b) Simulations of the delayed control signal for two areas with 99%, 99.5% and 99.9% packet drop.

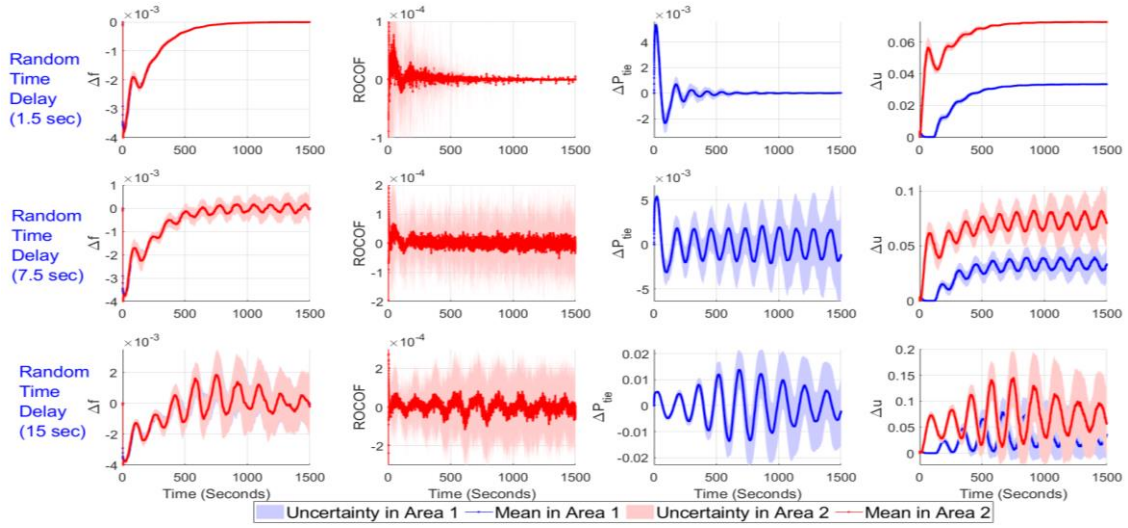

Figure 3-9: Step response of the LFC with μ_d = 1.5 seconds, 7.5 second and 15 seconds of random delay with 100 Monte Carlo runs.

Since the system was tuned with 1% packet transmission, the system is stable with the fluctuations being relatively small. The tie-line power fluctuations also quickly settle to steady-state values after the initial oscillations. The effect of stochasticity imposed by the imperfect communication networks is also small in case of 1% packet transmission, as we see a small deviation band between the ensemble runs. However, when p_{drop} is increased to 99.5%, the stochastic nature of the NCS becomes predominant, creating a more considerable fluctuation in the frequency, thus causing oscillations in tie-line power. The higher deviation between the simulated ensembles is also observed, which is mainly because the control packet is working at higher discrete levels, as seen in Figure 3-8. When p_{drop} is increased to 99.9%, the time instants of transmission decreases, which furthermore reduces N. Under these NCS settings, the oscillatory behaviour of the LFC system increases, making the system unstable.

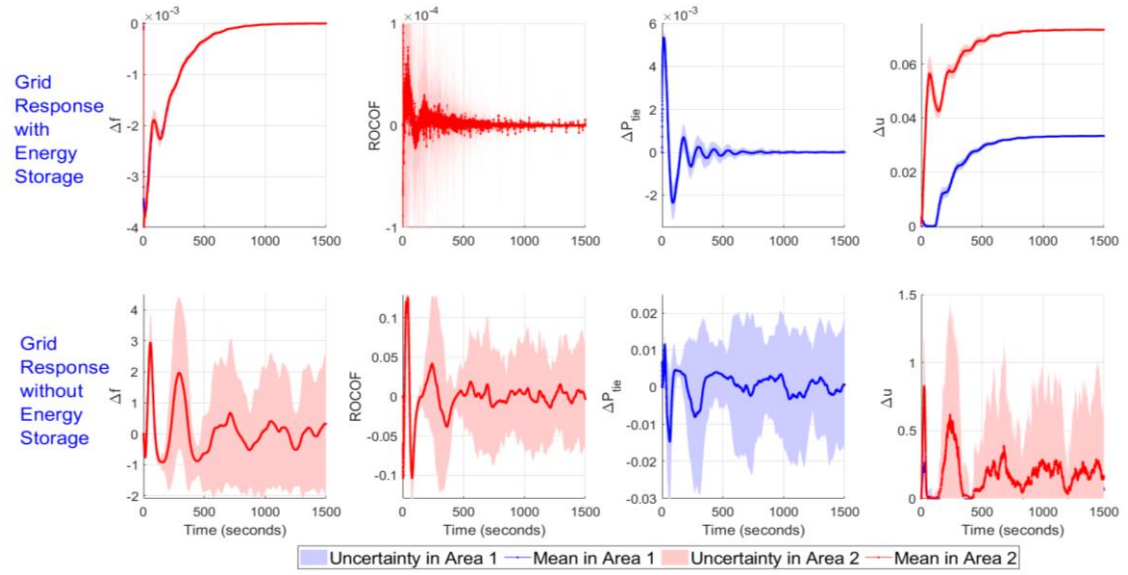

Figure 3-10: Step response of the system with and without energy storage elements with 100 Monte Carlo runs.

A similar effect is also visible by increasing the value of μ_d in the random time delay (τ_d) samples in the simulation as observed in Figure 3-9. An increase in the magnitude of the grid frequency and tie-line power is observed with the increase in μ_d. Even though μ_d is increased 10 times with the nominal controller parameters, it increases the oscillations of the systems, but it does not make the system to be unstable, unlike reduction in packet transmission rates. It confirms the fact that in an LFC problem as an NCS, the DoS cyberattack in the form of a high rate of packet losses are much more detrimental than simpler random communication delays. As observed in Figure 3-9, the effect of stochastic delays is reflected on the grid frequency fluctuations uncertainty over the ensembles. The uncertainties increase as we increase the value of mean time delay. Similar increase in uncertainty is also observed in tie-line power and control input.

Energy storage devices play an essential role in keeping the frequency fluctuations within specified limits and shown in Figure 3-10. The LFC system will undergo higher fluctuations without the presence of energy storage elements. The frequency and the ROCOF fluctuations obtained without energy storage in Figure 3-10 are unacceptable and might cause the relays in the protective system to trip, hence affecting the grid operation. Thus, while integrating stochastic RES

generation profiles, it is essential to tune the LFC system with energy storage elements.

3.1.8 Testing an Statistical Analysis with Stochastic RES and Load Demand Profiles on Non-Linear LFC

The LFC system with the PID controller parameters obtained has now been tested against stochastic profiles which has been defined in Section 0 after 100 Monte Carlo simulation runs on a Windows PC with Intel Core i5-8500 CPU, 3 GHz processor with 6 parallel cores. However, due to the complexity of the system, it becomes computationally intensive to run the Monte Carlo runs. The computation breaks down if the memory is not cleared after subsequent runs. The LFC model in Simulink was numerically integrated with $\texttt{ode8}(\ )$ Dormand-Prince solver with a fixed step size of 0.01 seconds.

The simulation was run for 300 seconds, thus generating 30000 samples per run. The memory was subsequently cleared after running the simulation 10 times, thus improving the computing performance of the algorithm. The input solar power generation and load demand profiles are generated based on 100 Monte Carlo simulations of the models as described before. The input files are generated in a batch of 10 Monte Carlo iterations and automatically saved, in order to reduce the memory overload of the PC while testing. The input profiles, as shown in Figure 3-11, is generated by reading each of these stored files. The variations in the wind power input profiles in the case of fBm and gBm for different areas are due to the consideration of the different range of wind speeds in the respective areas. The ROCOF fluctuations are calculated as per 0.1-sec interval as per the IEEE standards [75]. It is evident from Figure 3-12, Figure 3-13 and Figure 3-14 that the frequency fluctuations and the ROCOF are within the prescribed limits for connecting the RES to the smart grid [75] for different RNGs as filtered Gaussian, fBm, gBm and real data respectively. The standard for over-frequency (OF) and under-frequency (UF) trips are defined as 1.2 and 1.5 Hz (for 60 Hz grid) which turns out to be 0.02 and 0.025 pu respectively. It is evident from our results that the maximum fluctuations $\left(\Delta f_i\right)_{\max}$ are 0.0015 pu in the case of filtered Gaussian inputs, 0.004 pu in case of fBm and gBm input profile and

0.0035 for real data set which are much below the prescribed limit, hence showing the efficacy of the designed LFC system for future smart grids with NCS considerations. The results obtained is also better than the $\left(\Delta f_i\right)_{\max}$ obtained in [57], [59], [125], [126], [127], [128], [60] where this value lies in the range of 0.02, 0.1, 0.01, 0.02, 0.2 and 0.025 pu respectively where the LFC contains stochastic RES models.

The ROCOF for the IEEE standard is given as 0.5 Hz/sec (for 60 Hz grid), considering the minimum specifications in [75] which are calculated as 0.008 pu. We see in Figure 3-12, Figure 3-13 and Figure 3-14 that the maximum ROCOF are within 0.002 pu in the case of Gaussian input, 0.0005 pu in the case of fBm input, 0.003 pu in the case of gBm input and real input profile, which is bounded within the prescribed standards, showing the strength of our LFC design as a NCS.

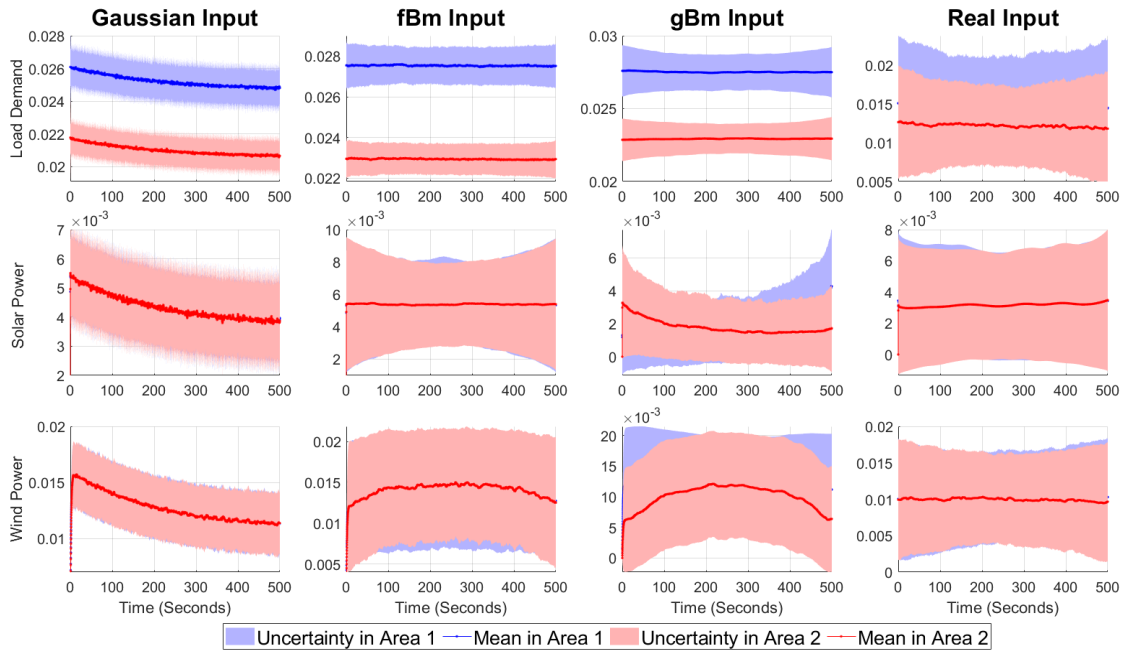

Figure 3-11: Stochastic input, real RES and load demand profiles for the smart grid LFC with the 100 Monte Carlo runs.

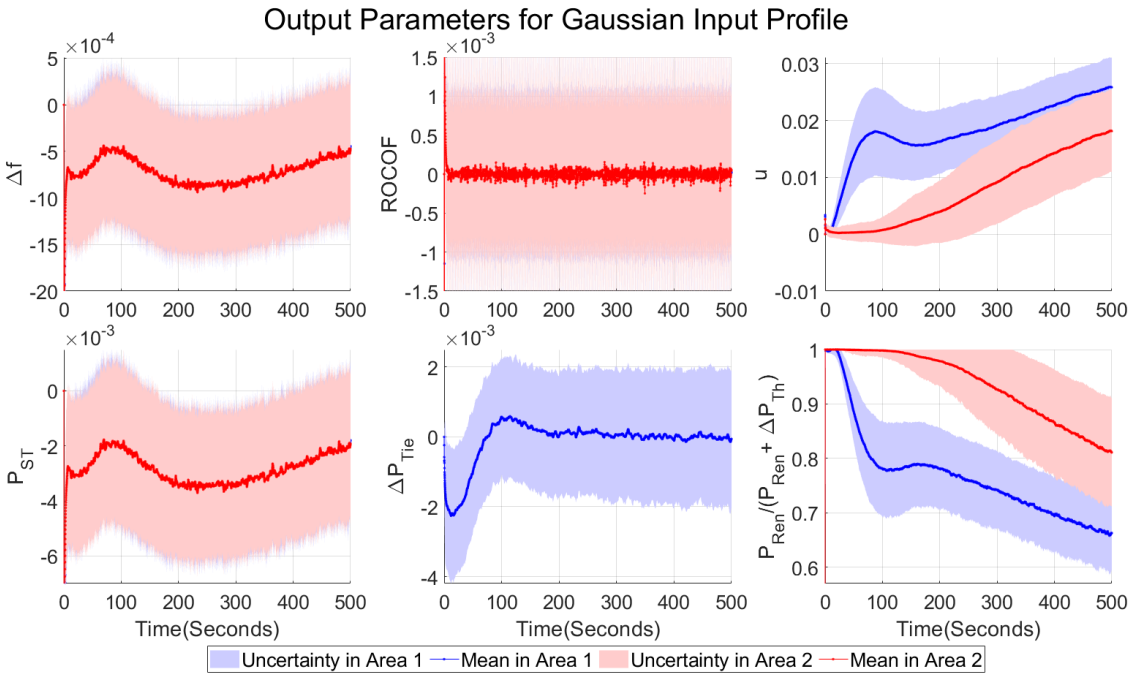

Figure 3-12: Smart grid performance indicators for Gaussian input profile: (top left) frequency deviation, (top center) rate of change of frequency, (top right) control input to the thermal power plant, (bottom left) energy storage output, (bottom center) tie-line power between two areas, (bottom right), proportion of renewable energy usage for the 100 Monte Carlo runs.

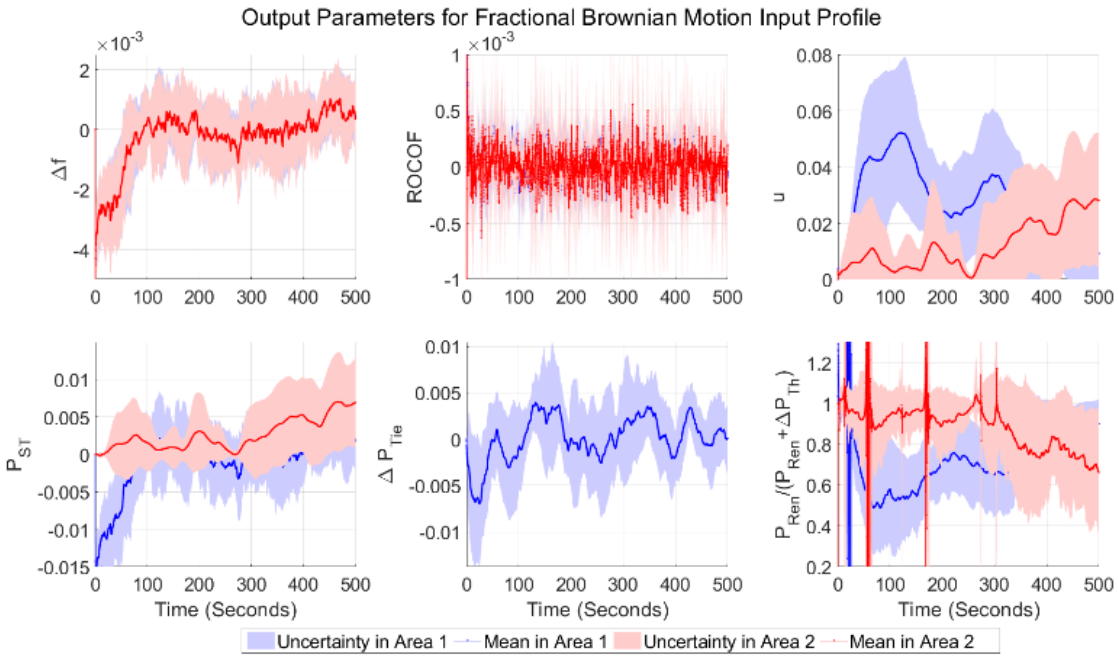

Figure 3-13: Smart grid performance indicators for fBm input profile: (top left) frequency deviation, (top center) rate of change of frequency, (top right) control input to the thermal power plant, (bottom left) energy storage output, (bottom center) tie-line power between two areas, (bottom right), proportion of renewable energy usage for the 100 Monte Carlo runs.

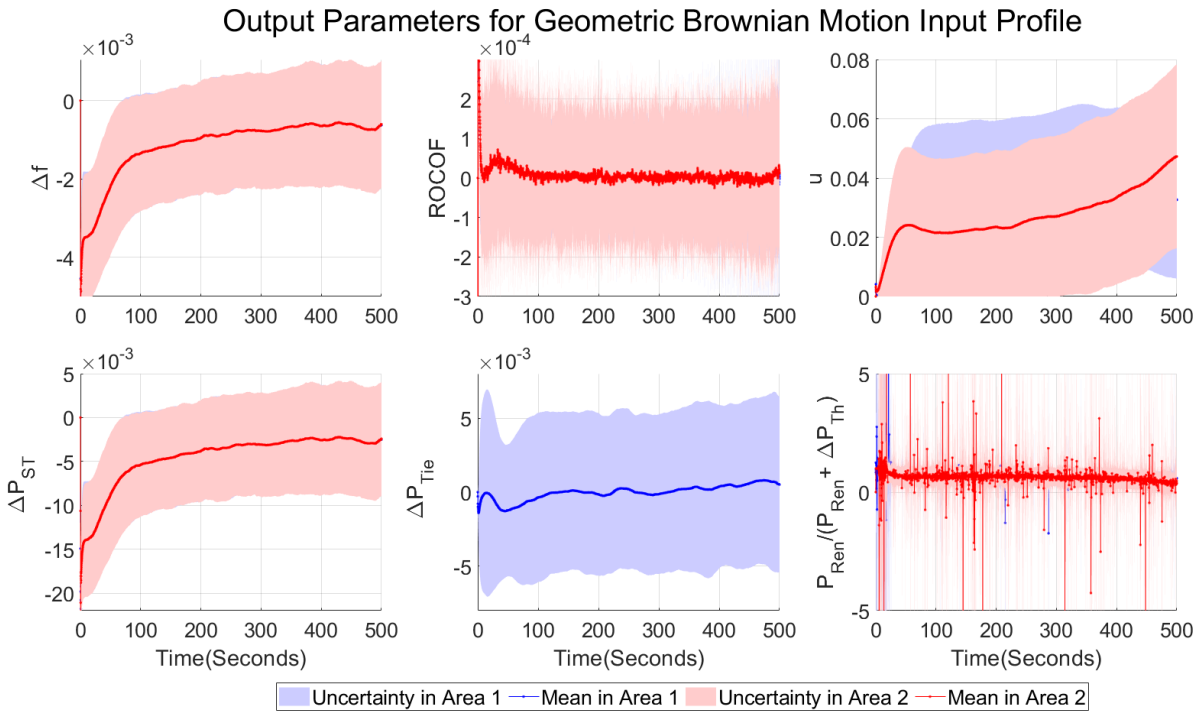

Figure 3-14: Smart grid performance indicators for gBm input profile (top left) frequency deviation, (top center) rate of change of frequency, (top right) control input to the thermal power plant, (bottom left) energy storage output, (bottom center) tie-line power between two areas, (bottom right) proportion of renewable energy usage for the 100 Monte Carlo runs.

The thermal power generation reduction against these profiles are analyzed along with the frequency deviation in both the areas. In order to monitor the utility of the proposed LFC scheme, we calculate a custom parameter as the ratio between the renewable power generation and the total generation using both the renewable and thermal units as:

$$PP_{ren} = \left(100 \times P_{ren}\right) / \left(\Delta P_{th} + P_{ren}\right), \tag{25}$$

where, ΔP_{th} represents a change in thermal power plant output meeting the stochastic load demand and P_{ren} represents the power generated by RES. We have now analyzed the results based on the values of PP_{ren} :

Case 1

$$PP_{ren} < 0 \Rightarrow \left(\Delta P_{th} + P_{ren}\right) < 0 \Rightarrow \Delta P_{th} < 0 \text{ since } P_{ren} \geq 0,$$

Case 2

$$0 < PP_{ren} < 1 \Rightarrow 0 < P_{ren} < \left(\Delta P_{th} + P_{ren}\right) \Rightarrow \Delta P_{th} > 0 \ \text{since} \ P_{ren} \geq 0,$$

Case 3

$$PP_{ren} > 1 \Rightarrow P_{ren} > \left(\Delta P_{th} + P_{ren}\right) \Rightarrow \Delta P_{th} < 0 \ \text{since} \ P_{ren} \geq 0. \quad (26)$$

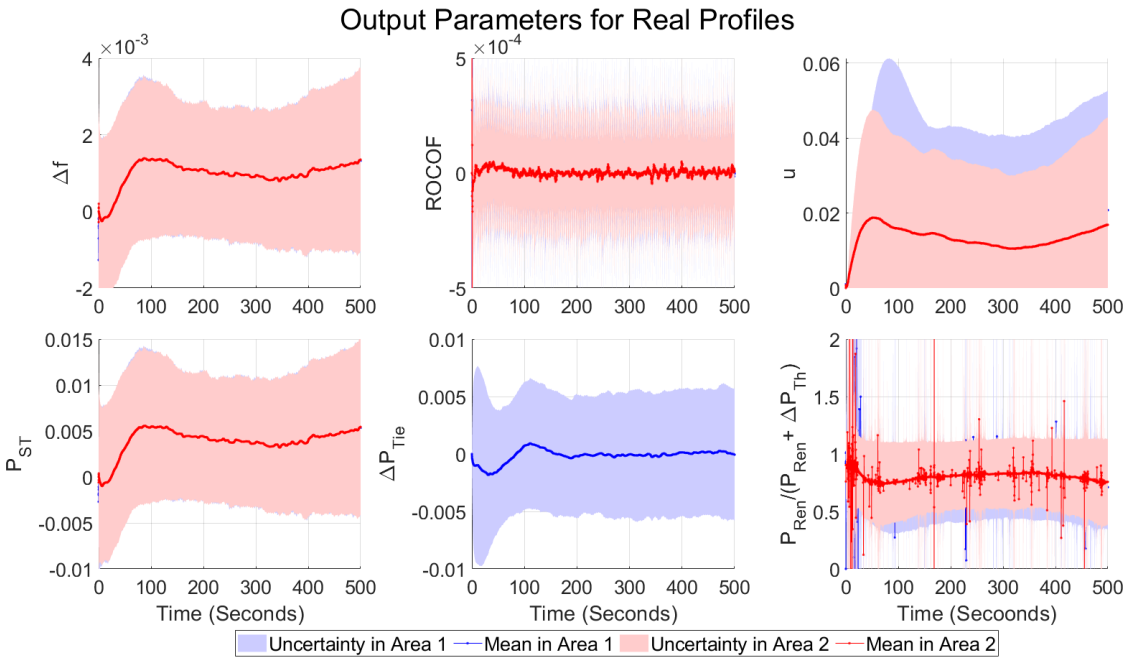

Figure 3-15: Smart grid performance indicators for real input profile (top left) frequency deviation, (top centre) rate of change of frequency, (top right) control input to the thermal power plant, (bottom left) energy storage output, (bottom centre) tie-line power between two areas (bottom right) proportion of renewable energy usage for the 100 Monte Carlo runs.

We observe from Figure 3-14, the value of the $PP_{ren} > 1$ for some time instants, hence $\{\Delta P_{th}\}_i < 0$, for real power profile. It suggests that there is a reduction in the thermal power plant output. Similar trends are also observed for system response for fBm and gBm inputs in Figure 3-13 and Figure 3-14, especially in the latter case where the maximum value of PP_{ren} goes beyond ± 5 suggesting that there is a considerable reduction in thermal power plant output $\{\Delta P_{th}\}_i$. The control inputs to the actuators are constrained to be positive which ensure that the thermal power plants are always operated to meet the base-load demand but otherwise will maintain a minimum constant firing rate or increase the firing when the RES and storage elements together are incapable of meeting the increase in

load demand. We can analyze the operation from the energy balance model. Since RES and thermal power plant produce power, we can write the expression of total power generated $\left(\mathrm{P}_{\mathrm{Gen}}\right)_i$ for each area *i* as:

$$\text{Power Generated } \left(\mathrm{P}_{\mathrm{Gen}}\right)_i = \left(\mathrm{P}_{\mathrm{ren}} + \Delta\mathrm{P}_{\mathrm{th}}\right)_i . \tag{27}$$

Considering energy storage devices as power-consuming devices, we can write the total power consumed as:

$$\text{Power Consumed } \left(\mathrm{P}_{\mathrm{Con}}\right)_i = \left(\mathrm{P}_{ST} + \Delta\mathrm{P}_L\right)_i . \tag{28}$$

Since the frequency fluctuations due to renewable energy sources are within limits, we can consider the energy balance condition is met. Hence from (27) and (28) we can write:

$$\begin{aligned} &\left(\mathrm{P}_{\mathrm{ren}} + \Delta\mathrm{P}_{\mathrm{th}}\right)_i \approx \left(\mathrm{P}_{ST} + \Delta\mathrm{P}_L\right)_i \\ &\Rightarrow \left\{\Delta\mathrm{P}_{\mathrm{th}}\right\}_i \approx \left\{\mathrm{P}_{ST} + \Delta\mathrm{P}_L - \mathrm{P}_{\mathrm{ren}}\right\}_i . \end{aligned} \tag{29}$$

Since for fBm, gBm and real input profiles $\mathrm{PP}_{\mathrm{ren}} > 1$, it is apparent that $\left\{\Delta\mathrm{P}_{\mathrm{th}}\right\}_i < 0$ .Thus we can infer from (29):

$$\left\{\mathrm{P}_{ST} + \Delta\mathrm{P}_L - \mathrm{P}_{\mathrm{ren}}\right\}_i < 0 \Rightarrow \left\{\mathrm{P}_{ST}\right\}_i < \left\{\mathrm{P}_{\mathrm{ren}} - \Delta\mathrm{P}_L\right\}_i \tag{30}$$

This means that the energy storage charging rate is not high enough to absorb the excess power generated by the renewable energy source. Hence thermal power plant output has to be reduced at some time instants. However, the value of $\mathrm{PP}_{\mathrm{ren}}$ is between $(0,1)$, as shown in Figure 3-12 when the RES and load are modelled by a Gaussian profile, which suggests that thermal power plant output is $\left\{\Delta\mathrm{P}_{\mathrm{th}}\right\}_i > 0$, which can be analyzed using the relation in (29) as:

$$\left\{\mathrm{P}_{ST} + \Delta\mathrm{P}_L - \mathrm{P}_{\mathrm{ren}}\right\}_i > 0 \Rightarrow \left\{\mathrm{P}_{ST}\right\}_i > \left\{\mathrm{P}_{\mathrm{ren}} - \Delta\mathrm{P}_L\right\}_i \tag{31}$$

As per the relation in (31), the discharging dynamics of energy storage elements are not fast enough to meet the load. Hence thermal power plant output is positive in the case of Gaussian input profiles. We also observe a common trend in these simulations that the fluctuations in energy storage outputs $\left\{\mathrm{P}_{ST}\right\}_i$ is similar to the frequency fluctuation of the grid. Similar patterns are observed in the control

signals to the thermal power plant, as shown in all the 4 stochastic input profile. The tie-line power exchange of nonstationary profiles like fBm and gBm are similar to the real input profile as compared to the Gaussian input profile. The similarity of the profiles can be ascertained more strongly in the next section by considering the norms of the frequency fluctuations and tie-line power and multivariate statistical analyses of the grid parameters.

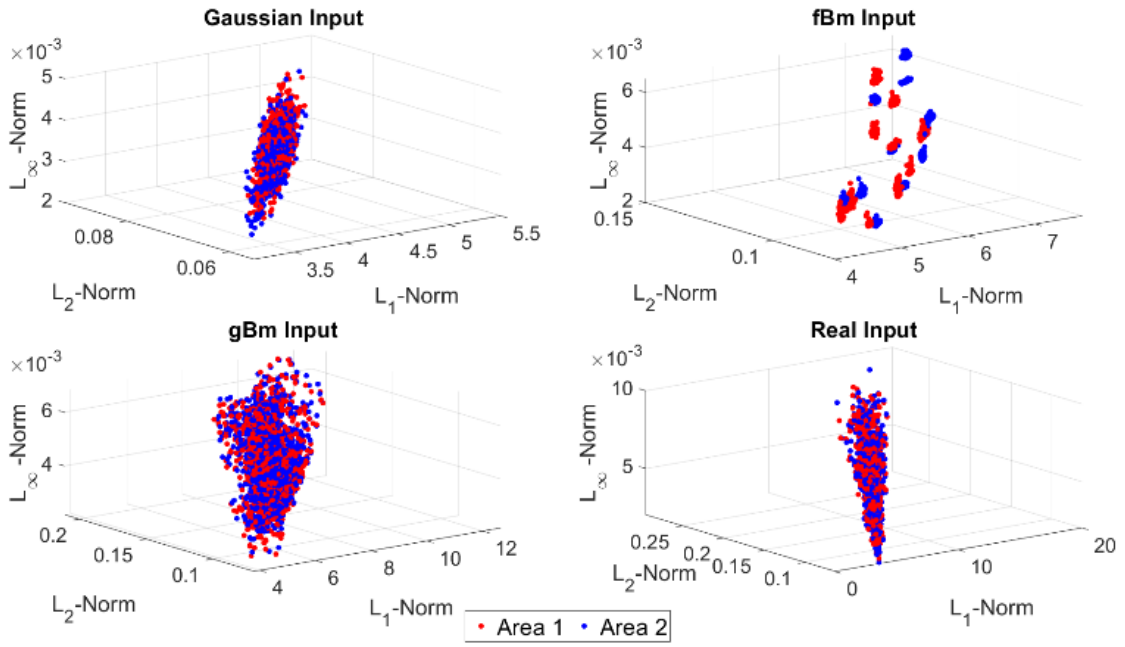

Figure 3-16: Scatter-plots of the L_1, L_2 and L_∞ norms of the frequency fluctuations with different RNGs: (left top) Gaussian inputs, (left-right) fBm inputs, (left bottom) gBm inputs, (right bottom) real inputs.

3.1.9 Hypothesis Testing Using the Datasets of Frequencies of Each Area and the Tie-Line Power Fluctuations

The norms of the simulated signals $\{\Delta f_1, \Delta f_2, \Delta P_{tie}\}$ from the LFC system are calculated next, considering the samples after 10 sec which discards the initial transient behavior of the solar and wind power generation systems due to filtered RNGs. The *p*-norm of a real valued signal $\bar{x} = \{\bar{x}_1, \ldots, \bar{x}_n\}$ is given as:

$$\|\bar{x}\|_p := \left(\sum_{i=1}^{n} |\bar{x}_i|^p \right)^{1/p}. \tag{32}$$

For p = 1, the $\|\bar{x}\|_1$ represents the projection of the signal $\bar{x}$ on the coordinate axis. For p = 2, $\|\bar{x}\|_2$ represents the Euclidean distance of the signal $\bar{x}$ from the origin. In the case of Δf , L_1-norm and L_2-norm represent the absolute deviation and squared deviation from the ideal value. The L_∞-norm of the signals are defined as:

$$\|\bar{x}\|_\infty := \max\left(|\bar{x}_1|,\ldots,|\bar{x}_n|\right). \tag{33}$$

It represents the maximum value of a signal along its length. In the case of $\{\Delta f\}_i$, it is defined as the maximum deviation from the ideal value. The frequency fluctuations are now visualized by a scatter plot between their L_1, L_2, L_∞-norms of the signals, obtained from the Monte Carlo runs, as shown in Figure 3-16.

We can observe from Figure 3-16 that the frequency fluctuation is highest and lowest in the case of real and Gaussian input profiles, respectively, which is evident from the L_1 and L_∞ norm axes. Lower fluctuation in the L_1 and L_∞ norm plots in the case of Gaussian input profile can be attributed due to the value of PP_{ren} between 0 and 1 thus making the $\Delta P_{th} > 0$ whose dynamics are slower than the RES, hence damping out the fluctuations. Higher L_1 and L_∞ norm in case of real input profiles can be attributed due to solar/wind power being zero at particular time instants since the power plant outputs have to deal with the stochastic nature of the load profiles. Range of variation of different norms are similar in case of fBm and gBm input profiles, but few small island formations are seen in the signal norms for the former case, which is because $\{\Delta f\}_i$ has high-frequency components in case of fBm profile as compared to gBm. These differences in the pattern can be attributed due to higher complexity captured by the Hurst exponent H in the input profile, causing wilder fluctuations. The hypothesis test is conducted on the L_1, L_2, L_∞-norms of the frequency fluctuation signals $\{\Delta f\}_i$ and tie-line power fluctuation ΔP_{Tie}, as obtained from the Monte Carlo runs for different stochastic generation and demand profiles as shown in Figure 3-16. The similarity in the system operation for different stochastic profiles can be analyzed by comparing the respective p-values and χ^2-values obtained

from the nonparametric Kruskal-Wallis hypothesis testing, as shown in the boxplot Figure 3-17. In order to decide whether to perform a parametric or nonparametric test on the processed data (and derived signal norms), it is necessary to check their univariate normality.

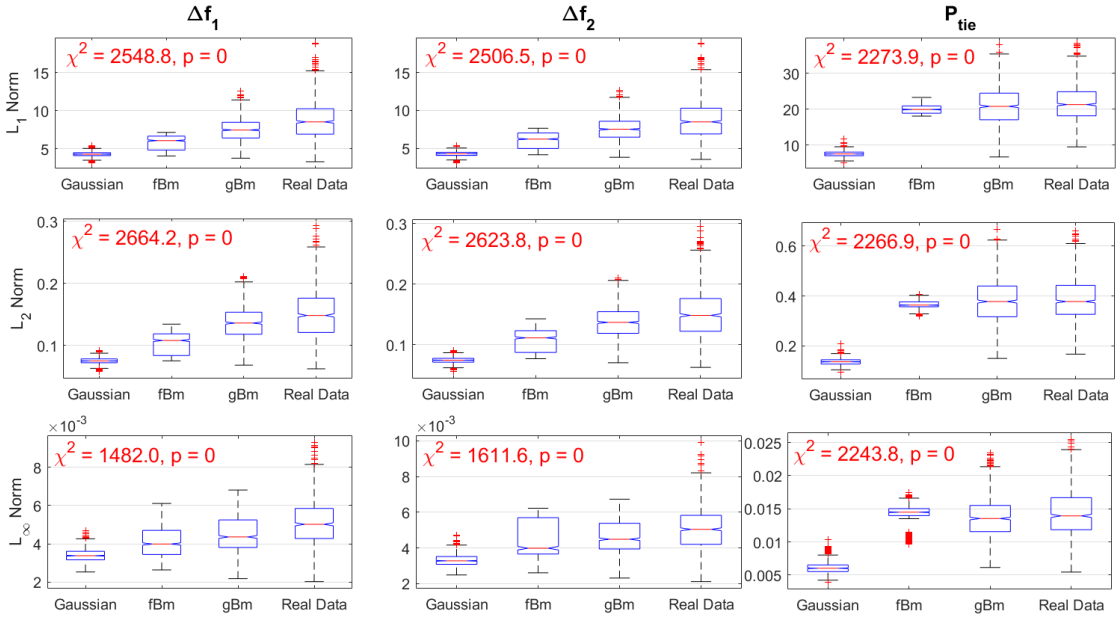

Figure 3-17: Box-plots of the L_1, L_2 and L_∞ norms of the frequency fluctuations in the two areas and tie-line power exchange for different input profiles. The *p*-values are also reported for each case using the Kruskal-Wallis test.

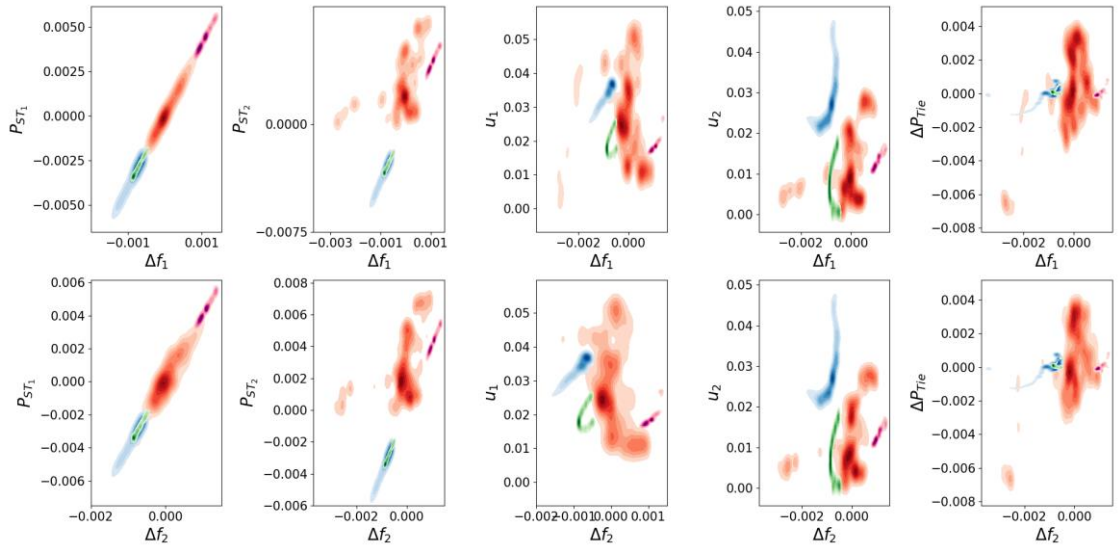

Figure 3-18: Multivariate KDE plots of the grid parameters with the frequency fluctuations in each area. The colors represent different RNGs: red = fBm, green = Gaussian, blue = gBm, magenta = real data.

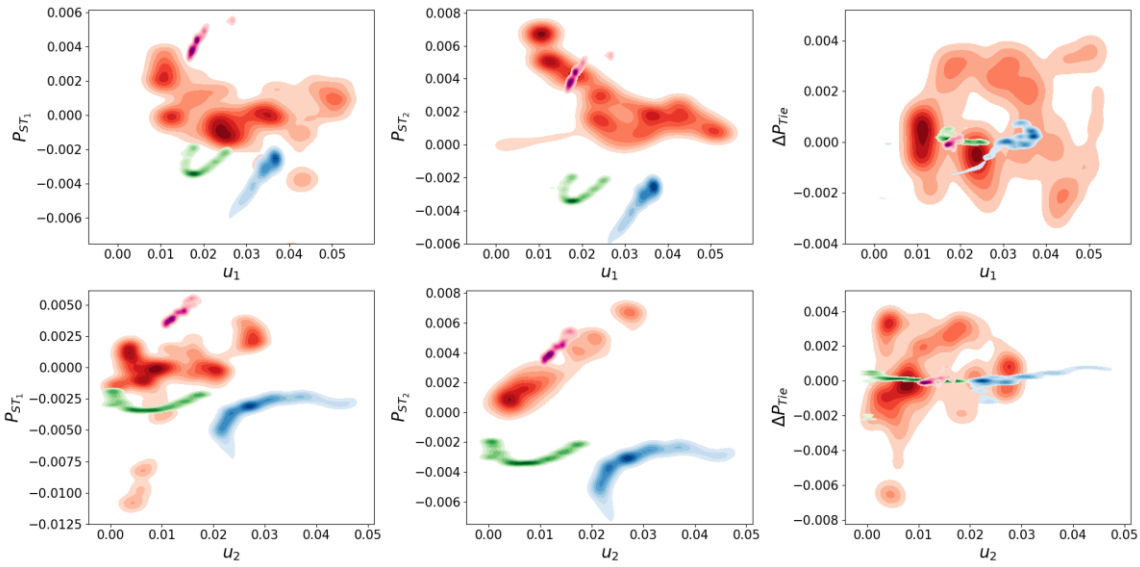

Figure 3-19: Multivariate KDE plots of the energy storage operation, tie-line power with the control input to the governor in two areas. The colors represent different RNGs: red = fBm, green = Gaussian, blue = gBm, magenta = real data.

The univariate normality checks are conducted using the Anderson-Darling, Kolmogorov-Smirnov [129] and Lilliefors test [130] where the significance levels of all tests are kept at 0.01. The tests are conducted using the functions `adtest()`, `kstest()` and `lillietest()` from the Statistics and Machine Learning Toolbox in MATLAB.

Some of the signal norms usually are distributed while in some other cases, they are not, but the joint normality of all the input profiles (Gaussian, fBm, gBm, real data) are not encountered anywhere. Hence, the parametric version – analysis of variance (ANOVA) test cannot be performed on these samples. Instead, the nonparametric version - Kruskal Wallis test [131] needs to be used to compare the medians of these four different input profiles. This test has been performed using the null hypothesis that all the 4 cases come from the same distribution, against the alternative hypothesis that they do not. The *p*-values and χ^2 values are obtained using the function `kruskalwallis()` from the Statistics

and Machine Learning Toolbox in MATLAB, which compares the medians of the samples.

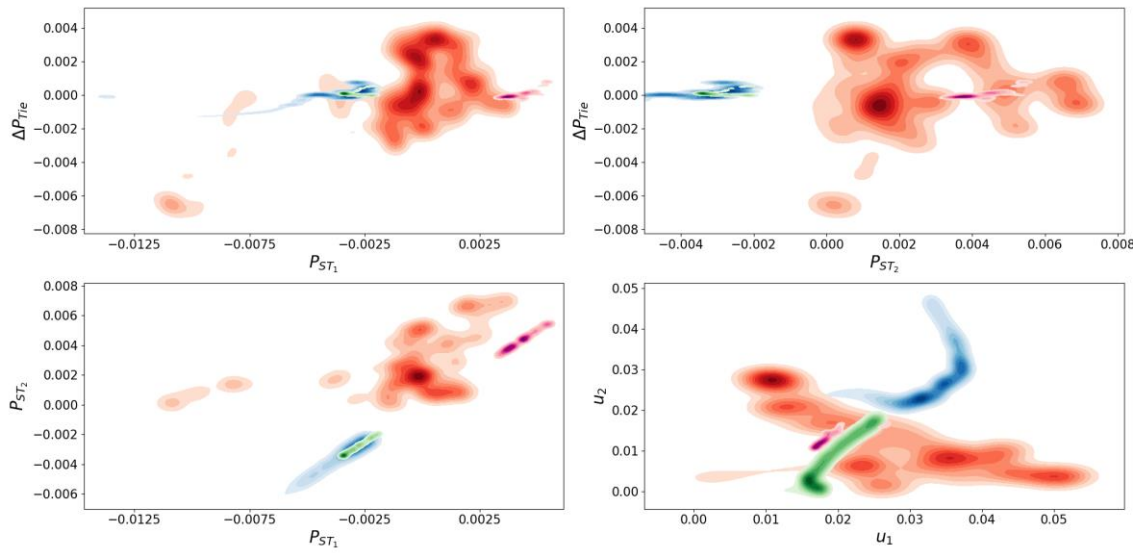

Figure 3-20: Multivariate KDE plot of (a) Tie-line power and storage operation in area 1 (top-left) (b) Tie-line power and storage operation in area 2 (top-right) (c) Storage operation in both the areas (bottom-left) (d) Control input for both the areas (bottom-right). The colors represent different RNGs: red = fBm, green = Gaussian, blue = gBm, magenta = real data.

The χ^2-values defined for the tests are defined as the critical values, and the *p*-values are defined as the probability that the test statistic is more than the critical value. The *p*-values are found to be zero, suggests that the norms of the input profiles do not follow a similar distribution. The χ^2-values are smaller for L_∞ norm as compared to χ^2-values for L_1 and L_2 norms which suggests that maximum fluctuation is greater than the sum of absolute and square of the fluctuations of $\{\Delta f_1, \Delta f_2, \Delta P_{tie}\}$ around zero due to the stochastic nature of the input fluctuation. It makes the frequency and tie-line powers hover around zero, but the PID controller for the thermal power plant will keep them maximum fluctuation within limits.

The L_∞-norms in case of frequency fluctuations are smallest in the case of Gaussian input profile, as compared to other profiles, which is primarily due to higher active operation of the thermal power plant $\Delta P_{th} > 0$. The frequency fluctuations for fBm and gBm input signals are similar to the fluctuations in the

case of real input profiles. These nonstationary profiles capture the behaviour of real input profiles more accurately and show a higher utilization of the RES since $\Delta P_{th} < 0$. The fluctuation of gBm input profiles resembles more to the real input data. Similar conclusions are also valid for the tie-line power ΔP_{Tie} between two areas except in the case of fBm where the variance is smaller than its other nonstationary counterparts. The small variance in the tie-line power within the ensembles can also be considered for the reason behind the small island formation in Figure 3-16. The norms for the tie-line power is similar for the gBm input profile as compared to the real input profile.

3.1.10 Multivariate Analysis of Grid Performance Measures

Multivariate kernel density estimate (KDE) plots are shown in Figure 3-18, Figure 3-19 and Figure 3-20, using the mean of the ensembles generated from the Monte Carlo simulations. There is a high correlation between the energy storage operation in both the areas and frequency fluctuations as shown in Figure 3-18, which suggests that they play a crucial role in damping out the frequency fluctuations in the grid. The mean profile suggests that the energy storage devices work in discharge mode in case of real and normal input, and charge mode in case of gBm input, and both the modes in the case of fBm input.

The higher control input to the governor is required to damp out the frequency fluctuations in area 1 in case of fBm input profile while control input is highest in area 2 for gBm input profile. We also observe a correlation between the control inputs in both the areas for normal and real input profile. High correlation is also observed between the storage operation in the two areas. The grid parameters show unusual behaviour when the input profile is fBm with higher fluctuation in the mean curve, thus creating an unusual spread in the multivariate plots and signifying low correlation amongst themselves which also explains the formation of the islands in the norm plots in Figure 3-16. The multivariate pattern is very usual when we compare the operations of tie-line power along with control inputs from both the areas.

3.1.11 Conclusion

We can summarize the results for the non-linear LFC model as

- PSO serves as an efficient optimizer for maintaining control performance of the LFC loops with interrupted packet transmission as DoS cyberattacks and random delays.
- The frequency fluctuations (Δf) and the ROCOF are within the prescribed limits, as per the IEEE standard [75].
- The renewable energy usage in the case of nonstationary profiles like fBm and gBm is similar to the real input profiles, where the LFC tends to decrease the thermal power plant output $\{\Delta P_{th} < 0\}_i$. However, the opposite trend is observed in the case of Gaussian input where $\{\Delta P_{th} > 0\}_i$. Hence frequency and tie-line power fluctuations are smaller in the case of Gaussian input. Hence, the variability in the norms obtained from the real input profile is highest and in the case of Gaussian input profiles, it is the lowest.
- The response of the LFC in the smart grid is more similar to real data in case of nonstationary profiles than the stationary profiles.

3.2 QoS-aware Decentralized Load Frequency Control with Packet Drop Rate and FDI Attack

In the previous chapter 3.1, the concept of load frequency control was introduced with the non-linearities of the components. The non-linear models in the LFC loop reflect the real-world physics of the devices. However, designing a controller for such systems, which ensures guaranteed stability, becomes very difficult. Real-world power systems are equipped with safety relays, preventing the system from functioning beyond specific operating points. Moreover, the allowable fluctuations of grid parameters are also relatively small. Hence, the non-linear models can be safely linearized around an operating point without losing the real-world functionalities. Furthermore, it becomes easier to derive necessary conditions which guarantee system stability for the linear models under disturbances.

The decentralized demand response, generation side and EV control are realized with cyber-physical systems while considering state-space linear model. The open communication channels render the smart grid to various cyber-physical issues like packet drops and false data injection (FDI) attack. Moreover, the participation of the consumers in DR involves significant time delays. The stability conditions for load frequency control are derived using a state feedback controller, where the states are estimated by an observer while considering bounded disturbances. It is formulated using an asynchronous dynamical switched system model of the network. The guaranteed stability conditions are obtained for different LFC configurations with EV and DR. The responses of various system configurations are tested with different packet drop rates, time delay, FDI attack and incorporation of stochastic renewable energies.

3.2.1 Previous Works

Dynamic DR model has been introduced in LFC [132] using a linear quadratic regulator (LQR). The control parameters of the smart appliances participating in the DR strategy deployed in LFC are designed in [133], based on the frequency deviation thresholds. Regional DR schemes were deployed in [134] based on the tie-line power flows. Dynamic adaptive demand response (DADR) is introduced in LFC [135] for frequency stability improvement of the distribution network.

Networked LFC with EV is derived using a stochastic jump system theory [136], linear operator inequality [137] and event-triggered control using the switching approach [138].

The stability conditions of NCS modelled as switched systems are derived while establishing the relationship between the packet dropout rate and Lyapunov stability criteria using average dwell time approach. A similar switched system concept is utilized in [139] to tackle a class of NCS with random sensor to controller and controller to actuator packet losses to solve the robust control problem. NCS modelling philosophy is utilized in [140], [141] using a switched system approach and linear Bernoulli function. The state feedback controller and observer are designed for the NCS modelled as a switched systems using asynchronous dynamical system (ADS) approach [84], [142] under packet drops and process and measurement disturbances. Both the state feedback controller and observer gains satisfying bounded H_∞ norm, obtained by solving the derived linear matrix inequalities (LMIs), ensure the exponential stability and state estimation for the system at an arbitrary packet drop rate and external disturbances. ADS model for the NCS provides an edge over the existing modelling strategies using Bernoulli drops in [140], [143] and Markovian jump model in [144], [145] as ADS approach takes into account the stochastic ordering and transmission of packets with a uniform sampling time. The stochastic packet transmission at an arbitrary rate helps us gauge the system performance. Stochastic protocol for packet scheduling and dropout rates are considered in [146], but the emphasis is more on obtaining the optimal parameters of the stochastic i.i.d protocol for facilitating signal transmission. Moreover, the aperiodic sampling rate for designing the communication protocol is challenging to implement in practice.

3.2.2 Contribution in this sub-chapter

This subchapter formulates an LMI for the NCS considering packet drop in a shared communication network from the sensor to controller and controller to actuator while extending the theoretical work in [147] for a state feedback controller and satisfying the norm bound of the output concerning the disturbance and noise as shown in [139]. The given controller design is utilized for an LFC

system while incorporating the DR strategies and EV control strategy. The state feedback control strategy helps us design a decentralized control strategy for multiple control input within the system, i.e. secondary controllers, EV and DR aggregators. This scheme is analogous to a server-client topology described in the IEEE Standard 2030.5-2018 [34] for smart energy profile application protocol. The energy controller gains form the back-end server, the secondary load controllers and independent EV and load aggregators are on the application frontend interface. The designed controller is based on the bound of the output and the disturbances, which will stabilize the system based on arbitrary packet loss at a specific rate, rather than finding the probability bound as given in [148].

The work in the subchapter represents the smart grid architectural model (SGAM) [149], [150] where the LFC, demand response and EV model represents the component layer. The shared communication medium in the feedback path between the PMU and EV power utilization measurement to the server computing the control gain and forward medium between the load aggregator to consumer, EV aggregator to the EV charging center and control centre to the governer control system represents the communication layer. The observer measuring represents the server estimating the system states forms the information layer. The control algorithm represents the functional layer. Usage of various EV and demand response configuration to reduce the spinning reserve costs forms the business layer objective. Hence, the significant contribution of the subchapter is listed as follows:

- Firstly, the NCS considering random packet drops in both feedforward and feedback path, with the observer and state feedback controller is modelled as ADS under L_2 bounded measurement noise and process disturbance. Secondly, Lyapunov stability criteria is utilized to find the observer and controller gains, with the existence of common quadratic Lyapunov function (CQLF) [94], [142], [147], [151] for the NCS while satisfying H_∞ norm bound and ensuring exponentially stability of the system.
- The state-space model of load frequency control, along with DR and EV, is considered for the analysis. The controller gain is obtained for different LFC configuration with DR and EV for an arbitrary packet drop rate. As far as previous literature is concerned, response with different packet drop rates and analysis for the varied LFC configuration with EV and DR is a novel work.

- The stabilized controller for different LFC configuration, EV and DR is tested against stochastic renewable energy source modelled by geometric Brownian motion (gBm) as given in [68]. The frequency, spinning reserve control, EV and DR output is analysed with 1,2 and ∞ norms of the signal obtained from Monte Carlo simulation. The norms are analysed using bivariate density plots and non-parametric statistical tests.

3.2.3 Decentralized Load Frequency Control with State Space Model

The generalized one area LFC, similar to the schematic used in [132] is shown in Figure 3-21. The scheme is similar to the decentralized control for i^{th} area in the power system decoupled from other geographical areas. This schematic can also be considered as a micro-grid operating in a small geographical region. Single control area is considered in this work as the LMIs derived in the later sections are too restrictive, and it is a challenging task to obtain an acceptable solution with higher-order systems.

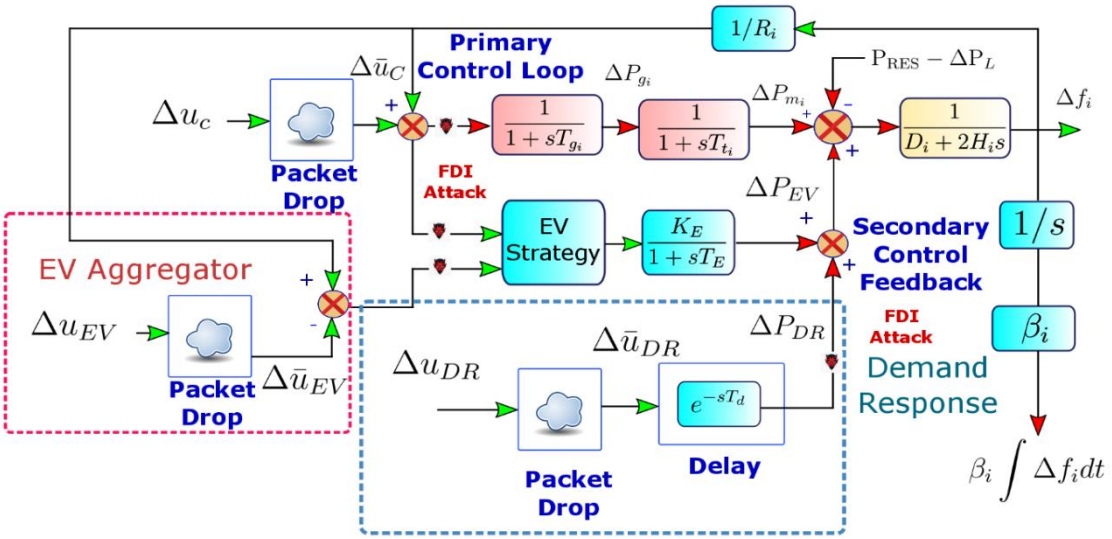

Figure 3-21: Schematic of Load Frequency Control with different strategies of EV and demand response. Packet dropout and FDI attack is shown at relevant places

The model of the power system is inherently nonlinear. However, linearized models of LFC is acceptable for analysis because the load fluctuations are quite small. The simplified LFC model consisting of the governor, non-reheated turbine, along with the machine models with load fluctuations as state disturbance, is represented as a linear state-space equation model as follows:

$$\Delta \dot{f}_i(t) = -\frac{D_i}{M_i}\Delta f_i(t) + \frac{1}{M_i}\Delta P_{m_i}(t) - \frac{1}{M_i}\Delta P_L(s). \tag{34}$$

$$\Delta \dot{P}_{m_i}(t) = -\frac{1}{T_{t_i}}\Delta P_{m_i}(t) + \frac{1}{T_{t_i}}\Delta P_{G_i}(t). \tag{35}$$

$$\Delta \dot{P}_{g_i}(t) = -\frac{1}{R_i T_{g_i}}\Delta f_i(t) - \frac{1}{T_{g_i}}\Delta P_{g_i}(t) + \frac{1}{T_{g_i}}\Delta u_{c_i}(t). \tag{36}$$

$$\frac{d}{dt}\left[\beta_i \int \Delta f_i(t)dt\right] = \beta_i \Delta f_i(t). \tag{37}$$

Here T_{t_i} and T_{g_i} represents the time constant of the governor and turbine, respectively. R_i represents the droop constant of the primary control loop. D_i is the damping coefficient of the system, and H_i is the equivalent system inertia. T_d represents the fixed equivalent delay in the demand response side. Δu_C represents the control input to the governor. As shown in Figure 3-21, the governor, turbine, and power system time constants govern the grid frequency dynamics. The droop component (R_i) is a part of the primary control loop, which acts upon the frequency deviation Δf_i. The primary feedback loop will activate the necessary over-and under-frequency relays in the thermal power station. $\beta_i \int \Delta f_i(t)dt$ represents the power needed to stabilize the frequency fluctuations Δf_i, which is utilized in the secondary control loop. It can also be considered a cumulative disturbance due to the frequency fluctuations in other areas, as given in [152]. The value of the parameters used in the state space model (34)-(37) is adopted from [138]. The model (34)-(37) can be written in the form:

$$\begin{aligned} \dot{\mathbf{x}}(t) &= \mathbf{A}\mathbf{x}(t) + \mathbf{B}_1 u(t) + \mathbf{B}_2 w(t), \\ \mathbf{y}(t) &= \mathbf{C}\mathbf{x}(t) + \mathbf{D}n(\mathbf{t}). \end{aligned} \tag{38}$$

where $\mathbf{A}$ is the system matrix, $\mathbf{B}_1$ is the control input matrix, $\mathbf{B}_2$ is the disturbance matrix, $\mathbf{C}$ is the observation matrix and $\mathbf{D}$ is the noise matrix. $\mathbf{x}(t)$ is the state vector, $\mathbf{u}(t)$ is the input vector, $w(t) \in L_2[0,\infty)$ is the disturbance vector. $\mathbf{y}(t)$ is the system output. $n(\mathbf{t}) \in L_2[0,\infty)$ is the output noise vector. Since we are designing an observer-based controller here, it is essential to measure certain

states to make the system observable. Corresponding to (34)-(37), we can write the system matrix as

$$\mathbf{A}=\begin{bmatrix} -\frac{D_i}{M_i} & \frac{1}{M_i} & 0 & 0 \\ 0 & -\frac{1}{T_{t_i}} & \frac{1}{T_{t_i}} & 0 \\ -\frac{1}{RT_{g_i}} & 0 & -\frac{1}{T_{g_i}} & 0 \\ 0 & 0 & 0 & 1 \end{bmatrix}, \mathbf{B}_1=\begin{bmatrix} 0 \\ 0 \\ \frac{1}{T_{g_i}} \\ 0 \end{bmatrix}, \mathbf{B}_2=\begin{bmatrix} -\frac{1}{M_i} \\ 0 \\ 0 \\ 0 \end{bmatrix}, \tag{39}$$

where,

states $\mathbf{x}=\begin{bmatrix} \Delta f_i(t) & \Delta P_{m_i}(t) & \Delta P_{g_i}(t) & \beta\int \Delta f_i(t)dt \end{bmatrix}^T$,

output $\mathbf{y}=\begin{bmatrix} \Delta f(t) & \beta\int \Delta f(t)dt \end{bmatrix}^T$,

control input $\mathbf{u}=\Delta u_{c_i}(t)$,

disturbance $\mathbf{w}=\begin{bmatrix} \Delta P_L & d_{\text{FDI}} \end{bmatrix}^T$. Here ΔP_L and d_{FDI} represents the load and FDI attack disturbance vector. The output vector is chosen such that the observability condition,

$$\text{rowrank}\left(\begin{bmatrix} \mathbf{C} \\ \mathbf{CA} \\ \mathbf{CA}^2 \\ \vdots \\ \mathbf{CA}^{n-1} \end{bmatrix}\right)=n. \tag{40}$$

3.2.3.1 Load Frequency Control with Demand Response

The power balance equation with the inclusion of demand response is written as shown in Figure 3-21:

$$\Delta P_{m_i}(s)+\Delta u_{DR}(s)G(s)-\Delta P_L(s)=2H_i s\Delta f_i(s)+D_i\Delta f_i(s), \tag{41}$$

where $G(s)$ represents the Pade approximation of the time delay induced by the

demand response. IEEE Std 2030.6- 2016 [153] suggests that the delay time is the cumulative sum of notification time sent to the consumer from the aggregator and the consumer response time. For the sake of simplicity, 2nd order Pade approximation is considered. Moreover, in [132] it is stated that the performance change is negligible with the reduction in the order. The second-order Pade approximation e^{-sT_d} is given as [154].

$$G(s) = \frac{T_d{}^2 s^2 - 6T_d s + 12}{T_d{}^2 s^2 + 6T_d s + 12}. \tag{42}$$

Now let us consider $X_{\text{temp}}(s) = \Delta\bar{u}_{DR_i}(s)G(s)$, Hence we can write,

$$X_{\text{temp}}(s) = G_1(s) \cdot \Delta\bar{u}_{DR}(s) = \frac{s^2 - \frac{6s}{T_d} + \frac{12}{T_d^2}}{s^2 + \frac{6s}{T_d} + \frac{12}{T_d^2}} \cdot \Delta\bar{u}_{DR}(s). \tag{43}$$

The above expression can be written as,

$$X_{\text{temp}}(s) = \Delta\bar{u}_{DR}(s) + X_1(s), \tag{44}$$

where,

$$X_1(s) = -\frac{\frac{12s}{T_d}}{s^2 + \frac{6s}{T_d} + \frac{12}{T_d^2}} \Delta\bar{u}_{DR}(s). \tag{45}$$

Now let us consider $X_2(s) = \frac{1}{s} \cdot X_1(s)$. Hence, we can write $x_2(t)$ as,

$$\dot{x}_2(t) = x_1(t). \tag{46}$$

Substituting the value of $x_2(t)$ in (44) and writing the equation in the time domain,

$$\dot{x}_1(t) = -\frac{6}{T_d} x_1(t) - \frac{12}{T_d^2} x_2(t) - \frac{12}{T_d} \Delta\bar{u}_{DR}(s). \tag{47}$$

Thus, two new states $x_1(t)$ and $x_2(t)$ are incorporated in the state-space model

due to the second-order Pade approximation of the time lag. The new states. The time delay T_d considered in this work is 1 second. The new states in (46)-(47) is incorporated along with (34)-(37), to form the following state space marix for LFC with demand response,

$$\mathbf{A}=\begin{bmatrix} -\frac{D_i}{M_i} & \frac{1}{M_i} & 0 & 0 & \frac{1}{M_i} & 0 \\ 0 & -\frac{1}{T_{t_i}} & \frac{1}{T_{t_i}} & 0 & 0 & 0 \\ -\frac{1}{R_i T_{g_i}} & 0 & -\frac{1}{T_{g_i}} & 0 & 0 & 0 \\ 0 & 0 & 0 & 1 & 0 & 0 \\ 0 & 0 & 0 & 0 & -\frac{6}{T_d} & -\frac{12}{T_d^2} \\ 0 & 0 & 0 & 0 & 1 & 0 \end{bmatrix}, \mathbf{B}_1=\begin{bmatrix} 0 & \frac{1}{M_i} \\ 0 & 0 \\ \frac{1}{T_{g_i}} & 0 \\ 0 & 0 \\ 0 & -\frac{12}{T_{d_i}} \\ 0 & 0 \end{bmatrix}, \mathbf{B}_2=\begin{bmatrix} -\frac{1}{M_i} \\ 0 \\ 0 \\ 0 \\ 0 \\ 0 \end{bmatrix}, \quad (48)$$

where,

states $\mathbf{x}=\begin{bmatrix}\Delta f_i(t) & \Delta P_{m_i}(t) & \Delta P_{g_i}(t) & \beta_i\int\Delta f_i(t)dt & x_1(t) & x_2(t)\end{bmatrix}^T$,

output $\mathbf{y}=\begin{bmatrix}\Delta f_i(t) & \beta\int\Delta f_i(t)dt\end{bmatrix}^T$, control input $\mathbf{u}=\begin{bmatrix}\Delta u_{c_i}(t) & \Delta u_{DR}(t)\end{bmatrix}^T$,

Disturbance $\mathbf{w}=\begin{bmatrix}\Delta P_L & d_{\text{FDI}}\end{bmatrix}^T$.

3.2.3.2 Load Frequency Control with Centralized and Decentralized EV Connection

As we observe in Figure 3-21, we can write the EV power output ΔP_{EV} as given in [138] as,

$$\Rightarrow \Delta\dot{P}_E(t)=-\frac{1}{R_i T_E}\Delta f_i(t)-\frac{1}{T_E}\Delta P_E(t)+\frac{K_E}{T_E}\Delta u_{St}(t). \quad (49)$$

Here K_E and T_E are the gain and time constant of the EV module. The $\Delta u_{St}(t)$ depends on whether it is coupled to spinning reserves or regulated independently from a decentralized strategy. Hence it can be characterized as:

$$\Delta u_{st}(t) = \begin{cases} \Delta u_C(t), & \text{EV Strategy = Centralized} \\ \Delta u_{EV}(t), & \text{EV Strategy = Decentralized} \end{cases}. \tag{50}$$

The parameters of the EV model defined in (49) is adapted from [138]. Hence we combine the power plant LFC model in (34)-(37) with the EV model in (49), to write the state space model of the form (38), with centralized strategy as:

$$\mathbf{A} = \begin{bmatrix} -\frac{D_i}{M_i} & \frac{1}{M_i} & 0 & 0 & 0 \\ 0 & -\frac{1}{T_{t_i}} & \frac{1}{T_{t_i}} & 0 & 0 \\ -\frac{1}{R_i T_{g_i}} & 0 & -\frac{1}{T_{g_i}} & 0 & 0 \\ 0 & 0 & 0 & 1 & 0 \\ -\frac{1}{R_i T_E} & 0 & 0 & 0 & -\frac{1}{T_E} \end{bmatrix}, \mathbf{B}_1 = \begin{bmatrix} 0 \\ 0 \\ \frac{1}{T_{g_i}} \\ 0 \\ \frac{K_E}{T_E} \end{bmatrix}, \mathbf{B}_2 = \begin{bmatrix} -\frac{1}{M_i} \\ 0 \\ 0 \\ 0 \\ 0 \end{bmatrix}, \tag{51}$$

here, states $\mathbf{x} = \begin{bmatrix} \Delta f_i(t) & \Delta P_{m_i}(t) & \Delta P_{g_i}(t) & \beta_i \int \Delta f_i(t) dt & \Delta P_{E_i}(t) \end{bmatrix}^T$,

output $\mathbf{y} = \begin{bmatrix} \Delta f_i(t) & \beta_i \int \Delta f_i(t) dt & \Delta P_E(t) \end{bmatrix}^T$, input $\mathbf{u} = \Delta u_c(t)$,

disturbance $\mathbf{w} = \begin{bmatrix} \Delta P_L & d_{\text{FDI}} \end{bmatrix}^T$.

We observe that we need to incorporate the change in EV output $\Delta P_E(t)$ in the output vector so that the observability condition defined in (40) is satisfied. In decentralized EV configuration the $\mathbf{A}$ and $\mathbf{B}_2$ remains the same as (51). However, $\mathbf{B}_1$ changes as follows,

$$\mathbf{B}_1 = \begin{bmatrix} 0 & 0 \\ 0 & 0 \\ \frac{1}{T_{g_i}} & 0 \\ 0 & 0 \\ 0 & \frac{K_E}{T_E} \end{bmatrix}. \tag{52}$$

This is due to the fact that we have two control inputs in this configuration $\mathbf{u} = \left[\Delta u_c(t) \quad \Delta u_{\text{EV}}(t) \right]^T$.

3.2.3.3 Load Frequency Control with Demand Response and Centralized and Decentralized EV configuration

In this case, we combine all the state space equations of traditional LFC from (34) -(37), along with the new state space variables obtained from demand response (46)-(47) along with the EV model in (49) with the configuration strategy defined in (50). We can write the state space equation of LFC, DR and with centralized EV configuration as:

$$\mathbf{A} = \begin{bmatrix} -\frac{D_i}{M_i} & \frac{1}{M_i} & 0 & 0 & \frac{1}{M_i} & 0 & 0 \\ 0 & -\frac{1}{T_{t_i}} & \frac{1}{T_{t_i}} & 0 & 0 & 0 & 0 \\ -\frac{1}{R_i T_{g_i}} & 0 & -\frac{1}{T_{g_i}} & 0 & 0 & 0 & 0 \\ 0 & 0 & 0 & 1 & 0 & 0 & 0 \\ 0 & 0 & 0 & 0 & -\frac{6}{T_d} & -\frac{12}{T_d^2} & 0 \\ 0 & 0 & 0 & 0 & 1 & 0 & 0 \\ -\frac{1}{R_i T_E} & 0 & 0 & 0 & 0 & 0 & -\frac{1}{T_E} \end{bmatrix}, \mathbf{B}_1 = \begin{bmatrix} 0 & \frac{1}{M} \\ 0 & 0 \\ \frac{1}{T_{g_i}} & 0 \\ 0 & 0 \\ 0 & -\frac{12}{T_d} \\ 0 & 0 \\ \frac{K_E}{T_E} & 0 \end{bmatrix}, \mathbf{B}_2 = \begin{bmatrix} -\frac{1}{M_i} \\ 0 \\ 0 \\ 0 \\ 0 \\ 0 \\ 0 \end{bmatrix} \tag{53}$$

where,

states $\mathbf{x} = \left[\Delta f_i(t) \quad \Delta P_{m_i}(t) \quad \Delta P_{g_i}(t) \quad \beta_i \int \Delta f_i(t) dt \quad x_1(t) \quad x_2(t) \quad \Delta P_E(t) \right]^T$,

output $\mathbf{y} = \left[\Delta f_i(t) \quad \beta_i \int \Delta f_i(t) dt \quad \Delta P_E(t) \right]^T$,

input $\mathbf{u} = \left[\Delta u_c(t) \quad \Delta u_{DR}(t) \right]^T$, disturbance $\mathbf{w} = \left[\Delta P_L \quad d_{\text{FDI}} \right]^T$.

Similar to the previous subsection, for decentralized EV configuration, $\mathbf{A}$ and $\mathbf{B}_2$ remains the same as (53), but $\mathbf{B}_1$ changes as follows:

$$\mathbf{B}_1 = \begin{bmatrix} 0 & \frac{1}{M} & 0 \\ 0 & 0 & 0 \\ \frac{1}{T_g} & 0 & 0 \\ 0 & 0 & 0 \\ 0 & -\frac{12}{T_d} & 0 \\ 0 & 0 & 0 \\ 0 & 0 & \frac{K_E}{T_E} \end{bmatrix}. \quad (54)$$

This is due to the fact that we have two control inputs in this configuration $\mathbf{u} = \begin{bmatrix} \Delta u_c(t) & \Delta u_{DR}(t) & \Delta u_{EV}(t) \end{bmatrix}^T$. However, to design the controller under packet drop, the continuous-time state-space system for different LFC, DR and EV configurations defined in (39), (48), (51)-(52) and (53)-(54) must be converted into discrete-time form with a specified sampling time T_s. Hence as per [155], generalized state space in discrete-time form can be written as,

$$\begin{aligned} \mathbf{x}(k+1) &= \mathbf{F}\mathbf{x}(k) + \mathbf{G}_1\bar{u}(k) + \mathbf{G}_2 w(k), \\ \mathbf{y}(k) &= \mathbf{C}\mathbf{x}(k) + \mathbf{D}n(k), \end{aligned} \quad (55)$$

where, $\mathbf{F} = e^{\mathbf{A}T_s}$, $\mathbf{G}_1 = \int_0^{T_s} e^{\mathbf{A}T_s}\mathbf{B}_1 dt$, $\mathbf{G}_2 = \int_0^{T_s} e^{\mathbf{A}T_s}\mathbf{B}_2 dt$. The stabilizing controller for the system defined by (55) is derived in the next section. $\bar{u}(k)$ represents the control input from the communication network after a packet drop. The concept of probabilistic observability is not used to analyze the system as given in [148]. Instead, the switched system is modelled, and joint observer and controller gain is obtained to ensure its stability based on the arbitrary number of packet drops, which is explained in the following sections.

3.2.4 Joint Observer and Controller Design for linear model

The controller and observer for the system (55) are shown in Figure 3-22. The observer, which is generally at the control centre, receives the measured signal from the communication channel to estimate the given states $\hat{\mathbf{x}}(k)$ for the next

time instant. The controller $\mathbf{K}$ has to be obtained from the estimated states to generate control signals. As shown in Figure 3-22, the controller is derived from the observer, whose form is given as,

$$\begin{aligned}\hat{\mathbf{x}}(k+1) &= \mathbf{F}\hat{\mathbf{x}}(k) + \mathbf{G}_1\mathbf{u}(k) + \mathbf{L}\left(\bar{y}(k) - \hat{y}(k)\right),\\ \hat{\mathbf{y}}(k) &= \mathbf{C}\hat{\mathbf{x}}(k).\end{aligned} \tag{56}$$

where $\bar{y}(k)$ represents the output received by the observer to estimate the system states $\hat{\mathbf{x}}(k)$ using observer gain $\mathbf{L}$. The control input $\mathbf{u}(k)$ is defined as:

$$\mathbf{u}(k) = -\mathbf{K}\hat{\mathbf{x}}(k). \tag{57}$$

The eigen values of the state estimation error dynamical system i.e. $\mathbf{e}(k) = \mathbf{x}(k) - \hat{\mathbf{x}}(k)$ where $\mathbf{x}(k)$ is obtained from the discretized system model in (55) and $\hat{\mathbf{x}}(k)$, play an essential role in the system response. As given in [155], that the estimation error dynamical system governed by the observer gain $\mathbf{L}$ should be much faster than the closed loop system response governed by the state feedback control gain $\mathbf{K}$. Ideally it should be four to five times faster for optimum system response. Physically an observer is a computer program, hence it is possible to increase the response speed so that the estimated state converges to the true state. However, the response of the error dynamical system is constrained by the noise and the sensitivity issues present in the system.

As described in [156], there are two different ways to model packet dropout in the literature. In the first method, the dropouts follow a certain probability distribution and a stochastic model like Markovian jump linear system is utilized to describe the NCS. Second approach is deterministic where, packet dropouts can be specified in time average sense or in the terms of maximum packet dropouts occurred. This is modelled using an asynchronous dynamical system [157] with a rate constraint on the deterministic events based on common Lyapunov approach. Thus, the packet dropouts on the feedback and forward path is considered as events, hence NCS is represented as a discrete switched system with arbitrary switching signal and its stability is studied using the switched system framework. Here the switched system means the hybrid dynamical system which has a finite number of subsystems modelled using a difference equation. A logical rule is used to facilitate switching between the

subsystems. There have been results on the stability studies of the switched systems with arbitrary switching signals [158], [159] . As given in [160], the switched system has to be modelled in such a way that the controller and observer makes use of the previous transmitted information to stabilize the system and estimate the system states respectively. A time-driven observer is utilized to design a state feedback controller (57), as an ADS under random packet dropouts as given in [151] with certain assumptions as follows:

- The data packets are time-stamped, containing the information of the sampling instant when it is sampled. As given in IEEE Std 1815-2012 [161], the DNP3 protocol supports data time-stamping, aiding the utilities to collect historical data.
- The sensor clock is considered as the reference. For load frequency control, the PMU clock can be considered.
- Both the controller and actuator are time-driven.

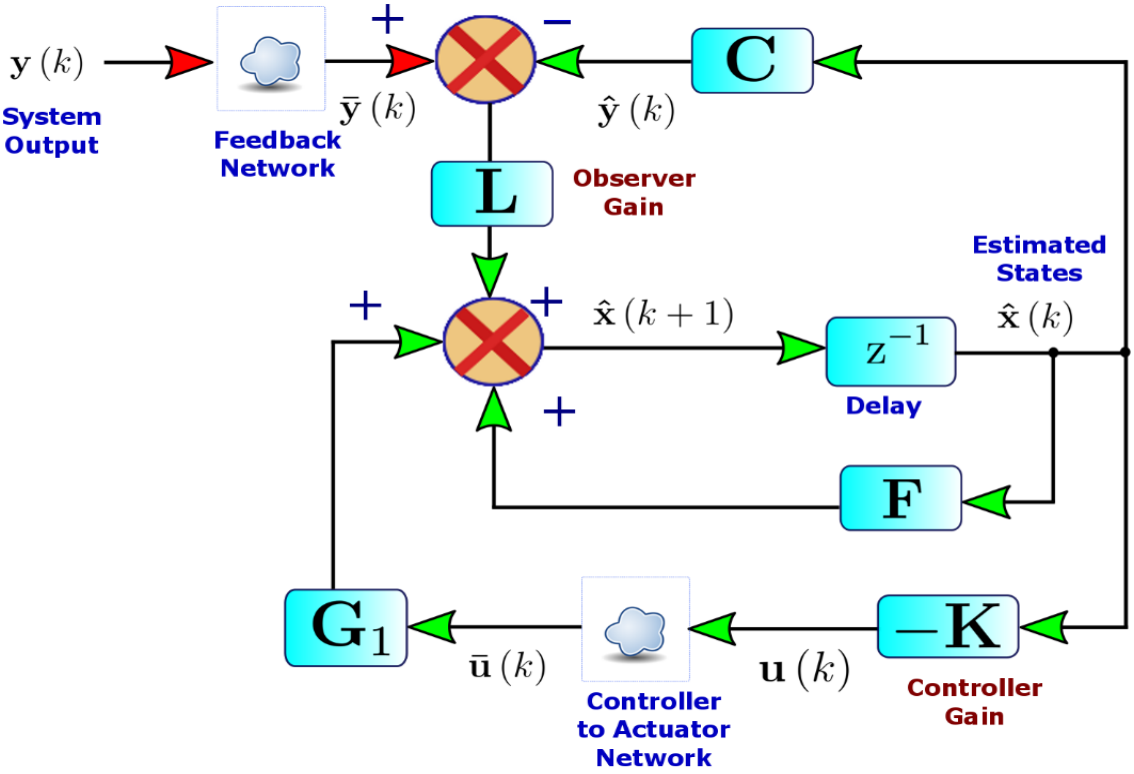

Figure 3-22: Schematic of the observer-based controller for the decentralized load frequency control system. The packet drops at feedback and feedforward are also shown in the figure, which helps obtain the switched system model.

The packet transmission from the controller to the actuator (in the forward path) and sensor to the observer (in the feedback path) is shown in Figure 3-21 and Figure 3-22, respectively, where it is assumed that the network in the feedback and forward path of the control loop can be represented by two switches i.e. s_1 and s_2 respectively . Depending on the switch position, system output $y(k)$ and control input at time instant can be modelled using Boolean variables, , which is represented as:

$$\left.\begin{array}{lll} s_1: & \bar{y}(k)=y(k) & \text{for effective transmission} \\ \bar{s}_1: & \bar{y}(k)=\bar{y}(k-1) & \text{for ineffective transmission} \\ s_2: & \bar{u}(k)=u(k)=-\mathbf{K}\hat{\mathbf{x}}(k) & \text{for effective transmission} \\ \bar{s}_2: & \bar{u}(k)=\bar{u}(k-1)=-\mathbf{K}\hat{\mathbf{x}}(k-1) & \text{for ineffective transmission} \end{array}\right\}. \quad (58)$$

where, $s_1(\bar{s}_1)$ represents the close (open) position of the switch s_1 in the feedback path and $s_2(\bar{s}_2)$ represents close (open) position of the switch s_2 in the forward path.As per Boolean switch configuration (58), four possible subsystems can be formulated as an ADS with the Boolean combinations $(s_1,s_2),(\bar{s}_1,s_2),(s_1,\bar{s}_2),(\bar{s}_1,\bar{s}_2)$. The resulting NCS from the combinations is represented as an ADS. It has a rate constraint (r) using the subsystems represented by $\mathbf{\Phi}_{\sigma(k)},\sigma(k)=1,2,3,4$ as:

$$\begin{aligned} &\mathbf{z}(k+1)=\mathbf{\Phi}_{\sigma(k)}\mathbf{z}(k)+\mathbf{\Gamma}_{\sigma(k)}\boldsymbol{\eta}(k), \quad \sigma(k)=1,2,3,4 \\ &\tilde{y}_z(k)=\tilde{\mathbf{C}}\mathbf{z}(k), \end{aligned} \quad (59)$$

where $\mathbf{z}(k),\boldsymbol{\eta}(k)$ represents the augmented system states, input states, and $\tilde{y},\tilde{\mathbf{C}}$ represents the output, output matrix of the subsystems. The stability of the estimation for the switched system (59) error is obtained with the help of Luenberger type observer by finding a common Lyapunov function with the help of LMIs in [162], [163]. In the following subsection, subsystems aof the switched systems are derived with different switching conditions.

Case 1: No Packet Drop Condition

As per the switching condition $\{s_1, s_2\}$, the system output and control input is represented as per (58) as,

$$\begin{aligned} \bar{y}(k) &= y(k) = \mathbf{C}\mathbf{x}(k) + \mathbf{D}n(k), \\ \bar{u}(k) &= u(k) = -\mathbf{K}\hat{\mathbf{x}}(k). \end{aligned} \tag{60}$$

The state estimation error $\mathbf{e}(k)$ is represented as:

$$\mathbf{e}(k) = \mathbf{x}(k) - \hat{\mathbf{x}}(k). \tag{61}$$

From the discrete-time systems in (55), and substituting the estimation error $\mathbf{e}(k)$ in (61) we can write,

$$\mathbf{x}(k+1) = (\mathbf{F} - \mathbf{G}_1 K)\mathbf{x}(k) + \mathbf{G}_1\mathbf{K}\mathbf{e}(k) + \mathbf{G}_2 w(k). \tag{62}$$

Similarly, we can write the discrete-time system at time instant $(k-1)$ as:

$$\mathbf{x}(k) = \mathbf{F}\mathbf{x}(k-1) + \mathbf{G}_1\bar{u}(k-1) + \mathbf{G}_2 w(k-1). \tag{63}$$

The corresponding state estimation error is derived as:

$$\begin{aligned} &\mathbf{e}(k+1) = \mathbf{x}(k+1) - \hat{\mathbf{x}}(k+1) \\ &\Rightarrow \mathbf{e}(k+1) = \left[\mathbf{F}\mathbf{x}(k) + \mathbf{G}_1\bar{u}(k) + \mathbf{G}_2 w(k)\right] - \left[\mathbf{F}\hat{\mathbf{x}}(k) + \mathbf{G}_1 u(k) + \mathbf{L}\left(\bar{y}(k) - \hat{y}(k)\right)\right] \\ &\Rightarrow \mathbf{e}(k+1) = \left[\mathbf{F}\mathbf{x}(k) + \mathbf{G}_1 u(k) + \mathbf{G}_2 w(k)\right] - \left[\mathbf{F}\hat{\mathbf{x}}(k) + \mathbf{G}_1 u(k) + \mathbf{L}\left(y(k) - \mathbf{C}\hat{\mathbf{x}}(k)\right)\right] \\ &\Rightarrow \mathbf{e}(k+1) = \left[\mathbf{F}\mathbf{x}(k) + \mathbf{G}_2 w(k)\right] - \left[\mathbf{F}\hat{\mathbf{x}}(k) + \mathbf{L}\left(\mathbf{C}\mathbf{x}(k) + \mathbf{D}n(k) - \mathbf{C}\hat{\mathbf{x}}(k)\right)\right] \\ &\Rightarrow \mathbf{e}(k+1) = \left[\cancel{\mathbf{F}\mathbf{x}(k)} + \mathbf{G}_2 w(k)\right] - \left[\mathbf{F}\left(\cancel{\mathbf{x}(k)} - \mathbf{e}(k)\right) + \mathbf{L}\left(\mathbf{C}\mathbf{e}(k) + \mathbf{D}n(k)\right)\right] \\ &\Rightarrow \mathbf{e}(k+1) = [\mathbf{F} - \mathbf{L}\mathbf{C}]\mathbf{e}(k) + \mathbf{G}_2 w(k) - \mathbf{L}\mathbf{D}n(k). \end{aligned} \tag{64}$$

Similarly, (60), we can write $\bar{u}(k)$ as:

$$\bar{u}(k) = -\mathbf{K}\mathbf{x}(k) + \mathbf{K}\mathbf{e}(k). \tag{65}$$

Now let us define the augmented states as,

$\mathbf{z} = \left[\mathbf{x}(k) \quad \mathbf{x}(k-1) \quad \mathbf{e}(k) \quad \bar{u}(k-1)\right]^T$ and

$\boldsymbol{\eta}(k) = \left[w(k) \quad w(k-1) \quad n(k) \quad n(k-1)\right]^T$.

The NCS (59) can be formulated using (62)-(65) as,

$$\mathbf{z}(k+1) = \boldsymbol{\Phi}_1 \mathbf{z}(k) + \boldsymbol{\Gamma}_1 \boldsymbol{\eta}(k) =$$
$$\begin{bmatrix} \mathbf{F}-\mathbf{G}_1\mathbf{K} & 0 & \mathbf{G}_1\mathbf{K} & 0 \\ 0 & \mathbf{F} & 0 & \mathbf{G}_1 \\ 0 & 0 & \mathbf{F}-\mathbf{LC} & 0 \\ -\mathbf{K} & 0 & \mathbf{K} & 0 \end{bmatrix} \mathbf{z}(k) + \begin{bmatrix} \mathbf{G}_2 & 0 & 0 & 0 \\ 0 & \mathbf{G}_2 & 0 & 0 \\ \mathbf{G}_2 & 0 & -\mathbf{LD} & 0 \\ 0 & 0 & 0 & 0 \end{bmatrix} \boldsymbol{\eta}(k). \tag{66}$$

Case 2: Packet Drop in Feedback Path

Under this condition, i.e. $\{\bar{s}_1, s_2\}$ the system output:

$$\bar{y}(k) = \bar{y}(k-1) = \mathbf{C}\mathbf{x}(k-1) + \mathbf{D}n(k-1). \tag{67}$$

The terms $\mathbf{x}(k+1), \mathbf{x}(k), \bar{u}(k)$ will remain the same as given in (62), (63) and (65) respectively. The estimation error $\mathbf{e}(k+1)$ can be written as:

$$\begin{aligned} \Rightarrow \mathbf{e}(k+1) &= \left[\mathbf{F}\mathbf{x}(k) + \mathbf{G}_1 u(k) + \mathbf{G}_2 w(k)\right] \\ &\quad - \left[\mathbf{F}\hat{\mathbf{x}}(k) + \mathbf{G}_1 u(k) + \mathbf{L}\left(\mathbf{C}\mathbf{x}(k-1) + \mathbf{D}n(k-1) - \mathbf{C}\hat{\mathbf{x}}(k)\right)\right] \\ \Rightarrow \mathbf{e}(k+1) &= \mathbf{F}\mathbf{e}(k) + \mathbf{L}\mathbf{C}\hat{\mathbf{x}}(k) - \mathbf{L}\mathbf{C}\mathbf{x}(k-1) - \mathbf{L}\mathbf{D}n(k-1) + \mathbf{G}_2 w(k) \\ \Rightarrow \mathbf{e}(k+1) &= \mathbf{F}\mathbf{e}(k) + \mathbf{L}\mathbf{C}\left[\mathbf{x}(k) - \mathbf{e}(k)\right] - \mathbf{L}\mathbf{C}\mathbf{x}(k-1) - \mathbf{L}\mathbf{D}n(k-1) + \mathbf{G}_2 w(k) \\ \Rightarrow \mathbf{e}(k+1) &= \left[\mathbf{L}\mathbf{C}\right]\mathbf{x}(k) + \left[\mathbf{F}-\mathbf{L}\mathbf{C}\right]\mathbf{e}(k) - \mathbf{L}\mathbf{C}\mathbf{x}(k-1) - \mathbf{L}\mathbf{D}n(k-1) + \mathbf{G}_2 w(k). \end{aligned} \tag{68}$$

Using (62), (63), (65) and (68), the matrix $\boldsymbol{\Phi}_2$ and $\boldsymbol{\Gamma}_2$ in (59) can be written from the augmented states as:

$$\mathbf{\Phi}_2 = \begin{bmatrix} \mathbf{F}-\mathbf{G}_1\mathbf{K} & 0 & \mathbf{G}_1\mathbf{K} & 0 \\ 0 & \mathbf{F} & 0 & \mathbf{G}_1 \\ \mathbf{LC} & -\mathbf{LC} & \mathbf{F}-\mathbf{LC} & 0 \\ -\mathbf{K} & 0 & \mathbf{K} & 0 \end{bmatrix},$$
$$\mathbf{\Gamma}_2 = \begin{bmatrix} \mathbf{G}_2 & 0 & 0 & 0 \\ 0 & \mathbf{G}_2 & 0 & 0 \\ \mathbf{G}_2 & 0 & 0 & -\mathbf{LD} \\ 0 & 0 & 0 & 0 \end{bmatrix}. \quad (69)$$

Case 3: Packet Drop in Feedforward Path

For $\{s_1, \bar{s}_2\}$, i.e. packet drop occurring in the forward path only,

$$\bar{u}(k) = \bar{u}(k-1). \quad (70)$$

Thus, we can write $\mathbf{x}(k+1)$ from (55) as

$$\mathbf{x}(k+1) = \mathbf{F}\mathbf{x}(k) + \mathbf{G}_1\bar{u}(k-1) + \mathbf{G}_2 w(k). \quad (71)$$

The term $\mathbf{x}(k)$ will remain the same as given in (63). The estimation error $\mathbf{e}(k+1)$ can be written as:

$$\begin{aligned}
&\mathbf{e}(k+1) = \mathbf{x}(k+1) - \hat{\mathbf{x}}(k+1) \\
&\Rightarrow \mathbf{e}(k+1) = \left[\mathbf{F}\mathbf{x}(k) + \mathbf{G}_1\bar{u}(k-1) + \mathbf{G}_2 w(k)\right] \\
&\qquad -\left[\mathbf{F}\left[\mathbf{x}(k) - \mathbf{e}(k)\right] + \mathbf{G}_1\left\{-\mathbf{K}\left[\mathbf{x}(k) - \mathbf{e}(k)\right]\right\} + \mathbf{L}\left(\mathbf{C}\mathbf{x}(k) + \mathbf{D}n(k) - \mathbf{C}\hat{\mathbf{x}}(k)\right)\right] \\
&\Rightarrow \mathbf{e}(k+1) = \left[\mathbf{F}\mathbf{x}(k) + \mathbf{G}_1\bar{u}(k-1) + \mathbf{G}_2 w(k)\right] \\
&\qquad -\left[\mathbf{F}\left[\mathbf{x}(k) - \mathbf{e}(k)\right] + \mathbf{G}_1\left\{-\mathbf{K}\left[\mathbf{x}(k) - \mathbf{e}(k)\right]\right\} + \mathbf{L}\left(\mathbf{C}\mathbf{e}(k) + \mathbf{D}n(k)\right)\right] \\
&\Rightarrow \mathbf{e}(k+1) = \left[\mathbf{F}\mathbf{x}(k) + \mathbf{G}_1\bar{u}(k-1) + \mathbf{G}_2 w(k)\right] \\
&\qquad -\left[\left[\mathbf{F} - \mathbf{G}_1 K\right]\mathbf{x}(k) + \left[-\mathbf{F} + \mathbf{G}_1\mathbf{K} + \mathbf{LC}\right]\mathbf{e}(k) + \left[\mathbf{LD}\right]n(k)\right] \\
&\Rightarrow \mathbf{e}(k+1) = \left[\cancel{\mathbf{F}} - \cancel{\mathbf{F}} + \mathbf{G}_1\mathbf{K}\right]\mathbf{x}(k) + \left[\mathbf{F} - \mathbf{G}_1 K - \mathbf{LC}\right]\mathbf{e}(k) + \mathbf{G}_2 w(k) - \mathbf{LD}n(k) + \mathbf{G}_1\bar{u}(k-1) \\
&\Rightarrow \mathbf{e}(k+1) = \mathbf{G}_1\mathbf{K}\mathbf{x}(k) + \left[\mathbf{F} - \mathbf{G}_1\mathbf{K} - \mathbf{LC}\right]\mathbf{e}(k) + \mathbf{G}_1\bar{u}(k-1) + \mathbf{G}_2 w(k) - \mathbf{LD}n(k).
\end{aligned} \quad (72)$$

Using (70)-(72) the matrix $\mathbf{\Phi}_3$ and $\mathbf{\Gamma}_3$ in (59) can be written from the augmented states as:

$$\boldsymbol{\Phi}_3 = \begin{bmatrix} \mathbf{F} & 0 & 0 & \mathbf{G}_1 \\ 0 & \mathbf{F} & 0 & \mathbf{G}_1 \\ \mathbf{G}_1\mathbf{K} & 0 & \mathbf{F}-\mathbf{G}_1\mathbf{K}-\mathbf{LC} & \mathbf{G}_1 \\ 0 & 0 & 0 & \mathbf{I} \end{bmatrix},$$
$$\boldsymbol{\Gamma}_3 = \begin{bmatrix} \mathbf{G}_2 & 0 & 0 & 0 \\ 0 & \mathbf{G}_2 & 0 & 0 \\ \mathbf{G}_2 & 0 & -\mathbf{LD} & 0 \\ 0 & 0 & 0 & 0 \end{bmatrix}. \tag{73}$$

Case 4: Packet Drop in Feedback and Feedforward Path

If the packet drop occurs in both the sides (feedback and forward path) of the control loop, i.e. $\{\bar{s}_1, \bar{s}_2\}$, the terms $\mathbf{x}(k+1), \mathbf{x}(k), \bar{u}(k)$ will remain the same as in the previous case. The estimation error $\mathbf{e}(k+1)$ can be written as:

$$\begin{aligned}
&\Rightarrow \mathbf{e}(k+1) = \left[\mathbf{F}\mathbf{x}(k) + \mathbf{G}_1\bar{u}(k-1) + \mathbf{G}_2 w(k)\right] - \left[\mathbf{F}\hat{\mathbf{x}}(k) + \mathbf{G}_1 u(k) + \mathbf{L}\left(\bar{y}(k-1) - \mathbf{C}\hat{\mathbf{x}}(k)\right)\right] \\
&\Rightarrow \mathbf{e}(k+1) = \left[\mathbf{F}\mathbf{x}(k) + \mathbf{G}_1\bar{u}(k-1) + \mathbf{G}_2 w(k)\right] \\
&\qquad - \left[\mathbf{F}\left\{\mathbf{x}(k) - \mathbf{e}(k)\right\} + \mathbf{G}_1\left\{-\mathbf{K}\left[\mathbf{x}(k) - \mathbf{e}(k)\right]\right\} + \mathbf{L}\left(\bar{y}(k-1) - \mathbf{C}\left\{\mathbf{x}(k) - \mathbf{e}(k)\right\}\right)\right] \\
&\Rightarrow \mathbf{e}(k+1) = \left[\mathbf{F}\mathbf{x}(k) + \mathbf{G}_1\bar{u}(k-1) + \mathbf{G}_2 w(k)\right] \\
&\qquad - \left[\left\{\mathbf{F} - \mathbf{LC} - \mathbf{G}_1\mathbf{K}\right\}\mathbf{x}(k) + \left\{-\mathbf{F} + \mathbf{G}_1\mathbf{K} + \mathbf{LC}\right\}\mathbf{e}(k) + \mathbf{L}\bar{y}(k-1)\right] \\
&\Rightarrow \mathbf{e}(k+1) = \left[\cancel{\mathbf{F}} - \cancel{\mathbf{F}} + \mathbf{LC} + \mathbf{G}_1\mathbf{K}\right]\mathbf{x}(k) \\
&\qquad + \left[\mathbf{F} - \mathbf{G}_1\mathbf{K} - \mathbf{LC}\right]\mathbf{e}(k) + \mathbf{G}_1\bar{u}(k-1) - \mathbf{L}\bar{y}(k-1) + \mathbf{G}_2 w(k) \\
&\Rightarrow \mathbf{e}(k+1) = \left[\mathbf{LC} + \mathbf{G}_1\mathbf{K}\right]\mathbf{x}(k) + \left[\mathbf{F} - \mathbf{G}_1\mathbf{K} - \mathbf{LC}\right]\mathbf{e}(k) + \mathbf{G}_1\bar{u}(k-1) - \mathbf{L}\bar{y}(k-1) + \mathbf{G}_2 w(k) \\
&\Rightarrow \mathbf{e}(k+1) = \left[\mathbf{LC} + \mathbf{G}_1\mathbf{K}\right]\mathbf{x}(k) + \left[\mathbf{F} - \mathbf{G}_1\mathbf{K} - \mathbf{LC}\right]\mathbf{e}(k) + \mathbf{G}_1\bar{u}(k-1) \\
&\qquad - \mathbf{L}\left[\mathbf{C}\mathbf{x}(k-1) + \mathbf{D}n(k-1)\right] + \mathbf{G}_2 w(k) \\
&\Rightarrow \mathbf{e}(k+1) = \left[\mathbf{LC} + \mathbf{G}_1\mathbf{K}\right]\mathbf{x}(k) + \left[\mathbf{F} - \mathbf{G}_1\mathbf{K} - \mathbf{LC}\right]\mathbf{e}(k) + \mathbf{G}_1\bar{u}(k-1) \\
&\qquad - \mathbf{LC}\mathbf{x}(k-1) - \mathbf{LD}n(k-1) + \mathbf{G}_2 w(k).
\end{aligned} \tag{74}$$

Using, (63), (70), (71), and (74), the matrix $\boldsymbol{\Phi}_4$ and $\boldsymbol{\Gamma}_4$ in (59) can be written from the augmented states as follows:

$$\mathbf{\Phi}_4 = \begin{bmatrix} \mathbf{F} & 0 & 0 & \mathbf{G}_1 \\ 0 & \mathbf{F} & 0 & \mathbf{G}_1 \\ \mathbf{LC}+\mathbf{G}_1\mathbf{K} & -\mathbf{LC} & \mathbf{F}-\mathbf{G}_1\mathbf{K}-\mathbf{LC} & \mathbf{G}_1 \\ 0 & 0 & 0 & \mathbf{I} \end{bmatrix},$$
$$\mathbf{\Gamma}_4 = \begin{bmatrix} \mathbf{G}_2 & 0 & 0 & 0 \\ 0 & \mathbf{G}_2 & 0 & 0 \\ \mathbf{G}_2 & 0 & 0 & -\mathbf{LD} \\ 0 & 0 & 0 & 0 \end{bmatrix}. \quad (75)$$

Therefore, the output of the subsystems can be written as:

$$\tilde{y}(k) = \tilde{\mathbf{C}}\mathbf{z}(k) = \begin{bmatrix} \mathbf{C} & \mathbf{0} & \mathbf{0} & \mathbf{0} \end{bmatrix}\mathbf{z}(k). \quad (76)$$

3.2.5 Stability Analysis of NCS using ADS and Joint Controller/Observer Design

The procedure aims to find the controller gain for the NCS defined in (59) ensuring guaranteed exponential stability for the system on the bounded H_∞ norm. We assume that the fraction of the effective data packet transmission be r_1 and r_2 across the switches s_1 and s_2 respectively. Here the switches s_1 and s_2 practically represents the situation where the data is transmitted from the PMU measurement to the control centre and load centre for the generation and demand response control system. Let us assume $r_1 = r_2 = r$, the effective transmission probabilities R_1, R_2, R_3, R_4 from the sensor to the actuator, for each of the following four cases, can be computed as:

$$\begin{aligned} &s_1, s_2 : R_1 = r^2, && \bar{s}_1, s_2 : R_2 = (1-r)r, \\ &s_1, \bar{s}_2 : R_3 = r(1-r), && \bar{s}_1, \bar{s}_2 : R_4 = (1-r)(1-r). \end{aligned} \quad (77)$$

Then as per [84], the NCS defined in (59) is exponentially stable under packet drop if the following inequality is satisfied as given in [84]:

$$\alpha_1^{R_1}\alpha_2^{R_2}\alpha_3^{R_3}\alpha_4^{R_4} > \alpha > 1 : \alpha_1, \alpha_2, \alpha_3, \alpha_4 \in \mathbb{R}_+. \quad (78)$$

Hence, we can derive the following theorem,

Theorem 1: The NCS (59) is exponentially stable with decay rate $\alpha > 0$ with random packet drop rate driven by arbitrary switching signal and external disturbances , if there exists a CQLF i.e. common quadratic Lyapunov function, $\mathbf{P} = \mathbf{P}^T > \mathbf{0}$ and state feedback controller and observer gains $\{\mathbf{K}, \mathbf{L}\}$ with the satisfaction of H_∞ norm bound $\gamma > 0$ by satisfying the following LMI:

$$\begin{bmatrix} \tilde{\mathbf{C}}^T\tilde{\mathbf{C}} - \alpha_\sigma^{-2}\mathbf{P} & \mathbf{0} & \mathbf{\Phi}_\sigma^T \\ \mathbf{0} & -\gamma^2\mathbf{I} & \mathbf{\Gamma}_\sigma^T \\ \mathbf{\Phi}_\sigma & \mathbf{\Gamma}_\sigma & -\mathbf{Q} \end{bmatrix} < \mathbf{0}, \quad \forall \sigma = 1,2,3,4, \tag{79}$$

where $\mathbf{P}^{-1} = \mathbf{Q}$, implying:

$$\mathbf{PQ} = \mathbf{I}. \tag{80}$$

Proof:

As proved in [84], the NCS (59) will be exponentially stable at transmission rate *r*, if (78) is satisfied and the discrete-time Lyapunov function satisfies the following inequality,

$$\Delta V(k) = V(\mathbf{z}(k+1)) - V(\mathbf{z}(k)) < (\alpha_\sigma^{-2} - 1)V(\mathbf{z}(k)),$$

(81)while considering the Lyapunov function $V(\mathbf{z}(k)) = \mathbf{z}^T(k)\mathbf{P}\mathbf{z}(k)$. In order to satisfy the H_∞ norm bound γ for the NCS (59), the following inequality has to be satisfied [164]:

$$V(\mathbf{z}(k+1)) - V(\mathbf{z}(k)) + \tilde{y}^T(k)\tilde{y}(k) - \gamma^2\mathbf{\eta}^T(k)\mathbf{\eta}(k) < \mathbf{0}. \tag{82}$$

Here, $V(\mathbf{z}(k+1))$ and $V(\mathbf{z}(k))$ should satisfy the inequality condition for the exponential stability of the switched system. Substituting $V(\mathbf{z}(k)) = \mathbf{z}^T(k)\mathbf{P}\mathbf{z}(k)$ in (59), to satisfy the relation (81), we can write the following inequality,

$$\begin{bmatrix} \mathbf{z}^T(k) & \mathbf{\eta}^T(k) \end{bmatrix} \begin{bmatrix} \mathbf{\Phi}_\sigma^T\mathbf{P}\mathbf{\Phi}_\sigma - \alpha_\sigma^{-2}\mathbf{P} & \mathbf{\Phi}_\sigma^T\mathbf{P}\mathbf{\Gamma}_\sigma \\ \mathbf{\Gamma}_\sigma^T\mathbf{P}\mathbf{\Phi}_\sigma & \mathbf{\Gamma}_\sigma^T\mathbf{P}\mathbf{\Gamma}_\sigma \end{bmatrix} \begin{bmatrix} \mathbf{z}(k) \\ \mathbf{\eta}(k) \end{bmatrix} < \mathbf{0}. \tag{83}$$

For satisfying the H_∞ norm bound of the output to the disturbance input as per (82), the following inequality hold:

$$\tilde{y}^T(k)\tilde{y}(k) - \gamma^2 \boldsymbol{\eta}^T(k)\boldsymbol{\eta}(k) \le \mathbf{0}. \tag{84}$$

Using the relation (76), in the above inequality yields

$$\begin{bmatrix} \mathbf{z}^T(k) & \boldsymbol{\eta}^T(k) \end{bmatrix} \begin{bmatrix} \tilde{\mathbf{C}}^T\tilde{\mathbf{C}} & \mathbf{0} \\ \mathbf{0} & -\gamma^2\mathbf{I} \end{bmatrix} \begin{bmatrix} \mathbf{z}(k) \\ \boldsymbol{\eta}(k) \end{bmatrix} \le \mathbf{0}. \tag{85}$$

Considering the strict inequalities in (83) and (85), we can write,

$$\begin{bmatrix} \mathbf{z}^T(k) & \boldsymbol{\eta}^T(k) \end{bmatrix} \begin{bmatrix} \boldsymbol{\Phi}_\sigma^T\mathbf{P}\boldsymbol{\Phi}_\sigma - \alpha_\sigma^{-2}\mathbf{P} + \tilde{\mathbf{C}}^T\tilde{\mathbf{C}} & \boldsymbol{\Phi}_\sigma^T\mathbf{P}\boldsymbol{\Gamma}_\sigma \\ \boldsymbol{\Gamma}_\sigma^T\mathbf{P}\boldsymbol{\Phi}_\sigma & \boldsymbol{\Gamma}_\sigma^T\mathbf{P}\boldsymbol{\Gamma}_\sigma - \gamma^2\mathbf{I} \end{bmatrix} \begin{bmatrix} \mathbf{z}(k) \\ \boldsymbol{\eta}(k) \end{bmatrix} < \mathbf{0}, \tag{86}$$

implying:

$$\begin{bmatrix} \boldsymbol{\Phi}_\sigma^T\mathbf{P}\boldsymbol{\Phi}_\sigma - \alpha_\sigma^{-2}\mathbf{P} + \tilde{\mathbf{C}}^T\tilde{\mathbf{C}} & \boldsymbol{\Phi}_\sigma^T\mathbf{P}\boldsymbol{\Gamma}_\sigma \\ \boldsymbol{\Gamma}_\sigma^T\mathbf{P}\boldsymbol{\Phi}_\sigma & \boldsymbol{\Gamma}_\sigma^T\mathbf{P}\boldsymbol{\Gamma}_\sigma - \gamma^2\mathbf{I} \end{bmatrix} < \mathbf{0}. \tag{87}$$

Thus we can write (87) as,

$$\begin{bmatrix} -\alpha_\sigma^{-2}\mathbf{P} + \tilde{\mathbf{C}}^T\tilde{\mathbf{C}} & \mathbf{0} \\ \mathbf{0} & -\gamma^2\mathbf{I} \end{bmatrix} + \begin{bmatrix} \boldsymbol{\Phi}_\sigma^T \\ \boldsymbol{\Gamma}_\sigma^T \end{bmatrix} \mathbf{P} \begin{bmatrix} \boldsymbol{\Phi}_\sigma & \boldsymbol{\Gamma}_\sigma \end{bmatrix} < \mathbf{0}. \tag{88}$$

Taking Schur complement of (88), we can write,

$$\begin{bmatrix} \tilde{\mathbf{C}}^T\tilde{\mathbf{C}} - \alpha_\sigma^{-2}\mathbf{P} & \mathbf{0} & \boldsymbol{\Phi}_\sigma^T \\ \mathbf{0} & -\gamma^2\mathbf{I} & \boldsymbol{\Gamma}_\sigma^T \\ \boldsymbol{\Phi}_\sigma & \boldsymbol{\Gamma}_\sigma & -\mathbf{Q} \end{bmatrix} < \mathbf{0} \tag{89}$$

where $\mathbf{P}^{-1} = \mathbf{Q}$ thus proving (79) and (80) □

The error convergence due to the observed and current state depends on the boundedness of noise and disturbance vector stated for the linear switched system [162]. Hence load disturbance and nature of FDI attack is considered to

be pulsed. Pulsed load disturbance can be considered from the naval shipboard power system [165] or a fast DC voltage electric vehicle charger [166].

Load demand is a pulse signal defined as:

$$\Delta P_L = \begin{cases} 0.01 & 10 < t < 100 \\ 0 & \text{otherwise} \end{cases} \tag{90}$$

The disturbance is considered as an FDI attack in a similar pattern as given in [167].

$$d_{\text{FDI}}(t) = \begin{cases} 0.04 & t > 100 \\ 0.09 & 120 < t < 150 \\ 0 & t > 150 \end{cases} \tag{91}$$

The FDI attack modifies the state variables like governor input $P_{g_i}(t)$ or the input signal to the EV, $P_E(t)$ as given in [167]. As far as DR is concerned, FDI attack modifies the state variable $x_1(t)$, which is indirectly affected by the attack on the data transfer between the load aggregator and consumers. The feasibility of the problem in Theorem 1 is non-convex due to matrix equality constraints as shown in (79) and (80) . As shown in [168], this type of problem is NP-hard. The efficiency of CCL algorithm is relatively high compared to other methods [169] while solving the LMIs with non-convex constraints. This algorithm has also been used to find the state feedback controller for the NCS considering network delay and packet dropout in [170]. The CCL algorithm states that the LMI $\begin{bmatrix} \mathbf{P} & \mathbf{I} \\ \mathbf{I} & \mathbf{Q} \end{bmatrix} \geq \mathbf{0}$ is feasible in the matrix variables $\mathbf{P} \in \mathbb{R}^n > \mathbf{0}$ and $\mathbf{Q} \in \mathbb{R}^n > \mathbf{0}$, then $\text{Tr}(\mathbf{PQ}) \geq n$ and at the optimum $\text{Tr}(\mathbf{PQ}) = n$ iff $\mathbf{PQ} = \mathbf{I}$. Hence in order to find the controller and the observer gain for the switched system (59) using the CCL algorithm, the equality constraints (80) are cast in the following LMI form:

$$\begin{bmatrix} \mathbf{P} & \mathbf{I} \\ \mathbf{I} & \mathbf{Q} \end{bmatrix} \geq \mathbf{0} \tag{92}$$

Hence in order to find the observer and controller gain, the following minimization problem has to be solved,

$$\min \mathrm{Tr}\left(\mathbf{PQ}\right) \tag{93}$$

subject to (78), (79) and (92).

The algorithm is summarized as follows:

Algorithm: Cone Complementary Linearization (CCL)

Initialize: Select the number of iterations *N* and switching rate *r* and exponential convergence rate $\{\alpha_i\}_{i=1}^{4}$. Set $j = 0$

If $\left(\sum_{i=1}^{4} r_i \log(\alpha_i) > 0\right)$

Find $\{\mathbf{P_0}, \mathbf{Q_0}\}$ solving (79) and (92)

for *j* = 0,*N* **do**

$\min_{\mathbf{P},\mathbf{Q}} \mathrm{Tr}\left(\mathbf{P}_j\mathbf{Q} + \mathbf{Q}_j\mathbf{P}\right)$ s.t. (79) and (92)

$\mathbf{P}_{j+1} \leftarrow \mathbf{P}$, $\mathbf{Q}_{j+1} \leftarrow \mathbf{Q}$

end

end

3.2.6 Joint Controller and Observer for State-Space LFC

The joint observer and controller for the NCS are found numerically by solving the above CCL algorithm in MATLAB using YALMIP toolbox [171]. The semidefinite optimization SeDuMi solver [172] is utilized in the YALMIP toolbox to implement the CCL algorithm, which solves (93), satisfying (78), (79) and (92)

.The solver can be initialized with the settings `solver ='sedumi'` `sedumi.eps = 10^-12`. The value of the data transmission rate (r) and exponential convergence rate, (α_i) as defined in, (78) is initialized as 0.1 and $\{1.50,1.25,1.25,1.1\}$ respectively, which means the system is tuned at a 90% packet drop rate. The convergence performance of the algorithm is tested on the LFC model with different DR and EV configuration is shown below.

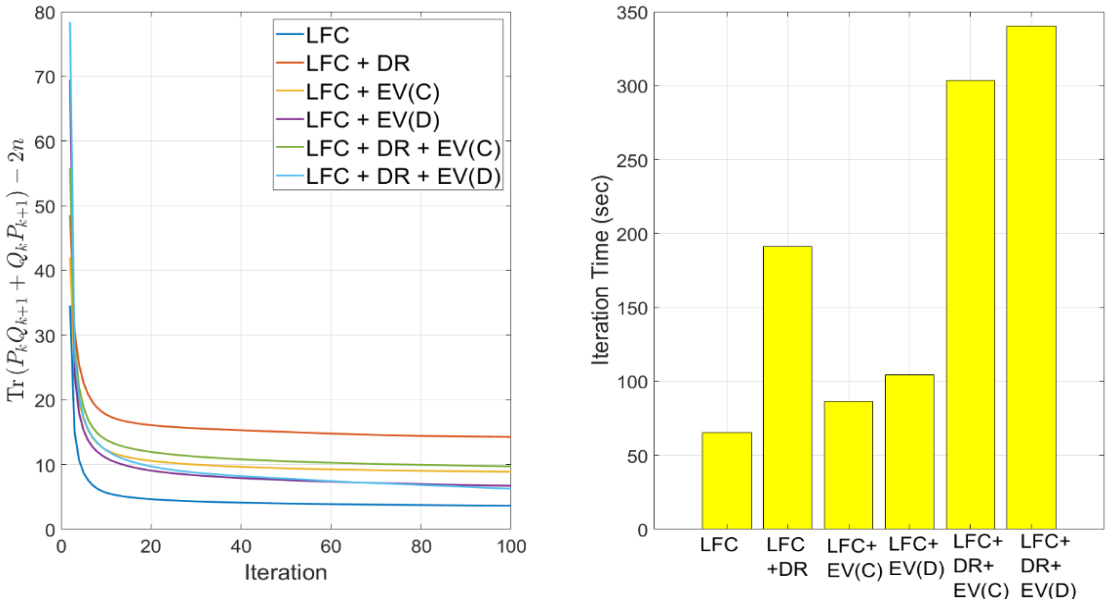

Figure 3-23: Convergence of the CCL algorithm when it is run for 100 iterations and time taken to for all the system configurations.

The algorithm converges to obtain $(\mathbf{P},\mathbf{Q},\mathbf{L},\mathbf{K},\gamma)$ and 100 iterations. We observe that the algorithm convergence rate is quite fast, as it requires around 20 iterations to settle down. The higher-order dynamics provided due to the DR time delay increases the total convergence time, as shown in Figure 3-23. The total iteration time is highest for LFC, DR and EV combination, as the system order is relatively high. Hence, we can say that the total iteration time depends linearly upon the order of the system. It is noted that the present work considers the CCL algorithm which is a well-known technique for solving LMIs (79) and (80) with strict and nonconvex constraints as a sequential optimization problem as reported in [147], [169], [173]. The CCL algorithm is ensuring the convergence of the CCL error i.e. $\mathrm{Tr}(\mathbf{P}_k\mathbf{Q}_{k+1}+\mathbf{Q}_k\mathbf{P}_{k+1})-2n$ at minimum value at time $t\to\infty$ for satisfying and feasibility of the LMIs (79) and (80), which is shown in Figure 3-23

for all the test-bench systems. Since the dynamics of the each test-bench power/energy systems are different, the minimization of convergence of the CLL error is different for the individual systems to obtain the feasible solution from the LMIs (79) and (80).

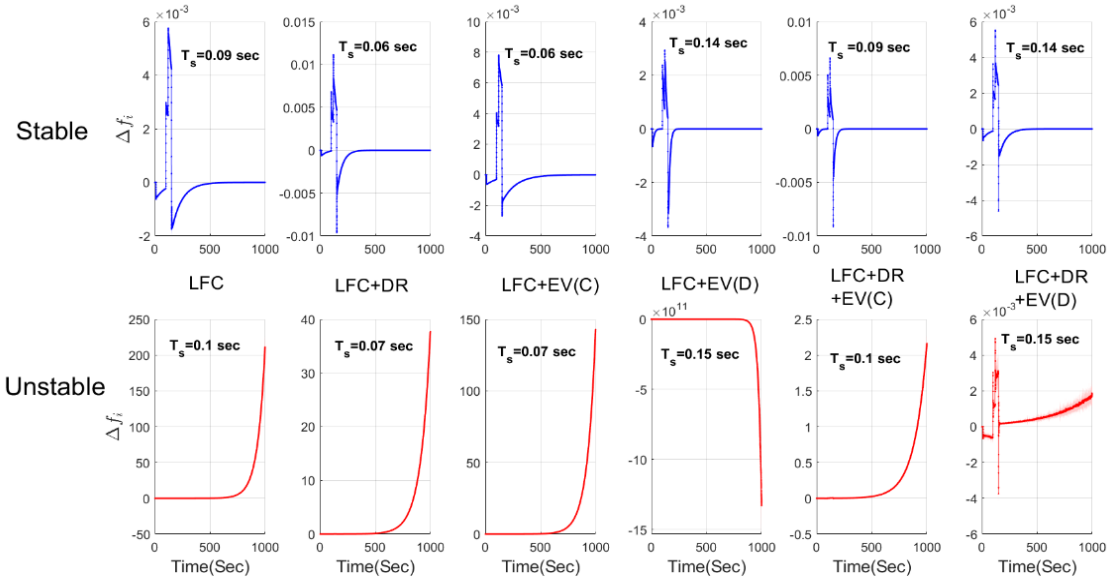

Figure 3-24: Stable and unstable system response for different sampling time for different configurations

3.2.7 System Response with Step Load Disturbance and Bounded Noise on Linear LFC

The system response with the state feedback controller and observer for a stable sampling time T_s is shown in Figure 3-24. We observe a spike in the frequency response at a time interval $10 < t < 200$, which is due to the bounded load disturbance and the FDI attack as mentioned in (90) and (91). The maximum frequency fluctuations are encountered with LFC with DR configuration, being marginally greater than 0.01 pu. The maximum frequency fluctuations $\{\Delta f_i\}_{\max}$ are comparable to the one obtained in [138]. Moreover, it is also in line with the smart grid industrial standards [75]. The sampling time T_s is varied at the rate of 0.01 seconds to find the discretized system, from which the LMI is solved to obtain the controller and observer gains. A low value of T_s utilizes that higher

communication bandwidth, while a higher value can make the plant unstable with the given controller gains.

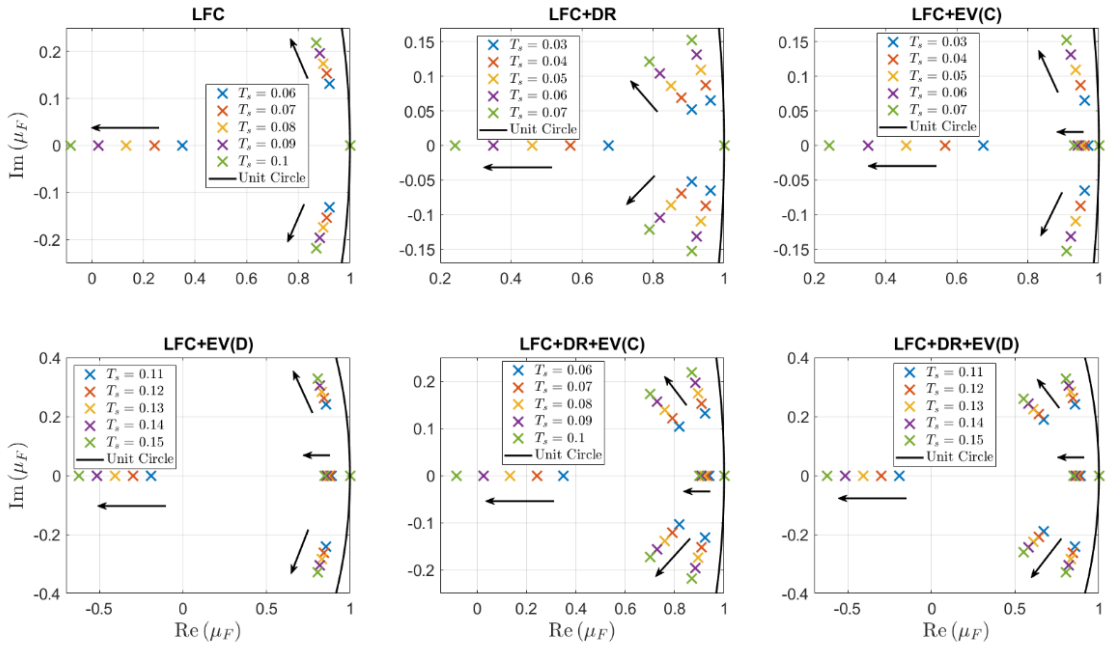

Figure 3-25: Eigenvalue configuration of the discrete-time system sampled at different sampling intervals for different system configurations.

Hence a threshold margin of the sampling time is obtained, beyond which, if increased, can make the system unstable, as shown in Figure 3-24. As per our analysis, the sampling time T_s for instability is least when LFC and EV/DR is utilized and highest for a mixed combination of LFC and EV decentralized scenario and in the case where LFC, EV and DR all working in a decentralized scenario. The system response in Figure 3-24 suggests that, the decentralized combination of LFC, EV, and DR utilizes minimum communication bandwidth for stability scenario while ensuring system stability. The above inference is supported in Figure 5, with the given eigenvalue pattern of **F** at different sampling times for different LFC, DR and EV configurations. LFC has an eigenvalue at the origin, a real and a pair of complex eigenvalue pairs. The eigenvalue at origin is responsible for making the steady-state value of Δf_i to zero. DR state variable adds another pair of complex eigenvalue pair, while a coupled EV configuration adds another eigenvalue on the real axis while pulling the resultant complex eigenvalue pair closer to the origin. With the decentralized EV configuration, the eigenvalue located at the real axis is not affected. However, the complex pair of

eigenvalues moves away from the origin, resulting in stability at a higher sampling rate and faster system performance in terms of settling time. A similar phenomenon is observed in LFC and DR with different EV configurations, centralized and and decentralized, where the complex and real poles are farther away from the origin. Controller designed on the system where poles are farther from origin gives faster response with a smaller peak overshoot. The degradation in stability for all systems under increasing sampling time is observed in Figure 3-25. It is seen that the eigenvalues of all the systems are shifting towards higher frequencies and lower damping region i.e. shifted away from the stability region when T_s is increasing. Again, when DR is considered in the LFC and in combination of LFC and EV, the number of complex conjugate poles are increasing (i.e. two pair of complex conjugate poles) as compared to other systems, which defines the increase in number of non-dominance poles. Therefore, it will be quite challenging to design pole placement-based controller. However, deeper insight into system characteristics is obtained while incorporating the controller and observer gains by considering the eigenvalues of $\{\Phi_i\}_{i=1}^{4}$ for all the systems, as shown in Figure 3-26. We can observe that the poles of the each sub-systems of the NCS (59) for all the systems lies within and on the unit circle at different sampling time. Although, the poles are shifting towards higher frequencies and lower damping ratio region in the unit circle with the increasing T_s. It is also seen that when packet drop occurs in both feedback and forward path i.e. for Φ_4 , the poles are more diverging in nature with higher T_s as compared to other sus-systems for the all systems.

For the system of LFC with DR and combination of LFC and EV with DR, the sub-systems under no drop case provides poles in dominant nature with the increasing T_s. Whereas, for the LFC with EV systems, Φ_4 provides poles with dominant nature when T_s is increasing. It is an interesting phenomenon to analyze the stability of the NCS modelled as switched systems under arbitrary packet drops. For instance, switched systems can be unstable or stable under certain switching between all the sub-systems even the sub-systems are stable, unstable or combination of both respectively [159], [174], [175]. This is due to the fact that the stability is not only depend on the dynamics of each sub-system but

also depend on the properties of switching signal (e.g controlled switching, arbitrary switching). There are many excellent reviews on the switched system's stability under controlled or restricted switching like dwell-time and average dwell-time [176], piecewise and multiple Lyapunov function [159] in the literatures. For example, Hespanha [177] has proposed that under the time-controlled class of switching signals (i.e., trajectory independent), uniform asymptotic stability of switched linear systems is equivalent to exponential stability and in [176] has shown that under slow switching, switched-system is exponentially stable. To ensure the stability of the switched systems with both stable and unstable sub-systems, an average dwell time approach has been proposed in [178], where the activation time of unstable sub-systems are chosen smaller than stable sub-systems. However the approach proposed in [176], [178] is not valid for switched systems under arbitrary switching, since these method requires to stay long enough in a stable sub-systems. An existence of CQLF using LMI approach has been presented for the switched systems under arbitrary switching in [94], [142], [147], [151], [175]. In the present work, NCS under packet drop has been modelled as switched systems using ADS approach, where the aim is to obtain observer and state feedback controller gains with CQLF and bounded H_∞ norm such that the LMIs (79) is satisfied ensuring exponential stability for the NCS subjected to packet drop modelled as switched systems under arbitrary switching. Therefore, it is an important issue to select appropriate T_s for dynamical systems such that the NCS to be exponentially stable, since the sub-systems are going towards instability region with the increasing T_s which leads to instability of the NCS (59) under arbitrary switching. Hence, it can be inferred that the selection of T_s should be smaller for the stable sub-systems to achieve the stability of the NCS modelled as switched systems under arbitrary switching. The selection of T_s for the NCS under arbitrary packet drop will be analytically explored in future.

With high packet drop rates in feedback and forward path, we can expect the switched system Φ_4 most of the time. Hence the poles of Φ_4 will dominate the dynamics of the overall system. As we saw in Figure 3-25, we also see a similar pattern for eigenvalues of $\{\Phi_i\}_{i=1}^{4}$ in Figure 3-26, where they move away from the

origin with an increase in sampling time. In a decentralized EV system with LFC, the eigenvalue movement is away from the real and imaginary axis. However, for LFC systems with DR, the eigenvalues drift away along the imaginary axis only. We observe in the case of decentralized EV systems with LFC, the complex conjugate eigenvalue pairs are further apart from the origin compared to the eigenvalues in other system configurations. As a result of that, we see a better response from the system.

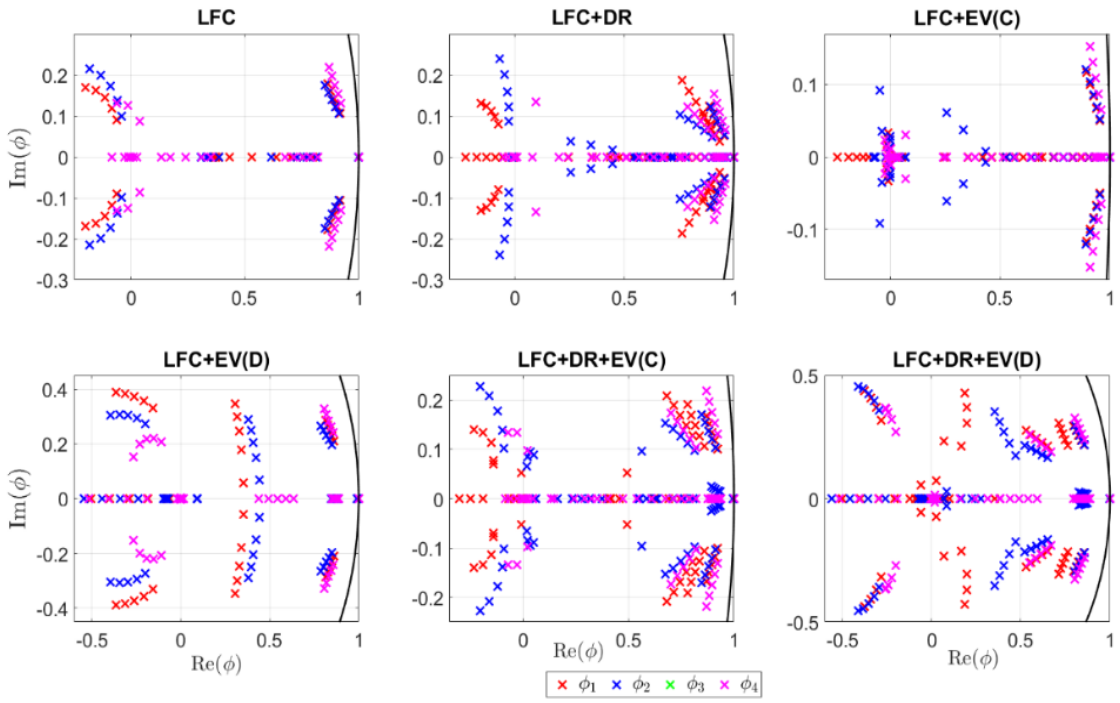

Figure 3-26: Eigenvalue configuration of the modelled switched systems at different sampling times for different system configurations.

3.2.7.1 State Estimation And Analysis Under Bounded Noise and Disturbance

The system response with the designed state feedback controller and observer gain obtained after solving the LMI in (89) using the CCL algorithm, is showed in Figure 3-27, Figure *3-28*, Figure 3-29, Figure *3-30*,

Figure 3-31 and Figure 3-32. The system response is obtained under bounded noise and disturbance which is defined as follows:

$$\Delta P_L = \begin{cases} 0.01 & 100 < t < 200 \\ 0 & \text{otherwise} \end{cases} \tag{94}$$

$$n(t)=\begin{cases}0.01 & 300<t<400\\ 0 & \text{otherwise}\end{cases} \tag{95}$$

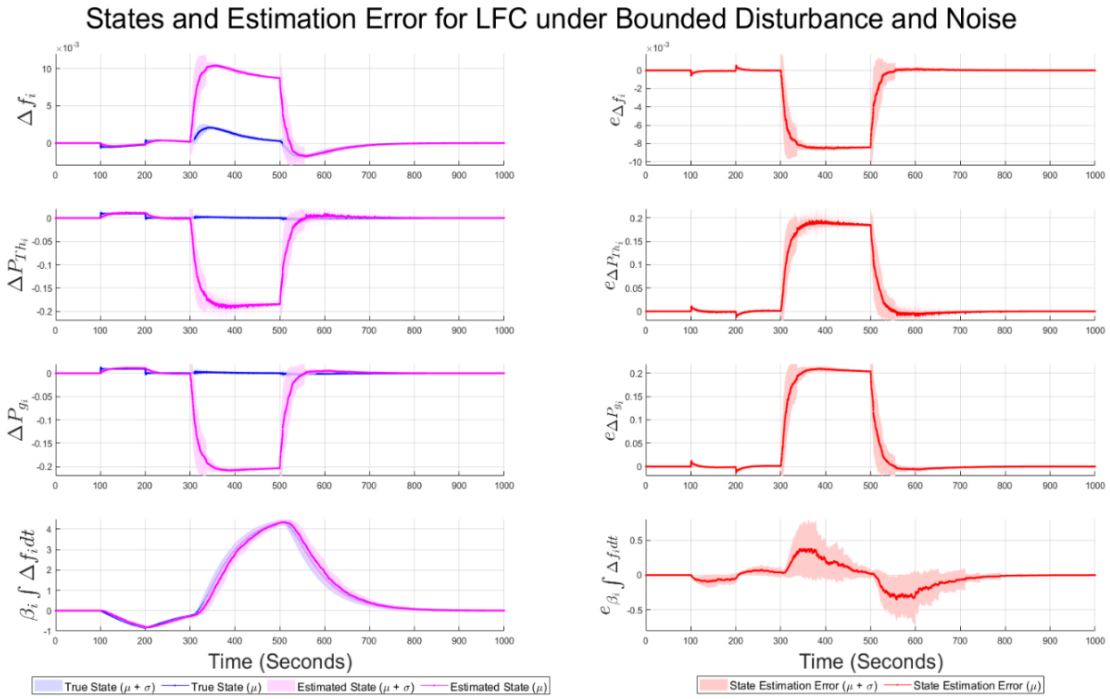

Figure 3-27: True/observed states and estimation error for the LFC under bounded disturbance and noise obtained after 100 Monte Carlo simulations at 99% random packet drop rate.

The FDI attack as a disturbance is not considered in this case as it was in the previous section. Pulsed load disturbance is considered for the analysis. The noise represents the error in measurement of variables in in the power control centre and EV aggregator centre, for those configurations where EV was deployed. The nature of the disturbance in (94)-(95) is such that it is L_2 norm bounded so that the controller and observer design is valid for linear switched system [162]. The system simulation is performed at 99% packet drop rate even though the control and observer gain was obtained at 90% packet drop rate. This was done to check the state estimation error and sensitivity of the system to higher packet drop rates and the validity of the control design. The sampling time T_s considered here is the one described in the previous section. We observe a common trend in all the system response is that the error due to disturbance input is higher as compared to the input load disturbance. Moreover, we also observe that the settling time and uncertainty of the estimated state for the system during the time interval bounded noise was applied, is quite higher as compared to the

settling time when the disturbance was applied. We observe for the states $\{\Delta f_i, \Delta P_{Th_i}, \Delta P_{g_i}\}$ the settling time for the estimation error is close to 200 seconds and for $\beta_i \int \Delta f_i dt$ it is around 400 seconds even though the noise duration was for 100 seconds as defined in (95).

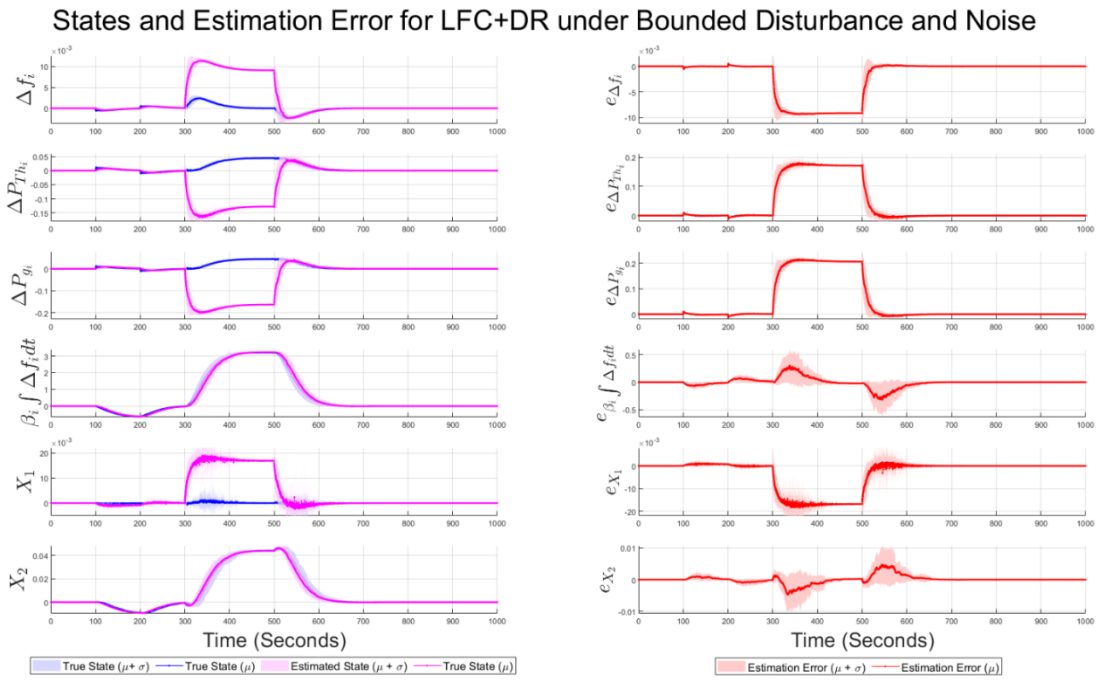

Figure 3-28: True/observed states and estimation error for LFC with DR under bounded noise and disturbance obtained after 100 Monte Carlo system simulations at 99% random packet drop rate.

However, we observe that the settling time for the state $\beta_i \int \Delta f_i dt$ is the highest for the LFC system in Figure 3-27 as compared to other states. The settling time is slower when the input disturbance ΔP_L is applied, hence we observe a steep jump in its value when the noise is applied is applied to the system, as the system is not settled due to the disturbance applied. This is evident in the finite uncertainty in the estimation error plot $e_{\beta_i \int \Delta f_i dt}$, during the time $200 < t < 300$, even when no disturbance or noise is present in the system. We also observe higher uncertainty in the estimation error for the state $\beta_i \int \Delta f_i dt$ for the LFC system. Physically we can say that the secondary control feedback for frequency deviation and its estimation by the observer is quite sensitive to system noise. For the remaining states, we observe higher uncertainty in the state estimation error when it is

settling down or reaching the peak under the persistent noise in the given time duration. We observe in Figure 3-28 that the response of the states $\{\Delta f_i, \Delta P_{Th_i}, \Delta P_{g_i}\}$ and estimation error is similar to what we observed for the LFC system with a similar settling time of the response. However, the settling time for estimation error of the state $\beta_i \int \Delta f_i dt$ is much smaller as compared to previous case. Moreover, the settling time for that state for input disturbance is also lower.

This can be attributed to the contribution of the demand response, where the requirement of secondary control input becomes lesser. However, we do observe an uncertainty in the error response of the state $\beta_i \int \Delta f_i dt$ at time $500 < t < 600$, even though no disturbance or noise is present during that interval. This phenomenon can be attributed due to the delay between the aggregator and consumer response. This delay is reflected on the estimation error of the state $\{X_1, X_2\}$ during the interval $500 < t < 600$. This delay is also evident on the uncertainty of estimation error of $\beta_i \int \Delta f_i dt$.

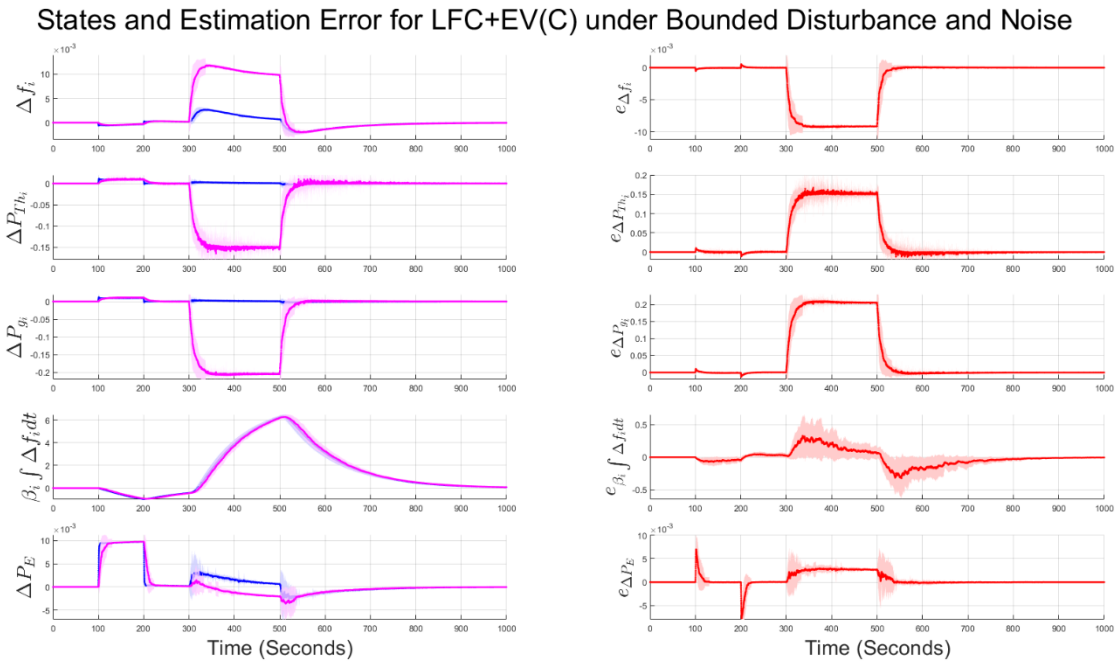

Figure 3-29: True/observed states for LFC with centralized EV configuration under bounded noise and disturbance obtained after 100 Monte Carlo simulations at 99% random packet drop rate.

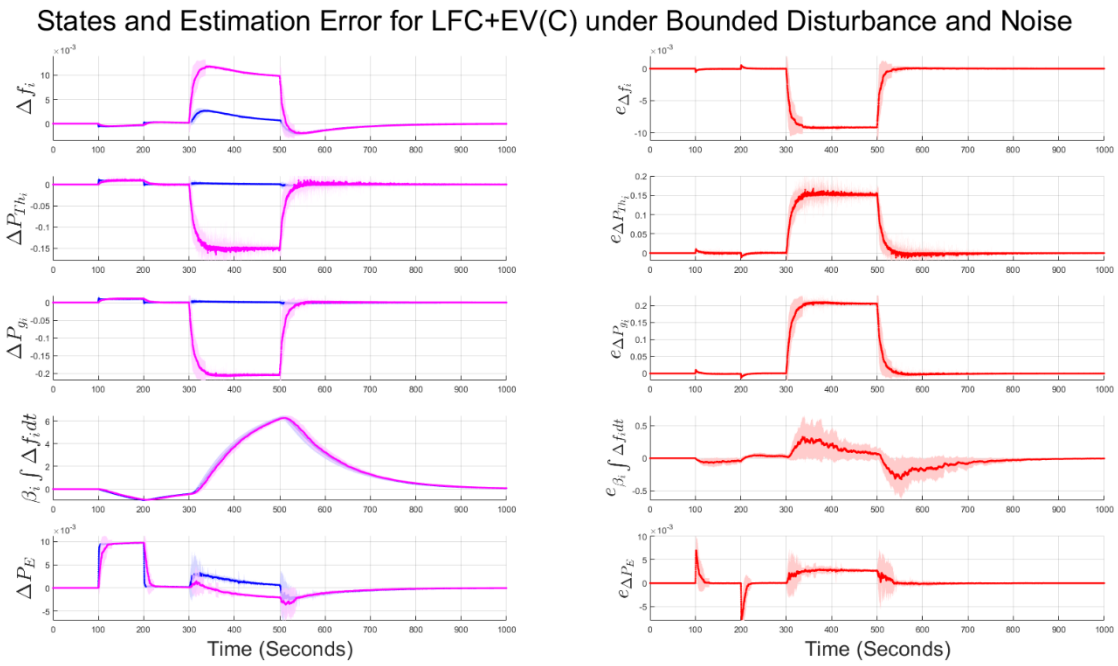

Figure 3-30: True/observed states for LFC with decentralized EV configuration under bounded noise and disturbance obtained after 100 Monte Carlo simulations at 99% random packet drop rate.

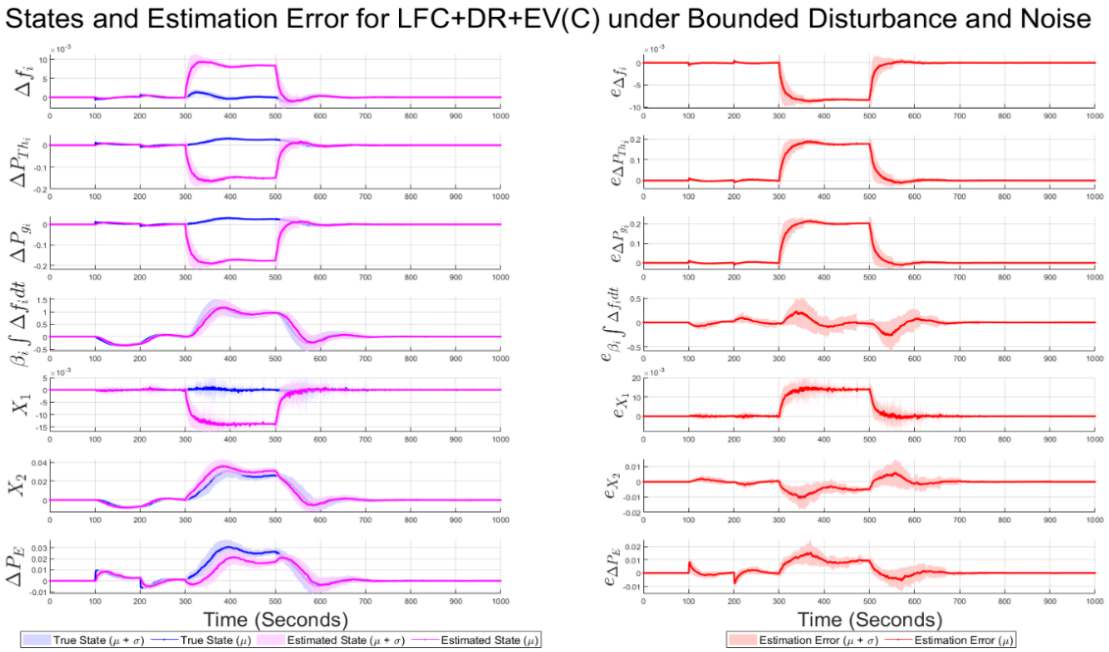

Figure 3-31: True and observed states for LFC with demand response and centralized EV configuration obtained after 100 Monte Carlo simulations at 99% packet drop rate.

We observe in Figure 3-29, that for the estimation error of the states $\{\Delta f_i, \Delta P_{Th_i}, \Delta P_{g_i}\}$ is quite similar as compared to previous cases for the LFC with

centralized EV configuration. However, we observe the uncertainty in the estimated value of ΔP_{Th_i} during the time interval $300 < t < 500$. However, the settling time for the state $\beta_i \int \Delta f_i dt$ is even higher than for the LFC system we observed in Figure 3-27. This is supplemented by the increase in the uncertainty of the estimation error of the state $\beta_i \int \Delta f_i dt$. Unlike the other states, the effect of load disturbance is higher for the state ΔP_E as compared to the measurement noise. This is evident by comparing the peak value of ΔP_E obtained after a disturbance and noise is applied at the given time intervals defined in (94)-(95). However, the settling time of the state ΔP_E is much faster as compared to other system states. However as compared to previous responses, the state estimation error is not settling down to zero as shown in Figure 3-30 for the LFC system with decentralized EV configuration. However, the mean of the estimation error is almost settling to zero for all the states. Higher uncertainty is caused for this system, due to the fact that the poles are further apart from the origin as shown in eigen value plot for the discretized system in Figure 3-25. An increase in any parameter moves the eigen values of the closed loop system closer to unit circle and hence making the system sensitive to parametric variations. We observe that the oscillations due to measurement noise is much higher as compared to system disturbances. However, the peak for the state $\beta_i \int \Delta f_i dt$, is much lower as compared to the previous cases.

For the LFC with demand response and EV configuration, the estimation error for the states $\left\{\Delta f_i, \Delta P_{Th_i}, \Delta P_{g_i}\right\}$ is similar for both centralized and decentralized configuration. However, for the state $\beta_i \int \Delta f_i dt$, the peak value is lower for decentralized configuration. However, for the centralized configuration, $\beta_i \int \Delta f_i dt$ settles faster when there is an input disturbance, but the settling time is similar for the same state, under bounded noise scenario for both the EV configurations. We observe a higher uncertainty for the estimation error of $\beta_i \int \Delta f_i dt$ for decentralized scenario, which may be due to higher sensitivity of the system to parametric variations. This is also reflected in the wiggles found for the mean

state of $\{X_1, X_2\}$ for the decentralized EV scenario. The wiggles are also persistent during the period when the noise and disturbance is not present in the system. However, we do not see any uncertainty or wiggles for the $\{X_1, X_2\}$, during the input disturbance period for the centralized EV configuration. However, the trend is opposite for the state ΔP_E, where we find higher uncertainty for the system with centralized EV configuration when the bounded noise is present in the system. Moreover, we also observe an improvement in setting time of the state ΔP_E for the decentralized EV configuration. However, the system response along with estimation error is similar for ΔP_E during the interval when input disturbance is applied to the system.

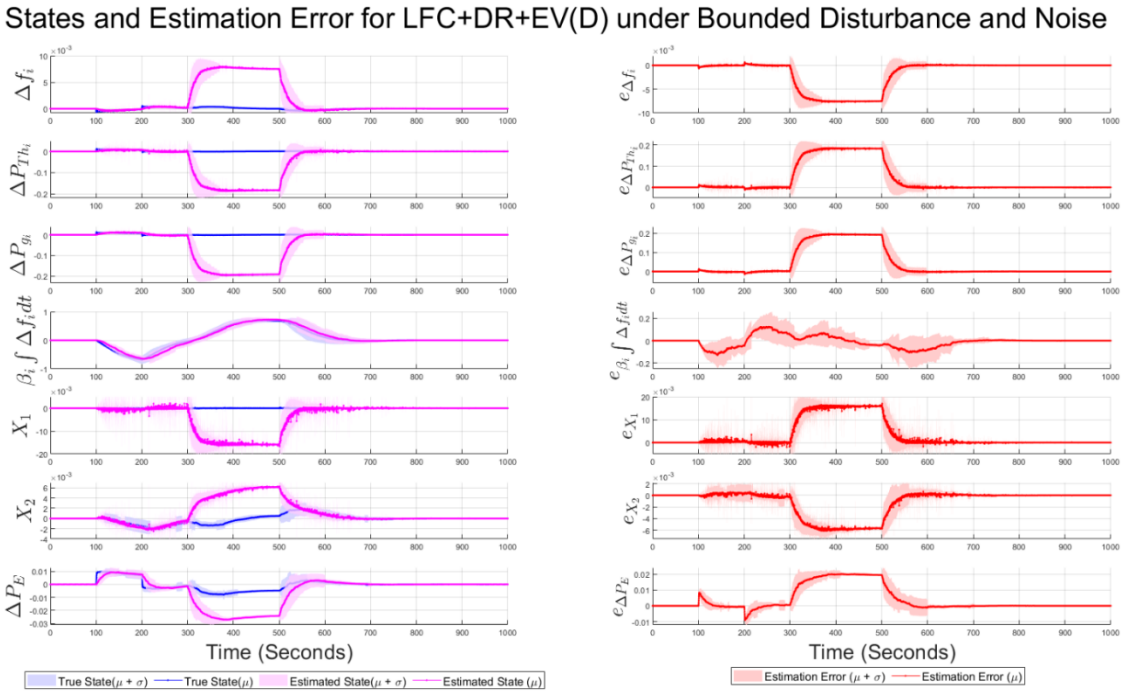

Figure 3-32: True and observed states for LFC with demand response and decentralized EV configuration obtained after 100 Monte Carlo simulations at 99% packet drop rate.

3.2.7.2 State Estimation and Analysis under FDI attack and load disturbance

In Figure 3-33, we observe the all the states are estimated perfectly by the observer, tracking in the given time interval. However, during the period when the FDI attack and load disturbance occurs, the real and the observed states vary. We only observe that the state $\beta\int \Delta f_i dt$ is estimated perfectly despite the FDI

attack and load disturbance, which may be due to the relative magnitude of the attack and the state value being higher than the remaining states. When the FDI attack and load disturbance occurs, $\{\Delta P_{g_i}, \Delta P_{m_i}\}$ increases for a while becomes for a while before it settles down to zero. It suggests that FDI attack on the input tends to increase the generation than what is required from the plants.

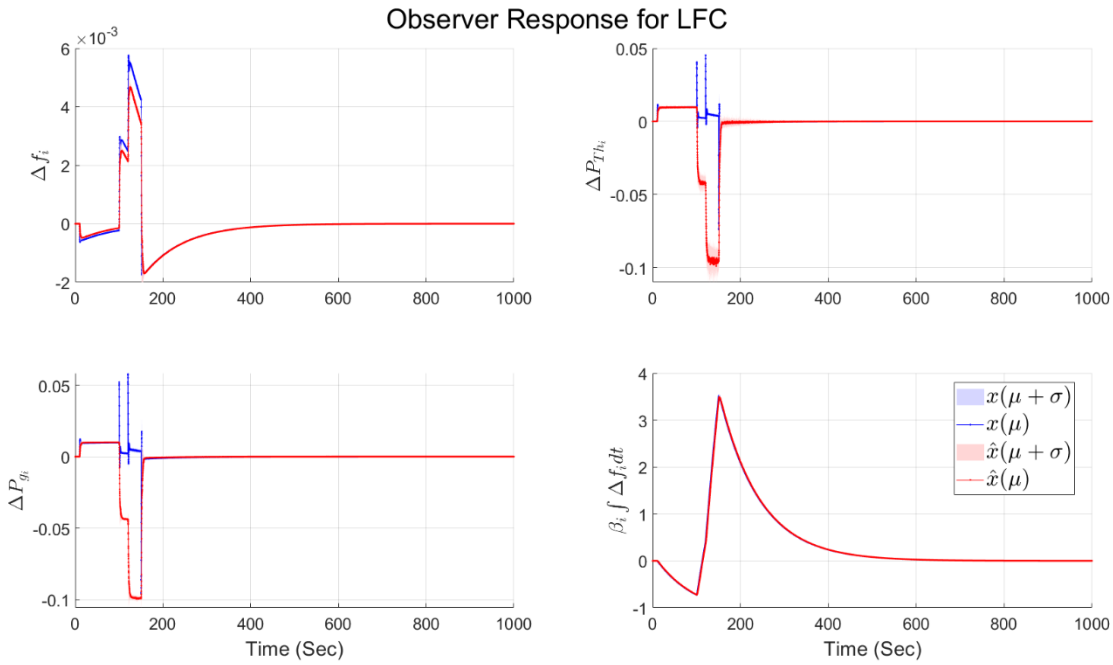

Figure 3-33: Observer Response for LFC system with mean and uncertainty calculated over 100 Monte Caro iterations

The impact of the FDI attack on $\{\Delta P_{g_i}, \Delta P_{m_i}\}$ is much more pronounced for LFC and DR, as seen in Figure 3-34, as the peak value is higher than what is observed in the previous case. However, the estimated states $\{\Delta \hat{P}_{g_i}, \Delta \hat{P}_{m_i}\}$ during FDI attack is negative maximum of the original state variables observed. For the DR state variables, $\{X_1, X_2\}$ we also observe a similar pattern, where estimation error occurs when the FDI attack occurs with the underestimation of both the parameters.

When we incorporate a centralized EV configuration with LFC, positive power output from the aggregator is expected as shown in Figure 3-35, which means either the EVs have to be in discharge mode during that period or energy has to

be provided from the storage devices owned by the aggregators. However, the peak of $\{\Delta P_{g_i}, \Delta P_{m_i}\}$ during load disturbance and FDI attack is much lower than in the previous case suggesting that the centralized EV provides better regulation of power plants during the grid disturbance as compared to DR. The EV state ΔP_E is almost correctly estimated even during the FDI attack.

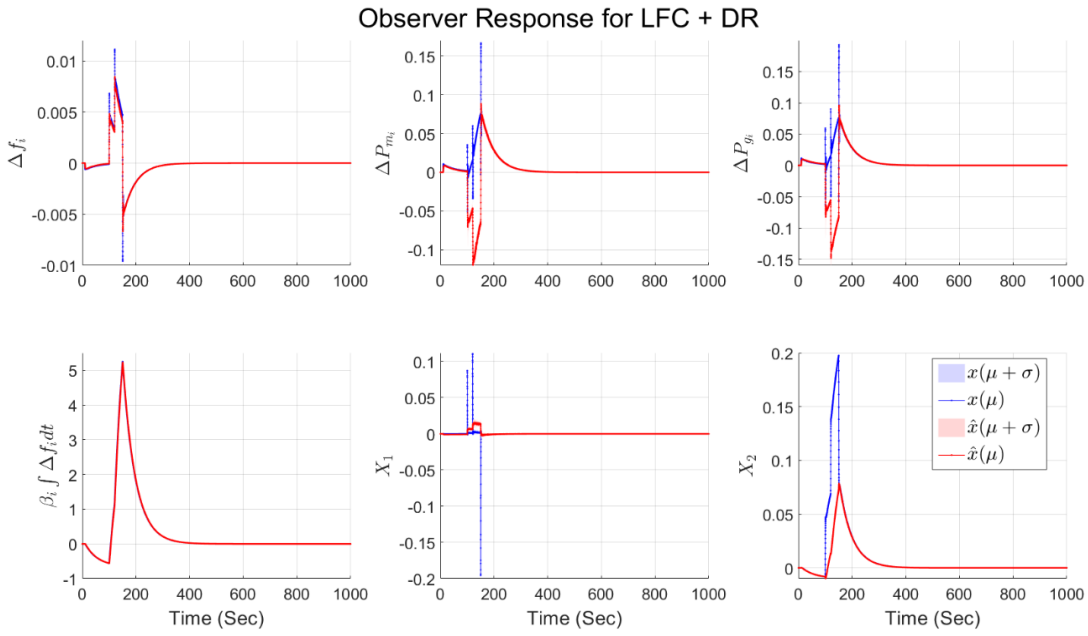

Figure 3-34: Observer Response for LFC and DR system configuration with mean and uncertainty calculated over 100 Monte Caro iterations

However, when EV is introduced in a decentralized configuration in the LFC loop, ΔP_{Th_i} is better estimated by the observer, as shown in Figure 3-36. Moreover, the peak of $\{\Delta P_{g_i}, \Delta P_{m_i}\}$ during load disturbance and FDI attack is much lower as compared to all the previous cases. We also observe a reduced ΔP_E requirement in the decentralized strategy as compared to the centralized strategy of the EV, which is mainly due to the introduction of the eigenvalues away from the origin. There is also a reduction of $\beta \int \Delta f_i dt$ required to stabilize the frequency of the grid.

When all the LFC, DR and EV configuration is combined, we observe a higher peak in the case of $\{\Delta P_{g_i}, \Delta P_{m_i}\}$. However, the secondary frequency feedback

$\beta\int \Delta f_i dt$ required is much lower during the disturbance. Similarly, we observe lower ΔP_E requirement from the aggregator when the EV works in a decentralized configuration compared to the centralized one. The estimation of the EV power is much better than the other state variables during the FDI attack and load disturbance.

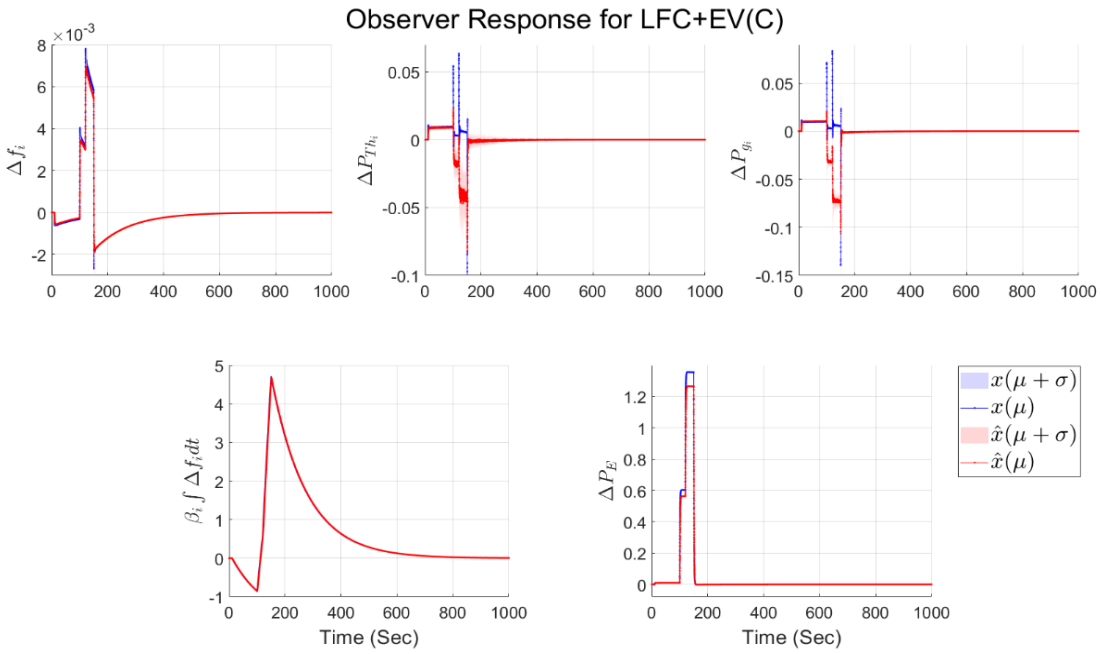

Figure 3-35: Observer Response for LFC and centralized EV system configuration with mean and uncertainty calculated over 100 Monte Caro iterations

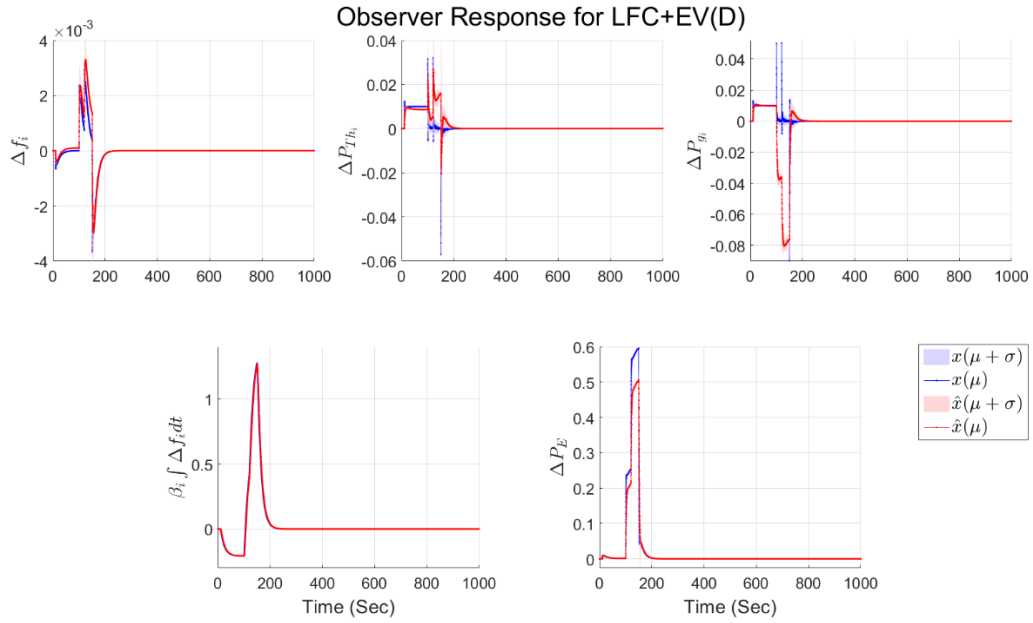

Figure 3-36: Observer Response for LFC and decentralized EV system configuration with mean and uncertainty calculated over 100 Monte Caro iterations

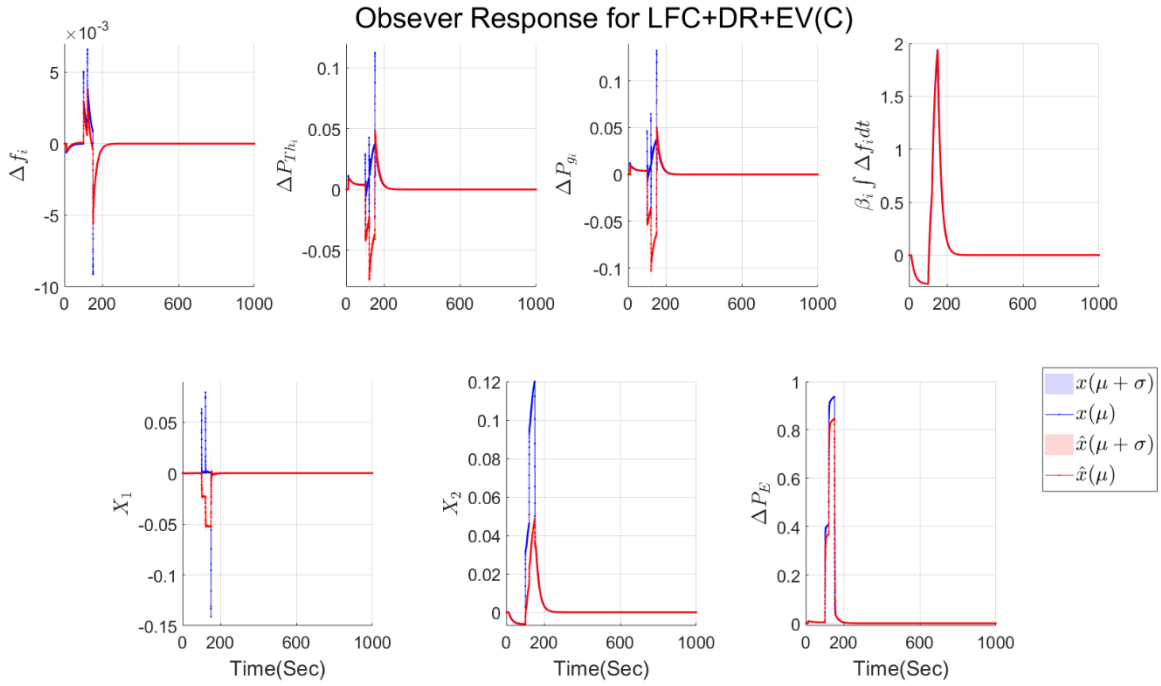

Figure 3-37: Observer Response for LFC, DR and centralized EV system configuration with mean and uncertainty calculated over 100 Monte Carlo iterations.

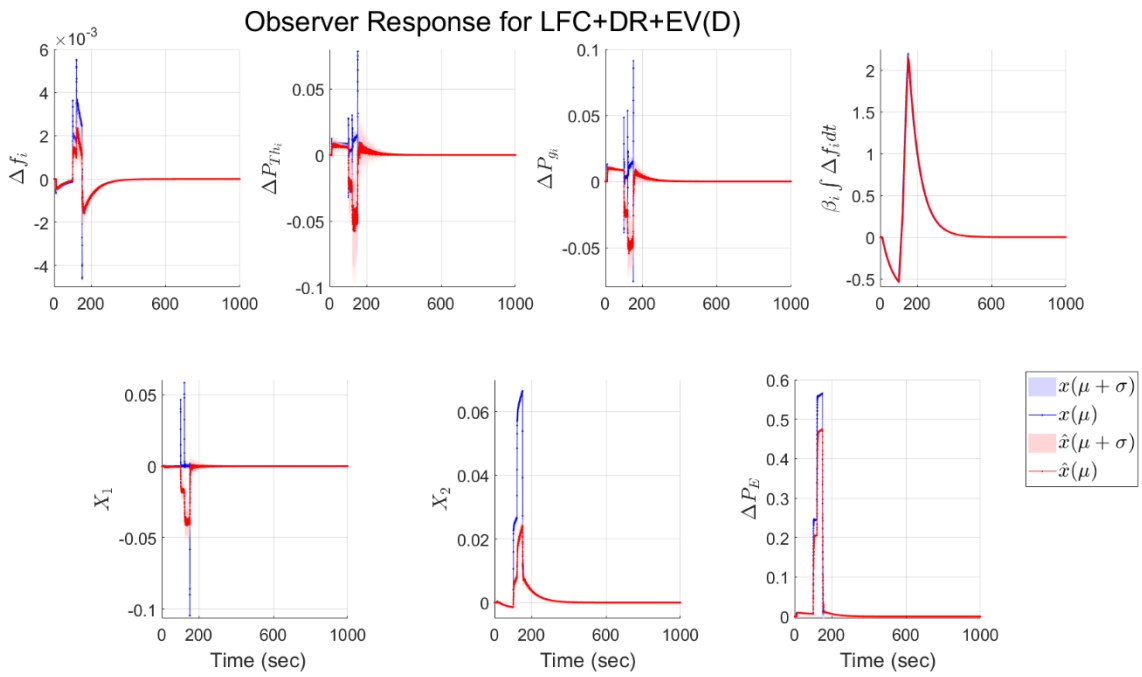

Figure 3-38: Observer Response for LFC, DR and decentralized EV system configuration with mean and uncertainty calculated over 100 Monte Caro iterations

3.2.7.3 System Response with Different Packet Drop Rate

As we increase the packet drop rate from 90 to 95%, we observe a marginal difference in the frequency fluctuation response shown in Figure 3-39. However, as we increase it to 99%, most system configurations remain stable except when EV is utilized in a decentralized fashion in conjunction with the classical LFC. We observe sustained oscillations in that case, which seems to increase with time along with higher uncertainty. The higher oscillations suggest that the system is fragile with high sensitivity to system parameters like packet drop rates. We also observe a higher uncertainty in frequency fluctuation due to random packet drop rates for LFC, DR and EV configurations. When the packet drop rates increase to 99.9%, the LFC with decentralized EV configuration becomes unstable with or without the demand response inclusion. However, when the EV configuration is centralized, we observe sustained oscillations of lower magnitude compared to LFC and LFC and DR configurations. The oscillations with LFC and LFC and DR have higher certainty and seem to grow bigger with time.

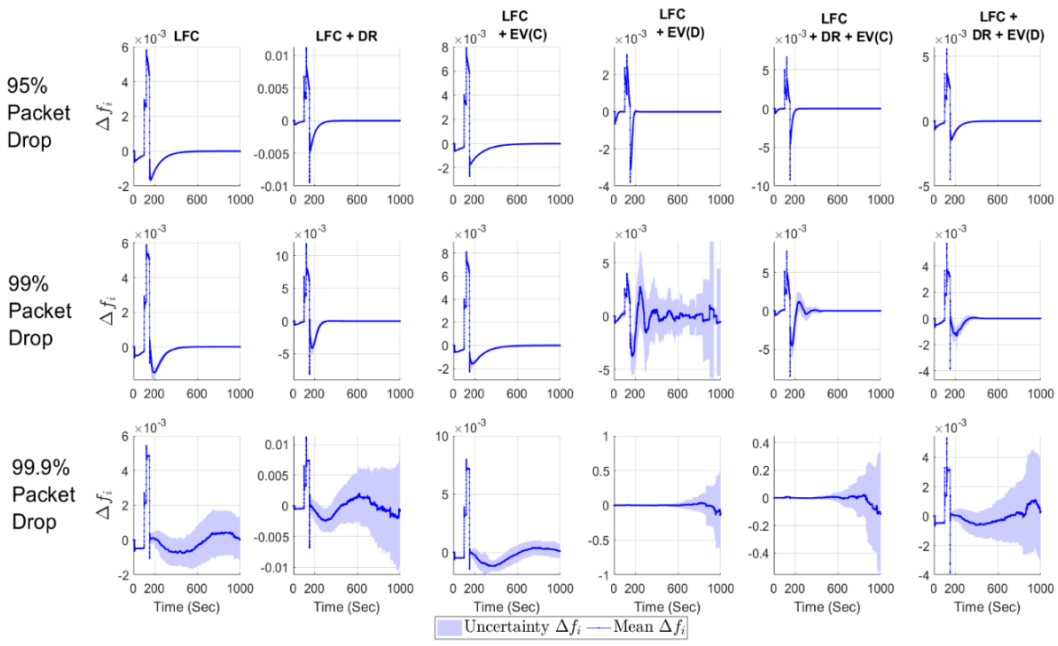

Figure 3-39: Frequency fluctuations for different system configurations with variation in the packet drop rates calculated for the over 100 Monte Carlo Simulations.

3.2.7.4 System Response with Various Demand Response Time Delays

As seen in Figure 3-40, the system configuration of demand response with LFC and LFC with centralized EV configuration is stable with an increase in demand

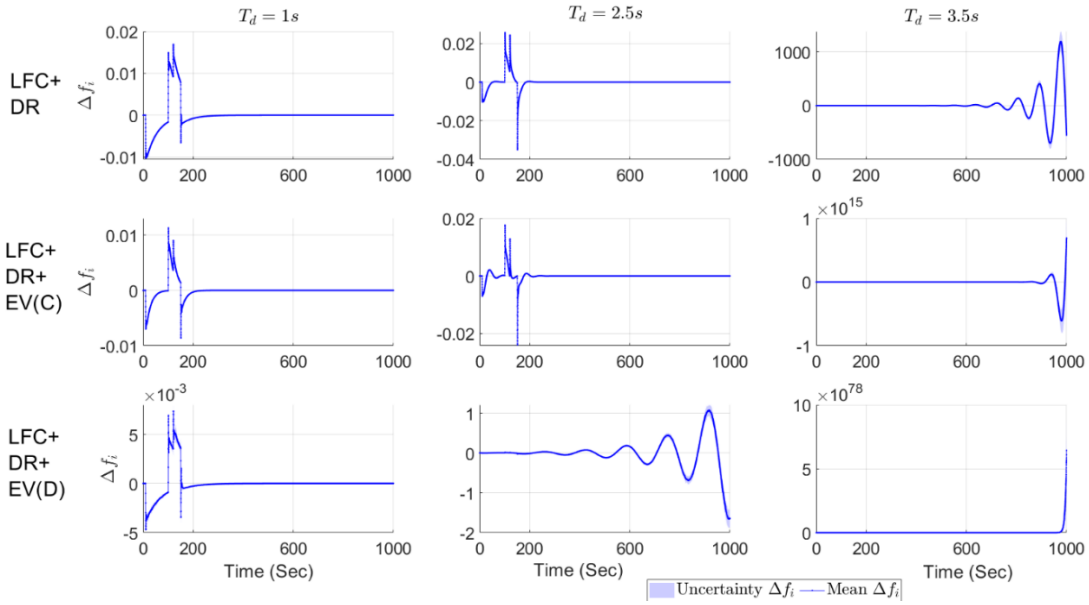

Figure 3-40: Frequency fluctuations for different demand response system configurations with variation in the packet drop rates calculated for the over 100 Monte Carlo Simulations

response time delay. However, the system is unstable when decentralized EV configuration is used with the increase in time delay. In Figure 3-25 and Figure *3-26*, we observe that the eigenvalues move away from the stability region in the decentralized EV operation. The eigenvalues tend to make the system fragile and sensitive to system parameters like the DR time delay. We also observe from the above figure that as the time delay T_d of the demand response increases, the eigenvalues move towards the unit circle. Hence due to switching behaviour, these eigenvalues move out from the stability region to render the system unstable.

3.2.8 Testing and Statistical Analysis with Stochastic RES and Load Demand Profiles on Linear LFC

The wind speed is considered between 0 to 30 m/s for the single area. The rate and the drift for solar irradiation and parameters to simulate Ornstein- Uhlenbeck for load demand and wind velocity are obtained from Section 3.1.5.4. Let's introduce a variable $k_{P_{Ren}}$ which is equal to the renewable energy utilization factor shown in Figure 3-43. Thus, considering its positive and negative oscillations we consider the absolute value of the variable. Hence, we can write,

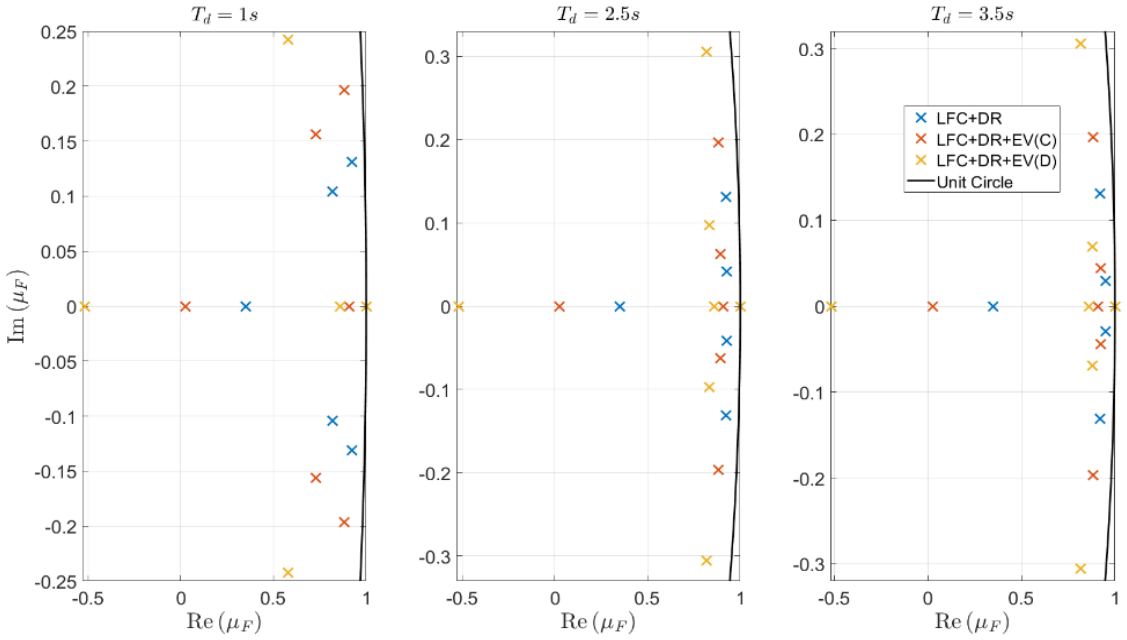

Figure 3-41: Configuration of the poles of different discrete systems with an increase in time delays due to demand response

$$\Rightarrow \frac{P_{\text{Ren}}}{P_{\text{Ren}} + \Delta P_{Th_i}} = \left|k_{P_{\text{Ren}}}\right| \Rightarrow \Delta P_{Th_i} = \left(\frac{1-\left|k_{P_{\text{Ren}}}\right|}{\left|k_{P_{\text{Ren}}}\right|}\right) P_{\text{Ren}} \Rightarrow \Delta P_{Th_i} = \left(\frac{1}{\left|k_{P_{\text{Ren}}}\right|} - 1\right) P_{\text{Ren}} \quad (96)$$

It suggests when $k_{P_{\text{Ren}}} < 0$ and $k_{P_{\text{Ren}}} > 1$ then $\Delta P_{Th_i} < 0$. However, when $0 < k_{P_{\text{Ren}}} < 1$, the $\Delta P_{Th_i} > 0$. Moreover, we also observe that for smaller value $\left|k_{P_{\text{Ren}}}\right|$ will increase thermal power output ΔP_{Th_i}. We observe in Figure 3-43, that the fluctuation of $\left|k_{P_{\text{Ren}}}\right|$ is highest when LFC is with centralized EV configuration. It suggests, when renewable energy is used for LFC, LFC with demand response and LFC with centralized EV configuration, it tends to reduce the thermal power output. The increase in thermal power output is observed only after $t > 600$, for LFC and LFC with demand response. However, with the LFC with decentralized EV configuration and LFC with demand response and centralized EV configuration, $k_{P_{\text{Ren}}}$ lies between 0 and 1 mostly after $t > 200$.

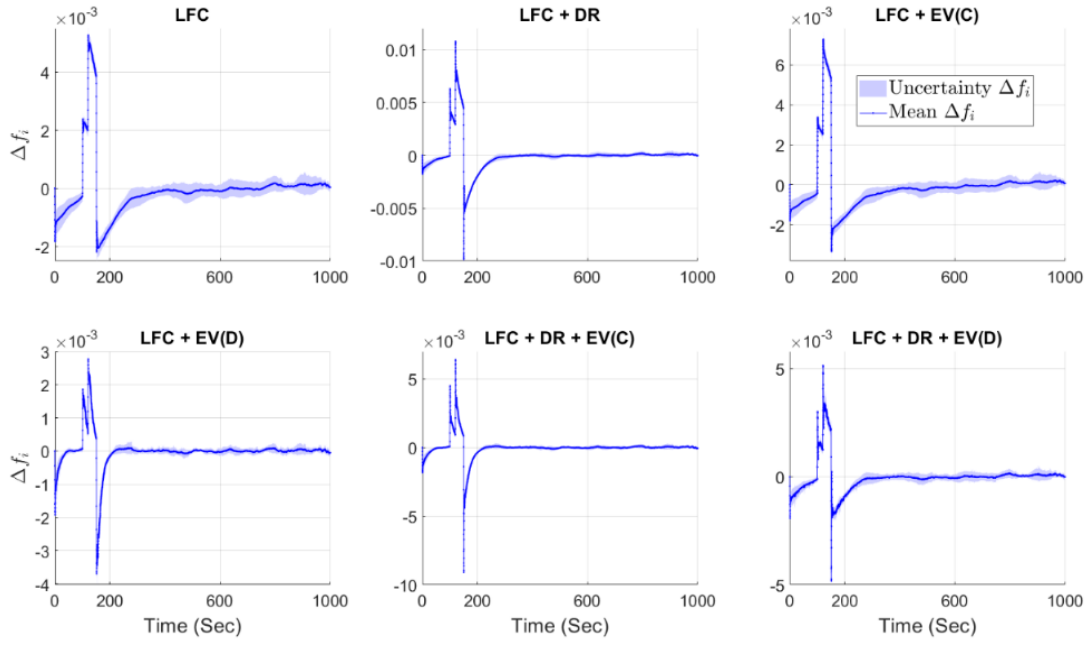

Figure 3-42: Frequency fluctuations for LFC and different fluctuations for the stochastic load demand and renewable energy with 500 Monte Carlo simulations

Moreover, initial fluctuation of $\left|k_{P_{\text{Ren}}}\right|$ is also lower as compared to last three cases. It suggests that LFC with decentralized EV configuration and LFC with demand response and centralized EV configuration, utilizes thermal power plant

output more as compared to other configuration. However, for LFC with demand response and decentralized EV configuration, the $\left|k_{P_{\text{Ren}}}\right| > 1$ most of the time, however maximum fluctuation is lower as compared to LFC with decentralized EV configuration and LFC with demand response and centralized EV configuration. The phenomenon in Figure 3-43, can be explained with the help of the power balance equation. Since the frequency fluctuation is close to zero, we can suggest that the power generation and demand is almost balanced,

$$\begin{aligned} &\Delta P_{Th_i} + P_{\text{Ren}} + \Delta P_{DR} + \Delta P_{EV} \approx \Delta P_L \\ &\Rightarrow \Delta P_{Th_i} \approx \Delta P_L - P_{\text{Ren}} - \Delta P_{DR} - \Delta P_{EV} \end{aligned} \tag{97}$$

Substituting the value of ΔP_{Th_i} from (97) in (98), we obtain,

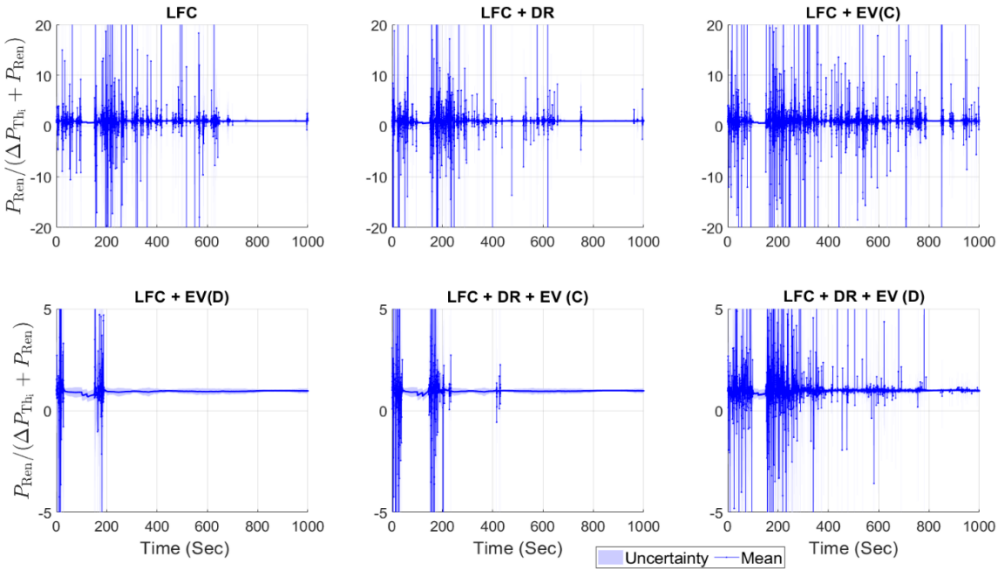

Figure 3-43: Renewable energy utilization for different system configurations obtained after 500 Monte Carlo simulations of renewable energy source. The uncertainty is considered at one standard deviation

$$\begin{aligned} &\Rightarrow \left(\frac{1}{\left|k_{P_{\text{Ren}}}\right|} - 1\right) P_{\text{Ren}} \approx \Delta P_L - P_{\text{Ren}} - \Delta P_{DR} - \Delta P_{EV}, \\ &\Rightarrow \Delta P_L \approx \frac{1}{\left|k_{P_{\text{Ren}}}\right|} P_{\text{Ren}} + \Delta P_{DR} + \Delta P_{EV} \end{aligned} \tag{98}$$

We observe that when $0 < k_{P_{\text{Ren}}} < 1$, P_{Ren} is highly utilized to meet the load fluctuations. Thus we can infer from (97) and (98) that the if we increase the

higher renewable energy fluctuation utilization leads to higher thermal power output. Higher value of $\left|k_{P_{\text{Ren}}}\right|$ for LFC system suggests that the load is mostly met by thermal power since there is no demand response and EV power. Hence, we can explain the higher uncertainty in the frequency fluctuation for the LFC system. When LFC is utilized with decentralized EV configuration and with demand response and centralized EV configuration, we observe $0 < k_{P_{\text{Ren}}} < 1$, suggesting that renewable energy is highly utilized for those configuration to meet the load fluctuations.

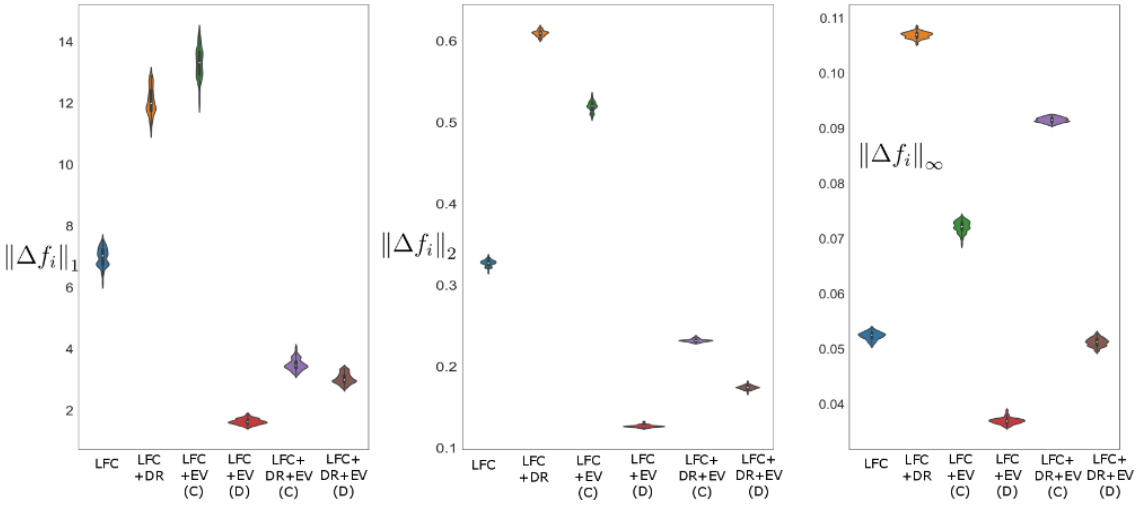

Figure 3-44: Boxplot for the L_1 norm, L_2 norm and L_∞ norm of frequency fluctuations for different system configurations.

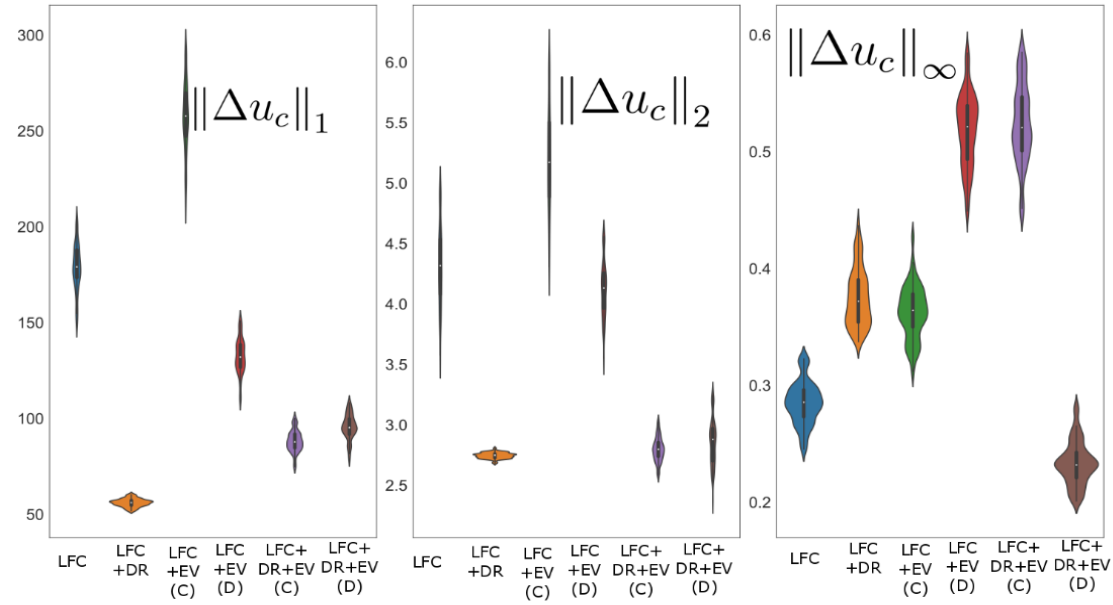

Figure 3-45: Boxplot for the 1-norm, 2-norm and ∞-norm of governor control input fluctuations for different system configurations.

However, when EV is utilized in decentralized configuration, demand response and EV output is mostly utilized for meeting the load fluctuation due to the higher value of $\left|k_{P_{\text{Ren}}}\right|$ for this system configuration. When renewable energy is introduced in the disturbance input, we see a frequency fluctuation within a specific limit while satisfying the requirement given in [75]. However, we observe that the uncertainty limit is low, which is due to the magnitude of FDI attack being much higher than the renewable energy generation fluctuations. We also observe that, due to demand response, the uncertainty in the frequency fluctuations is relatively low. The pattern of the maximum fluctuations in frequency is lowest when the decentralized configuration of EV is utilized with LFC.

The L_1 norm, L_2 norm and L_∞ norm of frequency fluctuations are shown in Figure 3-45, showing that total fluctuations are highest for LFC with DR and centralized EV configuration, while it is lowest for the case of LFC with a decentralized EV combination. The LFC, DR, an EV with the centralized configuration, has lower frequency fluctuations than the two combinations. The maximum fluctuations of LFC, DR, and EV with centralized configuration are much higher than in decentralized configuration. However, the total absolute fluctuation $\left\|\Delta f_i\right\|_1$ for two configurations are similar.

Table 3-1: Multivariate Normality Test Results on the frequency fluctuation and governor control signals norms

Signals	$\hat{\beta}_{1,\text{m}}$	$\hat{\beta}_{2,\text{m}}$	Critical Distance	*p*-value
$\left\|\Delta f_i\right\|_1, \left\|\Delta f_i\right\|_2, \left\|\Delta f_i\right\|_\infty$	6.795	12.585	7.814	0
$\left\|\Delta u_{c_i}\right\|_1, \left\|\Delta u_{c_i}\right\|_2, \left\|\Delta u_{c_i}\right\|_\infty$	1.787	11.524	7.814	0

Table 3-2: Results of non-parametric multivariate test for the frequency fluctuation and governor control signals norms considering different system configuration as the samples

Signals	Test Statistic (F)	Degrees of Freedom (df_1)	Degrees of Freedom (df_2)	*p*-value
$\|\Delta f_i\|_1, \|\Delta f_i\|_2, \|\Delta f_i\|_\infty$	7621.986	15	8260	0
$\|\Delta u_{c_i}\|_1, \|\Delta u_{c_i}\|_2, \|\Delta u_{c_i}\|_\infty$	3927.158	15	8260	0

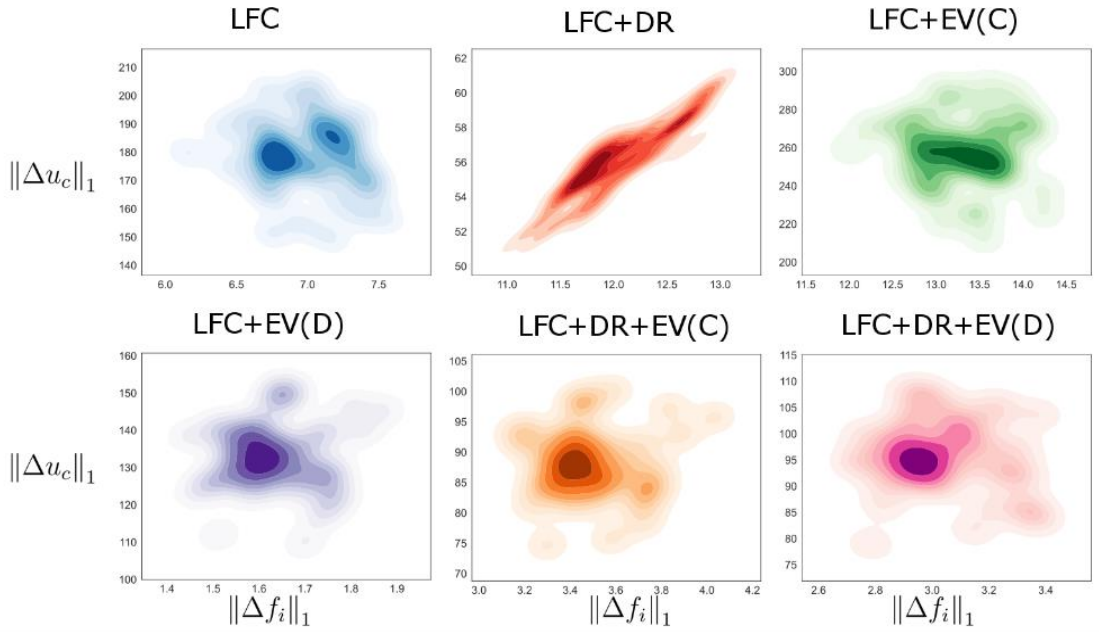

Figure 3-46: Bivariate analysis of the 1-norm of the frequency fluctuations and governor control input with 500 Monte Carlo simulations

For a quantitative check of Δf_i, we have to conduct a statistical test. Firstly, we need to check whether the signal norms are multivariate normal or not. The multivariate statistical test on the signal norms are performed similarly in [179], where multivariate normality is tested. The test is conducted with the help of the function mult.norm() in the QuantPsyc package in R [180].

The skewness and kurtosis coefficients $\hat{\beta}_{1,\mathrm{m}}$ and $\hat{\beta}_{2,\mathrm{m}}$ are used to compute the test statistic and the *p*-value for checking the normality. The details about the coeffieicnts are provided in [179]. As we see observe in univariate plot in Figure 3-44 and Figure *3-45*, that the data does not follow normal distribution. This is also confirmed by the *p*-value in Table 3-1, which is 0. The critical distance is same for both the signal a sit only depends on the sample size which are considered equal in this case. However, the skewness coefficient for the norms of governor control signal Δu_{c_i} is smaller than the the norms of the frequency fluctuation Δf_i. Since the *p*-value is 0, non-parametric multivariate test is to be conducted on the given data.

Then we perform a non-parametric multivariate test using the nonpartest() the *npmv* package in R [181], on the given data considering the three norms as the factor levels while testing 1000 Monte Carlo samples and different LFC system configurations. Wilk's lambda statistic is considered here which has an effective test statistic that follows a F-distribution having degrees of freedom df_1 and df_2. The expressions for the effective test statistic and degrees of freedom is mentioned in [179]. We observe in Table 3-2, that the *p*-value is 0, which confirms that the neither the frequency or the control norms are similar for the different system configurations. The degrees of freedom is same for both the signal norms as it only depends on the sample size. However, the test statistic for norms of governor control signal is lower as compared to the frequency deviations, which states that the governor control signal norms are similar for the different system configuration as compared to the frequency fluctuation norms.

Similarly, the comparison is also performed on the governor control input, based on the three norms as shown in Figure 3-45. $\|\Delta u_c\|_2$ represents the cost of the spinning reserves as given in [148]. We observe that with the combination of LFC, DR, and EV, the cost due to spinning reserves is reduced. Even with DR, only the cost is relatively low as well. However, the spinning reserve cost is highest when EV with centralized configuration is used along with LFC with high uncertainty per ensemble of disturbance vector.

When we see for the overall fluctuations, we see a positive correlation pattern for the relationship between the $\|\Delta u_c\|_1$ and $\|\Delta f_i\|_1$ for the LFC and DR configuration in Figure 3-46. Bimodal bivariate distribution is observed only in the case of LFC configuration. However, for the other configurations, no significant correlation pattern can be deduced. In Figure 3-47 we observe that the spinning reserve cost is positively correlated to the frequency fluctuations in LFC, DR and EV combinations. A slight positive correlation is obtained for simple LFC case. However, a slight negative correlation is obtained for the $\|\Delta f_i\|_2$ and $\|\Delta u_c\|_2$, with

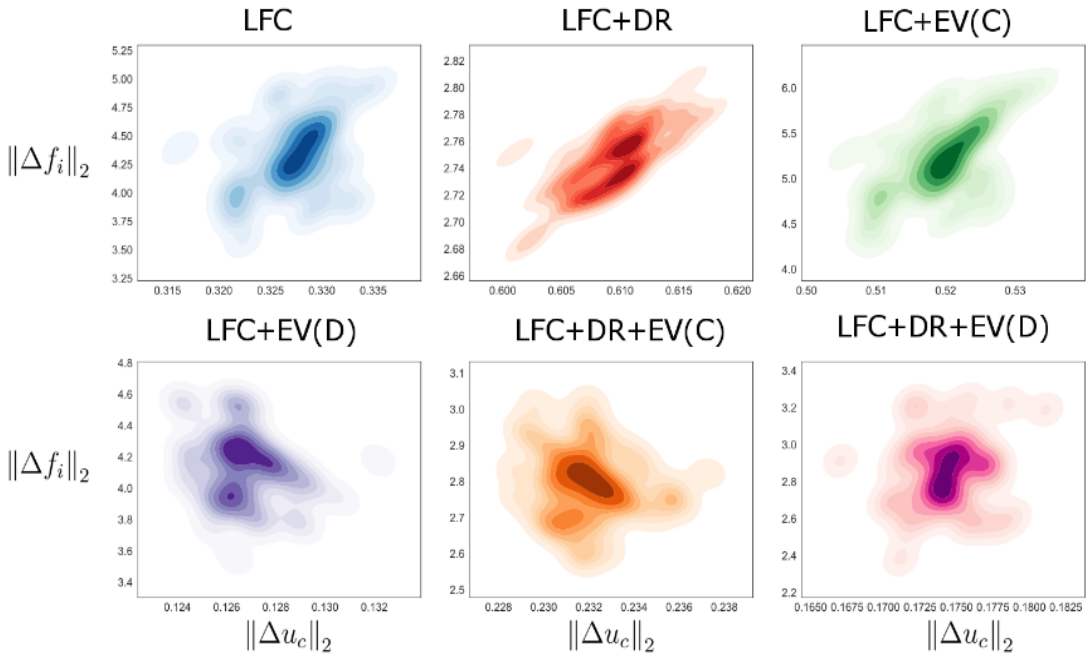

Figure 3-47: Bivariate analysis of the 2-norm of the frequency fluctuations and governor control input with 500 Monte Carlo simulations

no correlation obtained when LFC, DR and EV are used in a decentralized fashion. Thus we can say that with the incorporation of DR and EV in a centralized configuration, the rate of frequency fluctuations increase with a relative increase in the governor control input. As far as maximum fluctuation is concerned, we observe a positive correlation between frequency and control input in Figure 3-48. The bimodal pattern is observed for the LFC and centralized and decentralized EV configuration. Trimodal pattern observed for LFC, DR and centralized EV configuration.

We do not see any significant correlation between the governor control input and the DR output signal norms for LFC and DR configuration in Figure 3-49. However, tri-variate distribution in the case of 1 and ∞ the norm of the variables is observed. We observe a positive correlation when EV is added to the LFC and DR configuration, which states that increased control input is equally matched by increased DR output. The power output from the EV effectively nullifies the above power output as observed for 1 and 2 norm fluctuations in Figure 3-49.

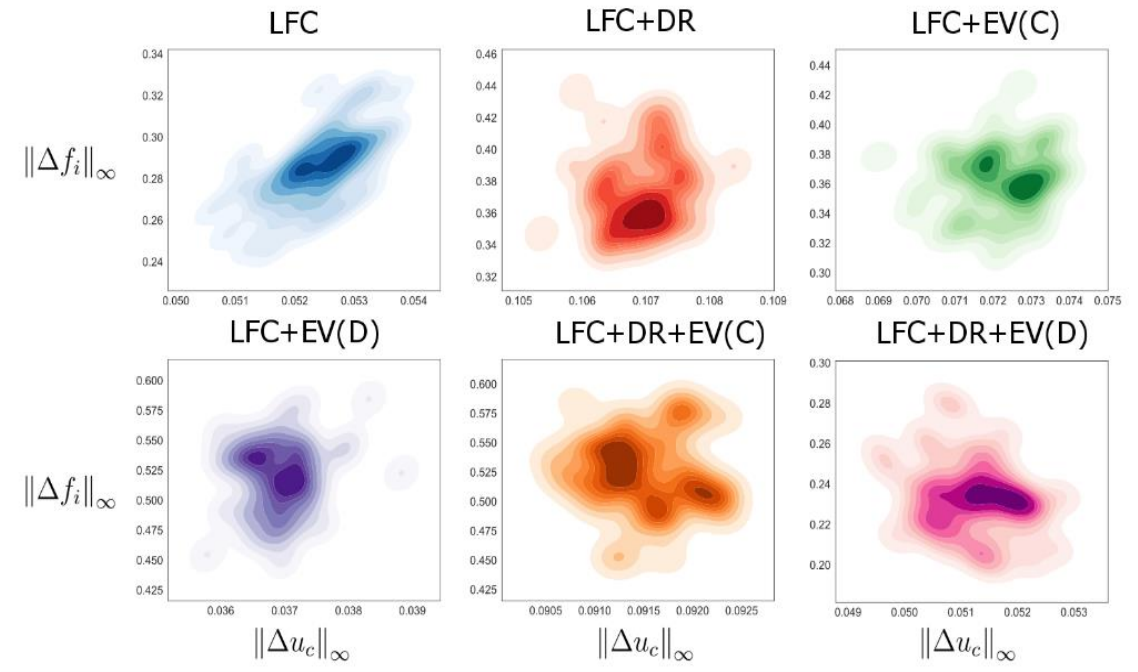

Figure 3-48: Bivariate analysis of the 2-norm of the frequency fluctuations and governor control input with 500 Monte Carlo simulations

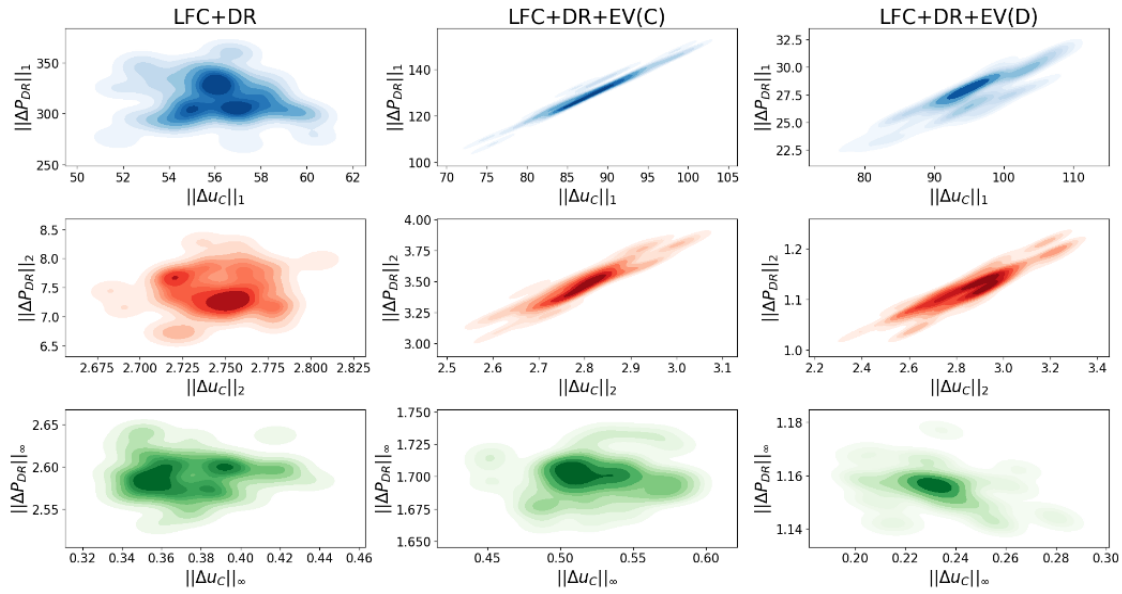

Figure 3-49: Bivariate analysis of the norms of the demand response and governor control input with 500 Monte Carlo simulations.

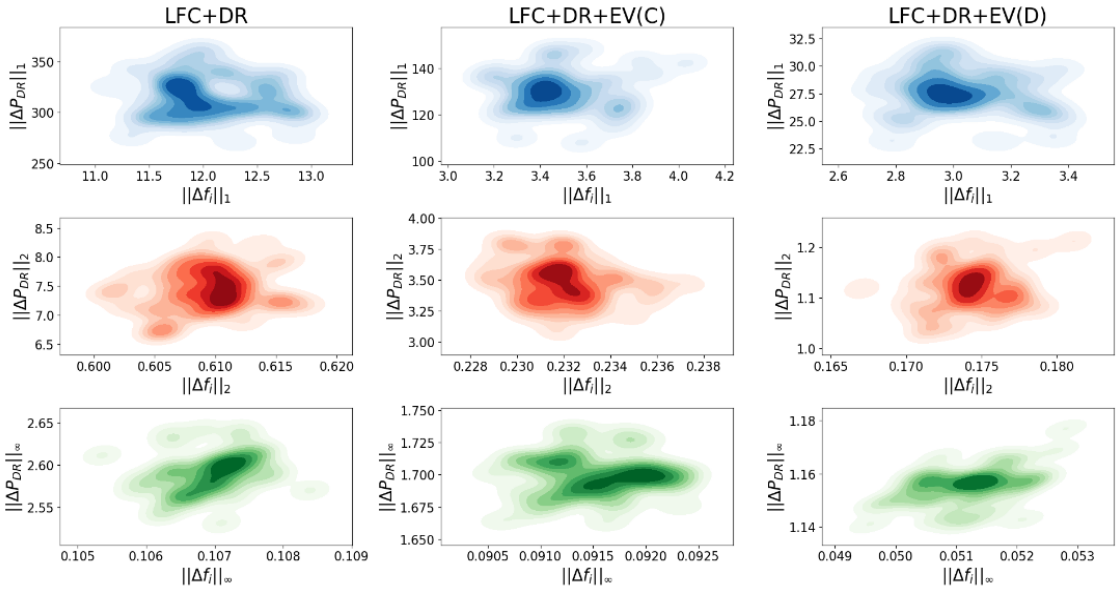

Figure 3-50: Bivariate analysis of the norms of the frequency fluctuations and demand response output with 500 Monte Carlo simulations.

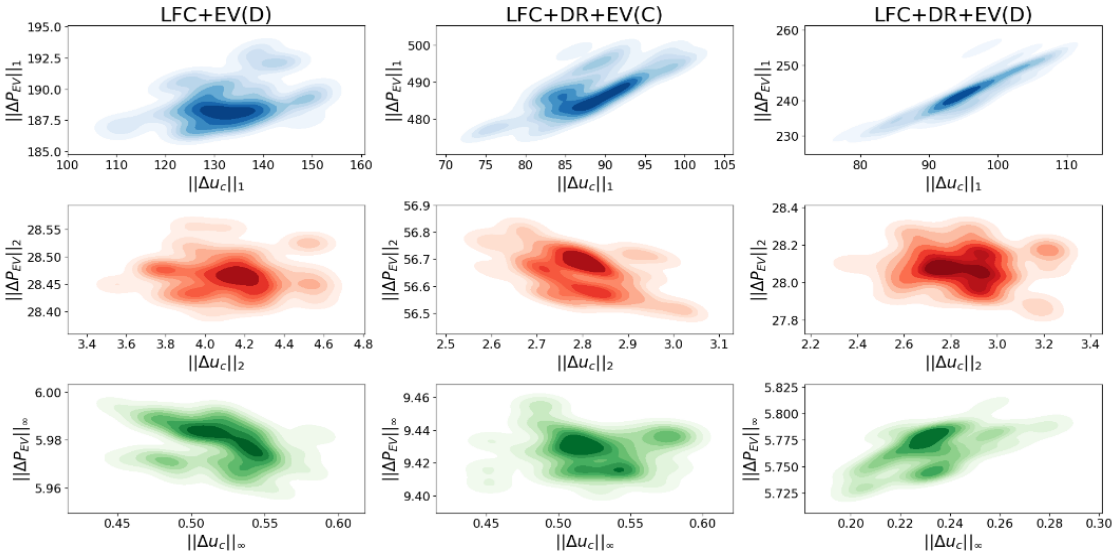

Figure 3-51: Bivariate analysis of the norms of the governor control input and electric vehicle output with 500 Monte Carlo simulations

However, we do not see any pattern of the demand response output ΔP_{DR} with the frequency fluctuation Δf_i in Figure 3-50. A slight positive correlation is observed in the case of ΔP_{DR} and Δf_i in the case of LFC and DR combination. The distribution is also mostly unimodal except in the ∞-norm of LFC, DR and

centralized EV combination. We observe a positive correlation in the 1-norm and 2-norm of the ΔP_{EV} and the governer control input Δu_c when using the LFC, DR and EV configuration in Figure 3-51. Some positive correlation is also observed in the ∞-norm relation for LFC, DR and decentralized EV configuration. Bimodal distribution is observed for the 2-norm and ∞-norm of the variables concerned. Moreover, an obtuse tilt of the KDE plot indicates a slight negative correlation between the 2-norm of ΔP_{EV} and Δu_c.

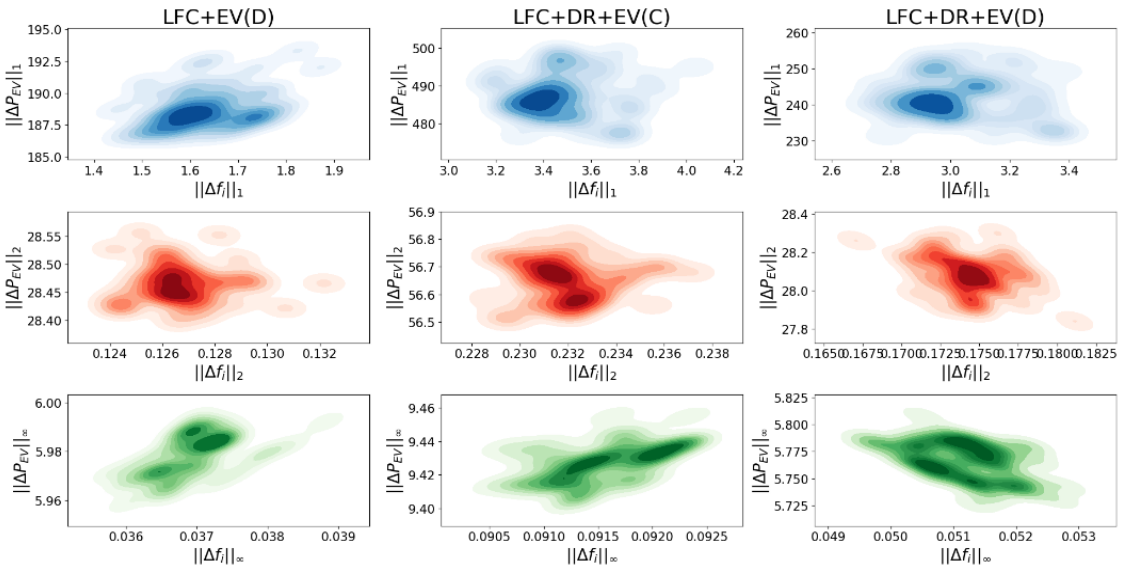

Figure 3-52: Bivariate analysis of the norms of the frequency fluctuations and electric vehicle output with 500 Monte Carlo simulations.

A positive correlation is observed for the ∞-norm between electric vehicle output ΔP_{EV} and frequency fluctuations Δf_i in the LFC case with decentralized EV configuration as observed in Figure 3-52. Similarly, a positive correlation with multimodal distribution is observed in LFC with DR and centralized EV configuration. However, a slight negative correlation and multiple modes are observed in the case of LFC, DR and decentralized EV configuration. For 1 and 2 norms bivariate plots, we do not observe a strong correlation pattern. However, we observe a significant bimodal data pattern in the case of 2-norm between ΔP_{EV} and Δf_i. A positive correlation is observed between the DR output and EV output 1-norm signal, as shown in Figure 3-53. However, in the norm, the correlation is slightly more negative for centralized strategy with demand response output than decentralized output. It proves that maximum fluctuations

of DR output will decrease with maximum fluctuations in EV output when operating as a centralized configuration. However, the pattern remains similar for both the cases suggesting that that the rate of change in EV output is similar for both the configuration, with the requirement more in centralized strategy than the decentralized one.

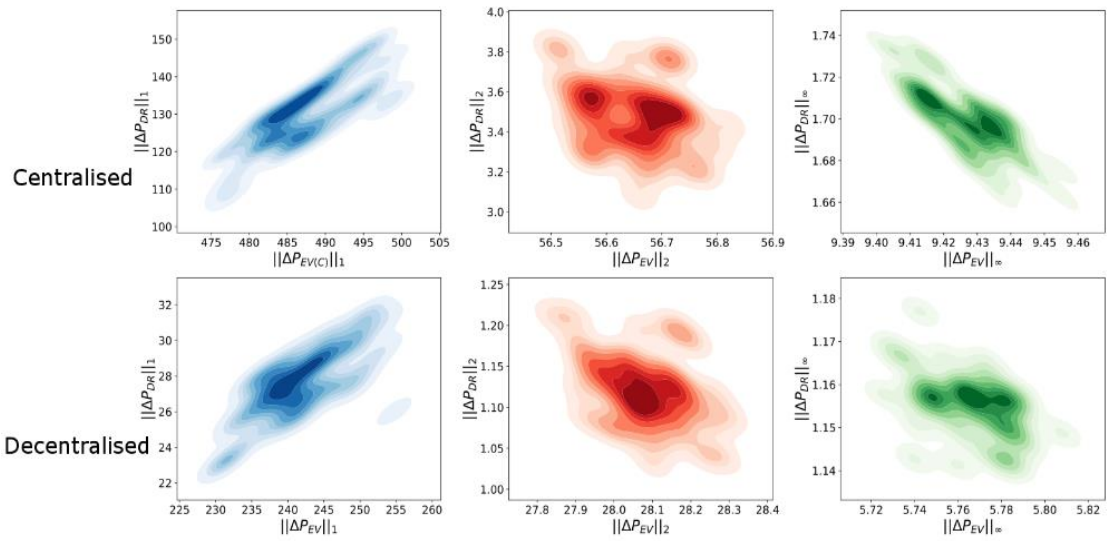

Figure 3-53: Bivariate analysis of the EV power output norms and demand response power for centralized and decentralized EV configurations obtained from 500 Monte Carlo simulations.

3.2.9 Conclusion

In thus subchapter a joint state feedback controller and an observer has been designed for the decentralized load frequency control system with demand response and EV. The stability conditions are derived using a switched system using an asynchronous dynamical system model, where the controller and observer gains were obtained using a CCL algorithm solving an LMI for different LFC, DR and EV configurations. The system response is checked at different packet drop rates and time delay due to demand response. The frequency fluctuations, governor control input, EV and DR output are analyzed using bivariate plots. The analysis is computed with the respective 1,2 and ∞-signal norms obtained when renewable energy is considered as disturbance vector. The analysis is also aided by the non-parametric statistical tests for frequency fluctuations and governor control input norms.

The results for the linear decentralized LFC can be explained as:

- The state feedback controller and observer gain obtained after solving the LMI can ensure stable operation under bounded load disturbance and FDI attack and at a higher packet drop rate of 90%.
- The combination of decentralized EV in the LFC loop leads to stable operation at higher sampling time, utilizing lower communication bandwidth.
- However, the system with decentralized EV configuration is susceptible to parametric variations like the demand response time delay or increase in packet drop rate as it can cause higher frequency fluctuations and instability.
- Combining LFC with EV and demand response strategies can lead to lower spinning reserves cost compared to standalone LFC or LFC with either EV or demand response.

The first subchapter focuses on the centralized control of the system frequency fluctuations, even though several models of renewable energy and energy storage are considered. However, the second subchapter introduces a decentralized strategy involving EV and demand response, representing the smart grid future vision. The second subchapter also shows that the decentralized strategy minimized the grid frequency fluctuations under several disturbances while reducing the control effort and minimizing spinning reserve costs.

3.3 Regression Analysis of Grid Stability with Consumer Response and Market Price Elasticity

In the previous subchapters we investigated the centralized and decentralized controllers for maintaining grid frequency stability. In this chapter, we consider the role of consumers along with the market price parameters in grid stability. Unlike the previous subchapters, angular stability is considered in the analysis. The analysis is performed using the regression coefficients obtained after fitting a linear model on the data, after feature selection is performed.

3.3.1 Previous Works

Several works have been done in the field of data mining for predicting the voltage [182], [183], angular stability [184]–[188] and blackouts [189]. Online transient stability prediction has been performed based on stream computing paradigm [184], which predicts the stability based on the rotor angle trajectories obtained from live synchro phasor data. Two class classification and data mining algorithm based on core vector machine (CVM) has been performed on the phasor measurement unit (PMU) big data in [185] for online transient stability assessment which makes it attractive to be used in real time. The stability problem of a high-dimensional power system has been solved using feature selection and support vector machine techniques in [186].

3.3.2 Contribution in this sub-chapter

Statistical relations of the stability index of the system has not been described in relation to demand response and price fluctuating index which is described in this paper with the help of regression and feature selection technique. Ordinary regression technique fits the parameters based on minimum least square technique while the Ridge regression penalizes the complexity of the model used for fitting the model. Bayesian regression aims to find the probabilistic model of the weights used in the regression problem to map the input parameters to the output space. Bayesian techniques for power grids has been applied in [190], [191] for load modelling and predicting the electricity demand, but these

techniques are used in this paper to study the relationship of the input variables with the grid stability parameters

3.3.3 Physical Model of the Synchronous Generator

The synchronous generator model is derived from the energy conservation model of the generators and loads with its mathematical form similar to the Kuramoto oscillator model [192] and can be represented as:

$$p_j^{\text{source}} = \frac{1}{2} M_j \frac{d}{dt}\left(\dot{\delta}_j^2\right) + \kappa\left(\dot{\delta}_j^2\right) - \sum_k P_{jk}^{\max} \sin\left(\delta_k - \delta_j\right), \tag{99}$$

where, *j* is the participant's index, *M* is the moment of inertia, κ is the friction coefficient and P_{jk}^{max} is the capacity of the line connecting the participant *j* and *k*. As from the generator angle equation given in [40] we see that it can be represented as follows:

$$\delta_j(t) = \omega t + \theta_j(t), \tag{100}$$

where ω is the grid frequency and $\theta_j(t)$ is the rotor angle relative to it. Hence, substituting the value of $\delta_j(t)$ from (100) in the above equation yields:

$$\frac{d^2\theta_j}{dt^2} = P_j - \alpha_j \frac{d\theta_j}{dt} + \sum_k K_{jk} \sin(\theta_k - \theta_j), \tag{101}$$

where,

$$K_{jk} = \frac{P_{jk}^{\max}}{M_j \omega}, \quad \alpha_j = \frac{2\kappa_j}{M_j}, \quad P_j = \left[P_j^{source} - \kappa_j \omega^2\right] / M_j. \tag{102}$$

As per [192] , the model in equation (101) is correct based on the following assumptions:

$$\frac{d\theta_j}{dt} \ll \omega, \quad \frac{d^2\theta_j}{dt^2} \ll \frac{2\kappa_j \omega}{M_j}. \tag{103}$$

3.3.4 Price Structure Model

The strategy for DGSC aims at encouraging the consumers to lower and increase their power consumption during high and lighter load respectively, and this is done with the help of a linear-price frequency fluctuation coefficient $p_i\left(\frac{d\theta}{dt}\right)$, which can be represented as follows:

$$p_i \frac{d\theta_j}{dt} = p_\Omega - c_1 \frac{d\theta_j}{dt}, \tag{104}$$

where p_Ω is the price when there is no fluctuation in frequency, the linearized price relations can be described as follows:

$$P_i(t) \approx P_i + c_2.(p_i - p_\Omega). \tag{105}$$

Hence plugging (105) into (104) we get:

$$P_i(t) \approx P_i - \gamma_i \frac{d\theta_i(t)}{dt}, \ \forall i \in \{1,...,N\}. \tag{106}$$

As given in [193] that the adaptation is not instantaneous as the response is generally delayed by a time τ due to measurement and reaction time. Hence, incorporating the economic aspects derived in (106) in (101), the overall equation for the power system dynamics becomes:

$$\frac{d^2\theta_j}{dt^2} = P_j - \alpha_j \frac{d\theta_j}{dt} + \sum_k K_{jk} \sin(\theta_k - \theta_j) + \gamma_i \frac{d\theta_i(t)}{dt}, \tag{107}$$
$$\forall i \in \{1,...,N\}.$$

As given in [40] that instantaneous value of $\theta_i(t)$ can cause grid instabilities even for smaller values of τ. Hence, frequency measurements averaged over an intervals of length T is preferred which can stabilize the performance of the grid for wider τ values. Hence such averaging yields:

$$\begin{aligned} \frac{d^2\theta_j}{dt^2} &= P_j - \alpha_j \frac{d\theta_j}{dt} + \sum_k K_{jk} \sin(\theta_k - \theta_j) \\ &\quad - \frac{\gamma_i}{T} \int_{t-T}^{t} \frac{d\theta_i}{dt}(t' - \tau) dt' \\ &= P_j - \alpha_j \frac{d\theta_j}{dt} + \sum_k K_{jk} \sin(\theta_k - \theta_j) \\ &\quad - \frac{\gamma_i}{T}\left(\theta_j(t - \tau) - \theta_j(t - \tau - T)\right). \end{aligned} \tag{108}$$

Several assumptions have been used in framing the models as described in [194] but the analysis is done considering the heterogeneous response of the consumers. The definition of the stability index for the grid is derived in the following section.

3.3.5 Stability Parameters

The stability of the dynamical system is found out based on the nature of the eigen values, which is calculated with the help of polynomial calculated from the Jacobian of the system, which is defined in [193] and given as:

$$J_\tau = \begin{bmatrix} \frac{\partial}{\partial \theta_{\tau,i}}\left(\frac{d}{dt}\theta_j\right) & \frac{\partial}{\partial \omega_{\tau,i}}\left(\frac{d}{dt}\theta_j\right) \\ \frac{\partial}{\partial \theta_{\tau,i}}\left(\frac{d}{dt}\omega_j\right) & \frac{\partial}{\partial \omega_{\tau,i}}\left(\frac{d}{dt}\omega_j\right) \end{bmatrix} \in \mathbb{R}^{2N\times 2N}, \tag{109}$$

where $\theta_{\tau,i} = \theta_i(t-\tau)$ and $\omega_{\tau,i} = \frac{d\theta_i}{dt}(t-\tau), i, j \in \{1,...,N\}$. The characteristic equation of the system for the Jacobian considering the two delays τ and $\tilde{T} = T + \tau$ is given by:

$$p(\lambda) = \det\left(J_0 + e^{-\lambda t} J_\tau + e^{-\lambda \tilde{T}} J_{\tilde{T}} - \lambda\right) = 0. \tag{110}$$

The data set used for analysis is formed with 10,000 randomly chosen initial values for the system defined in (108) and the eigenvalues calculated based on the solutions obtained after solving the polynomial, given in (110). The numerical values of the parameters used in the system is same as the one given in [194].

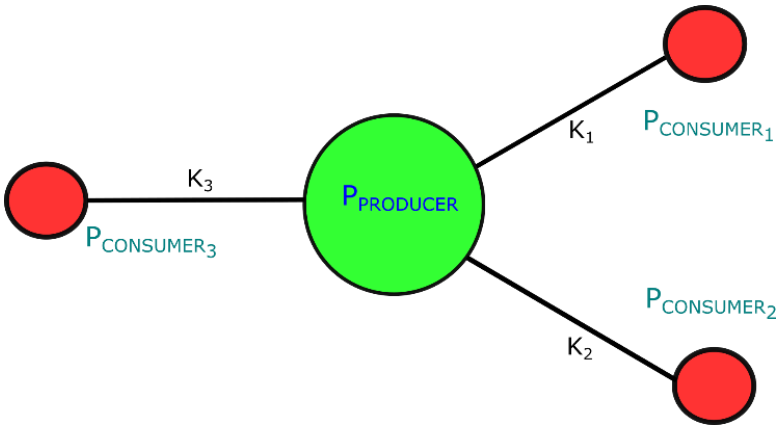

Figure 3-54: The decentralized control structure.

The stability analysis of the system with decentralized generation is considered for consumers in [193] having similar characteristics which makes the scheme unattractive for heterogeneous consumers as discussed before. Thus, the analysis in this study has been done based on heterogeneous response of the consumers connected to the producer shown in Figure 3-54 which is based on the scheme given in [194]. However, the dependence of the input parameters on the grid stability is discussed in this study using feature selection techniques and

Bayesian regression technique. Description of the statistical techniques used is given in the following section.

3.3.6 Statistical and Machine Learning Methods

3.3.6.1 Feature Selection

Feature selection is a commonly used technique used for model construction as it helps in simplification of models, which can be easily interpreted [195]. It is also helpful in avoiding the curse of dimensionality and it enhances generalization by reducing overfitting [196]. The most commonly used index for feature selection is Fisher score which is based on the selection of features where the distance of the data points, belonging in similar and different classes should be as small and large as possible respectively.

The Fisher score can be computed as follows and given in [197]:

$$F(\mathbf{Z}) = \text{trace}\left\{ \mathrm{S_b} \left(\mathrm{S_t} + \gamma I \right)^{-1} \right\}, \tag{111}$$

where, $\mathrm{S_b}$ is the between class scatter matrix and S_t is the total scatter matrix of the dataset. Considering the input data matrix as $X \in \mathbb{R}^{d \times n}$ and if μ_k^j and σ_k^j be the mean and standard deviation of the k^{th} class corresponding to the j^{th} feature. Now consider μ^j and σ^j be the mean and standard deviation of the whole data set with respect to the j^{th} feature, the Fisher score can be computed as follows:

$$F(x^j) = \frac{\sum_{k=1}^{c} n_k (\mu_k^j - \mu^j)^2}{(\sigma^j)^2}, \tag{112}$$

$$\text{where, } (\sigma^j)^2 = \sum_{k=1}^{c} n_k (\sigma^j)^2. \tag{113}$$

Hence based on the value of $F(x^j)$ computed from (112) we can rank the feature influencing the stability of the grid.

3.3.6.2 Regression Analysis

Regression is a method to model a mathematical relationship between the dependant variables and the response variables. If the relationship is linear in nature, they are called linear models [198], which can be expressed as:

$$y_i = X_i\beta + \epsilon_i = \beta_1 X_{i1} + \ldots + \beta_k X_{ik} + \epsilon_i, \quad i \in \{1,\ldots,N\}. \tag{114}$$

An equivalent representation of (114) is

$$y_i \sim \mathcal{N}\left(X_i\beta, \sigma^2\right), \quad i \in \{1,\ldots,N\}. \tag{115}$$

where X is n by k matrix with i^{th} row X_i .Using the multivariate notations, the response variable can be written as:

$$y_i \sim \mathcal{N}\left(X\beta, \sigma^2 I\right). \tag{116}$$

Fitting the model using (116) gives an estimate of β and σ from the given data. Standard error in the uncertainty from the coefficient estimates is represented in the form of the estimated covariance matrix $V_\beta\hat{\sigma}^2$ where the diagonal elements represent the estimated variance of the individual components of β and the off-diagonal represents the covariance of estimation. In order to measure the explained variance in the data from the linear model quantities such as residual standard deviation $\hat{\sigma}$ and explained variation R^2 is used which can be represented as follows and given in [199]:

$$\hat{\sigma} = \sqrt{\sum_{i=1}^{n} r_i^2 / (n-k)}, \tag{117}$$

$$R^2 = 1 - \hat{\sigma}^2 / s_y^2, \tag{118}$$

where, n and k represents the number of data points and coefficients to be estimated respectively. s_y is the standard deviation of the whole data and r_i is the residuals of the data which the difference between the data and the fitted values given as follows:

$$r_i = y_i - X_i\hat{\beta}. \tag{119}$$

Adjusted R^2_{adj} for the regression problem takes into account the value of explained variation which manages the number of explanatory terms relative to the number of data points [200] which can be described as:

$$\bar{R}^2 = 1 - (1 - R^2)\frac{n-1}{n-k-1}. \tag{120}$$

Above expression can also be written as:

$$\bar{R}^2 = 1 - \frac{\hat{\sigma}^2 / (n-1)}{s_y^2 / (n-k-1)}. \tag{121}$$

The *F*-statistic used for the linear regression checks the null hypothesis that whether the test statistic has *F*-distribution under null hypothesis. For regression problem, it checks whether a model which has p_1 parameters fits the data better than another model having p_2 parameters. The parameter can be calculated with the help of the mathematical relation given by:

$$F = \left(\frac{\mathrm{RSS}_1 - \mathrm{RSS}_2}{p_2 - p_1} \right) \Bigg/ \left(\frac{\mathrm{RSS}_2}{n - p_2} \right) \tag{122}$$

where, RSS_i is the residual sum of squares for the model i.

Quantile plots can be used to check the nature of the residuals obtained after regression [201]. It is generally used to check the distributions of the residuals comparing it with the standard normal distribution. If they are similar then they will fall along the straight line in the plot. They are generally plotted against the quantiles obtained after plotting against the indexes following the normal distribution. The initial step in the Q-Q- plot is to sort the residuals with increasing size thus $r_{(i)}$ is the i^{th} smallest residual and hence known as order statistic. Thus in order to compare it with the standard normal distribution, order statistics for the i^{th} sample is created for the sample size n with the help of the formula expression as described in [202]:

$$\mathbb{E}\left[z_{(i)} \right] \approx \Phi^{-1}\left[(i - 0.3175) / (n + 0.365) \right], \tag{123}$$

where, Φ^{-1} is the inverse of the standard normal distribution function.

3.3.7 Results and Discussions

The data for the analysis is taken from the UCI Machine Learning Repository database – *Electrical Grid Stability Simulated Data* [113] where the information regarding the grid stability nature and eigenvalues along with the test parameters are provided. Feature selection is performed on the test parameters namely, response time τ, price response index γ and the power produced *P* and

consumed. Since the data is based on the configuration given in Figure 3-54, the power produced is equal to the total consumption.

$$P_1 = P_2 + P_3 + P_4 \tag{124}$$

Subscript 1 in equation (124) in the given data belongs to the attribute of the producer while the remaining subscripts belong to the heterogeneous consumers. The features are summarized in Table 3-3.

Table 3-3: Feature Significance Data

Features	Significance
0-3	$\tau_1, \tau_2, \tau_3, \tau_4$
4-7	P_1, P_2, P_3, P_4
8-11	$\gamma_1, \gamma_2, \gamma_3, \gamma_4$

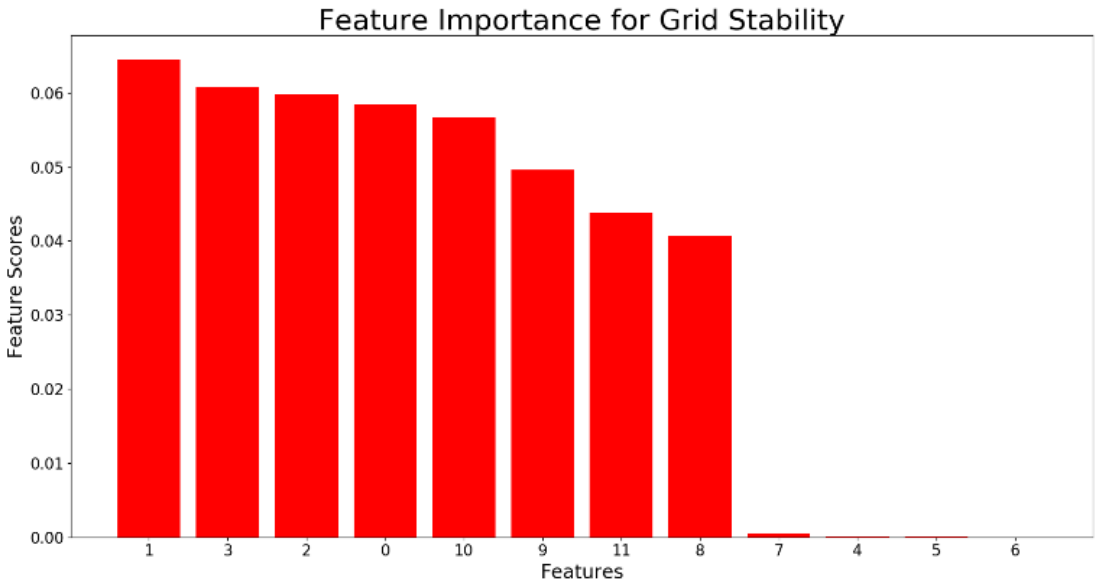

Figure 3-55: Feature selection results described as sorted feature scores.

Thus it is important to identify the features which play an important role in the determining the grid stability. It is done with the help of feature selection described in the previous section where the feature score is determined with the help of (112). The scores for the individual features have been shown in Figure 3-55.

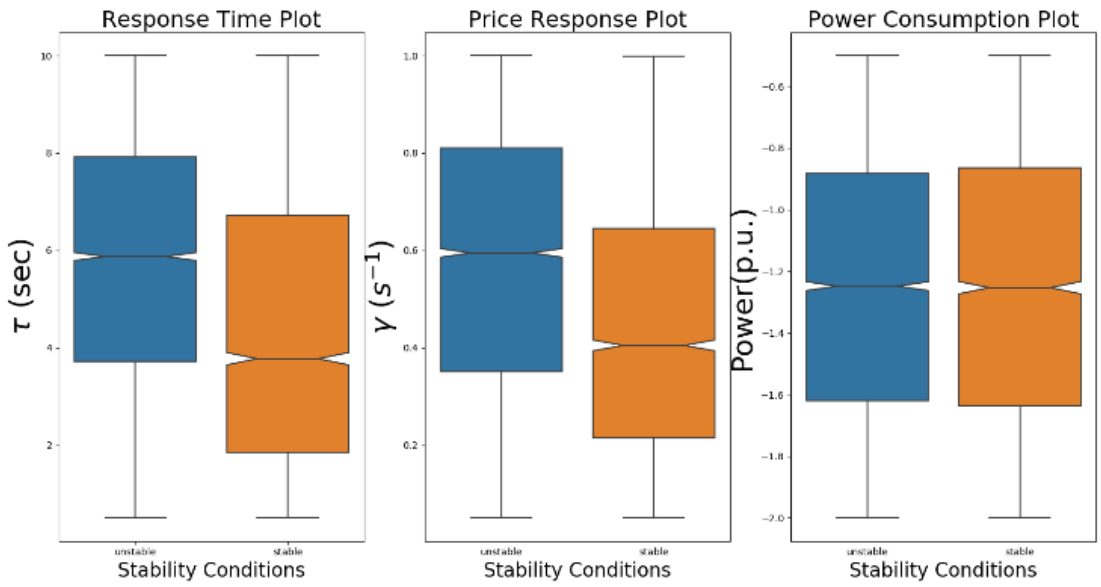

Figure 3-56: Parameters for consumers under grid stability conditions. Blue: unstable, red: stable condition.

Figure 3-55 that the power consumption or production by the producer and heterogeneous consumers do not influence the stability of the grid. The time response of the consumers and producer to the price fluctuation play a more important role in the grid stability, as compared to the price elasticity index. The time response and price elasticity of the producer influences the grid stability the least as compared to the parameters of the consumers. This analysis can be confirmed by checking the parameters of the grid during stable and unstable conditions.

We see in Figure 3-56 that unstable grid conditions generally prevail for higher values of τ and γ. However, the power consumption pattern does not show any difference under stable and unstable grid conditions thus conforming with the analysis of feature selection obtained. Similar plots can be obtained for the producers given in Figure 3-57, where expected results are found except the power production section when the variability is lower, as compared to the former case.

Now, regression analysis is performed based on the price response index γ and response time τ for the consumers and the producers relating the eigenvalues of the given system as per the solution of the characteristic equation given in (110). The results of the regression analysis have been shown in Table 3-4.

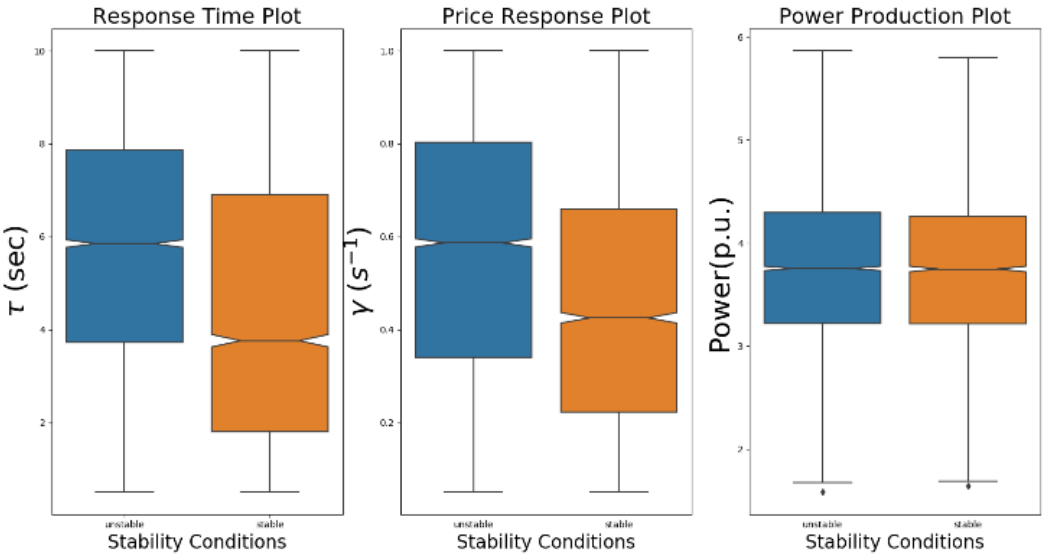

Figure 3-57: Parameters for producer under grid stability conditions. Blue: unstable, red: stable condition.

The R^2 value relates to the fact that linear regression model fitted as per (115) shows decent results in predicting the eigenvalue of the system based on the input parameters. High value of *F*-statistic suggests that intercept only model will fail to describe the data analysed here. The proximity in the values of R^2 and $\bar{R}^2$ suggests that the number of data points are good enough for the predicting the target value.

The quantile plot as shown in the Figure 3-58 indicate that the plot close to the straight line and hence revealing the distribution of the residuals being close to normal. The coefficients of regression $\hat{\beta}$ and the standard error $\hat{\sigma}$ obtained based on the estimate are shown in Figure 3-59.

Table 3-4: Regression Statistics

Statistic	**Value**
Multiple R^2	0.6468
Adjusted R^2	0.6465
F-Statistic	2287
Degrees of Freedom	9991

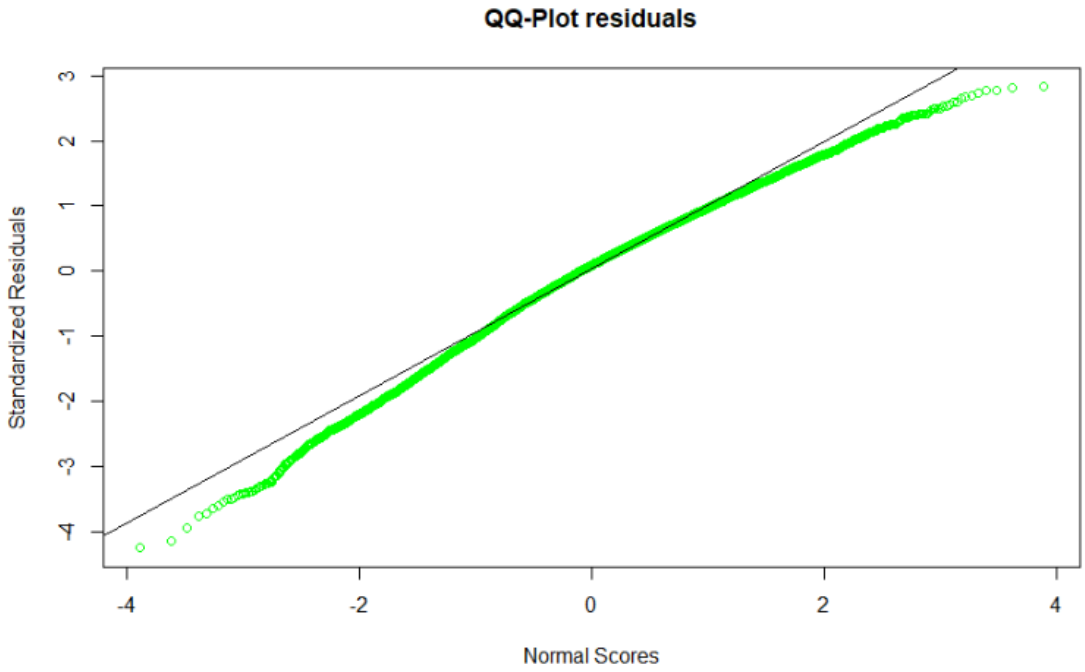

Figure 3-58 Quantile plot from the regression.

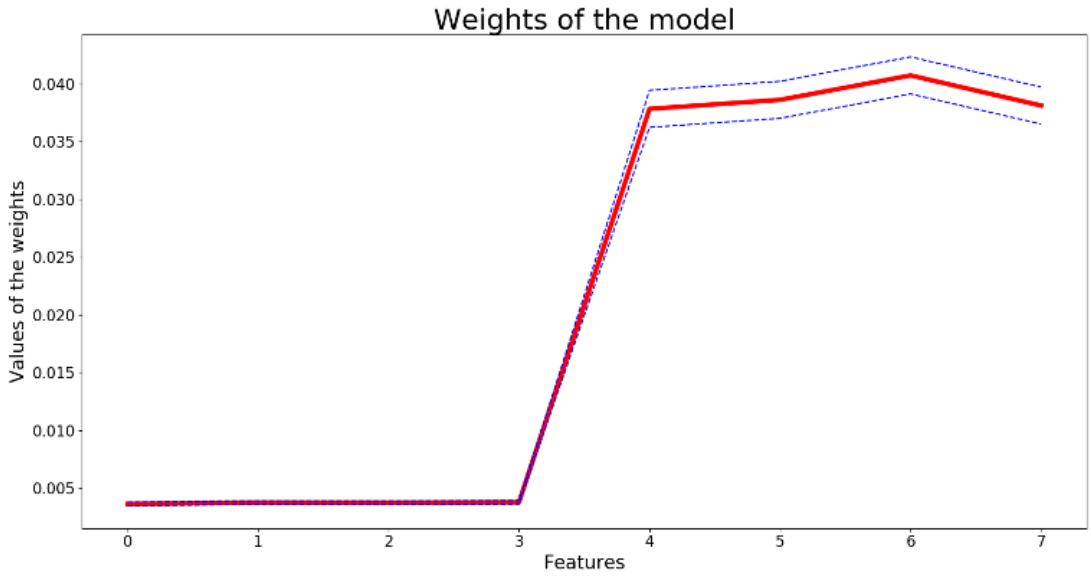

Figure 3-59 Coefficients of the model variables.

The coefficients suggests that the eigenvalues are more sensitive to the change in the price response index γ (X_8-X_{11}) as compared to the response time τ (X_0-X_3). We see from Figure 3-59 that the estimation error in the coefficients for γ is higher as compared to the error in coefficients of τ which is quite similar for all the consumers and producers. Hence, the regression analysis suggests that the eigenvalues of the system are more sensitive to the change in price response

index as compared to the response time of consumers and producer. In addition, the analysis suggests that power production and consumption (X_4-X_7) do not have any significant influence on the stability of the grid. Table 3-4 shows that the R^2 values are not high enough since the primary goal here is to identify the important variables using linear regression analysis after feature selection. However, owing to the complexity of the power system modelling involved, using higher order kernelized regression models may yield a better fitted model which will be pursued in a future research. Also, effect of other dimensionality reduction and shrinkage methods are also worth exploring in the current context. Cross-validation methods are also known to be very useful to prevent overfitting of complex regression models. We did not explore resampling and cross-validation methods in this study, since after feature selection, we applied a simple linear regression method as a feasibility study on this synthetic dataset which is less prone to overfitting.

The present regression analysis is shown on a simple grid model as shown in Figure 3-54 with 1 producer and 3 consumers. The modelling technique described above is generic and can be used to create a more complex synthetic dataset for such regression analysis and validate the findings on variable importance using larger power networks. Analysing this particular dataset can also be viewed as a classification problem, since one might not be interested in predicting the eigenvalues, rather intends to know the stability condition only. Also, some areas in the feature space may not be uniformly filled with the random selection of the initial conditions and are sparse in nature. Specific machine learning methods like the Gaussian processes may be useful for such problems that can produce the uncertainties in the regression modelling as a function of the covariates or selected features which will be explored in depth, in our future research.

3.3.8 Conclusion

Decentralized smart grid control has been shown here as a method for demand response. The control strategy has been formulated considering the assumptions, thus finding a deeper insight about the dependence of the parameters of the grid to its stability. The data used for the analysis consists of the response of heterogeneous consumers for different price fluctuations based on the power balance of the grid. The statistical and machine learning methods

such as feature selection and regression analysis are performed to find relationship between the input parameters with the eigenvalue and system stability conditions.

Chapter 4 Operational Analytics of Energy Storage Operation at Different Locations in the Grid for Generation Demand balance with Stochastic Contingencies and Wind Power

In the previous Chapter 3, the generation and demand balance was achieved by designing a controller for frequency stability under load disturbance and communication constraints. The results show that frequency stability is achieved in seconds. However, for generation and load demand balance problems on a larger scale, it becomes an optimal power flow (OPF) issue. If the generation and demand have to be balanced at every time interval, it becomes a multi-period OPF problem. The resilience of OPF can be carried out using security-constrained unit commitment problems. Battery energy storage can be used as a backup device to alleviate different contingencies. However, the placement of energy storage devices is a non-trivial problem.

In this sub-chapter, non-parametric multivariate statistical analyses of the energy storage operations in base and contingency scenarios are carried out to address these issues. Monte Carlo simulations of the optimization process for the overall cost involving unit commitment and dispatch decisions are performed with different wind and load demand ensembles. The optimization is performed for different grid contingency scenarios like transmission line trips and generator outages, along with the location of the ESS in different parts of the grid. The stochastic mixed-integer programming technique is used for optimization. The stochastic model load demand and wind power are obtained from real data. The uncertainty in the operational decisions is obtained, considering the different stochastic realizations of load demand and wind power. The data analytics is performed on ESS operations in the base and its corresponding contingency scenarios with different locations in the grid. Moreover, it is aided by non-parametric multivariate hypothesis tests to understand their dependence amongst various parameters and locations in the grid.

4.1 Previous Works

Security constrained unit commitment or SCUC is generally used to schedule the power dispatch for the controllable energy sources during grid contingencies

is shown in [203]. The algorithm is flexible enough to incorporate the changes in system network configurations for contingency. On occasions, the algorithm fails to converge due to violations of AC network constraints at steady and contingency states. Then, Benders mismatch cuts are used in [204] to shed local loads. The forced outage of the generation units, transmission lines, and load forecasting uncertainties are incorporated in [205], where it is modelled as a Markov process. . SCUC is solved considering the uncertainty of the load demand and wind power in [206], [207], [208]. Also, ramping and spinning reserves are used for the mitigation of the uncertainties of wind and load demand. Incorporating ESS in SCUC problems have been performed in [207], [209], [210], [211], [212]. The contingencies are modelled as a stochastic optimization based SCUC problem in [213] with energy storage. The optimization model involves incorporating the reserves as a part of the energy source during contingency scenarios. However, in [213], a detailed energy storage model is not considered in the optimization process. The model also does not involve Markov modelling of wind power as a part of the uncertainty. The work in [43] combines the detailed battery storage constraint model as a part of the stochastic unit commitment problem. In this problem, the contingency scenarios are considered as probabilistic. Two types of uncertainties are tackled in this paper – the first is wind power, which is modelled as a sequence of scenarios. In the second case, discrete events such as line or generator tripping (α) , which represents the fraction of the time, the system is in the base state, before branching off to contingency state.

4.2 Contribution in this chapter

As compared to existing literature, the work reported in this chapter analyses the energy storage operation at different locations in the grid. It combines the problem of SCUC and the placement of ESS in different grid locations. The analytics is focused mostly on the placement of ESS near the load, thermal generation, or wind power generation with the operational effects defined in [214]. However, the contingency effects on ESS operations are not mentioned and not worked upon much in recent literature. The contingency cases are carried out by extending the research reported in [43] to incorporate the fraction of time slice before contingency (α) in the energy storage model, along with its inter-temporal

constraints as defined in [215]. The energy storage operations during several contingencies, along with their location on several buses in the grid, have been analysed along with the base case scenarios. The operational analytics of the ESS is considered with respect to the economical running cost. The wind power forecasting error is modelled from the real-world data using Markov chains. The real-world load demand patterns are also used in the optimization problems during the Monte Carlo simulations. Hence, with the consideration of the ESS storage operations, while optimizing the total system cost along with real wind power and load demand patterns incorporating a variety of system contingencies, makes the problem very practical. The analysis is based on the ESS operational model, which is derived from the contingency scenarios of the grid. It also causes a relative change of the minimum and maximum energy that can be stored, which is reflected in the inter-temporal constraints of the ESS. These constraints, along with the charging and discharging models, play an essential role in the operation based with different location in the grid. Furthermore, this is the first work, where Monte Carlo simulations of different realization of the wind power and load demand uncertainty are conducted on multiperiod optimization problems for different contingency scenarios. . The operation was carried out on a small 3-bus system since, with the increase in scenarios, the computational burden will increase and cause ill-conditioned results as discussed in [216]. The analysis was conducted considering a range of grid contingency scenarios. As compared to the previous works, the main contributions and novelty of this paper are as follows:

- The wind and load power are modeled from real dataset in an appropriate form for performing the stochastic optimization algorithm for the solver.
- An analytical study is conducted comparing the nature of storage operations in base and contingency states.
- A detailed study is conducted on the ESS operations obtained from the unit commitment algorithm under base conditions with the energy storage placed at different locations in the grid.
- The similarity in base and contingency operational conditions is found from different locations of the energy storage in the grid using non-parametric multivariate hypothesis tests.

4.3 Overall Schematic

The scheduling of the generators as a multi-period optimization can be formulated as a unit commitment problem along with economic dispatch. Here the objective is to minimize the overall cost, considering the operational costs of the generator and energy storage devices. The stochastic optimization is formulated considering the uncertainty of wind power in multiple time steps. The multi-period stochastic optimization problem is solved at each time instant considering all the inter-temporal constraints.

The optimization problem and modelling are formulated based on the functionalities of the MATPOWER Optimal Scheduling Tool (MOST) as given in [43], [217]. The problem is solved using mixed-integer programming, which takes the stochastic input in the form of wind power. The wind power is modelled in the form of scenarios from the real data. The statistical model of load demand is formulated from the real data. Random samples of the load demand are used in the Monte Carlo simulation of the optimization problem. The transition probability matrix is used to define the Markov switching between the wind power states for various periods. The transition probability matrix is used as a random variable for each Monte Carlo ensemble. The overall scheme of statistical modelling, optimization, and analytics is shown in Figure 4-1. The MOST solver provides hourly unit commitment decisions for the generators, energy storage device, and dispatchable loads connected to the grid. The mathematical structure of the cost function for optimization, constraints, and energy storage operations, along with the stochastic variables, are presented in the following subsections.

4.4 Objective Function Formulation

The multiperiod mixed-integer stochastic programming is based on the concept of making optimal decisions based on the data available at that time, where the algorithm is generally solved in two steps given as:

$$\min_{x}\left\{g\left(x\right)=f_{\text{det}}\left(x\right)+\mathbb{E}_{\xi}\left[Q\left(x,\xi\right)\right]\right\}. \tag{125}$$

The constraints on x, solved in (125) given as $Tx \le h$, is incorporated in the

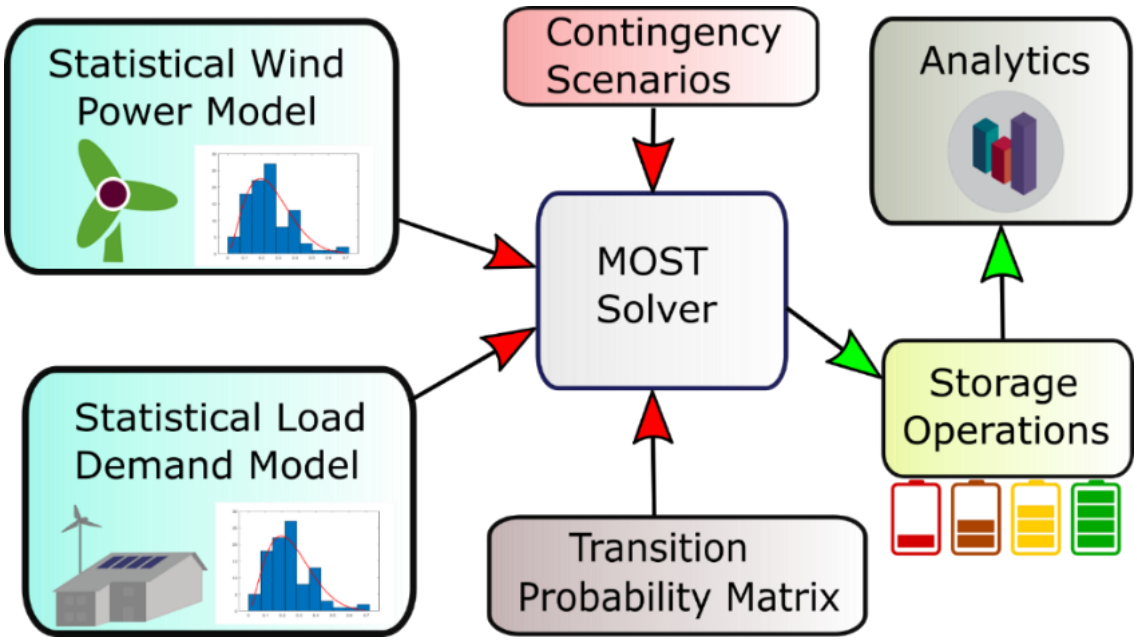

Figure 4-1: Operational scheme for generating operational ESS values from the stochastic load and wind power model along with various contingency scenarios.

second part of the problem, where $Q(x,\xi)$ is the optimal value obtained by solving:

$$\min_{y}\{q(y,\xi)|T(\xi)x+W(\xi)y=h(\xi)\}. \quad (126)$$

Thus, $x\in\mathbb{R}^n$ is the first stage decision variable while $y\in\mathbb{R}^m$ represents the second stage decision variables. Here, $f_{\text{det}}(x)$ and $\xi(q,T,W,h)$ represent the deterministic and the stochastic part of the objective function, respectively. $\mathbb{E}[\cdot]$ represents the expected value of the stochastic component of the objective function. In the case of SCUC problem, x represents the commitment status for the controllable generation sources found by solving $g(x)$ in (125) while y represents the power dispatch of the controllable generators found by solving (126). Since this is a multi-period optimization problem, we expect the optimization to be solved using the methodology described in (125) and (126). The objective function for SCUC along with unit commitment constraints are described in Appendix A.

4.5 Residual Energy Storage Constraints

4.5.1 Base Case Scenario

It is essential to compute the expected amount of stored energy s_F^{tij0} for the unit i at the end of the period *t* in the base state *j*. The losses are proportional to the average stored energy during the period. The process is to be represented as:

$$\begin{aligned} s_F^{tij0} &= s_I^{tij0} + s_\Delta^{tij0} - \Delta\eta_{loss}^{ti}\frac{s_I^{tij0} + s_\Delta^{tij0}}{2}, \\ &= \beta_1^{ti} s_I^{tij0} + \beta_1^{ti} s_\Delta^{tij0}, \end{aligned} \tag{127}$$

where,

$$\beta_1^{ti} \equiv \frac{1-\Delta\eta_{loss}^{ti}/2}{1+\Delta\eta_{loss}^{ti}/2},$$

$$\beta_2^{ti} \equiv \frac{1}{1+\Delta\eta_{loss}^{ti}/2},$$

$$s_\Delta^{tijk} \equiv -\Delta\left(\eta_{\text{in}}^{i} p_{sc}^{tijk} + \frac{1}{\eta_{out}^{i}} p_{sd}^{tijk}\right). \tag{128}$$

The total operational power from the storage is the net power used for charging and discharging:

$$p^{tijk} = p_{sc}^{tijk} + p_{sd}^{tijk}, \tag{129}$$

where,

$$p_{sc}^{tijk} \le 0, p_{sd}^{tijk} \ge 0. \tag{130}$$

Charging power is considered negative and discharging power as positive. The charging and discharging energy of the storage device should be operated within the following limits:

$$s_{-}^{ti} \ge S_{\text{min}}^{ti}, \quad s_{+}^{ti} \le S_{\text{max}}^{ti}. \tag{131}$$

The change in the stored energy per horizon during charging and discharging period can be represented as:

$$s_{-}^{ti} \le s_{-}^{(t-1)i} + s_{\Delta}^{tij0} - \Delta \frac{\eta_{loss}^{i}}{2}\left(s_{-}^{ti} + s_{-}^{(t-1)i}\right),$$
$$s_{+}^{ti} \ge s_{+}^{(t-1)i} + s_{\Delta}^{tij0} - \Delta \frac{\eta_{loss}^{i}}{2}\left(s_{+}^{ti} + s_{+}^{(t-1)i}\right). \quad (132)$$

4.5.2 Contingency Scenario

When the contingency occurs at a fraction α , the expected stored energy can be computed as follows:

$$s_{\alpha}^{tijk} = s_{I}^{tijk} + \alpha\left(s_{F}^{tij0} - s_{I}^{tij0}\right). \quad (133)$$

The losses occurred in the storage can be computed as:

$$s_{loss}^{tijk} = \Delta\eta_{loss}^{ti}\left[\alpha\frac{s_{I}^{tijk} + s_{\alpha}^{tijk}}{2} + (1-\alpha)\frac{s_{I}^{tijk} + s_{F}^{tijk}}{2}\right]. \quad (134)$$

The final stored energy is given as:

$$s_{F}^{tijk} = s_{i}^{tijk} + \alpha s_{\Delta}^{tij0} + (1-\alpha)s_{\Delta}^{tijk} - s_{loss}^{tijk}. \quad (135)$$

Substituting the values obtained in (133) and (134), we get:

$$s_{F}^{tijk} = \beta_{5}^{ti}s_{I}^{tijk} + \beta_{4}^{ti}s_{\Delta}^{tij0} + \beta_{3}s_{\Delta}^{tijk}. \quad (136)$$

where,

$$\beta_{3}^{ti} \equiv \left(\frac{1}{1-\alpha} + \Delta\frac{\eta_{loss}^{ti}}{2}\right)^{-1} = \frac{1-\alpha}{1+(1-\alpha)\Delta\eta_{loss}^{ti}/2}, \quad (137)$$

$$\beta_{4}^{ti} \equiv \frac{\alpha}{1-\alpha}\beta_{2}^{ti}\beta_{3}^{ti} = \frac{\alpha}{\left(1+\Delta\eta_{loss}^{ti}/2\right)\left(1+(1-\alpha)\Delta\eta_{loss}^{ti}/2\right)}, \quad (138)$$

$$\beta_{5}^{ti} \equiv \frac{\beta_{1}^{ti}}{\beta_{2}^{ti}}\left(\beta_{3}^{ti} + \beta_{4}^{ti}\right) = \left(1-\Delta\eta_{loss}^{ti}/2\right)\frac{\alpha + (1-\alpha)\left(1+\Delta\eta_{loss}^{ti}/2\right)}{\left(1+(1-\alpha)\Delta\eta_{loss}^{ti}/2\right)\left(1+\Delta\eta_{loss}^{ti}/2\right)}. \quad (139)$$

The constraints related to the minimum and maximum energy injection conditions can be described as:

$$\begin{aligned} s_{min}^{ti} &\le s_{-}^{(t-1)i} + \alpha s_{\Delta}^{tij0} + (1-\alpha) s_{\Delta}^{tijk}, k \neq 0, \\ s_{max}^{ti} &\ge s_{+}^{(t-1)i} + \alpha s_{\Delta}^{tij0} + (1-\alpha) s_{\Delta}^{tijk}, k \neq 0. \end{aligned} \tag{140}$$

The model of the energy storage operation described in (136), highlights its operational aspect when the grid is under contingency. This is also reflected in the minimum and maximum energy that can be stored along with the charging and discharging energy in the given time period as shown in (140).

4.6 Modelling the Uncertain Wind Power, Load Demand Conditions and Contingency Scenarios

Wind and load power are modelled as per Figure 4-1 from the Dalrymple project, Australia [113]. Its pattern for 30 days, along with its mean and confidence intervals are shown in Figure 4-2. The plot is created using the Seaborn library in Python. The data used for modelling is one-month data sampled at 4-sec intervals. It was then lumped to obtain hourly mean and standard deviation (SD) datasets. The data wrangling is carried out in the Pandas library in Python for missing data removal using previous samples and data reformatting from long stream to hourly interval calculation. Since the optimization approach is considered for 12 hours, the distribution of the wind power is modelled as per the scheme described in Figure 4-1 to represent the monthly data within this time interval.

In order to model the hourly characteristics of the data in [113], the data partition is done hourly. The standard deviation of the samples in the given hour is obtained. The hourly standard deviation and the mean of hourly wind power and load demand are uncorrelated as per the multivariate plot shown in Figure 4-3.

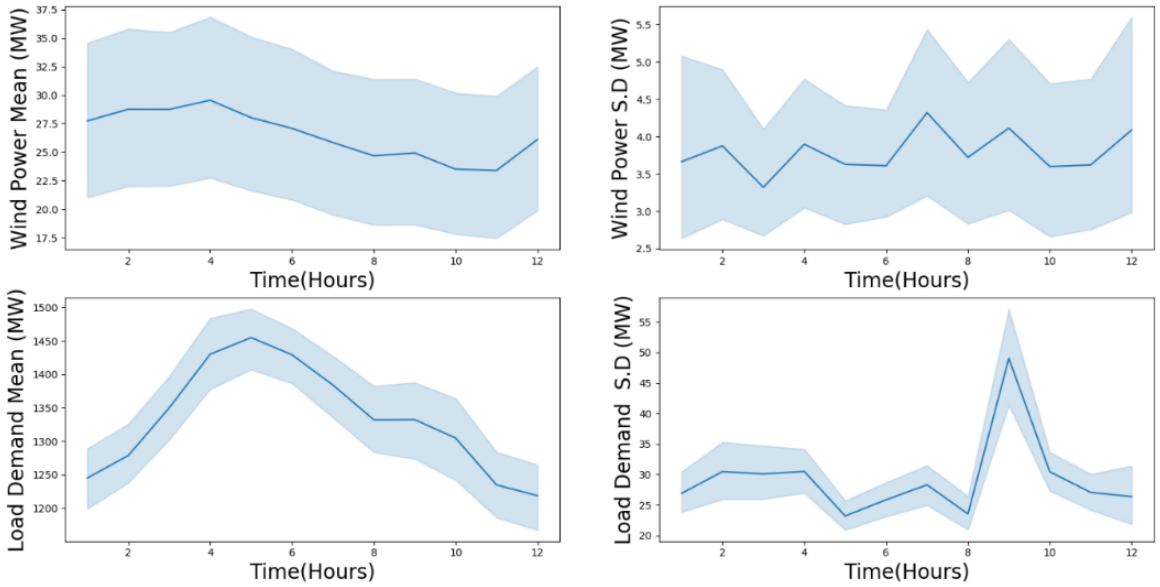

Figure 4-2. Wind power and load demand mean and standard deviation profiles at various hourly instants considered in the optimization algorithm. Confidence intervals are calculated based on 24×30/12 = 60 samples per hour.

The hourly standard deviation data is fitted with a chosen probability distribution. According to the data, the lognormal distribution provides the best fit for the hourly deviation data whose probability distribution function is given as:

$$\mathrm{WIND}_{\mathrm{SD}}(x) = \frac{1}{x\sigma_1\sqrt{2\pi}} \exp\left(-\frac{(\ln x - \mu_1)^2}{2\sigma_1^2} \right) \tag{141}$$

Here, x represents the samples from the above distribution μ_1 and σ_1 represents parameters of the distribution signifying expected mean and standard deviation of the natural logarithm of variable x. The `distributionFitter()` function in Statistics and Machine Learning Toolbox of Matlab is used to find the parameter value with maximum log-likelihood value. The estimated parameters of this density are $\mu_1 = -2.865$ and $\sigma_1 = 0.983$. The samples for the Monte Carlo simulation were generated using the function `random()` in the Statistics and Machine Learning Toolbox in Matlab. The samples are generated, incorporating the inverse transform sampling method. The inverse sampling method draws random numbers from probability distribution function (pdf) defined in (141) with specified parameters and its cumulative distribution function (CDF).

The mean wind power value is obtained by calculating the mean value of equally partitioned data as per 12 hours interval. The wind data follow a normal distribution at a particular hour, as given in [140]. Hence three random states are generated from the mean and standard deviations model. It is then quantized as a low, medium, and high wind power scenario, as shown in Figure 4-4. The MOST solver represents the wind power in per unit (pu). The mathematical relations between the wind states are described in (142).

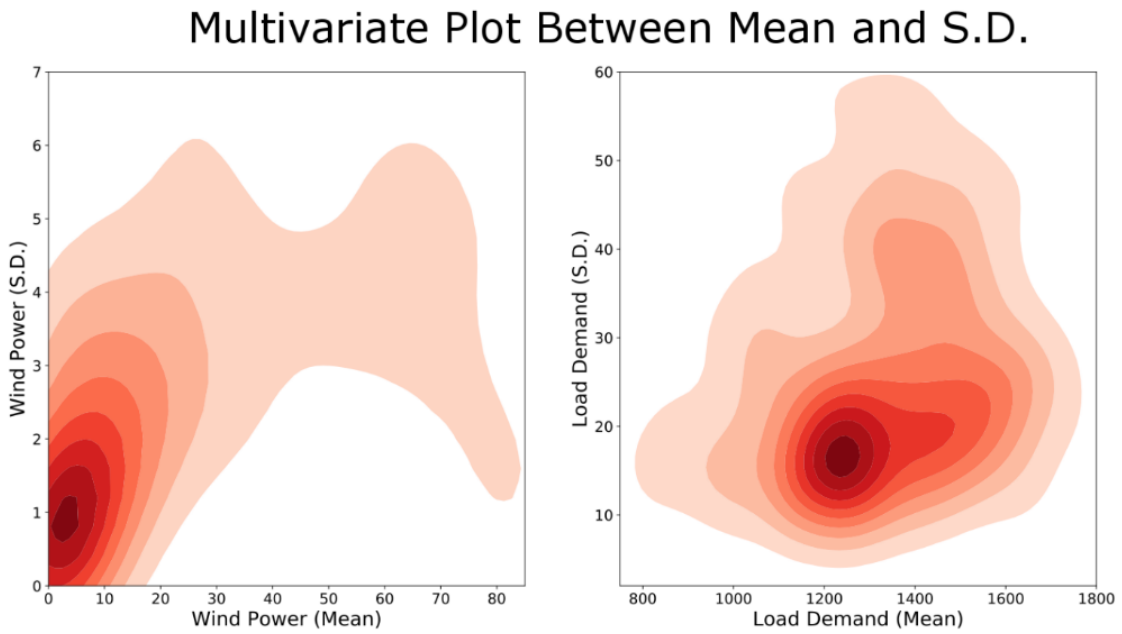

Figure 4-3. Correlation plot between the mean and standard deviation of load demand and wind power. Distributions of wind and load mean and SDs are calculated based on 24×30 = 720 data points.

The prediction error due to the wind follows a normal distribution, as given in [140]. Discrete probability values are used to represent continuous probability distribution. Three scenarios of wind power $p_w = \{p_{w1}, p_{w2}, p_{w3}\}$ are modelled as per the following set of equations:

$$\begin{aligned} &\omega_1 p_{w1} + \omega_2 p_{w2} + \omega_3 p_{w3} = \mu, \\ &\omega_1 p_{w1}^2 + \omega_2 p_{w2}^2 + \omega_3 p_{w3}^2 = \sigma^2 + \mu^2, \end{aligned} \tag{142}$$

where, μ and σ is obtained from the scheme defined in Figure 4-4.

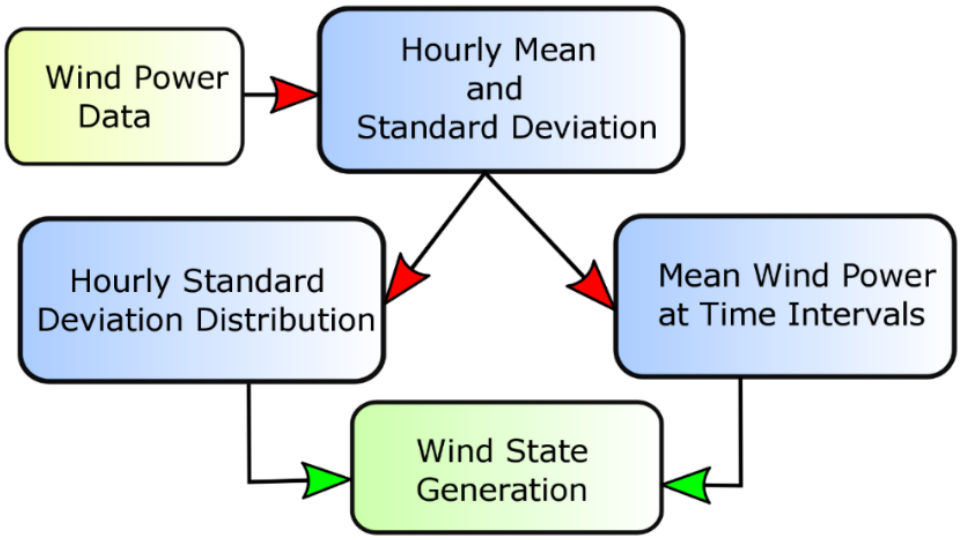

Figure 4-4. Procedure to generate the wind states from the standard deviation and mean wind power generated from the real data.

The wind states following Markovian behaviour, with the stationary distribution $\pi = \{\omega_1, \omega_2, \omega_3\}$, the following relations hold:

$$\pi \Psi = \pi, \tag{143}$$

where, Ψ represents the transition probability matrix for the states. The vector $\pi = \{\omega_1, \omega_2, \omega_3\}$ is modelled in the simulations from the `asymptotics()` function in the Econometrics toolbox in Matlab. Hence, the vectors obtained in (142) are used as states representing the low, medium, and high power states, as shown in Figure 4-4.

A similar approach is used for modelling the load power, as shown in Figure 4-5. The mean and standard deviation is calculated from equally partitioned data. The partitions represent the hourly horizons in the optimization algorithm. It is shown that the mean demand follows a normal distribution whose probability distribution is given as:

$$\text{LOAD}_{\text{MEAN}}(x) = \frac{1}{\sigma_2 \sqrt{2\pi}} \exp\left(-\frac{1}{2} \left(\frac{x - \mu_2}{\sigma_2} \right)^2 \right), \tag{144}$$

where, μ_2 and σ_2 represents the mean and standard deviation of the random variable *x* considered here. The estimated parameters for this density are given as $\mu_2 = 666.45$ and $\sigma_2 = 105.76$.

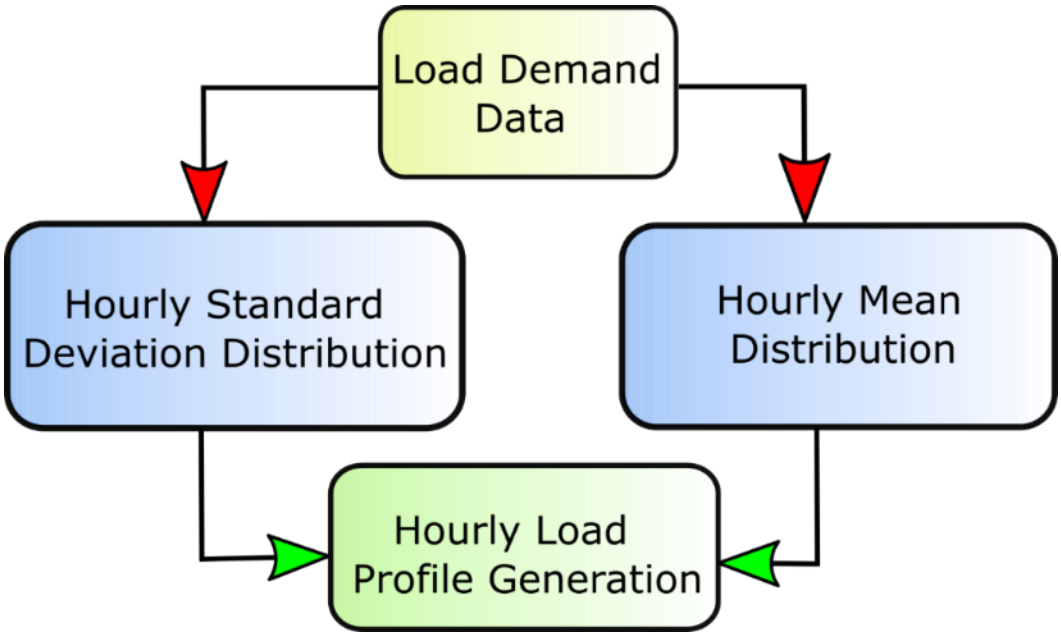

Figure 4-5. Hourly load profile generation from the hourly standard deviation and mean distribution obtained from the real data.

The standard deviation of the load demand data follows an inverse Gaussian distribution whose probability distribution is given as:

$$\text{LOAD}_{\text{SD}}(x) = \sqrt{\frac{\lambda}{2\pi x^3}} \exp\left[-\frac{\lambda(x-\mu_3)}{2\mu_3{}^2 x}\right]. \quad (145)$$

Here the value μ_3 is the mean of random variable *x* and λ represents the shape parameter. The estimated parameters for this density are $\mu_3 = 14.24$ and $\lambda = 49.48$. The histograms of the probability distribution of the variables used in Monte Carlo simulations are shown in

Figure 4-6. Since the optimization problem is a multi-period problem with the known dispatched and storage states. The transition of the given state to any scenario is considered as follows. The probability of operation in period *t*, with no contingency, realized in previous periods is represented as:

$$\gamma^t = \sum_{j \in J^{t-1}} \psi^{(t-1)j0} = \sum_{j \in J^t, k \in K^{tj}} \psi^{tjk} < 1, \text{ for } t > 1. \quad (146)$$

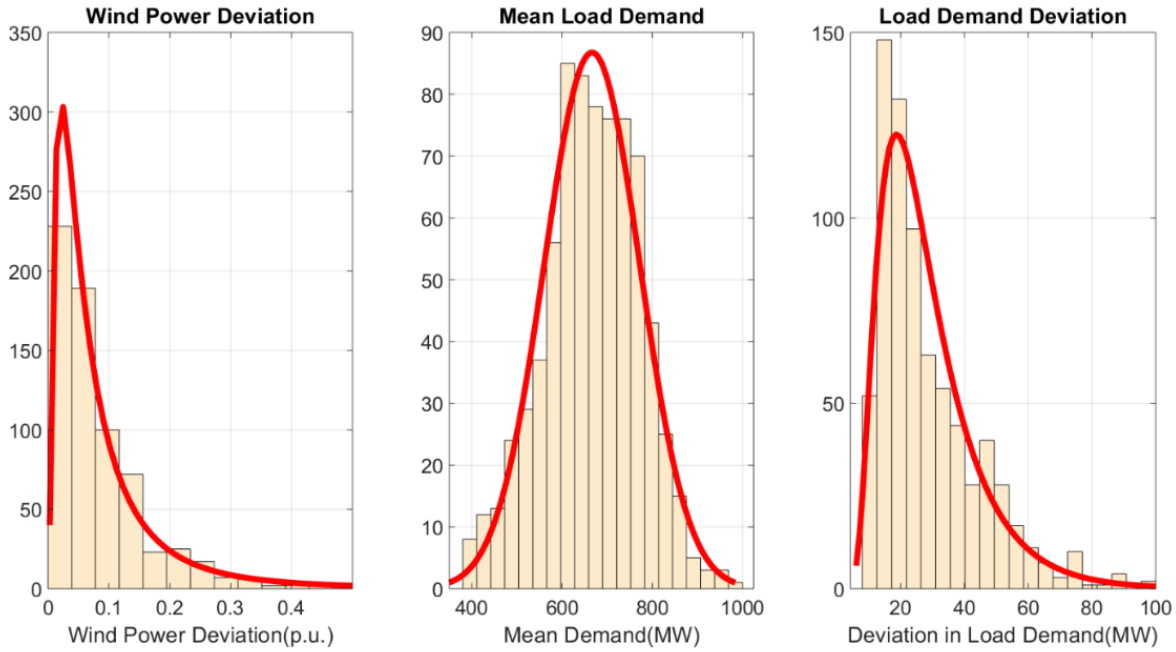

Figure 4-6. Best fitted probability distributions for the wind power deviation, mean load demand, and load demand deviation to generate Monte Carlo samples for the simulation studies.

Let us consider the probability of transitioning to the scenario j_2 in the time t provided that the scenario j_1 was realized at the time $(t-1)$ has a known value $\phi^{tj_2j_1}$. The transition probability at time step *t* is arranged in a probability transition matrix given by:

$$\Phi^t = \begin{pmatrix} \phi^{t11} & \cdots & \phi^{t1n_{j^{t-1}}} \\ \vdots & \ddots & \vdots \\ \phi^{tn_{j^t}1} & \cdots & \phi^{tn_{j^t}n_{j^{t-1}}} \end{pmatrix}. \tag{147}$$

Transition probability matrix, where each scenario at a time step $(t-1)$ can be transitioned to scenarios at *t* is represented as:

$$\begin{bmatrix} \gamma^{t1} \\ \gamma^{t2} \\ \vdots \\ \gamma^{tn_{j^t}} \end{bmatrix} = \Phi^t \begin{bmatrix} \psi^{(t-1)10} \\ \psi^{(t-1)20} \\ \vdots \\ \psi^{(t-1)n_{j^{t-1}}0} \end{bmatrix}, \tag{148}$$

where,

$$\gamma^{tj} = \sum_{k \in K^{tj}} \psi^{tjk}. \tag{149}$$

Since the sum across *k* of the conditional probabilities of contingencies ψ_0^{tjk} is 1, the values of γ^{tj} are scaled to get the correct state-specific probabilities:

$$\psi^{tjk} = \gamma^{tj} \psi_0^{tjk}. \tag{150}$$

In the case of generator outage contingency, the simulation does not take into account the dependency of the transition probability with the commitment status of the generator unit.

4.7 Non-Parametric Hypothesis Testing

Before we proceed for non-parametric hypothesis test, it is essential to check the normality condition as per the multivariate normal test described in Appendix B. The test statistic described in the Appendix B is applicable when the multi-period cases or sample sizes are significant. For the total sample size $\mathrm{N} \geq 30$, a normal or limiting χ^2 distribution may not describe the actual probability distribution of the test statistic as shown in [218], [219]. The F-approximation works well than the traditional χ^2 (chi-squared) approximation for the smaller sample size. The χ^2 distribution with *d* degrees of freedom is defined as the sum of squares of *d* independent standard normal variables. It is defined as:

$$\mathrm{U} = \sum_{\mathrm{i}=1}^{\mathrm{d}} \mathrm{Z}_{\mathrm{i}}^2, \tag{151}$$

where $\{\mathrm{Z}_1, ..., \mathrm{Z}_\mathrm{r}\}$ are independent standard normal variables. Hence, a random variable having F distribution with parameters d_1 and d_2 is defined as a ratio of two χ^2 variates as given in [220]:

$$\mathrm{F} = \frac{\mathrm{U}_1 / d_1}{\mathrm{U}_2 / d_2}., \tag{152}$$

where,

- U_1 and U_2 have χ^2 distribution d_1 and d_2 are degrees of freedom,
- U_1 and U_2 are independent.

Thus, F approximation of the test statistic of the multivariate samples is defined by:

$$\mathrm{F}_{\lambda} = \left[\left(1-\lambda^{1/t}\right)/\left(\lambda^{1/t}\right)\right]\left(df_2/df_1\right), \tag{153}$$

where,

$$\begin{aligned}
\lambda &= \frac{\det\left[\left(\mathrm{N}-\mathrm{A}\right)\mathbf{G}_1\right]}{\det\left[\left(\mathrm{N}-\mathrm{A}\right)\mathbf{G}_1+\left(\mathrm{A}-1\right)\mathbf{H}_1\right]},\\
df_1 &= \mathrm{m}\left(\mathrm{A}-1\right),\\
df_2 &= \mathrm{rt}-\left(\mathrm{m}\left(\mathrm{A}-1\right)-2\right)/2,\\
\mathrm{r} &= \left(\mathrm{N}-\mathrm{A}\right)-\left(\mathrm{m}-\left(\mathrm{A}-1\right)+1\right)/2.
\end{aligned} \tag{154}$$

The value t is defined as:

$$\begin{aligned}
&\text{if } \mathrm{m}\left(\mathrm{A}-1\right)=2, \text{ then } \mathrm{t}=1;\\
&\text{else, } \mathrm{t}=\sqrt{\frac{\mathrm{m}^2\left(\mathrm{A}-1\right)^2-4}{\mathrm{m}^2+\left(\mathrm{A}-1\right)^2-5}}.
\end{aligned} \tag{155}$$

Relative effects have been described in [221] which reflects the non-parametric tests complementing the inferential analysis in the form of probabilities. The statistic derived in (153) can be found out using `nonpartest()` function in the *npmv* package in R as described in [218].

4.8 Numerical Validation

A 3-bus power system has been considered for the numerical validation. The nominal values for the energy and load devices are shown in Figure 4-7. The security-constrained stochastic unit commitment problems generally become nonconvex when the system considered is large as stated in [222]. It is mainly due to the assumptions involving the parametric cost of the system. Moreover, the problem also becomes ill-conditioned under different opposing contingency schemes, which leads to numerical inaccuracies. Specific scenarios and

contingencies can make the computational procedure formidable for a larger grid [43]. Therefore, it becomes challenging to perform simulations under varied conditions. Thus, a smaller grid can provide a reasonable basis of multivariate analysis based on the contingency conditions of all the power system components. The grid structure in Figure 4-7 has been adopted from the MATPOWER MOST manual given in [223].

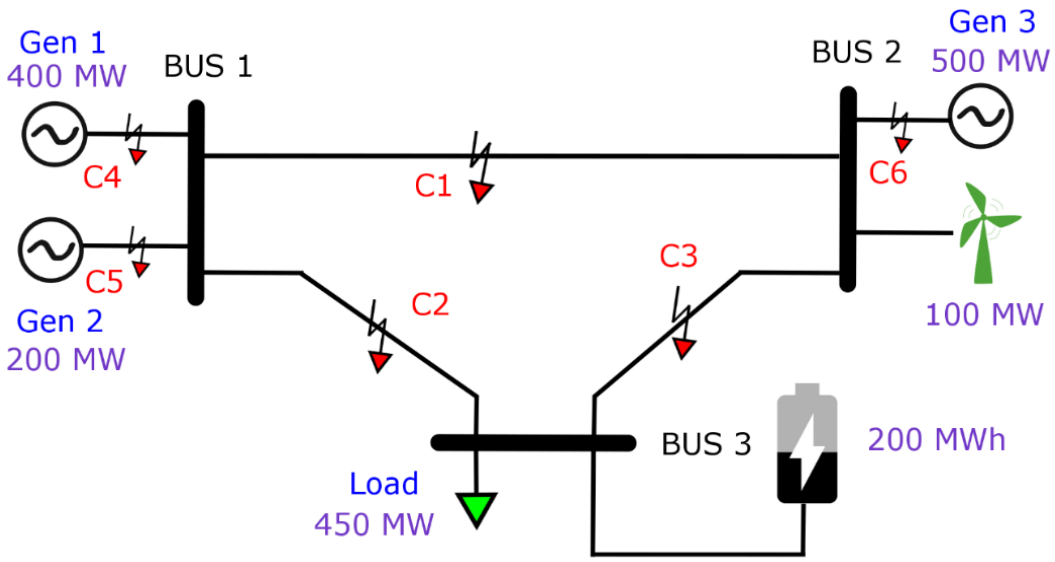

Figure 4-7: Grid structure for the 3-bus system with generators, wind, load, and battery. Here in the figure battery is placed near the load demand however, it varied throughout the simulation.

The MOST solver was run 1000 times from the random samples of the wind power, load demand, and probability transition matrix, where the *Gurobi* solver has been used to solve the optimization problem. The solver has the feature to solve the problem on a multi-threaded processor. The stochastic optimization algorithm was run on a 64-bit Windows PC Intel Core i5-8500 CPU, 3 GHz processor with six parallel cores. The test grid shown in Figure 4-7 involves two generators G1 and G2 connected to bus 1, which has a nominal rating of 250 MW and 125 MW but maximum peak operational capacity of 400MW and 200 MW, respectively, with the inclusion of locational reserves. G3 has a nominal rating of 200 MW with a capacity of 500 MW in the presence of locational reserves. Wind power is considered as the stochastic generation input, with 100 MW being considered as the base value. The dispatchable load is used in the analysis that is curtailable at a specific price with minimum load demand of 450 MW, as shown in Figure 4-7. Since the sizing problem of energy storage is not

considered here, the analysis is performed with an energy capacity of 200 MWh. Maximum charging and discharge rate of 80 MW is considered with an efficiency of 75% as given in [224]. The tripping of all transmission lines and generators are considered as the contingency scenarios shown in Figure 4-7. The value α of 0.06 is assumed in the simulation.

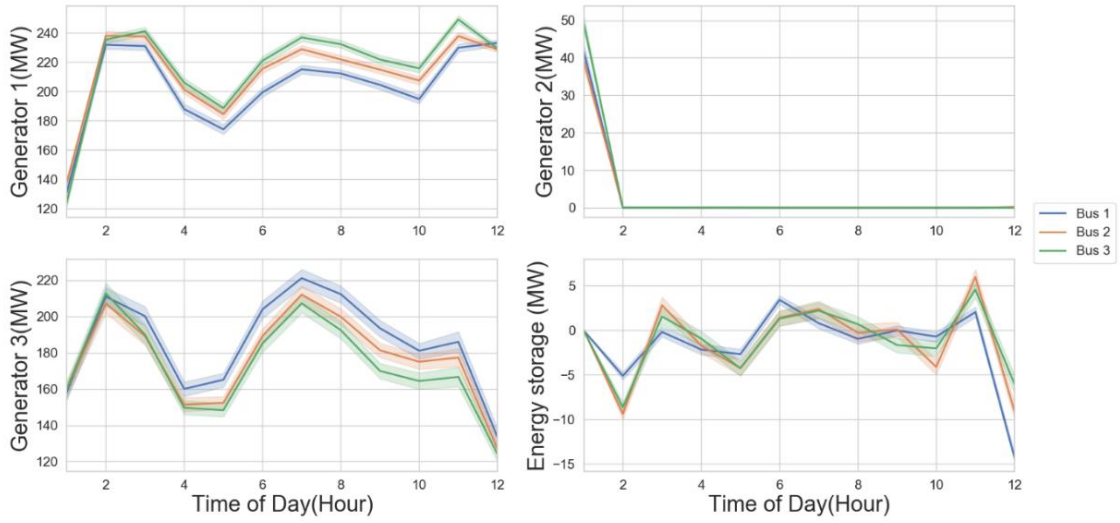

Figure 4-8. Multi-period optimization results for generator 1, generator 2, and generator 3 and energy storage operations at the base case scenario when the energy storage device is placed at different buses. Confidence intervals are calculated from 1000 independent runs of the stochastic optimization.

The power flow analysis of the grid structure, considering the nominal ratings of the generators and load, as shown in Figure 4-7, is performed. The results show that the branch connecting bus-1 to bus-3 is the most critical one as it carries bulk power. The branch connecting bus-1 to bus-2 is the least critical one. The simulation is performed with 1000 samples of wind power and load demand scenarios along with random Markovian transition matrices in each iteration. The decisions for the controllable energy sources without any contingency is shown in Figure 4-8. In the given figure, the simulations were conducted with the energy storage devices placed on different buses. We observe that G2 is mostly shut down for most of the time. It is mainly due to its lower rating and peak capacity. We also observe a distinctive pattern in the ESS operational data from Figure 4-8 when it is placed at different locations of the grid. The optimal conditions of energy dispatch for G1 are higher when the battery is placed at bus-3, the load bus. However, the pattern is reversed in G3, which is connected to the same bus as

the wind power source. The dispatch value is higher when the battery source is connected to bus-1, as compared to when it is connected to the load bus-3.

4.9 Results and Discussions

4.9.1 Analysis of the Storage Operations Based on Base Case and Contingency Scenarios

Ensembles of the wind energy and load demand pattern are used from the probability distribution of the mean and standard deviation, which is modelled from the real data, as shown in . Based on different values of load demand and wind power from the ensembles, the value of ESS committed will depend upon it. Hence it is expected to obtain charging and discharging patterns for different ensembles. In the case of contingencies, the expected ESS operation changes. In the base case scenario, it is expected to work as a bidirectional device. However, during contingency, ESS will act as a generator to meet the load demand to prevent load shedding. It is interesting to check how the bidirectional nature of ESS changes during different contingencies. Energy storage is expected to provide arbitrage, i.e., charging when the load demand is low and discharging when load demand is high. Regular arbitrage operation can be observed in Figure 4-8, where the ESS operates in both regions. If it operated in discharge mode, ESS should be able to provide higher power during a contingency.

Table 4-1:Multivariate normality test results on the energy storage operations data

Storage Location	Contingency Condition	$\hat{\beta}_{1,m}$	$\hat{\beta}_{2,m}$	Critical Distance	*p*-value
Bus-1, Bus-2, Bus-3	-	6.43	19.2	0.6	0
Bus-1	All cases	24	69.8	12.59	0
	C4, C6	1.21	7.38	5.99	0

	C1, C2, C3, C5	21.7	47.2	9.49	0
Bus-2	All cases	2.7	41.6	12.59	0
	C1, C2, C3	1.36	11.3	7.81	0
	C4, C5, C6	0.74	10.6	7.81	0
Bus-3	All cases	2.74	41.3	12.59	0
	C1, C4, C5, C6	1.36	18.8	9.49	0
	C2, C3	0.31	5.19	5.99	0

Similarly, it is expected to provide lower power if it acts in charging mode during the base case scenario since the load demand is expected to be less. Based on this logic, the ESS operational characteristic should ideally follow a linear region when observing the characteristics of base and contingency operations. However, we observe an atypical pattern in Figure 4-9, Figure *4-10*, and Figure *4-11*. The pattern is mainly due to the absence of the p_{sc} term in s_{Δ}^{tijk} as in (128) during the contingency scenario. The presence of p_{sc} creates a difference in the hourly change in stored energy in different scenarios. The difference in the operation of ESS in the base case scenarios for different contingencies is due to the inter-temporal constraints defined for the operation in [223]. Moreover, this is also due to the presence of γ^{tj} and ψ_{α}^{tjk} for total and ramping costs. Due to the presence of these probabilistic parameters referring to the transmission lines and generator outages, the operations during base conditions change during different contingency scenarios. We observe in Figure 4-8 that the ESS works in charging mode in the final hour. This is mainly because the mean load demand is low, as shown in Figure 4-2. However, there are certain

instances where the ESS works in discharging mode, especially when it is placed on the load bus, as shown in Figure 4-8.

The stored energy for contingency scenarios is dependent upon the $\beta_3^{ti}, \beta_4^{ti}$ and β_5^{ti}. It is calculated every hourly interval, which varies with α. Hence, these parameters also cause a difference in the minimum and maximum hourly energy discharge as given by (132) and (140) respectively. The data is spread in the linear zone in the first hours of operation. For the higher time, the data-points move along the periphery of the parallelogram. It signifies the nature of the operation of the energy storage devices in the grid at various locations and the type of contingency. Moreover, the peripheral spread in the pattern can also be attributed to the inter-temporal constraints given by (132) and (140). The hourly charging and discharging terms p_{sc}^t and p_{sd}^t in the base and p_{sd}^t contingency cases causes variation in ESS behaviour as explained with the non-parametric multivariate test in the next sections.

4.9.2 Multivariate Normality Test on the Storage Operations

The results obtained after conducting the multivariate normal test are given in Table 4-1. As we see from Table 4-1, the *p*-values obtained are all zero, which shows that the underlying data is not normal, hence a non-parametric multivariate test needs to be conducted as described in the next section.

4.9.3 Analysis of Storage Operations at Different Locations in the Grid

The data generated from the optimization consists of values obtained for different time horizons and 1000 random samples from wind, load, and transition probability matrix (as described in Section 4.6). The values of m (hourly instants) and n (number of Monte Carlo samples) are 12 and 1000, respectively. The value a depends on the comparison of various contingency conditions. The test statistic F, along with the degrees of freedom df_1 and df_2 are shown in Table 4-2. We observe from Table 4-2 that the *F*-statistic is quite high in the case when the storage operation is analysed under the base case scenario as compared to other contingencies which signify that the energy storage operation is more similar under no contingencies as compared to its operation when placed on

different buses during several contingencies. When the storage device is placed on bus 1, it operates in extreme regimes, as observed in Figure 4-9, which signifies that the storage operations are not similar for different contingencies. Moreover, it is also not statistically significant, as shown in Table 4-1.

4.9.3.1 ESS Located at Bus 1

We observe from Figure 4-9 that the operation of the ESS is susceptible to different tripping conditions. The maximum power obtained during contingencies C2, C3, C5 is minimal during later hours of operation. The ESS discharges at low rate during the corresponding charging base states during C1, C2, C3, and C5 contingency. In the case of C4 and C6 contingency, the ESS discharges power to compensate for the contingency of the outage of a higher capacity generator. The ideal case of operation is at the bottom left and top right corner for energy arbitrage, as it has to discharge less amount if it was working in the charging mode in the base case scenario and higher amount if it was working under discharge mode in base case scenario. It is observed partially in the case of all the contingencies except C4 and C6. It shows that the robustness of operation is affected when the energy storage device is placed near the generator bus. It is also observed that, in the case of the C6 contingency scenario, the ESS does not operate for the first few hours, which is not observed in the other contingency situations.

When we observe the discharge conditions of ESS, corresponding to the base case of C1, C2, C3, and C5 contingency, we observe operations mostly during the later hours. However, in the case of C4 and C6 contingency, we observe the ESS operates in discharge mode in the early hours. During the charge conditions of ESS, we observe that the ESS does not operate at full capacity during the contingency situations as compared to its respective base case scenario in the case of C2, C3 and C5 contingency where it works till maximum 12.5 MW, 15MW and 16 MW corresponding to the base case conditions. It operates at maximum capacity in the case of C1, C4, and C6 contingency only when the ESS is charging at a higher rate during the base case scenario.

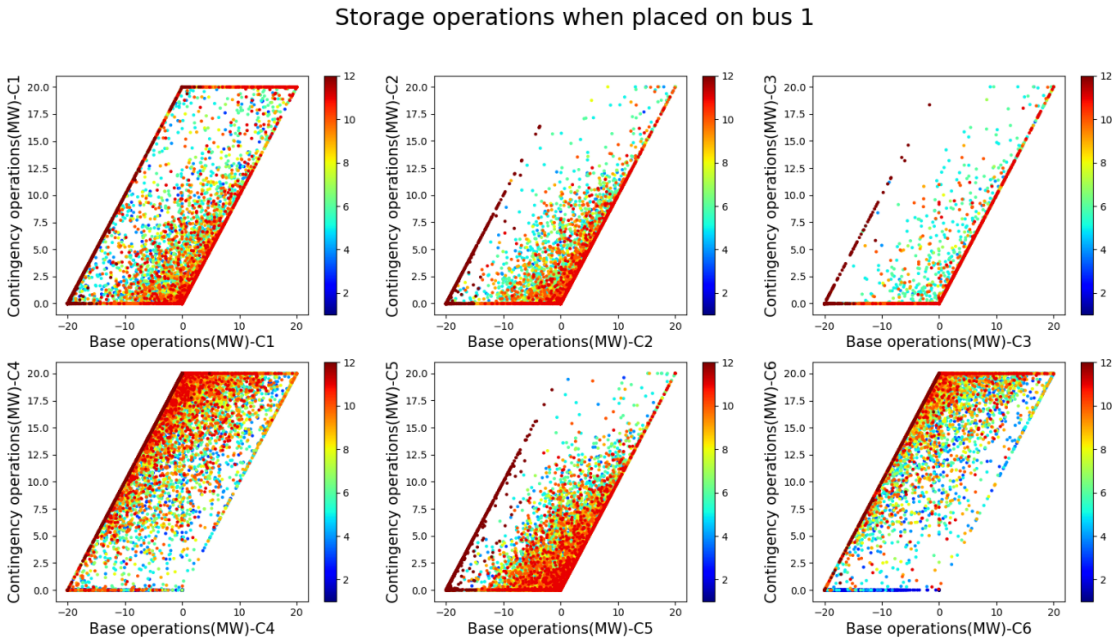

Figure 4-9. Energy storage operations when placed on bus-1 in the grid under various contingency scenarios for different wind power and load demand ensembles. Colours represent hour of operation between 1-12 hours.

We observe a similarity in operational patterns for C1, C2, C3, and C5 contingencies based on the test statistic with lesser degrees of freedom, as shown in Table 4-2. The operational dissimilarity is observed when lines between bus-1 and bus-2 and G2 is tripped. It is due to the low power flow and the generator capacity. However, it is more sensitive to trips of the lines connecting the load bus. F value of 578 is observed in Table 4-2, which is significantly higher as compared to other cases due to the outage of generators G1 and G3, which are of higher generation and capacity rating. Hence, the results show that the operation of energy storage is dependent on the tripping of the generator with higher ramping capacity. In addition to this, it is less sensitive to the line trips when placed near the conventional generators with a higher rating.

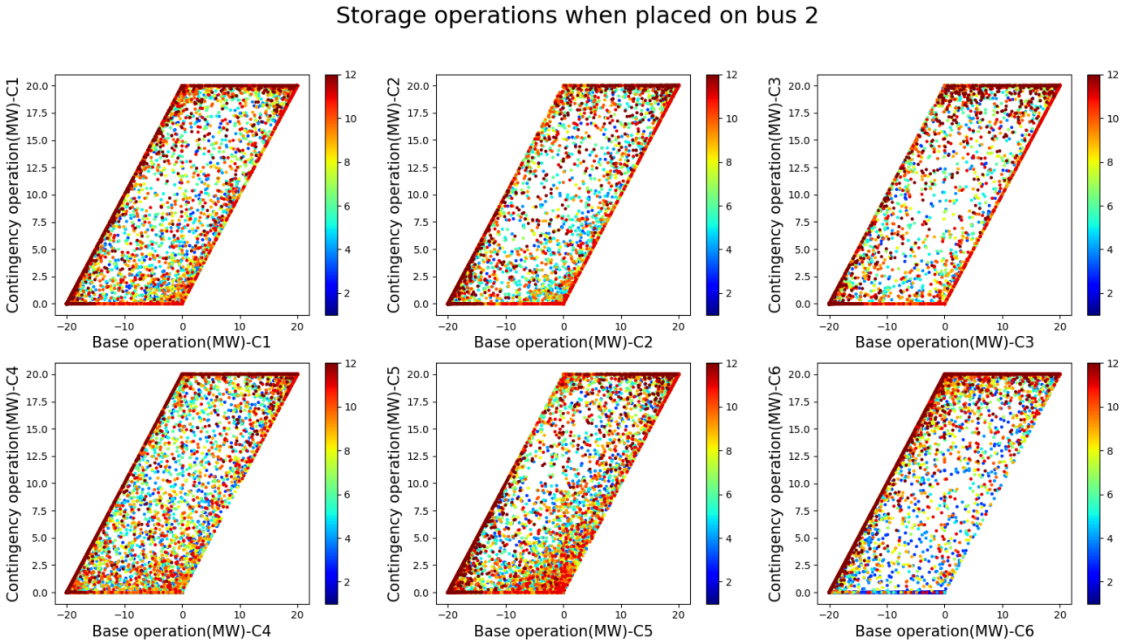

Figure 4-10. Energy storage operations when placed on bus-2 in the grid under various contingency scenarios. Colours represent hour of operation between 1-12 hours.

4.9.3.2 ESS Located at Bus 2

When the energy storage device is placed on bus-2 near the wind power, we observe a uniform operation across its spectrum as compared to the previous cases shown in Figure 4-10. It is observed that all ESS would be able to provide higher capacities for all types of contingencies. There are exceptions to the case where we observe a lower rate of ESS operation in case of C2 contingency when the base case charging operation is between 0 to 10 MW during the final hour of the period. However, we do observe a change in ESS operation in the case of C6 contingency. We do not observe a discharging condition during later hours, in the base case scenario. The ESS works mostly in the discharge condition during the base case scenario during the initial hours of operation. We also observe a limit in the maximum discharge during C2 and C5 contingency in the later hours of operation.

However, the F-statistic is lower as compared to the previous location, as shown in Table 4-2. It indicates a lesser overall similarity in operation. Higher F-statistics in the cases of C4, C5, and C6 contingency are observed in Table 4-2, which indicates similarity in storage operation in case of generator trips as compared to the line trips. We observe more uniform spread in the data in case of C1 contingency, as compared to C3, which signifies that the modes of

operation are more dependent on the tripping of the line connecting the storage to the load as compared to the line not connected between the loads when it is connected.

Table 4-2: Results of non-parametric multivariate test for storage operations on various grid locations and contingency scenarios

Storage Location	Contingency Condition	Test Statistic (F)	Degrees of Freedom (df_1)	Degrees of Freedom (df_2)	p-value
Bus-1, Bus-2, Bus-3	-	734.319	33	212084.7	0
Bus 1	All cases	373.364	66	64124.67	0
	C4, C6	578.988	22	23974	0
	C1, C2, C3, C5	372.736	44	45853.57	0
Bus 2	All cases	238.755	66	64124.67	0
	C1, C2, C3	182.738	33	35313.67	0
	C4, C5, C6	406.132	33	35313.67	0
Bus 3	All cases	229.655	66	64124.67	0
	C1, C4, C5, C6	196.135	44	45853.57	0
	C2, C3	498.661	22	23974	0

4.9.3.3 ESS Located at Bus 3

When the energy storage is placed in bus 3, we observe that the ESS works in discharge mode during the base case scenarios. However, it operates mostly in charging mode during the later hours of operation in case of C2 and C3 contingency for base case scenarios. It works on the ideal mode providing optimal energy arbitrage for all the contingency cases. There is a limit in power provided during the later hours in the case of C5 and C6 contingency. During C2 and C3 contingency, the ESS is not operating in discharge mode for the base case scenario. ESS operates between 15 to 20 MW in case of contingency scenario corresponding to the base case operation during C1, C4, C5, and C6 contingency. Non-operation of the ESS in discharge mode during the base case scenarios proves that the operation of ESS is susceptible to the line trips connecting the load to the generator sources. The uncertainty and the fluctuation of the load demand are reflected in the ESS operations.

Hence, the results show that the operation of the energy storage device is uniform when connected near the stochastic wind energy source as the operations are similar during generator trips. When the energy storage device is connected near the load on bus-3, we see less variation of its operation as compared to the previous cases. The overall F-statistic is similar to the one when the storage device was placed near the wind source. However, in Figure 4-11, we observe a substantial similarity in operation when the line connecting the load to the generation source trips due to a higher F-statistic in Table 4-2. There is more dissimilarity in operations in the case of generator trips. Thus, it is evident that the ESS operation, when placed near the load bus, is quite sensitive to trips in the power lines, connecting the bus to the generation source.

The analytics for ESS placement are always better when performed on a smaller grid as done in [25], where the respective net value is compared for different locations in the grid. When, ESS is located near the controlled generation source, it works in extreme modes with lower sensitivity to individual line trips and higher sensitivity to the tripping of generators, especially with high ramping capacity. Uniformity in energy storage operations is observed when ESS is placed in bus 2, near the stochastic renewable energy source. In addition to this, capacity of the ESS is enhanced to provide power during the respective

charging and discharging modes in the base case. When the energy storage device is located near the load bus, it is less sensitive to the generator trips and highly sensitive to the tripping of lines connecting the load bus to the generators. However, the operation is not much affected, when the transmission lines, which are not connected to the loads, is tripped. Therefore, the ESS operation is more robust in case of operational contingencies when it is placed near stochastic energy source.

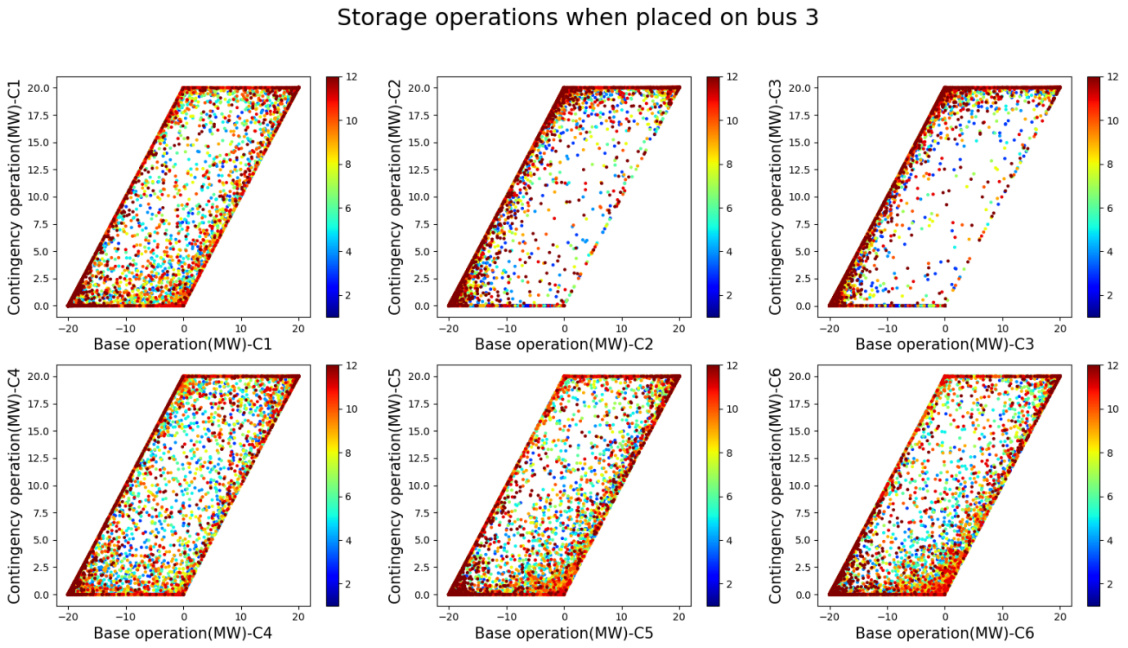

Figure 4-11: Energy storage operations when placed on bus-3 in the grid under various contingency scenarios. Colours represent hour of operation between 1-12 hours.

4.9.4 Conclusion

The significant research findings of this subchapter can be summarised as:

- When an energy storage device is located near the controlled generation source, it works in extreme modes with lower sensitivity to individual line trips and higher sensitivity to the tripping of generators, especially with high ramping capacity.
- When the energy storage device is located near the load bus, it is less sensitive to the generator trips and highly sensitive to the tripping of lines connecting the load bus to the generators.

- When the energy storage device is located near the stochastic renewable energy source, the operation is uniform with more similarity due to the generator trips and is recommended for placement.
- The energy storage operation is invariant to the trips of the lines, not connecting to the loads irrespective of its position in the grid.

Chapter 5 Statistics and Machine Learning for Stability and Resilience in Complex Transmission Power Network

In Chapter 3 and Chapter 4, the stability and resilience of the smart grid is studied on a smaller scale in the form of a LFC and optimal power flow problem. The common theme of the chapters is stability and resilience. As explained in Figure 2-1, we assume the generation demand balance problem is solved on a dynamic and steady state as we move on to larger networks. The results from smaller areas are not translatable on a larger network as the challenges are different. The frequency stability problem is based on transient models while voltage stability of the power network is from the steady state operation of the power network. The lens of the problem changes from micro level to macro size, hence the solution methodology will vary as well. The cascading of disturbances from smaller areas to large areas is a topic of future research.

In this chapter the concept of stability and resilience is introduced for large power network. In the previous chapters, the problem of generation demand balance is studied, which represents frequency stability problem on a dynamic scale. However, we as we move on to a larger power network, the problem of voltage stability becomes essential, as generation demand balance will not ensure power network stability. The joint consideration of frequency and voltage stability will be considered in the future studies. The relationship of the voltage stability of complex power network with the centrality measures is studied in this chapter using statistics and machine learning methods. Furthermore, mixed topological and electrical measure is utilized using spectral filters to identify the key nodes, if attacked, can cause instantaneous blackout.

5.1 Bayesian Regression Regression between Voltage Stability Index and Nodal Centrality Measures for Medium Sized Networks

Electrical node centrality for the power networks is an essential parameter to identify the critical nodes under attack. Topological analysis is vital for evaluating the network robustness while electrical characteristics have to be considered to make the analysis consistent for realistic power networks. However, the capacity limit of the power network changes under various nodal attacks. It is essential to find the relationship between the loading margin limit of the power network with

the node centrality features, so that appropriate measures can be considered to improve the robustness of the power networks. Thus, voltage stability index (VSI) is defined for every node, and its centrality features are modelled. The resilience problem of the power grid is studied in this subchapter by deriving a metric after removing nodes from the power network. The statistical relationship of the metric is explored with respect to electrical and topological centrality measures, where the latter can be utilized as a nodal attack model in a power network. Robust Bayesian regression is used to model the nodes responsible for a change in loading margin and causing grid blackout. The method has been validated on benchmark complex power networks like reduced Great Britain network, IEEE 57-bus and IEEE 118-bus systems.

Static voltage stability is essential for complex power networks incorporating a large share of renewable energy sources (RES). However, its estimation is a challenging task under network perturbation. Data mining methods can be readily utilized to predict voltage stability index. The regression problem has framed between the topological and electrical centrality measures with voltage stability margin. The motivation of the problem is to effectively predict the voltage stability margin (VSM) under topological and network parameter perturbation. The uncertainty of the VSM is also essential for different perturbations. Firstly, the linear and generalized linear models have been utilized, which gave poor results in training and testing. Hence, the Gaussian process gives excellent results in training and testing for specific kernels for different power networks. Secondly, the motivation of the subchapter is to formulate a digital twin for the power network from topological and electrical centrality measures. The commonly used method in digital twin in the research community is the Gaussian process, which accurately predicts the output mean and uncertainty.

Gaussian process-based prediction provides the mean and the uncertainty in the stability margin. Firstly, the critical network features responsible for voltage stability index are identified using the Bayesian feature selection technique. With the critical network features, we train the Gaussian process with the stability margin of the power network. We test the Gaussian process model to predict the voltage stability margin against topological perturbations like line trips and parametric line perturbation. The results are benchmarked on a large scale power network like IEEE 300 Bus, Texas, Great Britain and European power grids,

where the mean and uncertainty of the prediction for different kernel functions are used in the Gaussian process. Final results show that there is always a bias in the mean prediction of the stability margin for the critical nodes. Before we proceed the centrality measures are first defined.

5.1.1 Previous Works

The centrality measures of power networks are mainly utilized to analyze the network robustness to cascaded failure in an intentional attack [225]. The analysis of power networks on purely topological features, can be misleading, as it does not necessarily capture the complexity of the power grids. In many analyses, the centrality measures of the weighted power network are considered, utilizing the electrical and topological characteristics [226], [227].

Several indices of the power networks are introduced in [228] to identify the critical nodes in the skeleton network configuration which captures the topological and electrical characteristics of the power grid. Multi-criteria decision making (MCDM) strategies are leveraged using these features to identify the critical nodes in the network. The betweennness centrality [229]–[233] and its customized version with the line parameters [234]–[237] has been utilized in the analysis where the nodal and the power flow constraints are considered. Degree and weighted degree distribution [229], [230], [233]–[235] is also a common measure for studying the reliability. Others include shortest path length [229], [238], average path length [230], [237] characteristic path length [237] , eigen vector centrality [231], [232] and its weighted version [234], closeness centrality [230], [233], [238] and its electrical version [234], clustering coefficients [230], [234], [237]–[239].

The voltage stability index (VSI) is proposed in [240], [241] using the local voltage phasors, as measured by the phasor measurement units (PMUs). In [241], VSI based on Tellegen's theorem is proposed, which is simple, computationally tractable and easy to implement in a wide-area monitoring environment and the control centers. Various methods for VSI is mentioned in [242] based on the power network buses and branches. It has been analyzed while considering the power flow Jacobian matrix singularity [243], [244]. Some

investigations have been performed for static and dynamic voltage stability with the network connectivity structure like weighted load connectivity [245]–[247]. Thus we can consider that VSI is generally considered while incorporating some network parameter assumptions.

5.1.2 Contributions in this sub-chapter

5.1.2.1 Contributions for Medium Power Network

Firstly, for medium power networks, continuation power flow (CPF) technique is used to derive the voltage stability margin of the power networks. The measure is obtained for all the nodes, which are removed from the power grid, causing a change in network loading margin. The VSI, based on the local voltage measurements, as discussed in the previous literature, are not reliable enough to capture the power grid resilience in the case of a change in network topology. There are very few literatures available, which conduct a topological analysis of voltage collapse. In [248], theoretical insight is provided on the grid structure, which influences voltage collapse. However, the analysis fails near the voltage collapse points. The model has been validated on three-benchmark medium sized complex power networks viz. IEEE 57 bus, IEEE 118 bus systems and reduced Great Britain. The centrality measures for analysing VSI for the nodes is modelled along with the indices defined in [228]. Hence the main contributions in this subchapter can be summarized as:

- Voltage stability index of the power grid has been defined based on the relative change in the loading margin due to node removal.
- Robust Bayesian regression to find the dependencies of the network feature with VSI with the help of Hamiltonian Monte Carlo (HMC) sampling technique for the customized likelihood function defined for each node causing a blackout in the power network.

5.1.2.2 Contributions for Large Power Network

The centrality measures described in previous section are specifically for medium sized network having node size within 200. However, as we scale the analysis for larger power network having nodes more than 1000, all the centrality measures are to be considered for analysis.

Firstly, the critical centrality measures have to be indentified that influence power network voltage stability. In the previous works, the voltage stability index has only been analyzed with network structure while considering unweighted and weighted degree centrality measures [245]. New centrality measures have been defined in [249] by modifying the existing ones with the distance metric specifying the voltage-reactive power sensitivity. The critical centrality measures can be identified using a standard feature selection technique.

Once the key centrality features are identified, we train a Gaussian process for each power network using the key features and the stability index. The data mining methods for stability margin [183], [250] have not focused on the spatial and uncertainty aspects. The spatial aspects have been addressed in [251]. The probabilistic forecast of the voltage stability margin has been described in [252]. However, the analysis has been conducted on the overall network aspects rather at the nodal level. In our analysis, the spatial aspects are considered while incorporating the input centrality features and uncertainty is considered using Gaussian process regression. The model is trained on the entire dataset and tested on the features obtained from the perturbed network. The perturbation considered here is the modification of line parameters and transmission line trip. The mean and uncertainty of the predicted stability index are obtained for the perturbed network. One advantage of utilizing the Gaussian process as a digital twin method is the explainability of the features involved in prediction and the uncertainty. Hence we can summarize the contributions for large power network as:

- Identifying the critical centrality features which affect the voltage stability of the power network.
- Gaussian process model regression of the selected centrality features with the stability margin
- Analysis of the mean residuals and the uncertainty in predicting different kernels of the Gaussian process under parametric and topological perturbations.
- Benchmarking the results on IEEE 300 bus, European, Great Britain and Texas Power Network.

5.1.3 Nodal Centrality Measures

The power network can be considered as graph $\mathcal{G}$, having nodes (or buses) $\mathcal{V}$, edges (or branches) $\mathcal{E} \subset \mathcal{V} \times \mathcal{V}$, having complex edge weights $y_{ij} \in \mathbb{C}$. **A** represents adjacency matrix for graph $\mathcal{G}$. The power network has two types of buses: loads $\mathcal{L}$ and generators $\mathcal{G}$ where $\mathcal{V} = \mathcal{L} \cup \mathcal{G}$. Let us consider the cardinality of the set is defined by $n = |\mathcal{L}|$ and $m = |\mathcal{G}|$, where $n,m > 1$. We can associate a phasor voltage $U_i = V_i e^{j\Theta_i} \in \mathbb{C}$, where $V_i \geq 0$ being the voltage magnitude and $\Theta_i \in \mathbb{S}^1$, and complex power injections as $S_i = P_i + jQ_i$. The transmission lines are modelled as standard lumped parameter model Π-model, incorporating the inductive/capacitive shunts tap-changing transformers with line-charging capacitor [253]. The weights and topology are embedded within the bus admittance matrix $Y \in \mathbb{C}^{(n+m)\times(n+m)}$, which consists of $Y_{ij} = -y_{ij}$ and $Y_{ii} = -\sum_{j=1}^{n+m} y_{ij} + y_{\text{shunt},i}$, where $y_{\text{shunt},i}$ is the shunt element at bus *i*. The conductance matrix *G* and the susceptance matrix *B* is given by $G = \text{Re}(Y)$ and $B = \text{Im}(Y)$. For the transmission lines operating above 100 kV, the nature is highly inductive. In first case we conduct analysis on a smaller networks, hence we combine all the data set to study the overall relationship. The voltage level of the nodes are not an important criteria for the analysis. However, in the case of prediction of stability margin for large power networks, the voltage level of the nodes are very critical in the analysis. Hence the power network cases are considered as follows:

Table 5-1: The power networks that are considered here in the study. The table represents the number of generator nodes, load nodes and the voltage level of the load nodes

Cases	Case 300	Case2869 Pegase	ACTIVSG2000	GB Network

Parameters				
Load Nodes	231	2359	1456	1830
Generator Nodes	69	510	544	394
Base Voltage Levels (kV)	0.6,2.3,6.6,13.8, 66, 86, 115, 138, 230, 345	110, 150, 220, 380	13.2, 13.8, 18,20, 22, 24, 115, 161, 230, 500	6.6, 11, 22, 33, 132, 275,400

As observed in Table 5-1, we see four different power networks considered in the analysis. ACTIVSg2000 represents a synthetic 2000 bus case situated in the US state of Texas. The grid is synthetically designed to statistically represent the accurate Texas transmission line models [254]. Case2869 Pegase represents the European high voltage transmission network [255]. GB Network data is obtained from the National Grid Security and Quality of Supply Standard working report [256], [257] .Based on the graph of the power network, the network features are defined as:

5.1.3.1 Electrical Degree Centrality (EDC)

In the power network, the nodes having higher generation capacities and load demands are very critical. It represents a high amount of power going in and coming out of a node in the power network. Electrical degree centrality (EDC) for a power network having nodes *N* captures this aspect for node *i* as follows [258]:

$$I_{EDC_i} = \left(\sum_{j \in \Gamma(i)} A_{ij} \Big/ (N-1) \right) e^{-\rho}. \tag{156}$$

Here, $\rho = \left[\frac{\left(s_{G,i} + s_{L,i} \right)}{s_{G,\max}} - 1 \right]$, where $s_{G,i}$ and $s_{L,i}$ represents the generation and load capacity of the node *i,* while $s_{G,\max}$ represents the maximum generation capacity amongst the generators.

5.1.3.2 Electrical Closeness Centrality (ECC)

It is essential during a blackout that the restoration path of a power network contains less number of transmission lines and transformer branches, as it improves the restoration time with less charging capacitance in the transmission lines and reduces the possibility of over-voltage. Electrical closeness centrality (ECC) highlights this aspect of the power network [258], which is defined as:

$$I_{ECC}(i) = (N-1) \Big/ \sum_{j=1, j\neq i}^{N} d_{\min,ij}^{Q_C}, \tag{157}$$

where, $d_{\min,ij}^{Q_C}$ represents the minimum total capacitance of the transmission line between *i* and *j.*

5.1.3.3 Eigenvector Centrality (EVC)

Let us consider χ and $e = [e_1, e_2, \ldots, e_N]^T$ being the dominant eigenvalue and eigenvector for the $N \times N$ adjacency matrix $\{A_{ij}\}$ with *N* nodes. Thus from [258], we get:

$$\chi e_i = \sum_{j=1}^{N} A_{ij} e_j, \quad i = 1, 2, \ldots, N. \tag{158}$$

Hence, the eigenvector centrality (EVC) of the node can be defined as:

$$I_{EVC}(i) = \frac{1}{\chi} \sum_{j=1}^{N} A_{ij} e_j. \tag{159}$$

This index is essential for the importance of a node in terms of topological perspective.

5.1.3.4 Network Efficiency Centrality (NEC)

The network efficiency considering the electrical characteristics is given as:

$$E_B = \frac{1}{N(N-1)} \sum_{k,j \in V_N} \frac{1}{d_{\min,kj}^{X_L}}, \tag{160}$$

where, $d_{\min,kj}^{X_L}$ represents the shortest path with the minimum number of transmission lines and transformer branches to line reactance between node *k* and *j*. The V_N represents the set of nodes in the power network. Thus, network efficiency centrality (NEC) for node *i* is defined as the relative change in the efficiency after the respective node is removed. It is defined as:

$$I_{NEC}(i) = \left(E_B - E_{B,i}\right) / E_B, \tag{161}$$

where,

$$E_{B,i} = \frac{1}{(N-1)(N-2)} \sum_{\substack{k,j \in V_N \\ k \neq i, j \neq i}} \frac{1}{d_{\min,kj}^{X_L}}. \tag{162}$$

Here, $E_{B,i}$ represents the network efficiency after node *i* is removed.

5.1.3.5 Rate of Change of Spanning Trees (RST)

After removing specific key nodes from the graph, the number of spanning trees gets reduced hence making the network disconnected [258]. Hence change in spanning-tree (CST) centrality can be defined as the relative change in the number of spanning trees when node *i* is removed. It is defined as:

$$I_{CST}(i) = 1 - \left[\tau\left(\mathcal{G} - v_i\right) / \tau\left(\mathcal{G}\right)\right], \tag{163}$$

where, $\tau\left(\mathcal{G}\right)$ represents the number of spanning trees in the network graph *G* while $\tau\left(\mathcal{G} - v_i\right)$ represents the number of spanning trees with the node v_i removed.

5.1.3.6 Rate of Change of Network Closeness Centrality (NCC)

The importance of a node in the power network can be calculated as the relative change in the network closeness centrality (NCC) after node *i* is removed [258], as it highlights the impact of restoring a node in the power network by its contraction method [259]. It can be defined as:

$$I_{NCC} = 1 - \left(\psi_{ESC}\left(\mathcal{G}\right) / \psi_{ESC}\left(\mathcal{G}'_{vi}\right) \right), \tag{164}$$

where, the two functions are defined as:

$$\psi_{ESC}\left(\mathcal{G}\right) = \left(N-1\right) \Bigg/ \left(2 \sum_{1 \le k < j \le N} d_{\min,kj}^{X_L} \right), \tag{165}$$

$$\psi_{ESC}\left(\mathcal{G}'_{vi}\right) = \left(N_C - 1\right) \Bigg/ \left(2 \sum_{1 \le k < j \le N_C} d_{\min,kj}^{X_L} \right). \tag{166}$$

Here $\mathcal{G}'_{vi}$ is the new network after node *i* is removed from the original network $\mathcal{G}$ and functions $\psi_{ESC}\left(\mathcal{G}\right)$ and $\psi_{ESC}\left(\mathcal{G}'_{vi}\right)$ represents the network closeness centrality of the graph *G* and $\mathcal{G}'_{vi}$ respectively. N_C represents the number of nodes in $\mathcal{G}'_{vi}$.

5.1.3.7 Network Degree Centrality (NDC)

The connection of one node with the other nodes in the network is an averaged value given by:

$$NDC\left(i\right) = \frac{1}{N-1} \sum_{j \in \Gamma(i)} A_{ij} \ , \tag{167}$$

Here $\Gamma\left(i\right)$ represents the sets of nodes adjacent to node *i*.

5.1.3.8 Network Connectivity Index (NCI)

It represents the average fraction of generators connected by the load node.

$$NCI = \left\langle \frac{N_g^i}{N_g} \right\rangle_i \tag{168}$$

Where N_g represents the number of generators in the network.

5.1.3.9 Electrical Betweenness Centrality (EBC)

In the power flow analysis, the power flow might not always happen with the shortest route between the generator and the load. Electrical betweenness centrality (EBC) index is introduced in [260], which can be defined as:

$$I_{EBC}(i) = \sum_{g \in \Gamma_{SE}} \sum_{l \in \Gamma_{SK}} \left(\sum_{j \in \Gamma(i)} \left| f_{ij}^{gl} \right| \right), \tag{169}$$

where, $f_{ij}^{gl} = \left[\left(Z_{ig}^{eq} - Z_{il}^{eq} \right) - \left(Z_{jg}^{eq} - Z_{jl}^{eq} \right) \right] / \hat{x}_{ij}$ and $Z_{ig}^{eq} = \left(z_{ii} - z_{ig} \right) - \left(z_{ig} - z_{gg} \right)$. Here, Γ_{SE} and Γ_{SK} represent power and load set, respectively. f_{ij}^{gl} represents the power transferred between node g and node l with the transmission line connecting nodes *i* and *j*. $\hat{x}_{ij}$ represents the reactance of the transmission line. $Z_{ig}^{eq}, z_{ig}, z_{ii}$ and z_{gg} represents equivalent, transfer impedance and driving point impedance between node *i* and *j*. This is calculated using the power transfer distribution factor, as defined in [260].

5.1.3.10 k-Core Centrality (COR)

The k-core is the largest subnetwork comprising degree nodes at least *k* [261]. This function computes the *k*-core for a given binary undirected connection matrix by recursively peeling off nodes with degree lower than *k* until no such nodes remain.

5.1.3.11 Clustering Coefficient (CC)

It is the fraction of triangles around a node signifying the fraction of the nodes neighbours that are neighbours to each other.

5.1.3.12 Flow Centrality (FC)

f_{ij} represents the portion of the flow between the links *i* and *j* [262] defined as:

$$\bar{C}_{ij} = \frac{\sum_{u=1}^{m} \sum_{v=1}^{n} f_{ij}^{uv}}{\sum_{u=1}^{m} \sum_{v=1}^{n} f_{\max}^{uv}}. \tag{170}$$

The visualization of the described network features are shown in Figure 5-1 and Figure 5-2. If we consider smaller networks like GB Reduced Network, IEEE 57

Bus and IEEE 118 Bus, only fewer centrality measures are needed to be computed as shown in Figure 5-1. However for larger networks, the analysis has to be extended to a large set of centrality measures as described before. The rate of change of spanning trees is not applicable for large networks.

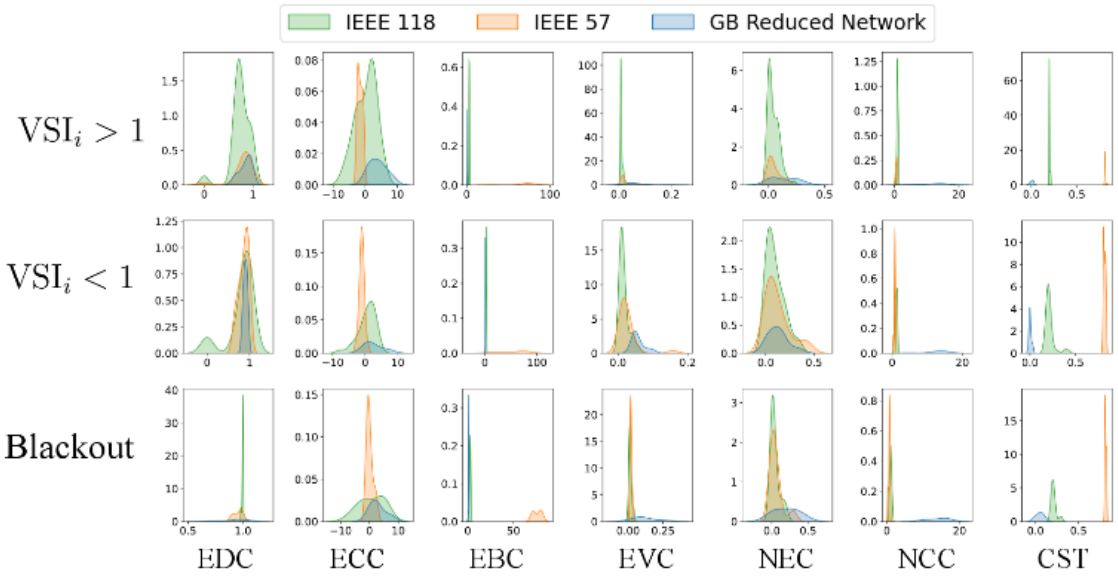

Figure 5-1 Univariate distribution of the node centrality measures for the three benchmark power networks: reduced GB network, IEEE 57 and IEEE 118 bus system with different VSI categories. (EDC- Electrical Degree Centrality, ECC- Electrical Closeness Centrality, EBC- Electrical Betwenness Centrality, EVC-Eigen Vector Centrality, NEC-Network Efficiency Centrality, NCC-Network Closeness Centrality, CST-Change in Spanning Trees).

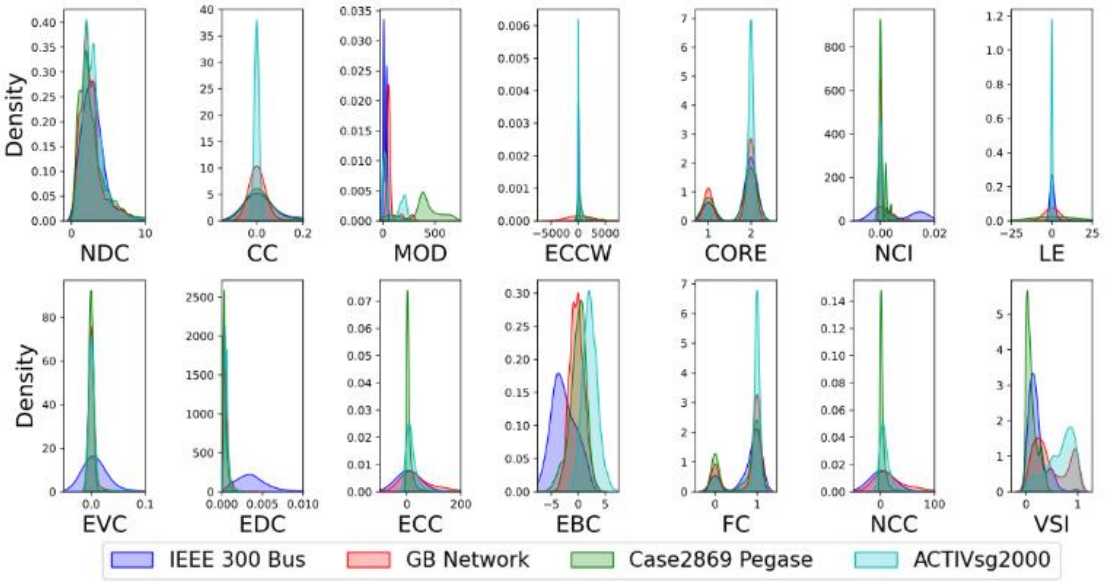

Figure 5-2: Univariate plot of all the complex network features along with voltage stability margin for IEEE 300 Bus system, GB Network, Case2869 Pegase and ACTIVSg2000

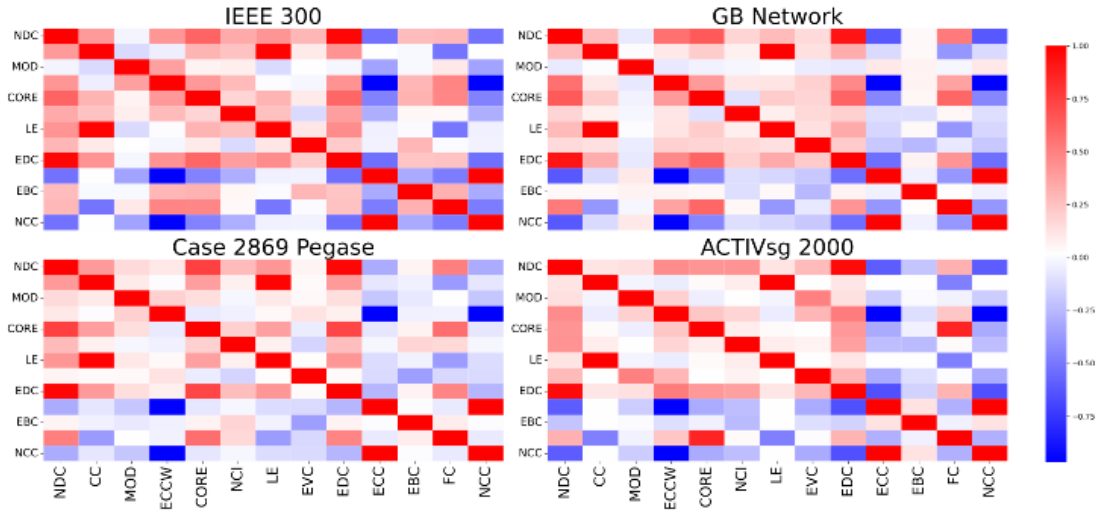

Figure 5-3: Pearson Correlation coefficient between the complex network features used for Bayesian feature selection for different power network test cases

The centrality metrics, as shown in Figure 5-2 and Figure 5-3, like modularity (MOD), Weighted eccentricity (ECCW), local efficiency (LE) are considered for feature selection along with the other centrality measures described before. However, as we will see later, they do not play an active role in influencing the voltage stability margin. The complex network features used in this work are visualized as a univariate plot in Figure 5-2. Their correlation is obtained using

the Spearman coefficient using a heat map in Figure 5-3 to capture the relationship between the variables using a monotonic function.

As we observe in Figure 5-3, the NDC and EDC are highly correlated. EDC is a weighted version of NDC, modified using the generation and the load capacity in (167). However, as per the univariate plot in Figure 5-2, the distribution of EDC is more skewed than NDC due to the scaling of generation and load capacity factor ρ. However, as observed in Figure 5-3, we do not find a strong correlation between the degree centrality measures like EDC and NDC with the weighted betweenness centrality measure, unlike reported in previous literature [263], [264]. The low correlation can be primarily due to an unweighted network in the analysis in [263], [264]. Generally, the correlation between the centrality measures is lower for the unweighted network than the weighted ones. The correlation coefficient between the betweenness centrality and degree centralities is shown to be 0.47 in [263] for an unweighted power network. Hence, we can expect a much lower value, as observed in Figure 5-3.

Similarly, in Figure 5-2, we have also observed a strong relationship between NCC and ECC, linked to closeness centrality. This strong relationship is similar to the closeness centrality and current flow closeness centrality in [263]. The relative distribution of the closeness centrality does not change even with the removal of nodes. Similarly, a strong correlation is also observed between the clustering coefficient and the *k*-core of the network, suggesting that nodes with similar degree distribution forms cluster of triangles. A similar relationship is also evident from one of the modes of the *k*-core centrality distribution in Figure 5-2. The right mode of *k*-core resembles the univariate distribution of the clustering coefficient.

5.1.4 Voltage Stability Index

The computation of voltage stability index is discussed for both smaller and large power networks. In small power networks, the index is computed from continuation power flow. However, computing the CPF becomes infeasible for large power network, especially with change in network topology.

5.1.4.1 Computing the Voltage Stability Index for Smaller Power Network

As per the schematic shown in Figure 5-5 to compute the index, the first task is to find the loading margin of the power network, which is found by solving the continuation power flow or CPF as given in [265]. It involves the solution of the following equation to find λ which is given as:

$$f(x,\lambda) = g(x) - \lambda b = 0, \tag{171}$$

where, $g(x) = 0$, represents the power flow solution of the *n* number of nonlinear algebraic equations, where *n* represents the number of buses in the power network and *b* is represented by the perturbation in the power network to change the base case scenario $\left(P^{j}_{\text{base}}, Q^{j}_{\text{base}}\right)$ to a given target $\left(P^{j}_{\text{target}}, Q^{j}_{\text{target}}\right)$ for the j^{th} bus. It is represented as $b = \begin{bmatrix} P^{j}_{\text{target}} - P^{j}_{\text{base}} \\ Q^{j}_{\text{target}} - Q^{j}_{\text{base}} \end{bmatrix}$. This is performed by modifying the load demand and the generation at each bus, respectively. The parameter λ signifies the amount of load demand that can be increased before the voltage collapse of the network occurs. It also signifies how far the power system is from voltage failure, which is obtained by finding the bifurcation point of the nonlinear algebraic equation of the power balance equation as given in (171). The parameterization of (x,λ) in (171) helps in quantifying the solution obtained between successive iterations. It is quantified using the parameter σ which is a continuation step-size parameter. Pseudo-arc length parameterization is used in [266], where the solution $\left(x^{j+1}, \lambda^{j+1}\right)$ is constrained to lie on the hyperplane of the tangent of $\left(x^{j}, \lambda^{j}\right)$ which is represented as:

$$p^{j}(x,\lambda) = \left(\begin{bmatrix} x \\ \lambda \end{bmatrix} - \begin{bmatrix} x^{j} \\ \lambda^{j} \end{bmatrix} \right)^{T} \bar{z}^{j} - \sigma^{j} = 0. \tag{172}$$

Here, $\bar{z}^{j}$ represents the normalized tangent vector of the solution $\left(x^{j}, \lambda^{j}\right)$ and σ^{j} is the adaptive step size parameter.

When i^{th} node is removed as shown in Figure 5-4, the topology of the network changes with the change in the admittance matrix constituting the power flow which gets reflected in the new power flow equation.

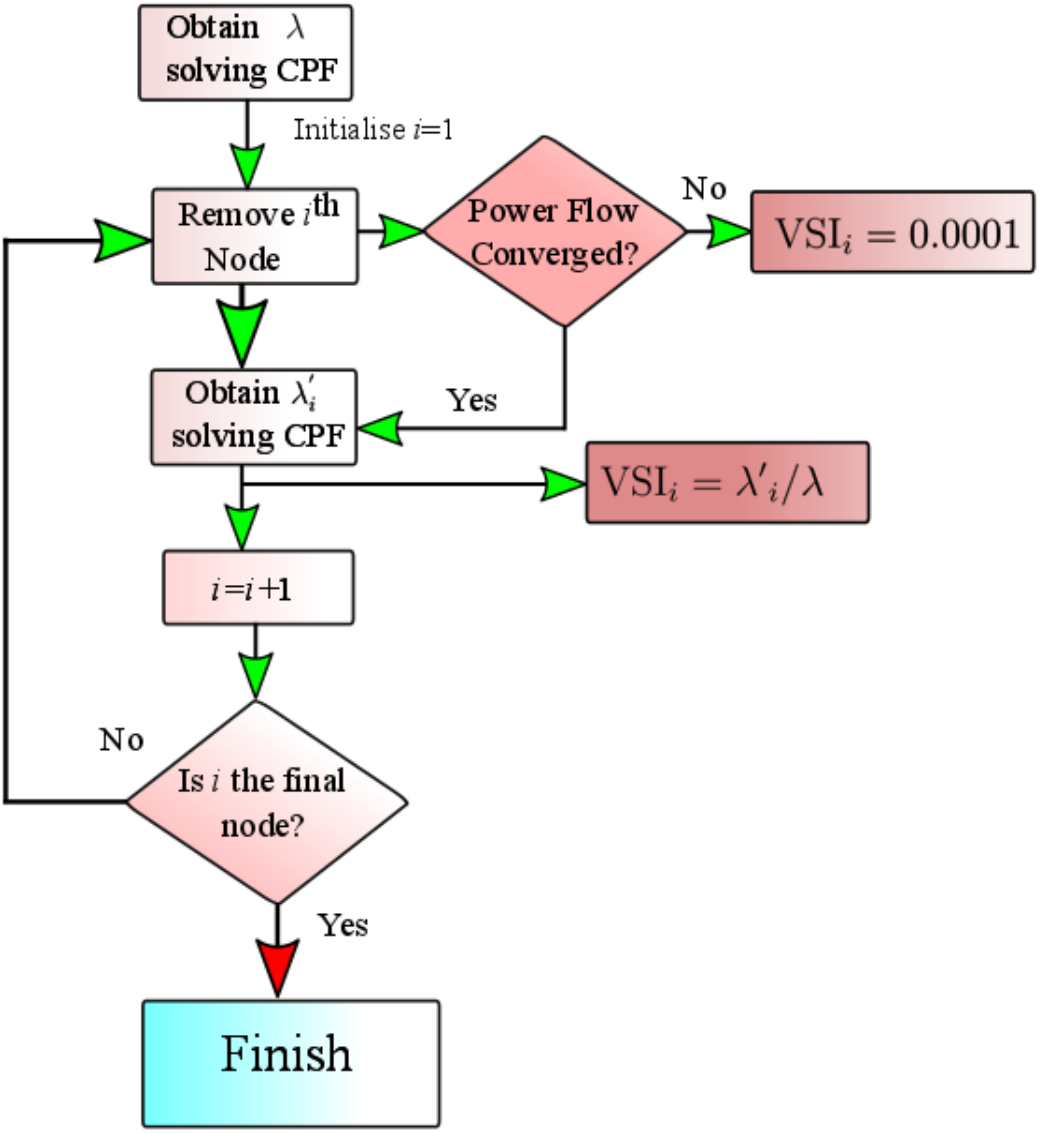

Figure 5-4: Schematic to calculate VSI for all the nodes in the power network.

Hence, in order to find the new loading margin limit λ', we can rewrite equation (171), as:

$$f'(x,\lambda) = g'(x) - \lambda'_i b' = 0. \tag{173}$$

When i^{th} node is removed and if the power flow $g'(x) = 0$ is not satisfied, hence (173) cannot be solved. Thus, the corresponding i^{th} node is very critical and hence a low value of stability index is allotted to that node as shown in Figure 5-4. After

solving (173), we obtain a new steady-state loading margin λ_i' for the i^{th} node. Hence, we define the voltage stability index of that particular node as:

$$\mathrm{VSI}_i = \begin{cases} 0.001 & \text{if } g'(x) = 0 \text{ does not converge,} \\ \lambda_i'/\lambda & \text{if } g'(x) = 0 \text{ converges.} \end{cases} \tag{174}$$

If $\mathrm{VSI}_i > 1$ then, the loading margin limit of the network increases. Similarly, if $\mathrm{VSI}_i < 1$, the network can handle smaller perturbations and the network stability decreases. A smaller value of VSI_i indicates that *i* is a critical node of the network, and removing it can cause a network-wide blackout. The parameters λ ,λ' are obtained by running the CPF routine in MATPOWER [267] for three different benchmarks power networks. The data for the reduced GB network is obtained from [257]. The nodes signifying the increase and decrease in loading margin of the network, along with the ones leading to complete blackout are shown in Figure 5-5. It is observed that the nodes which are topologically adjacent to each other have similar VSI characteristics.

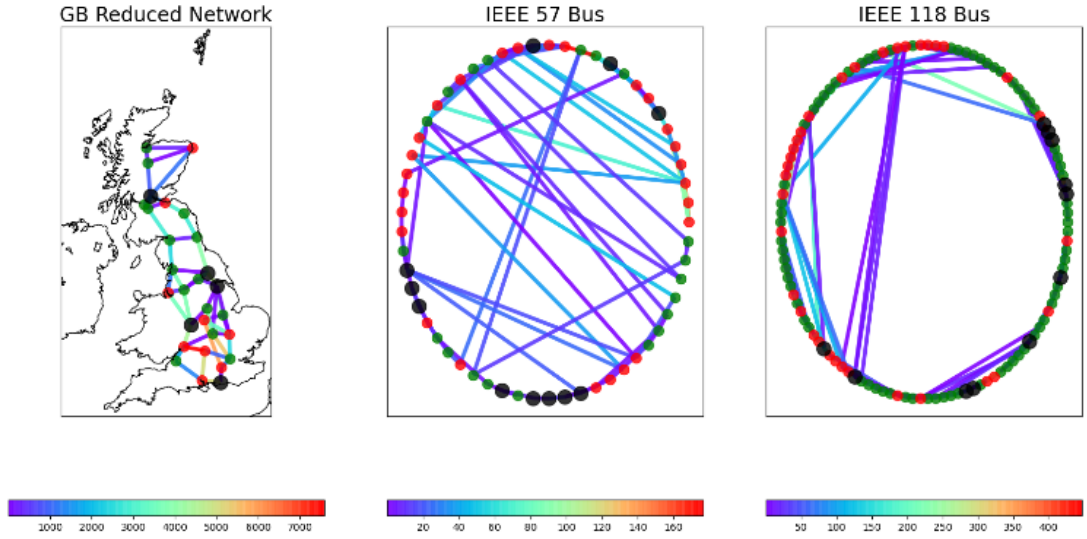

Figure 5-5: Voltage stability index obtained for the complex power networks for GB-reduced network, IEEE 57 bus and IEEE 118 bus systems. Meaning of the colors are as follows: Red- $\mathrm{VSI}_i < 1$(Decrease in loading margin), Green- $\mathrm{VSI}_i > 1$(Increase in loading margin), Black- $\mathrm{VSI}_i = 0.001$(complete blackout). The edges represent the active power flow between the nodes with the colourmap signifying its magnitude.

5.1.4.2 Voltage Stability Margin for Larger Power Networks

The voltage stability margin for the medium-sized power network lies in computing the loading margin of the modified power network using continuation power flow (CPF) techniques. However, as the size of the power network increases, it becomes computationally infeasible to evaluate the loading margin of the modified power network using CPF. Hence a metric has been utilized using the open circuit voltage of the power network while satisfying the assumptions stated in [248]. In this metric, only the power flow of the original network is computed along with open circuit voltage which is computationally feasible for larger power networks.

The definition of the voltage stability margin of the larger power network is dependent on the assumptions and properties of the susceptance matrix B. Let us consider that the power network does not have any phase-shifting transformer and series compensators for the nodes $i, j \in \mathcal{V}$. Hence we can state the following symmetry and sign structure properties of the susceptance matrix [268]:

- Symmetry: $B_{ij} = B_{ji}$.
- Sign: $B_{ij} \geq 0$ with $B_{ij} > 0$ if $\{i, j\} \in \mathcal{E}$.

The susceptance matrix B can be partitioned according to loads and generators:

$$B = \begin{bmatrix} B_{LL} & B_{LG} \\ B_{GL} & B_{GG} \end{bmatrix}. \tag{175}$$

The submatrices within the partitioned susceptance matrix have the following assumptions:

Assumption 1: The (negative) susceptance matrix $-B_{LL} \in \mathbb{R}^{n \times n}$ is a non-singular M-matrix.

It is applicable in practical power networks [269], and the property is satisfied due to the absence of line charging and shunt capacitors due to the dominance of the diagonal elements [270].

Assumption 2: The subgraph of $G(\mathcal{V},\mathcal{E},B)$ *formed by the load nodes* $\mathcal{L}$ *are connected.*

Assumption 3: The power angles are constant such that $|\theta_i - \theta_j| \leq \gamma$*, for some value* $\gamma \in [0, \pi/2[$ *for all the branches* $\{i,j\} \in \mathcal{E}$ *of the network.*

In a practical network, the value of γ considered is 5^{o}. The effective susceptance matrix can be defined by grouping the original line susceptances B_{ij} along with the power angle terms $\cos(\theta_i - \theta_j)$. Hence, we can write the power flow equations as:

$$Q_i + V_i \mathcal{I}_{\text{shunt},i} = -\sum_{j=1}^{n+m} V_i B_{ij} V_j \text{ for } i \in \mathcal{L}. \tag{176}$$

We can write the reactive power flow equation (176) by rearranging the susceptance matrix *B* in terms of load nodes as:

$$Q_L + [V_L]\mathcal{I}_{\text{shunt}} = -[V_L](B_{LL}V_L + B_{LG}V_G). \tag{177}$$

The equation in (177) can be rearranged to be written as,

$$Q_L = -[V_L]B_{LL}(V_L - V_L^*), \tag{178}$$

where, V_L^* is the open-circuit voltage at the load node defined as:

$$V_L^* = -B_{LL}^{-1}(B_{LG}V_G + \mathcal{I}_{\text{shunt}}). \tag{179}$$

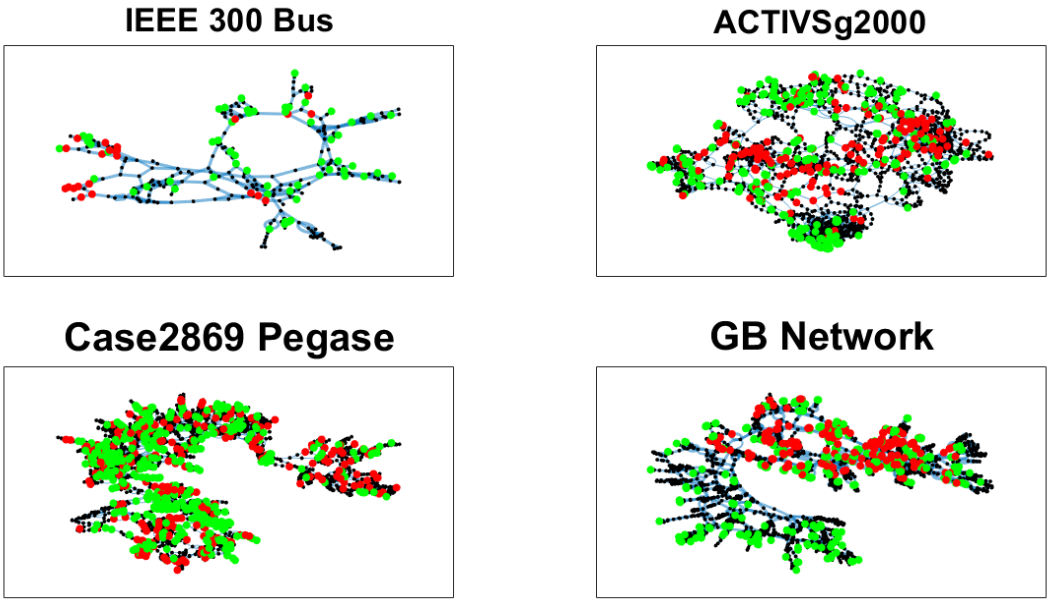

Figure 5-6: The representation of the power networks in forced layout, with the node colours representing the characteristics. Black- Generators Red- Critical nodes with higher voltage stability margin (top 10 percent) Green- Nodes with lower voltage stability margin

The concept of open-circuit voltage comes into play where the constant power load is open-circuited, which means $Q_L = 0$. Voltage stability margin states how much the voltage at the load end changes once it is fully loaded. It is defined as:

$$\text{VSM}_i = \left(V_i - V_L^*\right) \Big/ V_L^* . \text{ for } i \in \mathcal{L} . \quad (180)$$

Since the value of V_L^* is strictly greater than 0, the value of VSM_i lies between 0 and 1. The measure in (180) used to validate the new measure derived in [248] which predicts the voltage collapse in complex power networks. The V_i in (180) is obtained after solving the power flow equation for a given power network.

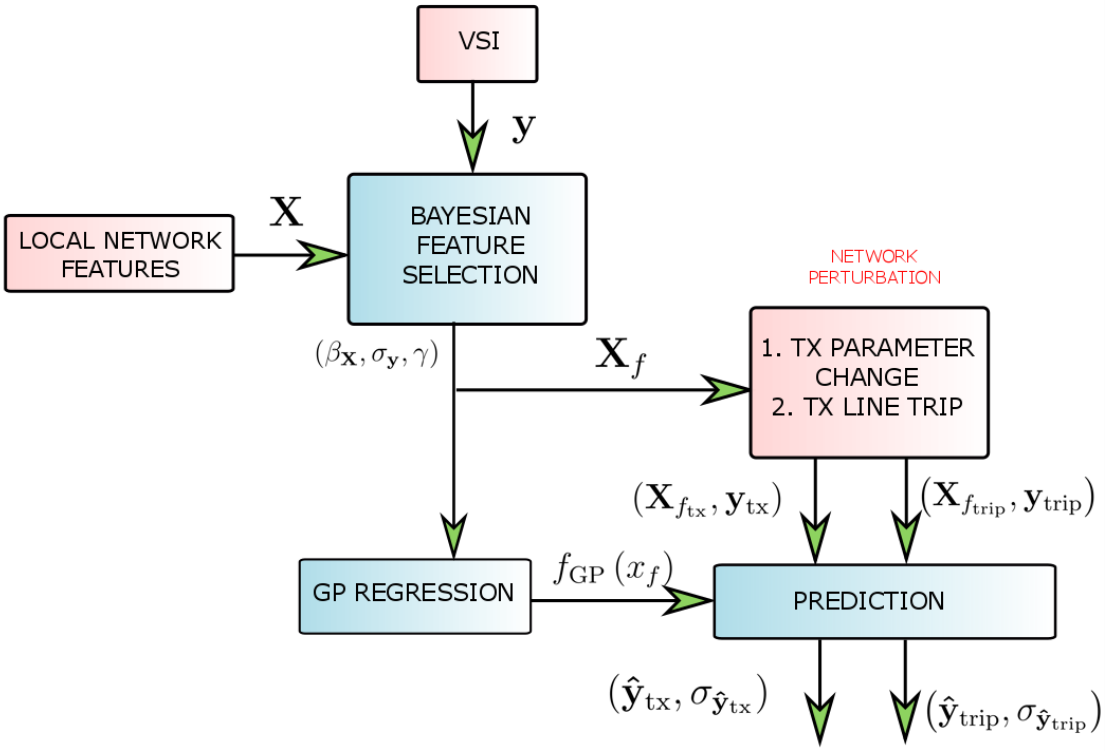

Figure 5-7: Schematic for the feature selection, training the Gaussian process model with local network features and voltage stability margin. The schematic also describes the prediction of the voltage stability index

After the voltage stability margin are computed for the smaller and larger power networks we fit the statistical model to find the relationship between the index and centrality measures. For smaller power networks, we fit a Bayesian model as we have smaller number of data with high number of outliers which cannot be computed. For the larger power networks, we select key centrality measures and predict the mean and uncertainty of the VSM using Gaussian process. The mean and uncertainty is computed for the perturbed network as shown in Figure 5-7.

As per the schematic in Figure 5-7 fit a GP model between features $\mathbf{X} = \{\mathbf{x}_{ij}\}$ where *i* represents the node number and *j* represents the local network feature. Voltage stability margin is indicated by $\mathbf{y}$. First, we find the optimal number of features $\mathbf{X}$ using a Bayesian feature selection technique. The Bayesian feature selection technique is selected because of two reasons. Firstly, it efficiently finds out the features without computing all the possible models, i.e. 2^p, *p* represents the total number of features used. The computation is faster than

the existing feature selection problems in regression. Secondly, the Bayesian feature selection is based on the linear equation:

$$\mathbf{y} = \beta\mathbf{x} + \varepsilon\,, \tag{181}$$

The linear form (181) is also used in the Gaussian process, which is used later for building the model. Hence top features obtained from Bayesian feature selection can be used directly to build a Gaussian process predictor $f_{\text{GP}}\left(x_f\right)$. We test the model on the testing dataset obtained after network perturbations. In one case, it is $\left\{\mathbf{X}_{\text{tx}}, \mathbf{y}_{\text{tx}}\right\}$ obtained after perturbing one of the transmission line parameters. In the following case, we have $\left\{\mathbf{X}_{\text{trip}}, \mathbf{y}_{\text{trip}}\right\}$ obtained after tripping the line carrying the most reactive power. After we evaluate the model, we obtain the mean and uncertainty for the cases as $\left(\hat{\mathbf{y}}_{\text{tx}}, \sigma_{\hat{\mathbf{y}}_{\text{tx}}}\right)$ and $\left(\hat{\mathbf{y}}_{\text{trip}}, \sigma_{\hat{\mathbf{y}}_{\text{trip}}}\right)$.

5.1.5 Statistical and Machine Learning Methods

Since the VSI defined in (174) has lower number of data points and in some cases the values are outliers. Hence, we need to fit robust Bayesian regression for the analysis.

5.1.5.1 Robust Bayesian Regression with Custom Likelihood

It is crucial to find out the relationship between the defined node centrality measures defined before with the VSI defined in the previous section. As we see in (174), for some of the nodes the VSI_i is low, leading to a complete blackout. It is essential to model these nodes from their respective node centrality measures. These values are modelled as an outlier, and the robust regression model is fitted. It is done by placing a *t*-distribution prior to the observed data [271] and sampling the posterior accordingly. However, as we see in Figure 5-5, it is difficult for the *t*-distributed priors to capture the nodes which have similar outlier values. Hence it is vital for customizing the likelihood to label the network nodes causing a complete network blackout when node is removed [272]. Those observed indices are modelled with a binary indicator, to segregate them from the normal nodes where we get a definitive VSI. The outlier binary parameter is modelled with larger deviations from the usual Gaussian noise estimates which are

generally known as “sigma clipping” [273]. Let us consider the VSI with the centrality measures as

$$\text{VSI} = \boldsymbol{\beta}^T \varkappa, \tag{182}$$

where, $\varkappa = \begin{bmatrix} I_{EDC} & I_{ECC} & I_{EBC} & I_{EVC} & I_{NEC} & I_{NCC} & I_{CST} \end{bmatrix}^T$ and $\boldsymbol{\beta} = \begin{bmatrix} \beta_1 & \beta_2 & \dots & \beta_7 \end{bmatrix}$. There are *N* nodes with the binary integers q_i for each nodes, where it is zero if the node causes a blackout and one converges. Prior probability $\mathcal{P}_b$ is set for each node which are modelled. $\left(\Upsilon_b, \vee_b\right)$ represents the mean and variance of the VSI of critical nodes. Hence, we obtained $(N+3)$ extra parameters which are later marginalized to obtain $\boldsymbol{\beta}$ at the end with the observed I data. Hence, we can write the likelihood function as:

$$\begin{aligned} \mathcal{L} &= p\left(\left\{\text{VSI}_i\right\}_{i=1}^N \middle| \boldsymbol{\beta}, \left\{q_i\right\}_{i=1}^N, \Upsilon_b, \vee_b, I\right) \\ &= \prod_{i=1}^N \left[p_{\text{fg}}\left(\left\{\text{VSI}_i\right\}_{i=1}^N \middle| \boldsymbol{\beta}, I\right)\right]^{q_i} \left[p_{\text{bg}}\left(\left\{\text{VSI}_i\right\}_{i=1}^N \middle| \Upsilon_b, \vee_b, I\right)\right]^{[1-q_i]}, \end{aligned} \tag{183}$$

where, $p_{\text{fg}}(.)$ and $p_{\text{bg}}(.)$ represent the distribution from where the VSI for the non-blackout and blackout nodes are sampled. In order to separate the different nodes in $\left\{q_i\right\}_{i=1}^N$, the binomial probability distribution function (pdf) $\mathcal{P}_b$ is used as:

$$\begin{aligned} p\left(\boldsymbol{\beta}, \left\{q_i\right\}_{i=1}^N, \mathcal{P}_b, \Upsilon_b, \vee_b \middle| I\right) &= p\left(\left\{q_i\right\}_{i=1}^N \middle| \mathcal{P}_b, I\right) \cdot p\left(\boldsymbol{\beta}, \mathcal{P}_b, \Upsilon_b, \vee_b \middle| I\right) \\ p\left(\left\{q_i\right\}_{i=1}^N \middle| \mathcal{P}_b, I\right) &= \prod_{i=1}^N \left[1-\mathcal{P}_b\right]^{q_i} \mathcal{P}_b^{[1-q_i]}. \end{aligned} \tag{184}$$

Applying this principle in the likelihood function in (183) yields:

$$\begin{aligned} \mathcal{L} = \prod_{i=1}^N & \left[\frac{1-\mathcal{P}_b}{\sqrt{2\pi\sigma_{VSI_i}^2}} \exp\left(-\frac{\left(VSI_i - \beta x_i\right)}{\sigma_{VSI_i}^2} \right) \right] \\ & + \left[\frac{\mathcal{P}_b}{\sqrt{2\pi\left[V_b + \sigma_{VSI_i}^2\right]}} \exp\left(-\frac{\left[VSI_i - Y_b\right]^2}{2\left[V_b + \sigma_{VSI_i}^2\right]} \right) \right]. \end{aligned} \tag{185}$$

In order to find the probability distribution of $\boldsymbol{\beta}$ from other parameters, marginalization is done accounting for the covariance and other parameters $\left(\mathcal{P}_b, \Upsilon_b, \vee_b\right)$ given as:

$$p\left(\boldsymbol{\beta}\middle|\left\{\mathrm{VSI}_i\right\}_{i=1}^{N}\right)=\int \mathrm{d}\left\{q_i\right\}_{i=1}^{N}\mathrm{d}\mathcal{P}_b\mathrm{d}\Upsilon_b\mathrm{d}\vee_b p\left(\boldsymbol{\beta},\left\{q_i\right\}_{i=1}^{N},\Upsilon_b,\vee_b,I\right). \tag{186}$$

Numerical methods for Markov Chain Monte Carlo (MCMC) sampling are to be used next to find the high dimensional marginal distributions. Hamiltonian Monte Carlo sampler [274] has been used here, which is useful in high dimensional inference. The numerical results have been explained in the next section. In case of larger power networks in Figure 5-5, which consists of a large of centrality measures, it is essential to select a few subset of centrality measures which highly influences the voltage stability margin.

5.1.5.2 Bayesian Feature Selection

The role of Bayesian feature selection given the dependant variable Υ along with a set of potential predictors $\mathbf{X}=\left\{X_1,\ldots,X_p\right\}$ to select the best fit model of the form

$$\mathcal{Y}=X_1^*\beta_1^*+\ldots+X_q^*\beta_q^*. \tag{187}$$

where, $\left\{X_1^*,\ldots,X_q^*\right\}$ is the best-selected subset out from $\mathbf{X}$. Model selection procedures AIC (Akaike Information Criteria) and BIC (Bayesian Information Criteria and sequential methods like stepwise regression are based on statistical significance. However, Bayesian feature selection involves embedding the regression setup in the hierarchical Bayes Normal mixture model to infer the latent variable responsible for selecting the optimal number of subsets [275] in a probabilistic sense. One advantage of stochastic search using Gibbs sampling is to avoid computing over 2^p models called regimes, the set of possible choices are sampled directly from the posterior distribution. The latent variables suggest how frequently the predictors appear in the Gibbs samples. If we consider the regression setup, as

$$p\left(\mathbf{Y}\middle|\beta,\sigma^2\right)\sim\mathcal{N}\left(\mathbf{X}\boldsymbol{\beta},\sigma^2 I\right), \tag{188}$$

Where, $\boldsymbol{\beta}=\left[\beta_1,\ldots,\beta_p\right]$. If a certain number of predictors are not incorporated in

the model, then corresponding β is equal to 0. If we consider a mixture of Gaussian distributed prior, we can write as:

$$p\left(\beta_i|\gamma_i\right) \sim (1-\gamma_i)\mathcal{N}\left(0,\sigma^2 V_{1k}\right)+\gamma_i \mathcal{N}\left(0,\sigma^2 V_{2k}\right). \quad (189)$$

Where $V_{1k} < V_{2k}$ so that β_i effectively close to zero in case $\gamma_i = 0$. The prior specification of γ which has a cardinality of 2^{p+1} models where *p* represents the number of predictors and the additional term is due to the inclusion of intercept. We use a Bernoulli model for γ, which suggests

$$P\left(\gamma_i = 1\right) = 1 - P\left(\gamma_i = 0\right) = p_i. \quad (190)$$

We can represent (190) in the form of g_k as

$$\gamma_k \sim \text{Bernoulli}\left(g_k\right). \quad (191)$$

The third part of the hierarchical model specifies the prior on the residual variance σ^2. Hence inverse Gamma prior is utilized:

$$p\left(\sigma^2|\gamma\right) \sim \text{IG}\left(A,B\right). \quad (192)$$

Where A and B are the shape factor. The primary aim is to obtain the posterior $f\left(\gamma|\mathbf{Y}\right) \propto f\left(\mathbf{Y}|\gamma\right) f\left(\gamma\right)$, containing the information concerning variable selection. Here we consider $\left(\beta,\sigma\right)$ being independent of the data, being dependent on each other. Hence the task is to compute the fully conditional posterior distribution of the probability *k* to be incorporated in the model:

$$P\left(\gamma_k = 1|\beta,\sigma^2,\gamma_{\neq k}\right) \propto g_k \mathcal{N}\left(\beta_k;0,\sigma^2 V_{1k}\right). \quad (193)$$

Gibbs sampler is used to compute the posterior once the priors are specified, and models are defined [275]. The characteristics of β and σ^2 are computed along with the posterior estimates of g_k.Gibbs sampler generates the sequence $\boldsymbol{\gamma} = \left\{\gamma_1,\ldots,\gamma_m\right\}$ which converges to the distribution $\boldsymbol{\gamma} \sim \breve{f}\left(\boldsymbol{\gamma}|\mathbf{Y}\right)$. The given sequence will contain the information relevant to variable selection. Stochastic

Search Variable Search (SSVS) implements the Gibbs sampler to generate the sequence of γ along with β and σ^2. The γ sequence is initialized with 1s while β and σ^2 is initialized based on the least square estimate of (188). The vector of latent variables γ^j is obtained by sampling consecutively from the conditional distribution:

$$\gamma_i^j \sim \breve{f}\left(\gamma_i^j \middle| \mathbf{Y}, \beta^j, \sigma^j, \gamma_{(i)}^j\right) = \breve{f}\left(\gamma_i^j \middle| \beta^j, \sigma^j, \gamma_{(i)}^j\right), \tag{194}$$

Where $\gamma_{(i)}^j = \left\{\gamma_i^j, \ldots, \gamma_{i-1}^j, \gamma_{i+1}^{j-1}, \ldots, \gamma_p^{j-1}\right\}$. Since (194) does not depend upon $\mathbf{Y}$, the simplification causes a computational improvement and faster convergence to the sequence of $\{\gamma_1, \ldots, \gamma_m\}$. The distribution in (194) is Bernoulli with the density

$$P\left(\gamma_j^j = 1 \middle| \beta^j, \sigma^j, \gamma_{(i)}^j\right) = a/(a+b), \tag{195}$$

where,

$$a = \breve{f}\left(\beta^j \middle| \gamma_{(i)}^j, \gamma_i^j = 1\right) \times \breve{f}\left(\sigma^j \middle| \gamma_{(i)}^j, \gamma_i^j = 1\right) \breve{f}\left(\gamma_{(i)}^j, \gamma_i^j = 1\right),$$

and $b = \breve{f}\left(\beta^j \middle| \gamma_{(i)}^j, \gamma_i^j = 0\right) \times \breve{f}\left(\sigma^j \middle| \gamma_{(i)}^j, \gamma_i^j = 0\right) \breve{f}\left(\gamma_{(i)}^j, \gamma_i^j = 0\right)$.

5.1.5.3 Gaussian Process

Gaussian process is the collection of random variables with a joint Gaussian distribution [276]. Let us consider a training set $\mathcal{D} = \left\{(\mathbf{x}_f, y_i) \middle| i = 1, \ldots, n\right\}$ that $\mathbf{x}_f$ denotes the input vector with dimensions D obtained after the feature selection and y denotes scalar output and target. The column vector input for all cases is formulated in a design matrix X_f whose dimensions are $D \times n$. Here the targets are collected in the vector $\mathbf{y}$. Gaussian process is specified by its mean $m(\mathbf{x})$ and covariance function $k(\mathbf{x}, \mathbf{x}')$. From the function space point of view, we define the Gaussian process as $f(\mathbf{x})$ such that,

$$y(\mathbf{x}) \sim \mathcal{GP}\left(m(\mathbf{x}), k(\mathbf{x}, \mathbf{x}')\right), \tag{196}$$

Where, $\mathbb{E}\left[y(\mathbf{x})\right] \sim m(\mathbf{x})$ and $\text{Cov}\left[y(\mathbf{x}), y(\mathbf{x}')\right] = k(\mathbf{x}, \mathbf{x}')$. The general convention is to use $m(\mathbf{x}) = 0$ or $m(\mathbf{x}) = \beta^T \mathbf{x}$. The property satisfies the condition where $(y_1, y_2) \sim \mathcal{N}(\boldsymbol{\mu}, \boldsymbol{\Sigma})$, with the properties $y_1 \sim \mathcal{N}(\boldsymbol{\mu}_1, \boldsymbol{\Sigma}_1)$, $\boldsymbol{\Sigma}_1$ being the submatrix of $\boldsymbol{\Sigma}$. Let us consider $\mathbf{y} = f(\mathbf{x}) + \varepsilon$ which is of the same form used in Bayesian feature selection, where ε represents the additive independent identically distributed Gaussian noise having the variance σ_n^2, hence the prior on the noisy observations is given by:

$$\text{cov}\left(y_p, y_q\right) = k\left(x_p, x_q\right) + \sigma_n^2 \delta_{pq} \ , \tag{197}$$

or in the vectorial notation as $\text{cov}(\mathbf{y}) = K(\mathbf{X}, \mathbf{X}) + \sigma_n^2 I$. The δ_{pq} represents the Kronecker delta function if $p = q$ otherwise zero. The equation (197) is valid while considering the independent samples. Now let us consider the function defined at test inputs $\mathbf{x}_*$ as $\mathbf{f}_*$. If we incorporate the noise term σ_n^2 and write the joint distribution of the observed target values while considering the function $\mathbf{f}_*$ at the test locations as the prior, we can write as:

$$\begin{bmatrix} \mathbf{y} \\ \mathbf{f}_* \end{bmatrix} \sim \mathcal{N}\left(0, \begin{bmatrix} K(X, X) + \sigma_n^2 I & K(X, X_*) \\ K(X_*, X) & K(X_*, X_*) \end{bmatrix}\right). \tag{198}$$

If we derive the conditional distribution, we arrive at the equations for the Gaussian process regression as:

$$\mathbf{f}_* \big| X, \mathbf{y}, X_* \sim \mathcal{N}\left(\bar{\mathbf{f}}_*, \text{cov}(\mathbf{f}_*)\right). \tag{199}$$

where,

$$\bar{\mathbf{f}} = \mathbb{E}\left[\mathbf{f}_* \big| X, \mathbf{y}, X_*\right] = K(X_*, X)\left[K(X, X) + \sigma_n^2 I\right]^{-1} \mathbf{y},$$
$$\text{cov}(\mathbf{f}_*) = K(X_*, X_*) - K(X_*, X)\left[K(X, X) + \sigma_n^2 I\right]^{-1} K(X, X_*).$$

The inverse operation is generally conducted by converting the matrices via Cholesky decomposition. The covariance is a function of $r = |\mathbf{x} - \mathbf{x}'|$ then it is called isotropic. If *k* is a function of $|\mathbf{x} - \mathbf{x}'|$ and invariant to all the rigid motions,

they are called radial basis functions. A kernel is a function that maps a pair of inputs. If we have a set of inputs, $\{\mathbf{x}_i | i = 1,\ldots,n\}$ the Gram matrix K can be computed, where the entries are defined by $K_{ij} = k(\mathbf{x}_i, \mathbf{x}_j)$, k representing the covariance function and positive semi-definite. The squared exponential (SE) covariance function has the form

$$k_{\text{SE}}(r) = \exp\left(-\frac{r^2}{2l^2}\right), \tag{200}$$

Where, l is the characteristic length scale, where the mean number of level-zero crossings in a SE process is given as $(2\pi l)^{-1}$. This covariance function is infinitely differentiable, where the GP with this covariance function has the mean square derivative of all the orders. However, the strong smoothness assumptions might be unrealistic for modelling general physical processes. The Matern class of covariance functions are given by:

$$k_{\text{Matern}} = \frac{2^{1-\upsilon}}{\Gamma(\upsilon)}\left(\frac{\sqrt{2\upsilon}r}{l}\right)^{\upsilon} K_{\upsilon}\left(\frac{\sqrt{2\upsilon}r}{l}\right). \tag{201}$$

Where υ and l represents positive parameters, K_{υ} is a modified Bessel function. The scaling is performed so that $\upsilon \to \infty$ and we obtain the SE covariance function as defined above. In the case of the Matern class of kernel, the function $f(x)$ is k-times mean square differentiable, which is possible if $\upsilon > k$. The function becomes simple when υ becomes half-integer, given by $\upsilon = \bar{p} + 1/2$, considering p to be a non-negative integer. The interesting variants used in machine learning are:

$$\begin{aligned} k_{\upsilon=3/2}(r) &= \left(1+\frac{\sqrt{3}r}{l}\right)\exp\left(-\frac{\sqrt{3}r}{l}\right), \\ k_{\upsilon=5/2}(r) &= \left(1+\frac{\sqrt{5}r}{l}+\frac{5r^2}{3l^2}\right)\exp\left(-\frac{\sqrt{5}r}{l}\right). \end{aligned} \tag{202}$$

For $\upsilon = 1/2$, the process becomes very rough. In order to find the optimal value of kernel parameters, the hierarchical model is utilized. The lowest level in the model is the parameters $\mathbf{w}$ that can be the linear model parameters or weights of the neural network. The upper level has kernel hyperparameters that control the distribution of the parameters at the bottom level. The marginal likelihood is maximized to obtain the value of the hyperparameters, as it is a trade-off between the model fit and model complexity, following the concept of Occams razor. The marginal likelihood computed for the data $\mathbf{y}$ having the parameters $\mathbf{X}$ and parameters θ in the model given as:

$$\log p\left(\mathbf{y}\middle|\mathbf{X},\theta\right) = -\frac{1}{2}\mathbf{y}^{\mathrm{T}}K_y^{-1}\mathbf{y} - \frac{1}{2}\log\left|K_y\right| - \frac{n}{2}\log 2\pi, \tag{203}$$

where $K_y = K_f + \sigma_n^2 I$, acting as the covariance matrix for the noisy targets $\mathbf{y}$. The log value is considered as it involves marginalization over the latent function. The three terms can be explained as:

- $\frac{1}{2}\mathbf{y}^{\mathrm{T}}K_y^{-1}\mathbf{y}$ contains the target term $\mathbf{y}$.
- $\frac{1}{2}\log\left|K_y\right|$ is the complexity penalty depending on the covariance function.
- $\frac{n}{2}\log 2\pi$ is the normalization constant.

The likelihood of the model fitting the data decreases monotonically with the increase in the length scale where the model becomes less flexible. If we try to maximize the value of marginal likelihood, the covariance matrix $\mathbf{K}$ inversion is needed. Bayesian optimization is used to find the kernel parameters while optimizing marginal likelihood [277].

5.1.6 Results and Discussion for Medium Power Network

The complex network measures discussed are obtained from the brain connectivity toolbox [278], and the graph and network functions in MATLAB. The nodal measures are plotted in Python package Seaborn [279] along with several categories of VSI for different power grids, shown Figure 5-5. We observe a distinct pattern in the change of the number of spanning trees for the three VSI

cases considering different power grid topologies. Distinctness is also observed in the case of EBC and NCC. The patterns do not overlap for the three power grids considered here, which confirms that the fractions of the nodes involved in power flow are different for different power grids. The closeness factor of the nodes is also quite distinct for the power grid considered. We observe a distinct overlap in the EDC, ECC and NEC. However, it is also observed that the nodes, which causes blackout, have low EDC, which is evident from the network plot shown in Figure 5-5. It is interesting to check the relation of the network centrality indices with the VSI, which is obtained by running a robust Bayesian regression model with the likelihood defined in (185) implemented using the PyMC3 package in Python [280].

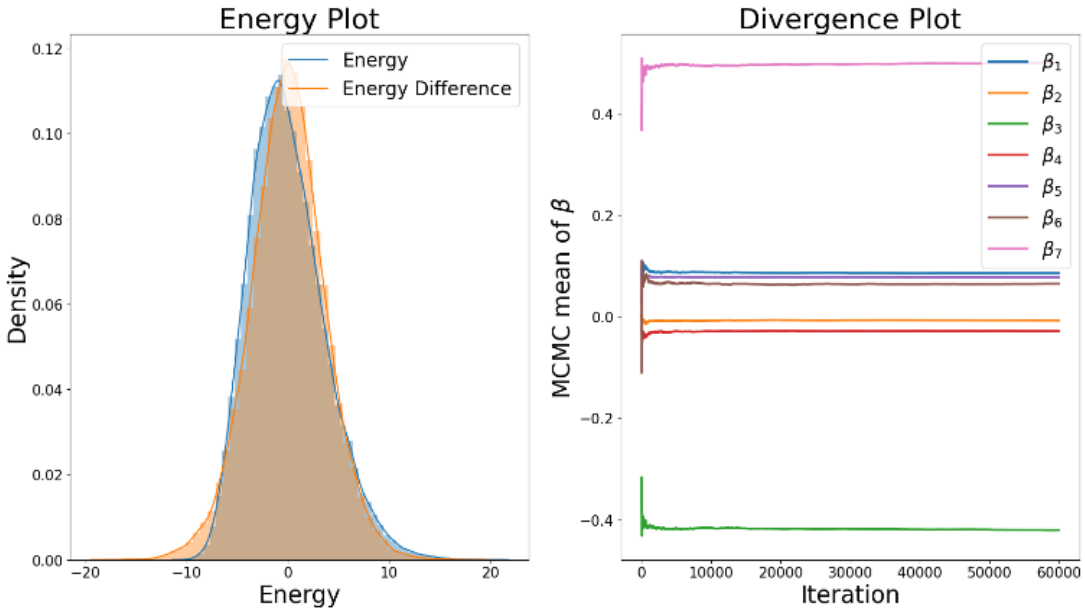

Figure 5-8: Hamiltonian Monte Carlo sampling diagnostics using energy and divergence plot.

Since we are using binary indicators $\{q_i\}_{i=1}^{N}$ along with the continuous variables for modelling the characteristics of the nodes, it is helpful we scale the continuous variables by two standard deviations for efficient regression modelling [281]. The prior for $\boldsymbol{\beta}$ is considered to be $\mathcal{N}(0,10)$. As given in [282], the prior for the standard deviation of VSI $\sigma_{\hat{\text{VSI}}}$ is considered to be inverse gamma distribution with $\alpha = 3$ and $\beta = 0.5$. The prior for $\sigma_{\hat{\text{VSI}}}^{\text{out}}$ is considered to be half Normal distribution as discussed in [272]. The standard deviations $\sigma_{\hat{\text{VSI}}}$ and $\sigma_{\hat{\text{VSI}}}^{\text{out}}$ are used along with the $\boldsymbol{\beta}$ to model the VSI of the node, causing network blackout. The

binary index of the distribution $\mathcal{P}_b$ is obtained from the Bernoulli distribution, which takes a uniform prior between 0 and 0.5 suggesting the fraction of the nodes causing the entire power grid blackout when it is attacked. The No-U turn sampler (NUTS) [274] which adaptively sets the path length of the Hamiltonian Monte Carlo sampler, is utilized for finding the posterior distributions.

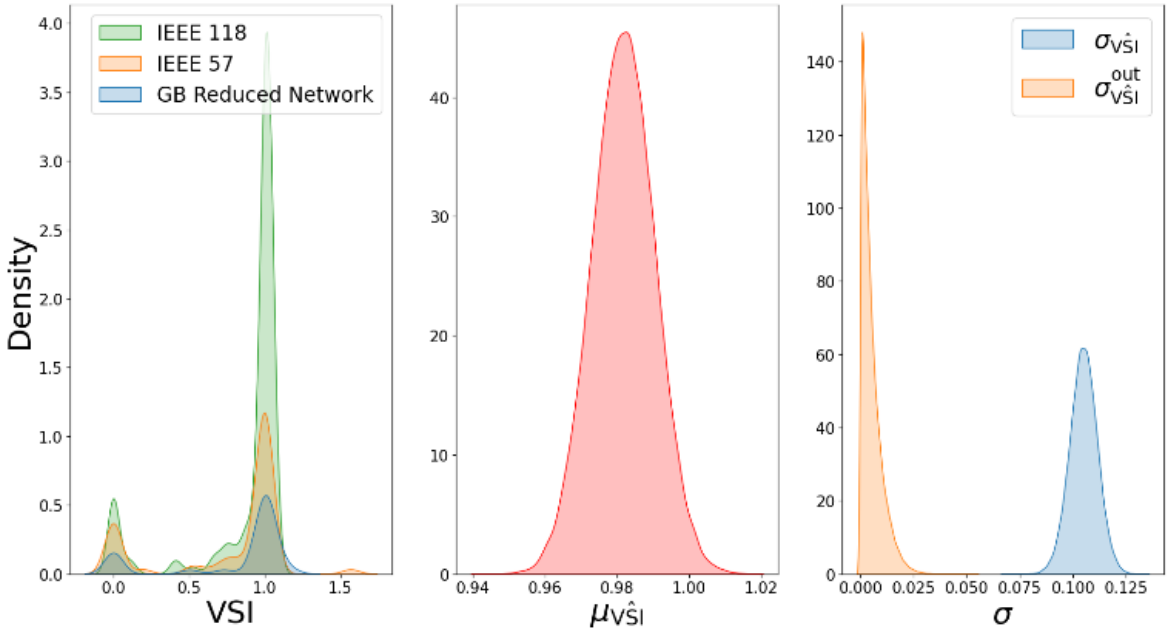

Figure 5-9: Visualization of the VSI data for different benchmarks power networks. The mean and standard deviations obtained using the HMC sampling.

The sampling algorithm for the robust Bayesian regression modeling has been run on a 64-bit Windows PC with Intel Core i5-8500 CPU, 3 GHz processor with six parallel cores. The `sample()` function is utilized in PyMC3 package in the sampling process, by running multiple parallel chains on the 6 parallel CPU cores to speed up the computationally expensive sampling process. Four different chains are used for the inference with the symplectic integrator to generate the trajectories, thus preserving the phase space volume of Hamiltonian transition. Random walk Metropolis-Hastings (MH) is utilized for adaptive step length of the symplectic integrator, thus reducing bias in the resultant Hamiltonian transition and yielding the samples from target distribution [274].

The target acceptance probability of 0.95 for the Metropolis-Hastings (MH) sampler used with symplectic integrator used in the process. We used 15000 samples for each chain, and it was assigned to each parallel cores of the CPU.

Computation time was also checked considering the sampler running on a single core. The computation time was ~1159 seconds = 19.3 mins for the chains to run on a single core while it took ~380 seconds = 6.3 mins when all the cores of the CPU were utilized, thus indicating a multicore vs. single core speedup factor of 3.05X. The diagnostics of the sampling is shown in Figure 5-8. As observed from Figure 5-9, the distribution of the VSI is similar for all the buses, hence a resultant robust statistical model is formulated based on the likelihood in (185) for the centrality features and voltage stability index of the nodes.

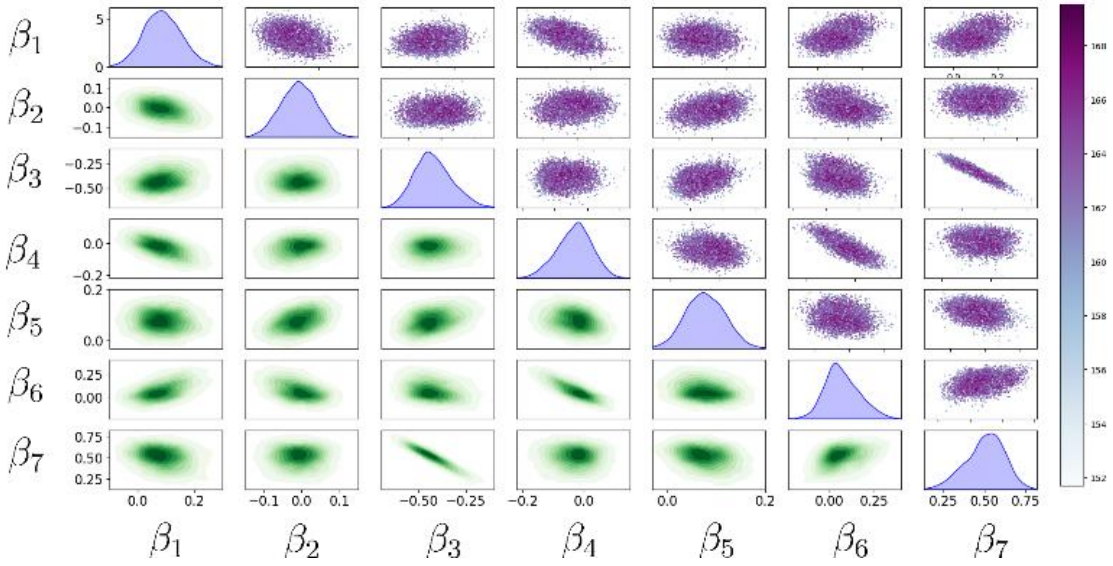

Figure 5-10: Bivariate and univariate marginal plots of the posterior distribution obtained from the HMC sampling. The scatterplot is scaled according to the cumulative loglikelihood function (185)

The trajectory of the data from the HMC sampler is confined in an energy set. Hence, the chains decouple into a deterministic and stochastic exploration of the samples amongst level sets. As we observe from Figure 5-8, the energy difference between the level sets is similar to the samples between the level sets suggesting that the random walk of the chain has explored the marginal energy distributions efficiently. In the second plot in Figure 5-8, we observe that mean of the parameter is converging to a single value. It suggests that the transition energy between the samples remains finite with sufficient exploration with no divergence. This is mainly due to the high acceptance rate of the MH sampler. Hence, it makes the sampling process slower but negates any divergence occurring due to infinite energy occurred during the transitions. The Gelman-Rubin statistic [283] for $\boldsymbol{\beta}$ is found to be 1.01. It confirms the efficiency of the

sampling process used. The samples from the posterior are obtained from the converged chains and are shown in Figure 5-9.

We observe that the $\mu_{\hat{VSI}}$ captures the peak obtained from the original VSI data for the different buses. The variation in the $\boldsymbol{\beta}$ models the variation in VSI for the nodes, which does not cause an instant voltage collapse on nodal attack. The VSI of the remaining nodes causing blackout is effectively modelled by $\sigma^{out}_{\hat{VSI}}$. However, the posterior spread in $\sigma^{out}_{\hat{VSI}}$ is thinner as compared to the $\sigma_{\hat{VSI}}$, which effectively models the low VSI of the nodes which cause instant voltage collapse on the attack using (174). The $\mu_{\hat{VSI}}$ in Figure 5-9 is similar to the VSI obtained from the grid as given in the univariate distribution in Figure 5-9. Now we examine the dependence of the centrality measures of the VSI by analyzing the univariate and multivariate posterior distributions of $\boldsymbol{\beta}$ defined in (182) as shown in Figure 5-10.

We observe from Figure 5-10, that the mean of β_7 has the highest positive value while that of β_3 has the highest negative value suggesting that the VSI of the nodes increases with an increase in the spanning trees. However, an increase in the EBC reduces the VSI of the nodes. It physically means that if the nodes, which generally forms a part of the shortest power flow route, is removed, then it increases the load margin of the power network. However, loading margin of the network reduces if the nodal attack makes the graph disconnected. Hence, we can conclude that the VSI is related to the closeness of the nodes in the graph. We observed from in Figure 5-10 that the relationship between β_3 and β_7 are inverse of each other. It signifies the complementary nature of the EBC and CST on the VSI. We also observe a similar negative correlation between β_4 and β_6. An increase in the network closeness increases the VSI of the nodes, while the nodes which are on the higher end of the eigenvalue spectrum reduces the VSI. The relation of the network closeness with VSI is also evident with the network plots in Figure 5-5, where the nodes having high VSI are close to each other topologically. There is also a positive correlation of β_1 with the VSI, which suggests that attacking the nodes with high connectivity or closer to other nodes

does not effectively decrease loading margin of the network. However, attack on the nodes with high I_{EVC} significantly decreases the loading margin of the network increasing the risk of voltage collapse.

5.1.7 Results and Discussion for the Large Power Network

5.1.7.1 Implementation Details

The power networks used in this work, as described in are obtained from the MATPOWER [267], from which the graphs with weighted adjacency matrices are created. The test cases are selected so that the assumptions 1, 2 and 3, as described in 5.1.4.2, are satisfied. The voltage stability margin (180) is only applicable for the load nodes. Hence the network centrality measures are evaluated for the load nodes.

The network features are obtained from the Brain Connectivity Toolbox [278]. The voltage V_i for the i^{th} load node, as described (180) , is obtained from the power flow solution of the given network. Bayesian feature selection is performed after computing the input features and voltage stability. Bayesian feature selection is performed in MATLAB using the command `estimate( )` in the Econometric Toolbox [284]. Firstly it is essential to select the suitable prior parameter of the Gaussian mixture model (189) , i.e. (V_{1k}, V_{2k}). As we observe in Figure 5-2, the feature scales are different; hence they are normalized using z-scores. Then the normalized input features and the respective output are split into training and testing datasets. In the prior, we have specified that (β, σ^2) are dependent variables. Then we fit the linear model (187) and obtain the posterior (β, σ^2) through Gibbs sampling as described in [275]. The models are obtained for various values of the prior parameters (V_{1k}, V_{2k}). The values of V_{1k} and V_{2k} are swept from 10 to 100 and 0.05 to 0.5, respectively. After obtaining the posterior, the fitted model is evaluated on the test dataset, and root mean square error is computed. Based on prediction on test data, the following results are obtained for (V_{1k}, V_{2k}) giving the minimum RMSE.

Table 5-2: The values of V_{1k} and V_{2k} with the minimum RMSE value on the test data

Cases / Parameter	Case 300	Case2869 Pegase	ACTIVSG2000	GB Network
V_{1k}	10	10	70	10
V_{2k}	0.15	0.05	0.45	0.45

Full features are then utilized to obtain the posterior for (γ, β) , as shown in Figure 5-12. The Gibbs sampling is used to fit the Bayesian linear model by specifying the prior as Gaussian mixture model of the values given in Table 4-2 for the respective power network. 10000 samples are used to draw the samples from the posterior, and the simulation is run with 2 Markov chains. The mean threshold value of 0.1 is considered for γ of the respective features to be incorporated in the GP model. The essential features are utilized to fit the GP model using the `fitrgp( )` in Statistics and Machine Learning toolbox in MATLAB [285]. Eight different kernels are used for capturing for modelling the variances, including Matern32, Matern52, Exponential, Squared Exponential and their respective automatic relevance determination (ARD) variants. Since the data points for all the cases other than Case 300 are greater than 1000, the GP is fitted on approximate data points. The data points are selected using a greedy optimizer based on differential entropy as described. The kernel parameters are obtained using the Bayesian optimization technique, where expected improvement plus is considered the acquisition function strategy. The evaluation for Bayesian optimization is considered to be 30. Once the GP model is trained, it is tested against the features from the perturbed network, and the residuals of the prediction and variance are analyzed for different kernel functions.

5.1.7.2 Bayesian Feature Selection Results

As we observe in Figure 5-11, centrality measures involving degree correlations highly influence the voltage stability margin as observed for IEEE 300 bus, Case 2869 Pegase and ACTIVSg2000. The analysis aligns with the derivation of the VSM from weighted load connectivity in weighted load connectivity [245]–[247]. However, we observe that other centralities like closeness centrality also play an essential role in influencing VSM. However, the influence of EDC and NDC on the voltage stability margin is the opposite, as evident in Figure 5-12.

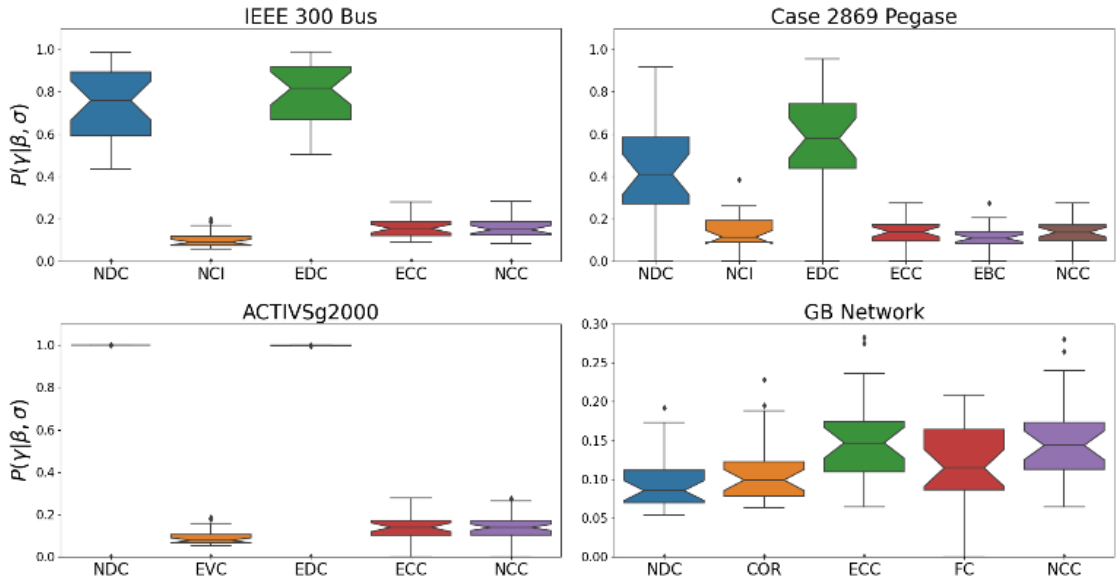

Figure 5-11: The value of γ sampled from the posterior, which denotes the inclusion of a particular centrality measure that influences voltage stability margin of the power networks

The effect is more pronounced for ACTIVSg2000, where the absolute value of β is higher than the rest of the networks. However, we do not observe a similar pattern for GB networks, as all the centralities shown in Figure 5-11 have similar values of γ. It can be attributed to the multi-modal distribution form of VSM, as shown in Figure 5-2. It suggests that degree centrality do not play a key role if with an increase in the number of critical nodes with high VSM. We observe that the closeness centrality measures like NCC and ECC have similar roles in influencing VSM. Due to the multi-modal nature of the VSM, we observe a high intercept value in the GB network. Moreover, we also observe a high intercept value for ACTIVSg2000, which can be attributed due to the high β, from degree centralities effectively cancelling each other out. The flow centrality and k-core

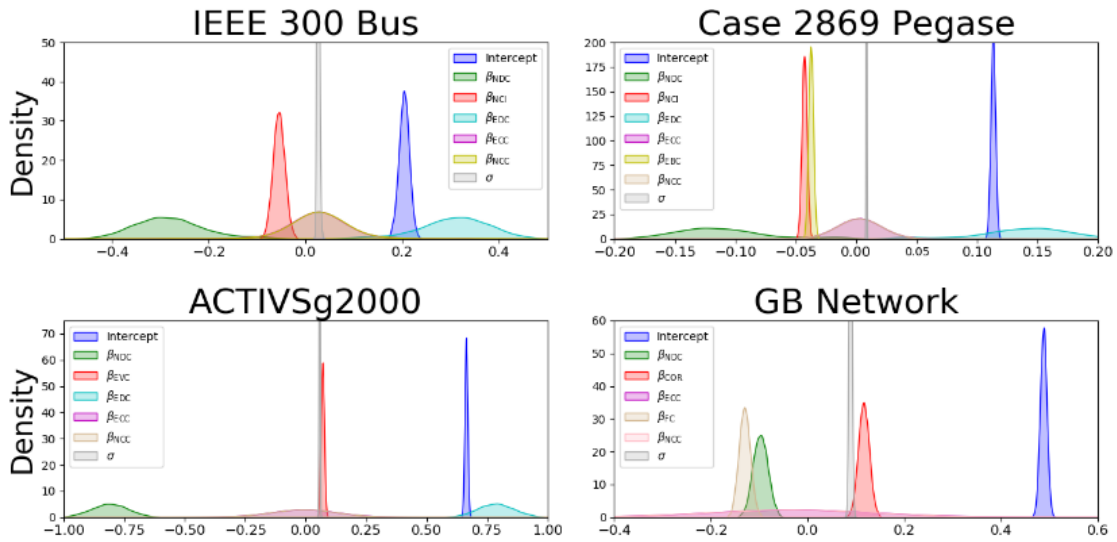

Figure 5-12: Posterior of the regression coefficients obtained from Gibbs sampling for the essential centrality features influencing the voltage stability margin

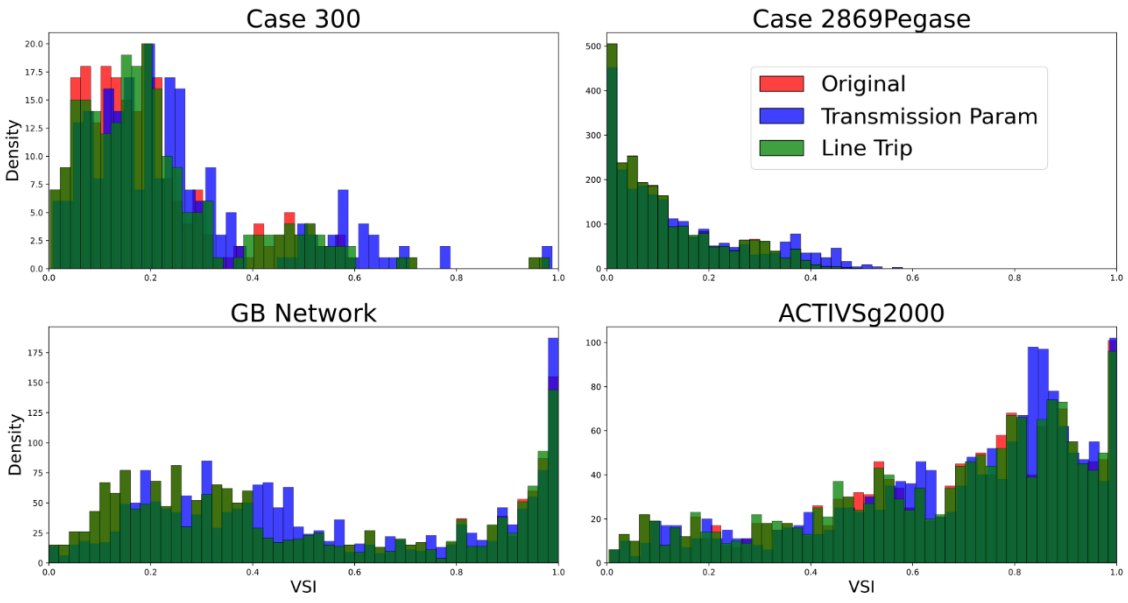

Figure 5-13: The distribution of the voltage stability margin for all the nodes. The distribution of the voltage stability margin is also incorporated for transmission line parameter modification and tripping the line which carries the highest reactive power.

centrality play an essential role for the GB network in influencing the voltage stability. Moreover, they are also highly correlated, as shown in Figure 5-3. Thus we can conclude that when degree centrality does not influence the VSM, other correlated centrality measures like NCC and ECC and *k*-core centrality and flow centrality play an essential role. These key centrality measures will be utilized to

predict the VSM using GP, and the analysis is performed for critical and non-critical nodes in the following subsection.

5.1.7.3 Gaussian Process Regression Training Results

After the critical centrality features are obtained based on (γ,β) as shown in Figure 5-11, the GP regression model is obtained. As discussed, the GP is fit by optimizing the marginal likelihood. We observe that for Case 300, Case 2869 Pegase, and ACTIVSg2000, we get a higher optimized log-likelihood when the ARD is incorporated with the standard kernels. However, the trend is the opposite for the GB network, where GP with standard kernels provides the highest log-likelihood. The trend can be considered due to the multi-modal nature of the VSM for the GB network compared to other networks. The length scales in the ARD is considered as a kernel hyper-parameter. As the hyper-parameter space is increased, the training time is longer. Hence care has to be taken, as a kernel without ARD parameters fits better for multi-modal distribution. Once the GP model is fit, i.e. we obtain the kernel hyperparameters by maximizing the marginal likelihood, the fitted is tested against the features from the perturbed network. In the first case, the maximum reactive power line is tripped for the individual networks.

However, the power flow balance did not occur when the line was tripped. Hence the algorithm was modified to trip the line carrying the maximum reactive power, and the modified network is still operational. The power flow solution of the modified network is obtained to find the VSM (180) represented by y_{reac}, whose distribution is shown in Figure 5-13.

In the second case, parameters of randomly selected 30% transmission lines are increased by 20% to incorporate the RES. The change in line parameters affects the voltage stability margin as it changes the operating point of the power grid [286] . The power flow solution with the modified network parameter is found to compute the VSM (180). The change in the voltage stability margin is shown in Figure 5-13. We observe that the distribution of the VSM for two network perturbations remains similar for 2869 Pegase and GB networks, and it remains moderately close to each other for the other two power networks.

We also notice that the distribution of the VSM shifts to the left for all the given networks, which needs to be predicted using the fitted Gaussian process model.

Table 5-3: The training and testing performance measure for different kernels and networks used in the analysis

Networks	Kernel / Condition	MAT32	MAT 52	EXP	ARD SQ EXP	ARD MAT 32	ARD MAT 52	ARD EXP	ARD SQ EXP
Case 300	Training	0.402	0.430	0.421	0.364	**0.685**	**0.670**	**0.746**	**0.658**
	Network	0.349	0.355	0.349	0.323	0.642	0.629	0.675	0.619
	Line Trip	0.354	0.385	0.376	0.314	0.677	0.661	0.736	0.651
Case2869 Pegase	Training	0.394	0.369	0.443	0.373	**0.679**	**0.999**	**0.998**	**0.999**
	Network	0.344	0.331	0.363	0.329	0.677	0.998	0.997	0.998
	Line Trip	0.396	0.370	0.444	0.375	0.679	0.242	0.712	0.630
ACTIVSg2000	Training	0.300	0.292	0.343	0.289	**0.773**	**0.828**	**0.822**	**0.951**
	Network	0.264	0.261	0.272	0.260	0.753	0.809	0.788	0.843
	Line Trip	0.303	0.294	0.346	0.291	0.672	0.694	0.705	0.827
GBNetwork	Training	**0.985**	**0.987**	**0.976**	**0.988**	0.345	0.350	0.622	0.348
	Network	0.070	0.062	0.097	0.023	0.341	0.340	0.370	0.339
	Line Trip	0.984	0.986	0.975	0.987	0.350	0.350	0.621	0.348

If we observe the pattern between the original VSM and the predicted ones from training, we observe that for Case 300, Case 2869 Pegase and ACTIVSg2000 in

Table 5-3, the results are much better with the ARD kernels with a high correlation between the predicted VSM from training input and original VSM. High correlation is typical for these networks due to the univariate distribution of VSM. The values are much higher for Case 2869 Pegase and ACTIVSg2000 than Case 300, as the former are bigger networks than the latter, suggesting that the digital twin concept is more applicable for networks having a large number of nodes. However, the relationship is the opposite for the GB network as the training performance is good for standard kernels. The opposite trend is visible in the GB network due to the bivariate distribution of VSM.

As we observe the correlation values, we find that the correlation measure for prediction from line trip perturbation in Case 300 is closer to the measure obtained from training performance. However, for ACTIVSg2000 and Case 2869 Pegase, the correlation measure for prediction from network parameter perturbation is similar to the training performance. Hence, we can say that the digital twin is effective for the prediction of VSM in line trip perturbation for smaller power networks and in network perturbation for larger power networks. However, the trend is the opposite for GB Network, as it has bivariate VSM distribution. In the case of ARD kernels, the results are much better for line trip perturbation than network parameter perturbation.

5.1.7.4 Analysis of Residuals and Uncertainty on Testing Data for Critical and Non-Critical Nodes

The residuals after the mean prediction are shown in Figure 4-14a and Figure 4-14b for the critical and non-critical nodes respectively. The top 10% of nodes are considered critical for each network. We observe a specific pattern in residuals that the VSM of non-critical nodes is under-estimated while the critical nodes are overestimated. For IEEE 300 bus, the fit for R is slightly better for line trip perturbation than network parameter perturbation. The better model fit is attributed to the lower absolute value of the former residuals, closer to zero. However, the variance of $\left(\mathbf{y}_{tx} - \hat{\mathbf{y}}_{tx}\right)$ is higher for critical nodes as compared to $\left(\mathbf{y}_{reac} - \hat{\mathbf{y}}_{reac}\right)$. In the case of 2869 Pegase, the $\left(\mathbf{y}_{tx} - \hat{\mathbf{y}}_{tx}\right)$ ARD kernels are very low for critical and non-critical nodes. The network 2869 Pegase is the most stable as the maximum VSM is the lowest out of all the networks. The mean prediction for network parameter perturbation is perfect for ARD kernels.

However, we see a reversed pattern for the same kernels in the case of line trips perturbation, where there is an overestimation of VSM for critical nodes. For standard kernels, the pattern of residuals is the same for both the perturbation. For ACTIVSg2000, the mean prediction is slightly better for network parameter perturbation than line trip perturbation with the higher R for the mean function. However, this result is more applicable for the kernels with ARD, as we observe a minor variance in the residuals of critical and non-critical nodes for $\left(\mathbf{y}_{\text{tx}} - \hat{\mathbf{y}}_{\text{tx}}\right)$ as compared to $\left(\mathbf{y}_{\text{reac}} - \hat{\mathbf{y}}_{\text{reac}}\right)$. Moreover, it is also accompanied by a higher estimated value of β and lower noise variance σ for the GP model. However, the trend is the opposite for GB networks, where the $\left(\mathbf{y}_{\text{reac}} - \hat{\mathbf{y}}_{\text{reac}}\right)$ are better than $\left(\mathbf{y}_{\text{tx}} - \hat{\mathbf{y}}_{\text{tx}}\right)$. Unlike the previous cases, the predictions are better with standard kernels. We observe a significant variance of the residuals for the non-critical nodes in the case of network parameter perturbation compared to other networks. Hence, we can say that for GB networks with multi-modal VSM distribution, the chances of underestimating VSM for non-critical nodes are pretty high.

The value of prediction uncertainty suggests that $\sigma_{\hat{\mathbf{y}}_{\text{tx}}}$ is higher than $\sigma_{\hat{\mathbf{y}}_{\text{reac}}}$. In the case of line trip perturbation, we observe that for IEEE 300 bus system, the uncertainty for ARD kernels is lower than the standard kernels. However, the trend is the opposite for GB networks, where the ARD kernels have higher uncertainty than the standard ones. The ARD exponential and squared exponential kernels used in predicting the VSM of line perturbed 2869 Pegase network have larger variations in prediction uncertainty than the other kernels. The effect is magnified in the ACTIVSg2000 network, where the predictive uncertainty variation is small across the nodes in the network when ARD kernels are used.

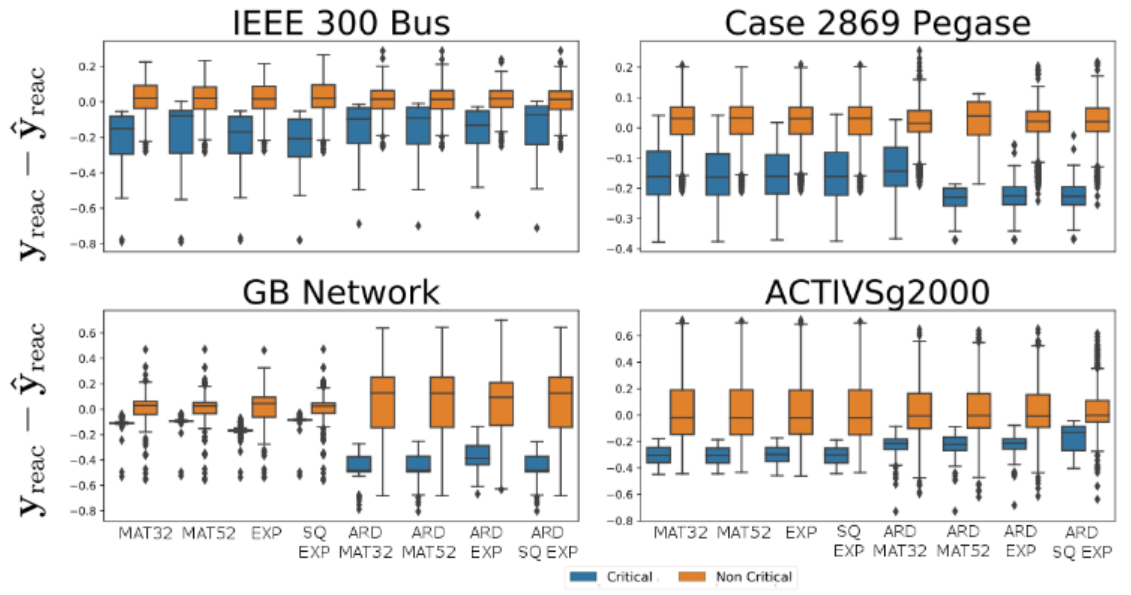

(a)

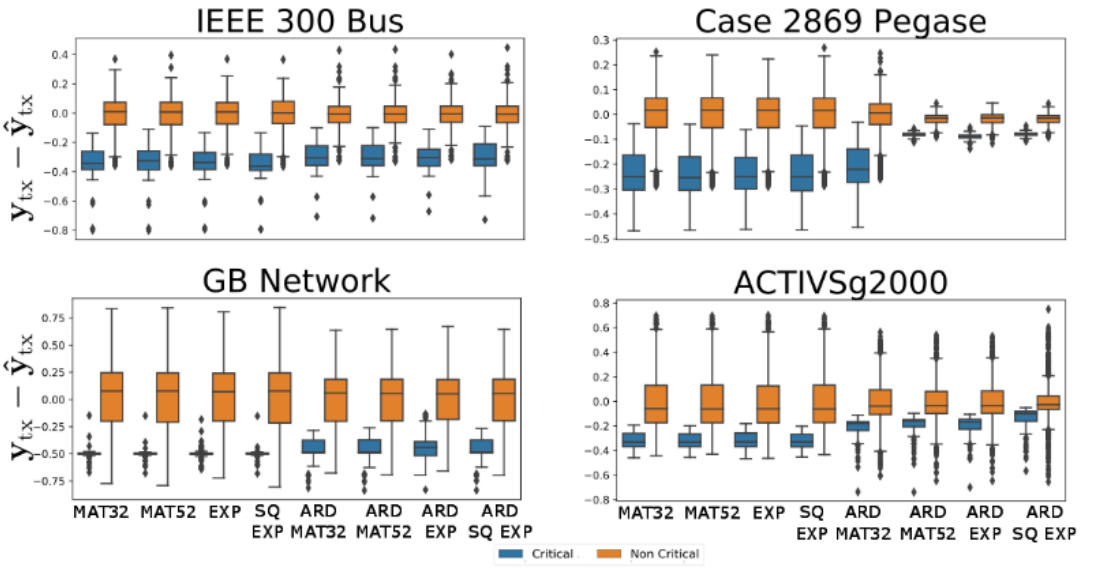

(b)

Figure 5-14a: The residuals of the critical and non-critical nodes for different networks and kernels to predict the voltage stability margin when the line carrying the highest reactive power is tripped. Figure 5-14b: The residuals of the critical and non-critical nodes for different networks and kernels to predict the voltage stability margin when the parameter of transmission lines are modified.

In the case of network parameter perturbation, case 300 bus and ACTIVSg2000 network shows a similar trend as the previous case. However, for the 2869 Pegase network, the predictive uncertainty variation is higher for standard kernels than ARD. The variation of predictive uncertainty remains the same for all the

standard kernels for the GB network. If we compare the predictive uncertainty for critical and non-critical nodes, we observe a negligible difference in variation for the GB network and case 2869 Pegase. For the ACIVSg2000 network, a higher variation is observed for ARD kernels, but there is no difference in the critical and non-critical nodes. However, for IEEE 300 Bus, we find that the variation in uncertainty is very high for the critical nodes for both line trip and network parameter perturbations.

5.1.7.5 Analysis of Residuals and Uncertainty on Testing Data for Lower and Higher Voltage Nodes.

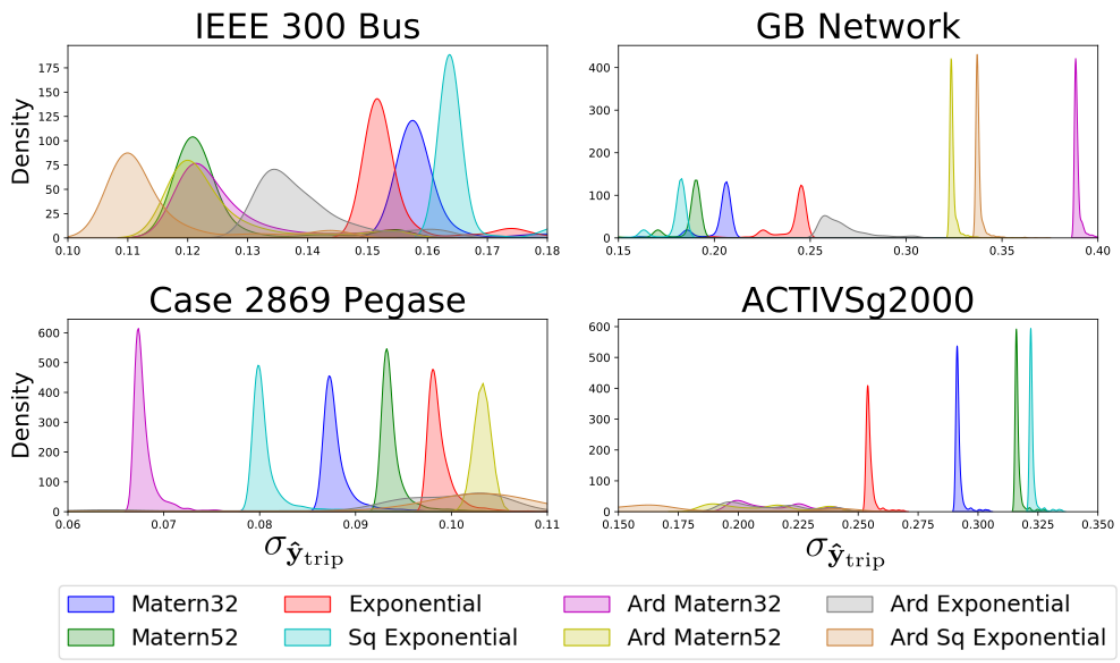

(a)

As given in [229], the nodes with higher voltage tend to have a higher degree centrality. Moreover, as we have observed in Figure 5-11, degree centrality features influence the VSM as compared to other centralities. Hence analysis of the residuals is conducted based on lower and higher voltage nodes. The nodes are considered higher if their based voltage is more than 140 kV. If we see the operating base voltages of the load nodes as given in Table 5-1, we find that other than Case 2869 Pegase, all other networks have nodes with much lower operating voltage, including the distribution network voltage level. Hence we observe in Figure 4-14a that the pattern of the residuals is similar except for the 2869 Pegase case. Here we observe a significant underestimation for the VSM

for the lower voltage nodes. For IEEE 300 bus, we observe a minor variation across the kernels for line trip perturbation. For line trip perturbation in IEEE 300 bus, the predictive uncertainty is higher for LV nodes for all the kernels. Similar phenomena are also observed in GB networks for LV nodes in ARD kernels. In the case of 2869 Pegase, the variation is higher in LV nodes for standard kernels and higher variation in HV nodes for ARD kernels for line trip perturbation

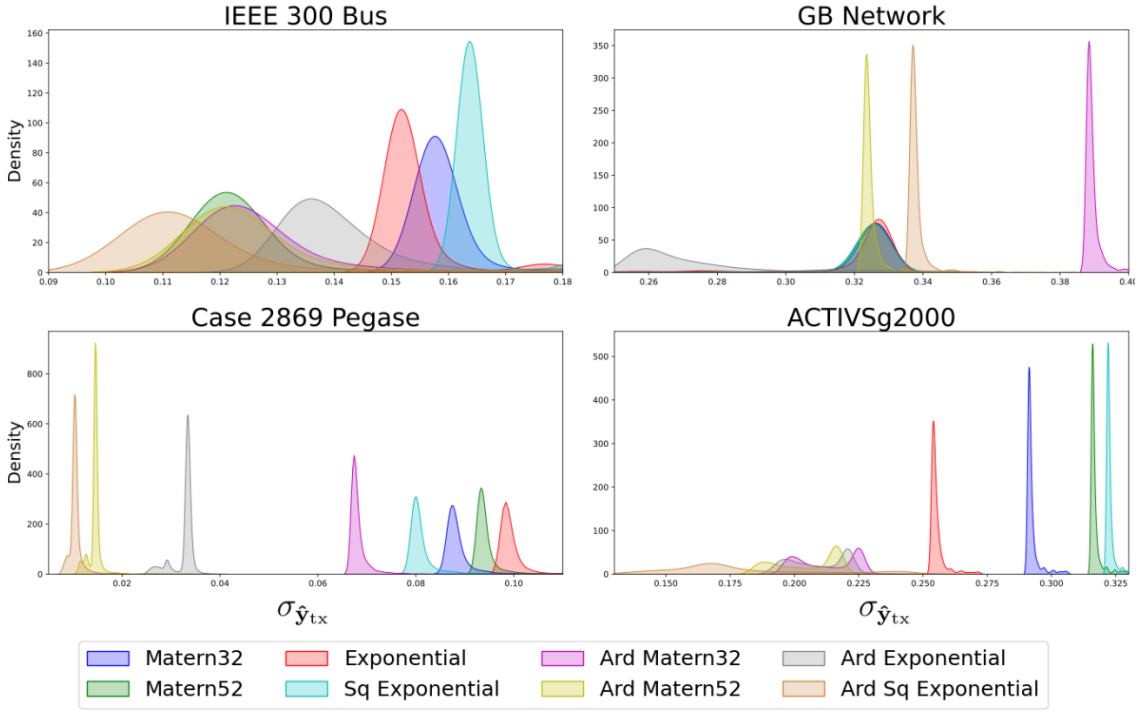

(b)

Figure 5-15: The VSM prediction uncertainty for the different power networks for the different Gaussian Process kernels while considering network perturbations like (a) Line Trip (b) Network Parameters

In line parameter perturbation, we observe a higher variation in predictive uncertainty for LV nodes than HV for case 300, similar to the previous case. In ACTIVSg2000, we observe a higher mean of predictive uncertainty for the LV nodes than the HV nodes. In 2869 Pegase, we observe higher variation for the LV nodes in the case of standard kernels where the prediction for the mean function is poor.

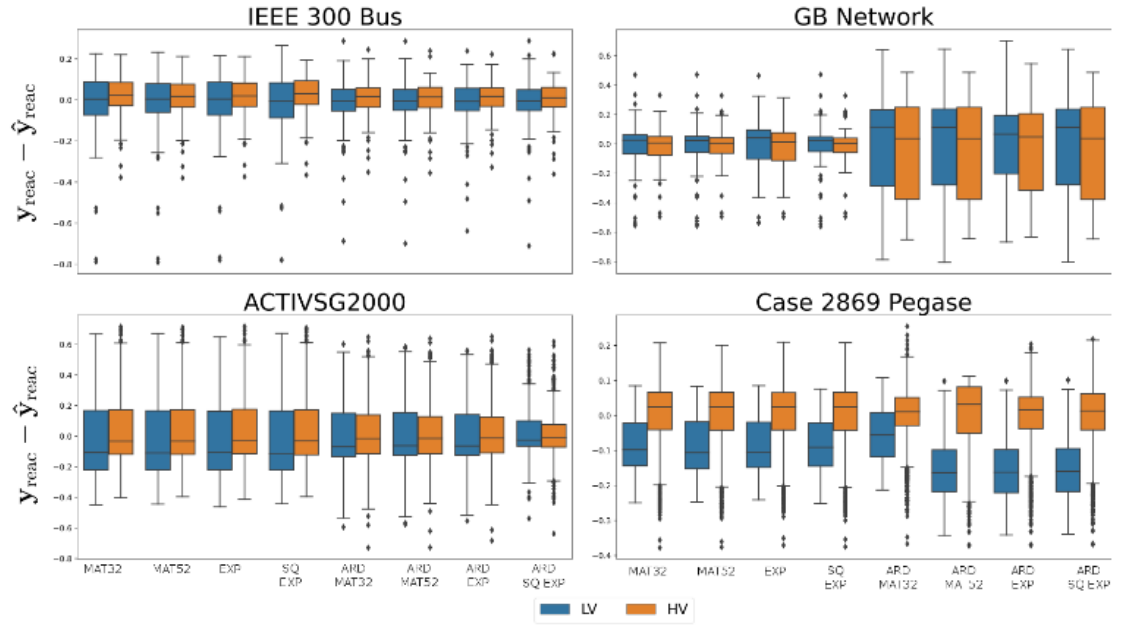

(a)

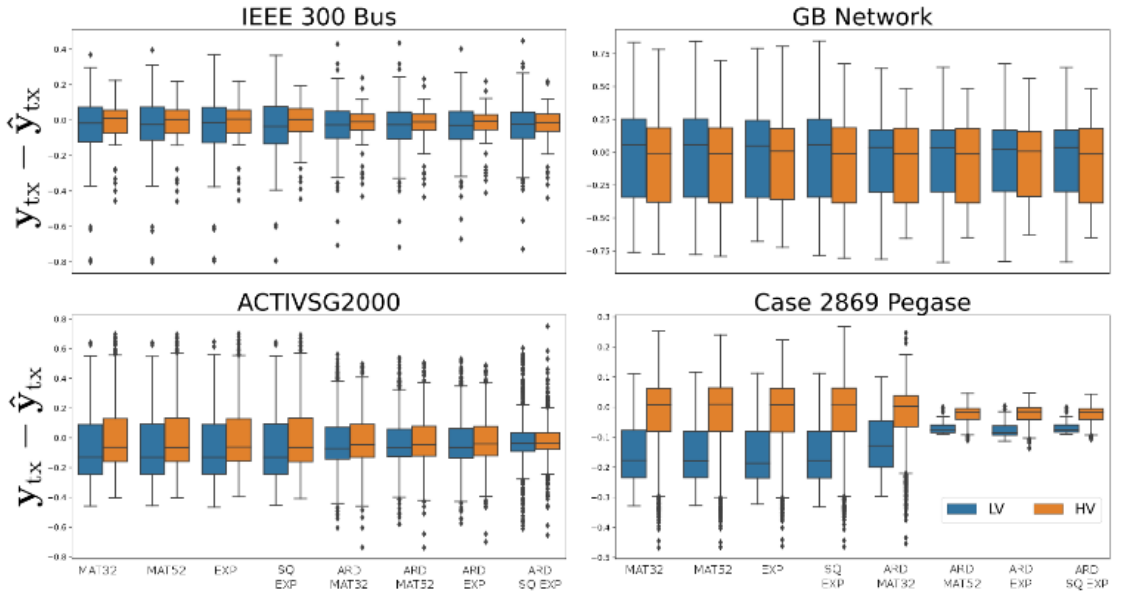

(b)

Figure 5-16: The residuals of the LV and HV nodes for different networks and kernels to predict the VSM when the (a) line carrying the highest reactive power is tripped (b) for network parameter perturbation.

5.1.8 Conclusion

The posterior distributions from the statistical model obtained from the smaller power network indicate that the nodes which are in the path of shortest power flow within the network along with the nodes which are in the higher end of the

eigenvalue spectrum play a significant role in deteriorating the VSI of the network. However, the loading margin of the network improves if the network closeness and centrality decrease after nodal attack. This suggests that the community structure of the network is robust to nodal attacks.

The significant findings of the regression model for large power network are as follows:

1. Degree centrality primarily influences the VSM of the power network only when the latter has a unimodal structure. Under bimodal distribution, other closeness centrality and other correlated centrality metrics primarily influence the VSM.
2. The mean prediction of non-critical nodes is under-estimated while the critical nodes are overestimated. It specifies a bias prediction method used in weather forecasts to predict the VSM accurately.
3. The predictive mean and uncertainty vary across the standard and ARD kernels. For the unimodal VSM, ARD kernels predict the VSM better under network perturbation. In the case of bimodal VSM, prediction using standard kernels are better.
4. The networks having primarily HV transmission nodes, there is a significant difference in the mean prediction between the LV and HV nodes, as evident for 2869 Pegase network.

5.2 Clustering the Critical Community of Nodes Using Spectral Filters in Power Networks

The results from the VSI obtained in the previous subchapter 5.1, can be extended to find the critical community of nodes using the hierarchical structure of the power networks, having set of critical and non-critical nodes. This method helps in real-time identification of nodes, so that preventive measures can be taken to avoid complete blackout on critical node removal.

5.2.1 Previous Works

The functionality of the real world infrastructure networks is significantly affected when a node is removed. The performance of the real-world network improves, degrades, or fragments entirely due to the congestion phenomena [287], [288] after a specific node is removed.

The impact of the node removal in a complex network is generally studied using percolation theory [289], by analyzing the evolution of the giant connected component. However, percolation theory is a purely topological feature that does not incorporate observed phenomena like congestion, which can disintegrate a real-world network without transition.

The critical percolation threshold can be predicted topologically using the leading eigenvalue of the backtracking matrix operator [290], [291]. The eigenvalue distribution of a weighted and unweighted scale-free network is dependent on the degree distribution along with its bounded moment [292], [293]. Hence the set of critical node identification is framed as a community detection problem utilizing the eigen spectrum of the weighted network. The communities are identified from spectral filters [294] using the spectral clustering of the sampled covariance matrix of noisy graph signals. The eigenvalue spectrum has to be utilized to find the critical communities as the spectral gap is linked with the complex network resiliency [295]. Modularity is only associated with the largest magnitude of the absolute eigenvalue [296]. There have been no proper work regarding finding critical nodes of real world weighted infrastructure network, especially utilizing its eigen spectrum.

5.2.2 Contributions in this subchapter

The set of critical node identification is framed as a community detection problem utilizing the eigen spectrum of the weighted network. . The nodal hub with a high degree distribution forms a hierarchy with the critical nodes in the network [297]. Hence agglomerative clustering with single linkage normalization [298] has been utilized to find the critical community of nodes. The communities, identified from nodal influence and eigenvalue spectrum, consist of non-critical and critical nodes within the same cluster. The resultant communities can improve power network resilience by using preventive strategies [299] like conversion of transmission lines from overground to underground [300], earthquake-resistant substation building design [301], substation relocation and improving the network design for more extreme events [302].

5.2.3 Overall Description of the Methodology

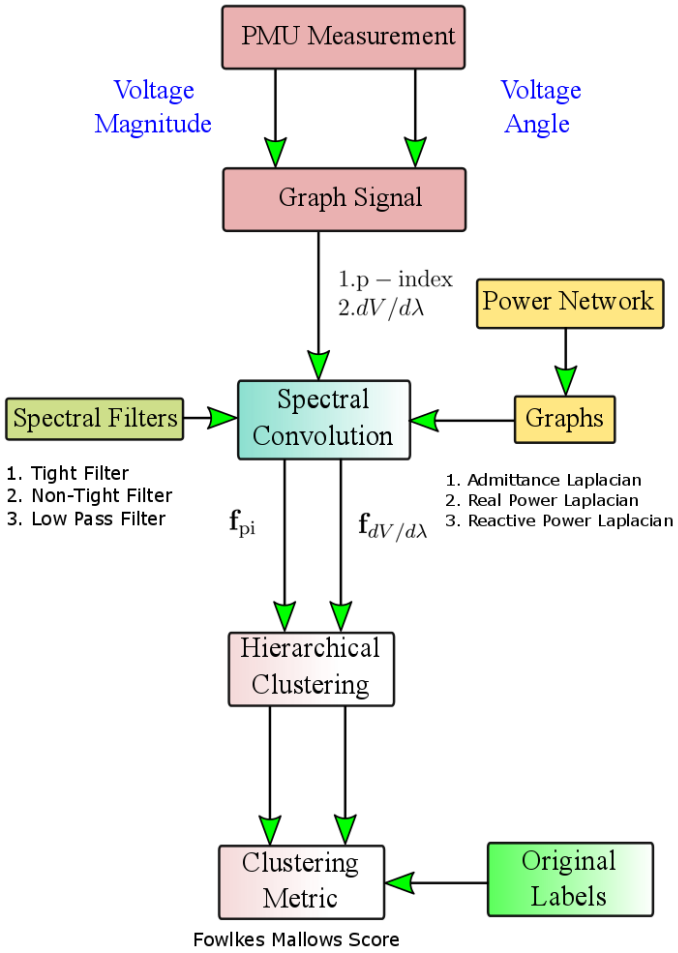

Figure 5-17: Schematic to obtain the critical node community, having the highest overlap with the original labels. The community is obtained after hierarchical clustering of the features obtained

after convolving graph signals and spectral filters, and the overlap is validated by Fowlkes Mallows Score

The schematic in Figure 5-17, shows methodology to find the critical set of nodes for a power network from the parameters of the PMU measurements and spectral filters. *P*-index and tangent vector $(dV/d\lambda)$ is defined, which is the graph signal. Hierarchical clustering is performed on the features obtained after convolution of graph signals and various spectral filters. The set of nodes obtained from hierarchical clustering is compared with the original set of nodes using Fowlkes Mallows Scores.

5.2.4 Reference Label of the Nodes

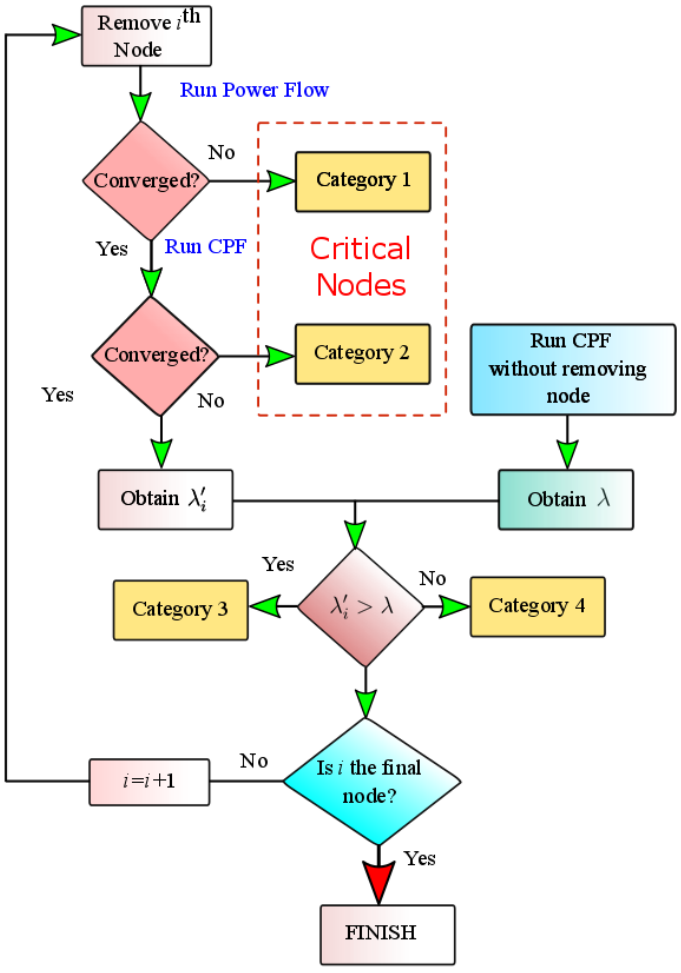

Figure 5-18: Schematic to obtain critical nodes in power network by examining the network characteristics after the nodes one by one. Category-1 and category -2 form critical nodes. The

power network functions at a different operating point when a node from category-3 and category-4 is removed

The solution set $\{V', \delta', \lambda'\}$ is found from (173) as iterated with the similar parameterization technique and thus evaluating λ'_{crit}. However, in a modified topology, $\{V', \delta', \lambda'\}$ cannot be obtained for some value of λ as the power balance is violated. Hence, we categorize these nodes as Type-2 nodes, as shown in Figure 5-18. When a node from this category is removed, the network becomes vulnerable to load and generation perturbation with a risk of widespread blackout. The type-1 and type-2 nodes belong to a category of critical nodes.

If we remove the node which does not belong to either Type-1 or Type-2 category, the power network functions at a different operating point. The functionality is represented by the value λ'_{crit}. So this is either greater than λ_{crit} or smaller than that. If we remove the nodes where the λ'_{crit} is less than the λ_{crit} from the unperturbed power network, we label these nodes as Type-3; otherwise, we label them as Type-4. This set of nodes forms a category of non-critical nodes. However, we do not know the node categorizations unless we run the power flow or continuous power flow solvers. Hence graph signal and spectral filters are utilized to find nodal communities that overlap with the labels obtained here.

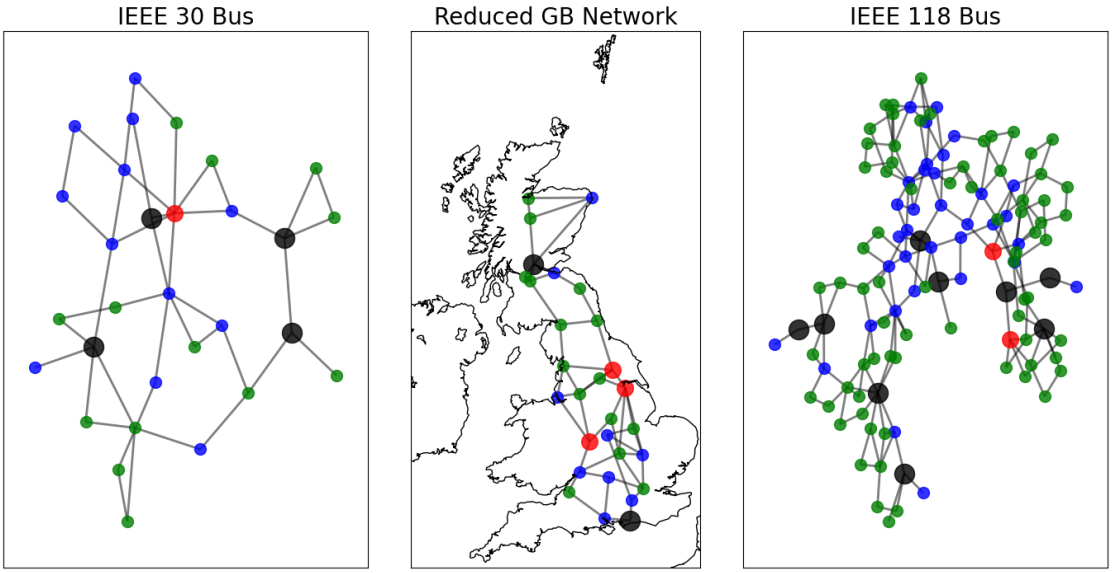

Figure 5-19: The node labels in the network, where black, red, green and blue represents the category-1, 2, 3 and 4 nodes, respectively. The category 1 nodes in IEEE-30 and 118 bus are closer to each other than the reduced GB network

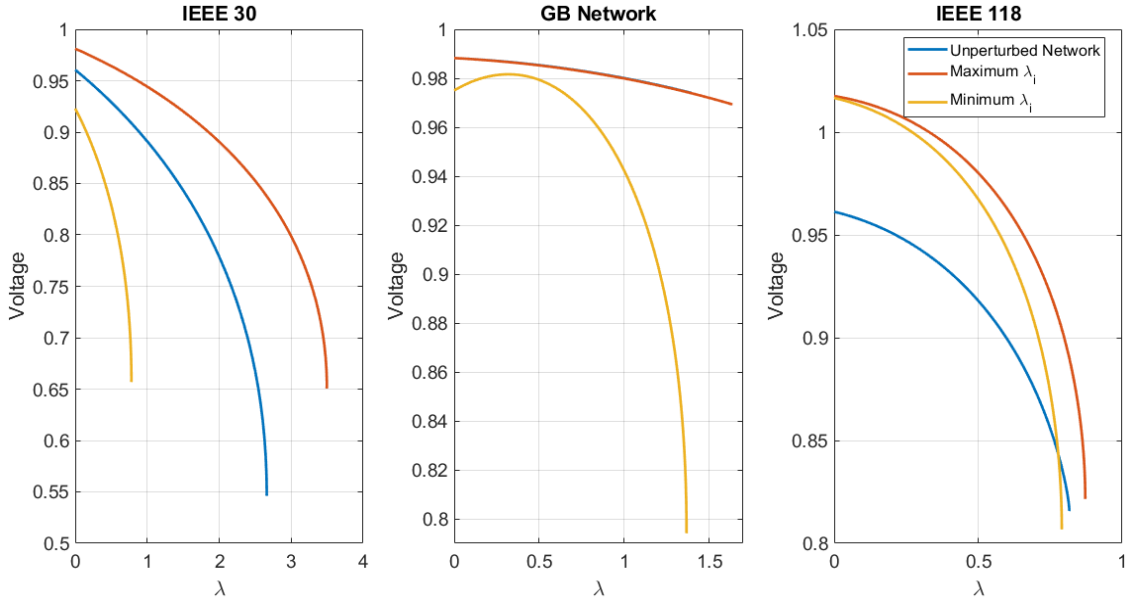

Figure 5-20: The $V-\lambda$ characteristics of the weakest node in the power network for three cases, blue-with all nodes intact, red-when category 4 node with the maximum $\left(\lambda'_{crit}/\lambda_{crit}\right)$ is removed from the network, yellow- when category 3 node with the minimum $\left(\lambda'_{crit}/\lambda_{crit}\right)$ is removed from the network.

Before, the graph signals and the properties of spectral filters are discussed; we explore the eigen spectrum of the power network for different Laplacian matrices.

5.2.5 Eigen Spectrum of Power Network

Let us consider the power network as a weighted graph $\mathcal{G} = \{V, E, w\}$, where V represents the set of vertices, E represents the edges and w_{ij} represents the edge weight between node i and j. The active power, reactive power and admittance magnitude (described in Methods) are considered the edge weights. Let us consider $\{(\lambda, \chi)\}_{i=0,\ldots,N-1}$ be the eigenvalue and eigenvector pair for the graph laplacian $\mathcal{L}$, defined as

$$\mathcal{L} = D - W, \tag{204}$$

where, $D = \text{diag}(d_i), d_i = \sum_{i \neq j} w_{ij}$. The graph Laplacian is a symmetric matrix consisting of orthonormal eigenvectors represented by χ_l for $l = 0, \ldots, N-1$. Here N represents the nodes in the graph with the eigenvalues λ_l as:

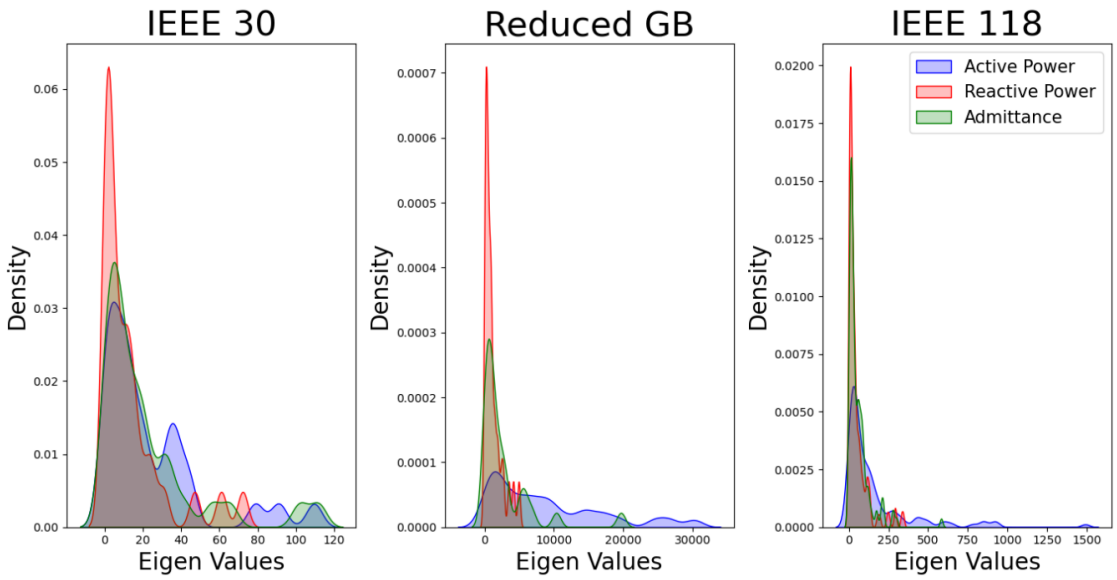

Figure 5-21: The eigen spectrum of the Laplacian of the weighted power graph is proportional to the network degree distribution. The spectrum of the reduced GB network is similar to the IEEE 118 bus considering the skewness, while the spectrum of the IEEE 30 bus is smoother than the remaining ones

$$\mathcal{L}\chi_l = \lambda_l \chi_l. \tag{205}$$

The distribution of eigenvalues for different edge weights is shown in Figure 5-21

for different power networks. We observe a skewed eigenvalue distribution for all three cases with a similar statistical exponent of degree distribution in scale-free networks. The eigen energy distribution is dependent on degree distributions [292]. However, in Figure 5-21, we see that the eigenvalue distribution for reduced GB-network is not as skewed as the other networks, especially with active power as the Laplacian, attributed due to relatively higher clustering coefficient [293], thus shifting the distribution to the right. Moreover, the reduced GB network has a better community structure than the other networks, as evident from the critical node location in the network. The eigenvalue distribution for IEEE 118 bus is quite different from the other networks due to the absence of multi-modality.

When we observe the eigenvectors associated with lower and higher eigenmodes of the Laplacian, the former is associated with increased modularity supporting a strong community structure Figure 5-22. However, the latter localize a specific set of nodes in the network Figure 5-23. If we compare these localized nodes with the node category in Figure 5-19, critical nodes are localized with non-critical ones at higher eigenmodes. It signifies that critical nodes are also identified from the high eigenmodes of the network. However, a group of eigenvectors are linked with the reliability of the networks [293]; hence we need to utilize the entire spectrum of the network using spectral filters to obtain the critical nodes.

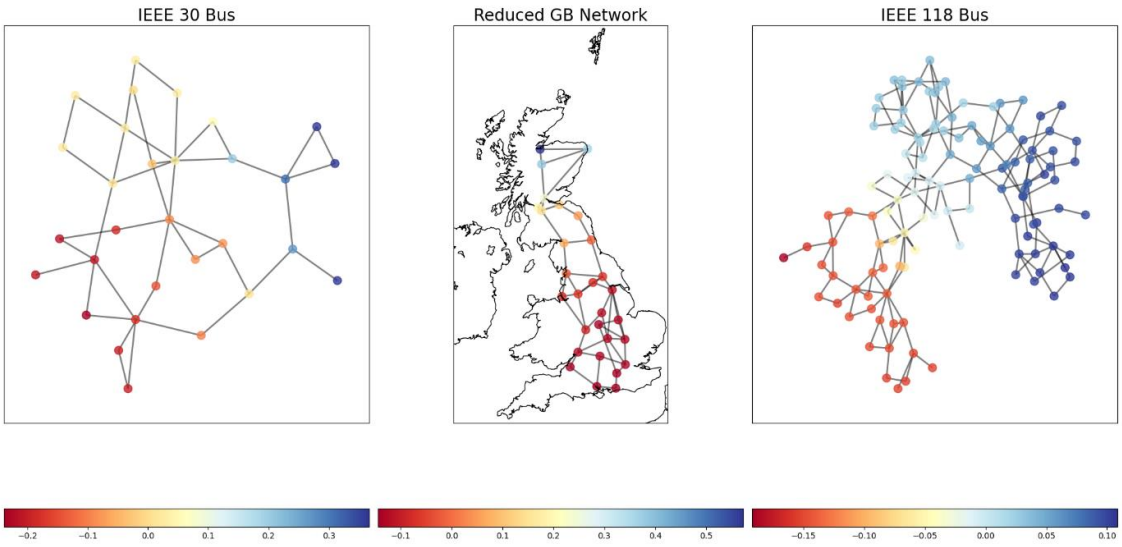

Figure 5-22: The eigen vectors associated with the second smallest eigen value which depicts the community structure within the network. The graph can be easily partitioned into several communities which are close to each other.

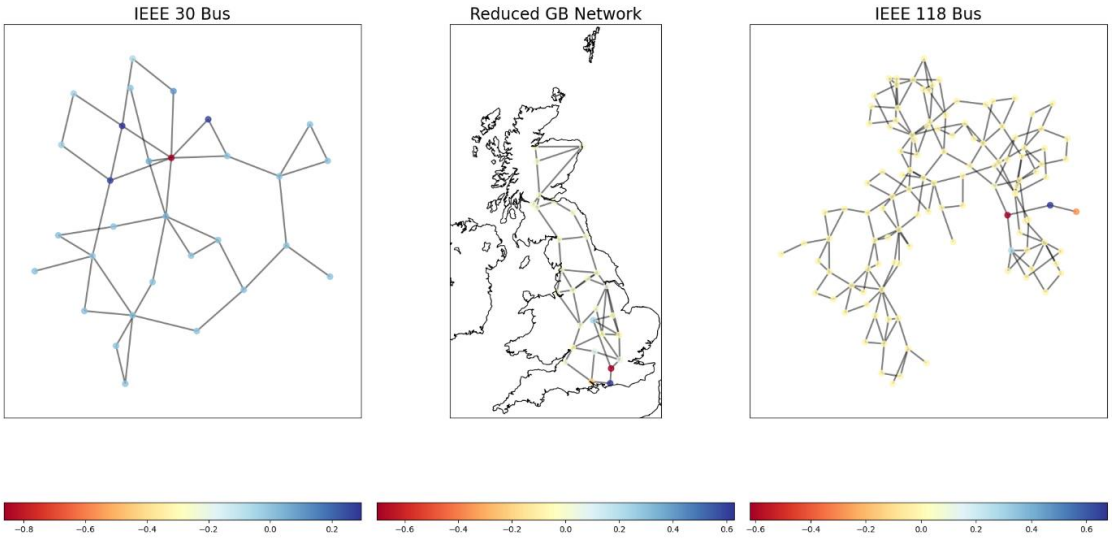

Figure 5-23: The eigen vector associated with the highest eigen value which depicts a small subset of nodes which are different from other set of nodes in the network. Within these nodes, contain critical nodes too. It suggests that critical nodes are associated with the high eigen modes of the network

5.2.6 Graph Signal

Nodal property has to be utilized for obtaining the critical nodes. The stability index [303] is used as a graph signal, which helps identify the weak nodes. This index has advantages over the traditional stability index as this can also be used as a reliability measure. If we consider the load in two bus system to be $P_L + jQ_L$

and voltage magnitude being V . If the load admittance is represented by $\underset{\frown}{G}_L - jB_L$,we can write,

$$\underset{\frown}{G}_L = \frac{P_L}{V^2}, \underset{\frown}{B}_L = \frac{Q_L}{V^2}. \tag{206}$$

Let us consider the load is increased by $(\Delta P, \Delta Q)$. The increase in the admittance is given by $(\Delta \underset{\frown}{G}_L, \Delta \underset{\frown}{B}_L)$. Due to additional loading, voltage magnitude changes ΔV , and the new voltage becomes $V + \Delta V$. Now we can represent the power increment a the bus as:

$$\Delta P_L = (V + \Delta V)^2 (\underset{\frown}{G}_L + \Delta \underset{\frown}{G}_L) - V^2 \underset{\frown}{G}_L = (V + \Delta V)^2 \Delta \underset{\frown}{G}_L + (2V + \Delta V) \underset{\frown}{G}_L \Delta V, \tag{207}$$

where,

$(V + \Delta V)^2 \Delta \underset{\frown}{G}_L$ represents the power gained due to additional load $\Delta \underset{\frown}{G}_L$ and

$(2V + \Delta V) \underset{\frown}{G}_L \Delta V$ represents power loss due to voltage drop ΔV .

The balance of the opposing term represents the net power gain. At the stability limit, above terms cancel each other. Any increase in load demand represents the net reduction in power. Thus we can write the *p*-index as the ratio of power loss to the power gain due to additional load $\Delta \underset{\frown}{G}_L$ as,

$$p\text{-index} = -\frac{(2V + \Delta V) \underset{\frown}{G}_L}{(V + \Delta V)^2} \cdot \frac{\Delta V}{\Delta \underset{\frown}{G}_L}. \tag{208}$$

Considering the limiting case, $\Delta \underset{\frown}{G}_L \to 0, \Delta V \to 0$, we can write the *p*-index as:

$$p\text{-index} = -\frac{2 \underset{\frown}{G}_L}{V} \cdot \frac{dV}{d \underset{\frown}{G}_L}. \tag{209}$$

In order to compute $dV / d \underset{\frown}{G}_L$, we need to obtain the power and voltage sensitivities,

$$\frac{dV}{d\underset{\frown}{G}_L} = \frac{dV}{dP_L} \cdot \frac{dP_L}{d\underset{\frown}{G}_L}. \tag{210}$$

We can write. $P_L = V^2 \underset{\frown}{G}_L$, then we differentiate it to obtain,

$$\begin{aligned} dP_L &= V^2 d\underset{\frown}{G}_L + 2V\underset{\frown}{G}_L dV \\ \Rightarrow \frac{dP_L}{d\underset{\frown}{G}_L} &= V^2 + 2V\underset{\frown}{G}_L \frac{dV}{d\underset{\frown}{G}_L} \end{aligned} \tag{211}$$

Substituting the relation (211) in (210) we obtain,

$$\begin{aligned} \frac{dV}{d\underset{\frown}{G}_L} &= \frac{dV}{dP_L} \cdot \left[V^2 + 2V\underset{\frown}{G}_L \frac{dV}{d\underset{\frown}{G}_L} \right] \\ \Rightarrow \frac{dV}{d\underset{\frown}{G}_L} &= V^2 \frac{dV}{dP_L} + 2V\underset{\frown}{G}_L \left(\frac{dV}{dP_L} \cdot \frac{dV}{d\underset{\frown}{G}_L} \right) \\ \Rightarrow \frac{dV}{d\underset{\frown}{G}_L} \left[1 - 2V\underset{\frown}{G}_L \frac{dV}{dP_L} \right] &= V^2 \frac{dV}{dP_L} \\ \Rightarrow \frac{dV}{d\underset{\frown}{G}_L} &= \frac{V^2 \dfrac{dV}{dP_L}}{\left[1 - 2V\underset{\frown}{G}_L \dfrac{dV}{dP_L} \right]} \end{aligned} \tag{212}$$

Substituting the value of $\frac{dV}{d\underset{\frown}{G}_L}$ obtained in (212), with the *p*-index expression in (209), we obtain

$$p\text{-index} = -\frac{2\underset{\frown}{G}_L}{V} \cdot \frac{V V^2 \dfrac{dV}{dP_L}}{\left[1 - 2V\underset{\frown}{G}_L \dfrac{dV}{dP_L} \right]} = \frac{-2\underset{\frown}{G}_L V \dfrac{dV}{dP_L}}{1 - 2\underset{\frown}{G}_L V \dfrac{dV}{dP_L}} \quad . \tag{213}$$

While expressing the load as $\underset{\frown}{G}_L = P_L / V^2$, we can formulate *p*-index as:

$$p\text{-index} = = \frac{-2\dfrac{P_L}{V}\dfrac{dV}{dP_L}}{1 - 2\dfrac{P_L}{V}\dfrac{dV}{dP_L}}. \tag{214}$$

Let us consider the system loading increasing from P_{L0j}, Q_{L0j} to P_{Lj}, Q_{Lj}. Inverse

Jacobian matrix equation to represent increment in $\{\Delta\delta, \Delta V\}$ is given as:

$$\begin{bmatrix} \Delta\delta \\ \Delta V \end{bmatrix} = \begin{bmatrix} H & N \\ J & L \end{bmatrix} \cdot \begin{bmatrix} \Delta P_L \\ \Delta Q_L \end{bmatrix}. \tag{215}$$

From this equation we can write,

$$\begin{aligned} \Delta V_j &= \sum_{\substack{i \in L, \\ i \in G}} j_{ji} \Delta P_{Li} + \sum_{i \in L} l_{ji} \Delta Q_{Li} \\ \Rightarrow \frac{\Delta V_j}{\Delta P_{Lj}} \to \frac{dV_j}{dP_L} &= \sum_{\substack{i \in L, \\ i \in G}} j_{ji} \alpha_{ji} + \sum_{i \in L} l_{ji} \alpha_{ji} \beta_{ji} \end{aligned} \tag{216}$$

Here, $\alpha_{ji} = \frac{\Delta P_{Li}}{\Delta P_{Lj}}$ which forces the load increment to be same as of the present loading. Thus we can write,

$$\beta_j = \frac{\Delta Q_{Lj}}{\Delta P_{Lj}} = \tan\phi_j \tag{217}$$

Now if we consider $P_{Lj} = \lambda P_{L0}$, then we can represent the *p*-index as:

$$\text{p-index} = \frac{-2\frac{\lambda}{V}\frac{dV}{d\lambda}}{1 - 2\frac{\lambda}{V}\frac{dV}{d\lambda}} \tag{218}$$

One assumption while deriving the *p*-index is that the system generation and load will change at the same proportion. It also depends on the linearity of the $V - \underset{\frown}{G}_L$ relationship. The above derivation assumes that the power factor remains unchanged with an incremental increase in the load demand. The calculation of the *p*-index is convenient as it requires system states and node power.

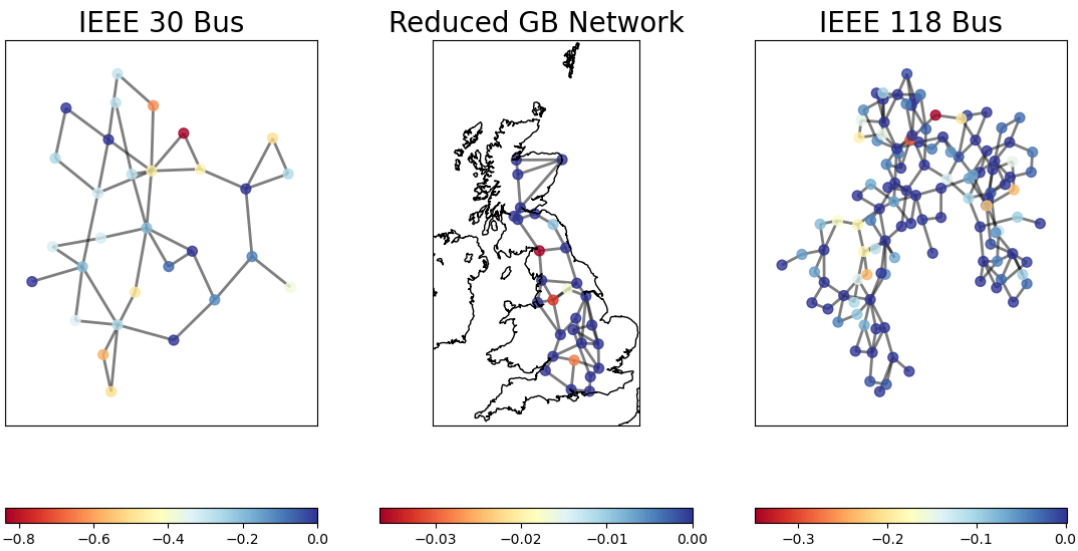

Figure 5-24: The p-index for the given networks, where red is the lowest and blue is the highest value for all the three networks. Unlike the tangent vector, the p-index does not categorize the adjacent nodes

The second graph signal used for analysis is the tangent vector stability indicator $dV/d\lambda$ [304], calculated from the iterations of continuation power flow at the operating point. Moreover, it is also used in the corrector method for continuation power flow. Under given load conditions, it is a better indicator of system voltage collapse than the right eigenvector of power flow Jacobian. The tangent vector can be readily computed from the real-time voltage measurement. As we observe in Figure 5-25, the tangent vector highlights the nodes which are adjacent to each other. The set of nodes having similar $dV/d\lambda$ exhibits finite modularity in the network. Moreover, it proves that the tangent vector excites the lower eigenmodes of the network Laplacian.

5.2.7 Spectral Filters

We can consider the power network a weighted undirected graph [305] $\mathcal{G} = \{V, E, w\}$, where V represents the set of vertices, E represents the edges and w_{ij} represents the edge weight between node *i* and *j*. We have considered different edge weights as absolute active power (P_{ij}), absolute reactive power (Q_{ij}) and complex admittance magnitude $|y_{ij}|$.

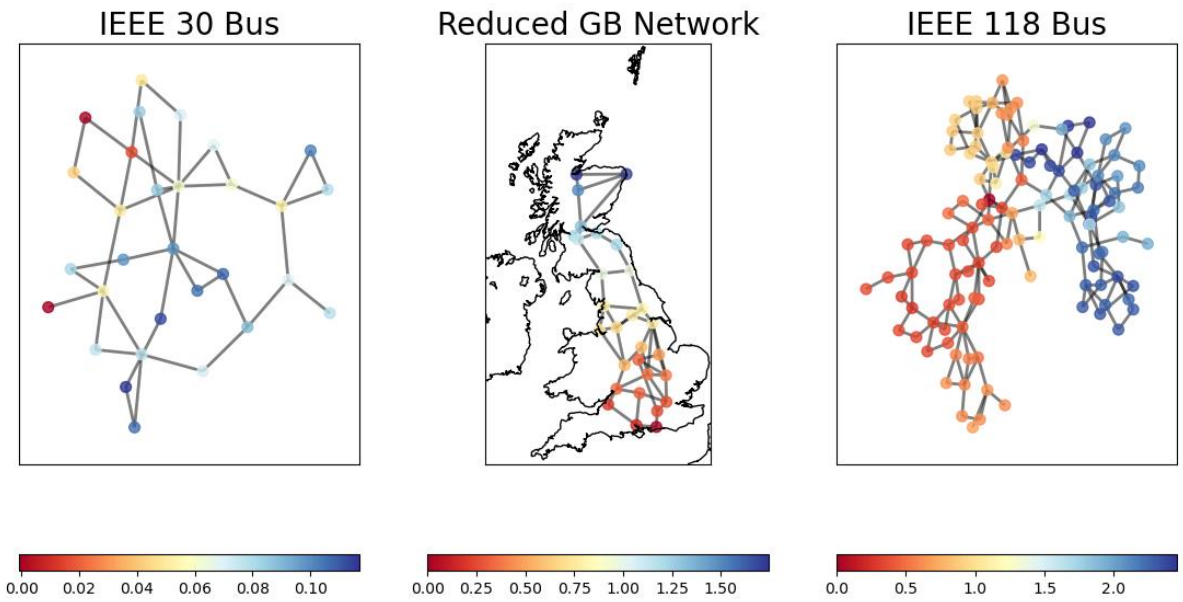

Figure 5-25: The tangent vector $dV/d\lambda$ for the given networks where red is the lowest and blue is the highest value for all the three networks. We observe that the adjacent nodes have similar values, and a sharp change is observed within the network

Here,

$$P_{ij} = \frac{\left|P_{T_{ij}}\right| + \left|P_{T_{ji}}\right|}{2},$$
$$Q_{ij} = \frac{\left|Q_{T_{ij}}\right| + \left|Q_{T_{ji}}\right|}{2}, \qquad (219)$$
$$y_{ij} = \sqrt{g_{ij}^2 + b_{ij}^2}.$$

Here $\{g_{ij}, b_{ij}\}$ represents the conductance and susceptance between the nodes *i* and *j*. $\{P_{T_{ij}}, Q_{T_{ij}}\}$ represents active and reactive power flow between the nodes *i* and *j*. They are represented as:

$$P_{T_{ij}} = V_i V_j y_{ij} \cos\left(\delta_i - \delta_j - \nu_{ij}\right),$$
$$Q_{T_{ij}} = V_i V_j y_{ij} \sin\left(\delta_i - \delta_j - \nu_{ij}\right). \qquad (220)$$

The term $P_{T_{ij}} \neq P_{T_{ji}}$ is due to the active power loss from the resistive part of the transmission line. A similar philosophy applies to reactive power transmission as well. Hence the terms are calculated based on the mean of the absolute sending and receiving active and reactive powers. Let us consider the eigenvalue and

eigenvector pair for the graph G is denoted as $\{(\lambda,u)\}_{l=0,1,\ldots,N-1}$ where λ represents the eigenvalue and u represents the corresponding eigenvector of the graph Laplacian $\mathcal{L}$, defined as:

$$\mathcal{L} = D - W, \tag{221}$$

where, $D = \mathrm{diag}(d_i)$, $d_i = \sum_{i \neq j} w_{ij}$ based on the active, reactive and admittance in (219). The spectral graph wavelet kernel $g : \mathbb{R}^+ \to \mathbb{R}^+$ such that it acts as a bandpass filter satisfying,

$$g(0) = 0 \text{ and } \lim_{x \to \infty} g(x) = 0. \tag{222}$$

The wavelet operator given as $T_g = g(\mathcal{L})$ which acts on the graph signal function $f(\cdot)$ to modulate the Fourier mode as:

$$T_g f(l) = g(\lambda_l)\hat{f}(l). \tag{223}$$

Employing the inverse Fourier transform yields

$$\begin{aligned}(T_g f)(m) &= \sum_{l=0}^{N-1} g(\lambda_l)\hat{f}(l)\chi_l(m), \\ &= \sum_{l=0}^{N-1} g(\lambda_l)\left[\sum_{n=1}^{N} \chi_l^*(n) f(n)\right]\chi_l(m).\end{aligned} \tag{224}$$

The wavelet operators at scale *t* are defined by $T_g^t = g(t\mathcal{L})$. In the spatial domain, i.e. the graph signal is discrete, and kernel *g* is continuous so that scaling is defined for any operator *t*. The continuous kernel is converted into spectral graph wavelets by localizing these continuous functions on the vertices of the graph by applying an impulse, i.e.

$$\psi_{t,n} = T_g^t \delta_n, \tag{225}$$

where, $\psi_{t,n}$ is the spectral wavelet from the operator at scale. The wavelet operator T_g^t,with the impulse function δ_n, is used expand in the graph domain to obtain the operator wavelet basis as:

$$\psi_{t,n}(m) = \sum_{l=0}^{N-1} g(\lambda_l)\chi_l^*(n)\chi_l(m). \tag{226}$$

The wavelet coefficients for a given graph signal $f(\cdot)$ is obtained by taking the inner product of the graph signal with the operator wavelet basis i.e.

$$W_f(t,n) = \langle \psi_{t,n}, f \rangle. \tag{227}$$

We can write the coefficient exploiting the orthonormality condition of the eigenvector as

$$W_f(t,n) = (T_g f)(n) = \sum_{l=0}^{N-1} g(t\lambda_l)\hat{f}(l)\chi_l(n), \tag{228}$$

The above relation $W_f(t,n)$ signifies how much of the wavelet $\psi_{t,n}$ is present in the signal *f*. The properties of the spectral filter and their characteristics are explained in Appendix C. Three types of filters are considered for analysis namely tight filters, non-tight filters and heat kernels as showed in Figure 5-26, Figure *5-27* and Figure 5-28 respectively.

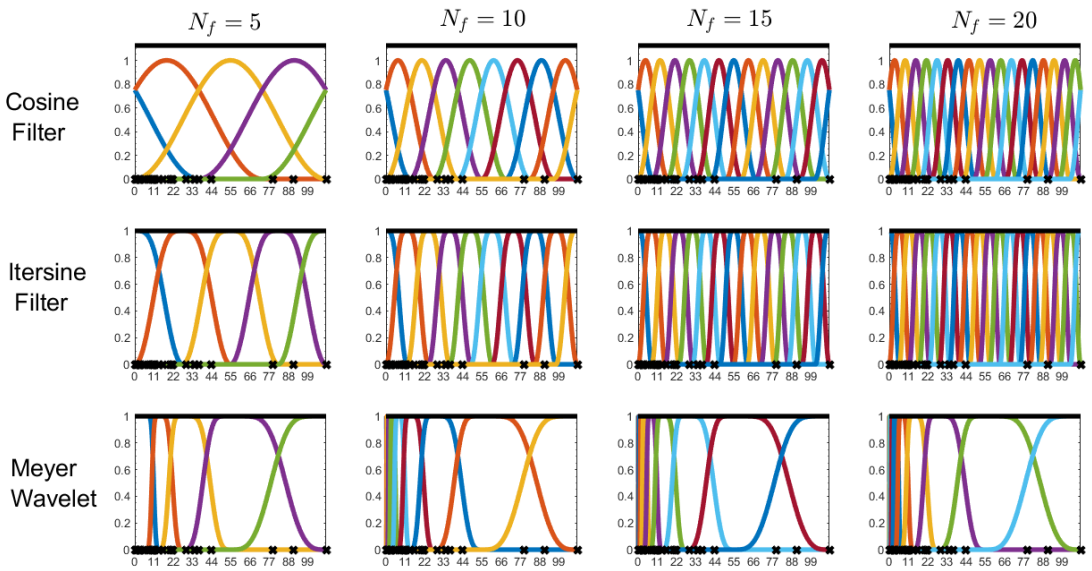

Figure 5-26: The spectrum of the cosine, itersine and Meyer wavelets as tight filters, where the energy density of graph signal is preserved in the spectral space. The features become very similar with the increase in the number of filters.

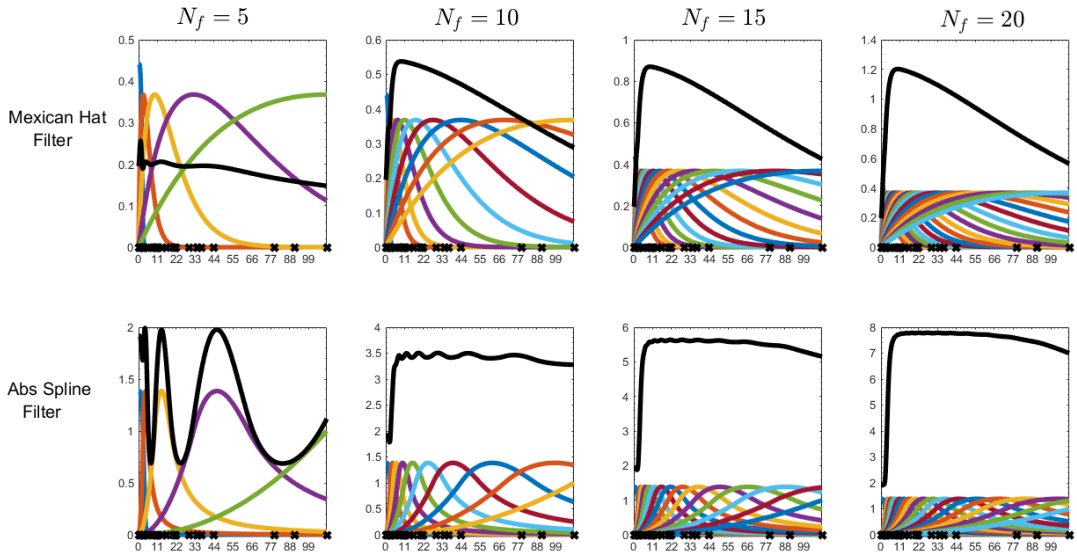

Figure 5-27: The spectrum of Mexican hat, abs spline filter as a part of the non-tight filter, which considers the skewed distribution of the eigenvalues. Like tight filters, the overall characteristics become similar with the increase in filters

5.2.8 Hierarchical Clustering and Evaluation

Hierarchical clustering is performed based on the features obtained from the convolution of the graph signal with various spectral features as described above. Two reference labels are considered for comparing the nodal clusters. In the first case, all the four label categories A_{cat} are considered, as shown in Figure 5-19 In the second case, the binary labels A_{crit}, critical and non-critical, is considered. The comparison is performed using Fowlkes Mallows (FM) Score [306], which gives an appropriate measure of the overlap between the clusters A_{hc} obtained from hierarchical clustering.

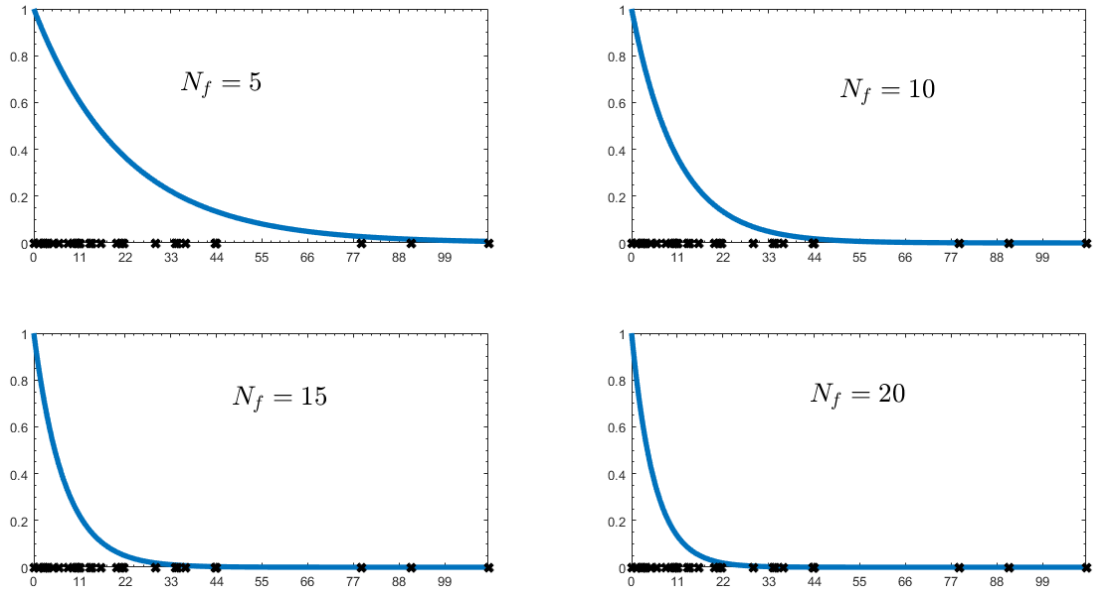

Figure 5-28: The spectrum of the heat kernel with variation in N_f, as with its increase it starts acquiring characteristics as a low-pass eigenvalue filter.

Hierarchical clustering forms a hierarchy of clusters where it broadly falls into two categories of node classification: bottom-up called agglomerative and top-down approach called divisively. The cluster merging and splits occur to satisfy a specific objective function. The clustering is presented in the form of a dendrogram. The criteria used here for merging and dividing the cluster is the Wards criterion, based on the variance of the clusters involved. The specific criteria obtain the till threshold when the hierarchical structure is valid.

The similarity of hierarchical clusterings is measured depending on the topologies of two trees representing the clusters, the terminal node labels, and the internal node height. The configuration $\left(k, B_k\right)$ has some interesting observations for both null and non-null clustering cases. The values of B_k are studied for the different variance of the normal distribution. The matrix $\mathbf{M}$ becomes sparser with an increase in the number of clusters. The hierarchical cluster overlap is measured using Fowlkes Mallows Score [306]. Let us consider A_1 be the cluster of the critical and non-critical nodes while A_2 be the hierarchical clusters obtained from spectral filters for n objects. Let us consider that there are $k = 2,\ldots,n-1$ clusters for each tree. For each value of k, we can label the clusters of A_1 and A_2 to form the matrix $\mathbf{M} = \left[\underset{\sim}{m}_{ij}\right]$ for $\left(i = 1,\ldots,k; j = 1,\ldots,k\right)$ where $\underset{\sim}{m}_{ij}$

represents the number of common objects between the i^{th} cluster of A_1 and j^{th} cluster of A_2. The association can be defined using the following measure

$$B_k = \underline{T}_k \Big/ \sqrt{\underline{P}_k \underline{Q}_k}, \tag{229}$$

where,

$$\begin{aligned} \underline{T}_k &= \sum_{i=1}^{k}\sum_{j=1}^{k} \underset{\sim}{m}_{ij}^2 - \underline{n}, m_{i\cdot} = \sum_{j=1}^{k} \underset{\sim}{m}_{ij}, m_{\cdot j} = \sum_{i=1}^{k} \underset{\sim}{m}_{ij}, m_{\cdot\cdot} = \underset{\sim}{n} = \sum_{i=1}^{k}\sum_{j=1}^{k} \underset{\sim}{m}_{ij}, \\ \underline{P}_k &= \sum_{i=1}^{k} m_{i\cdot}^2 - \underline{n}, \underline{Q}_k = \sum_{i=1}^{k} m_{\cdot j}^2 - \underline{n}. \end{aligned} \tag{230}$$

5.2.9 Clustering Results

We observe a specific pattern in Figure 5-29, Figure *5-30* and Figure *5-31* regarding the FM score.

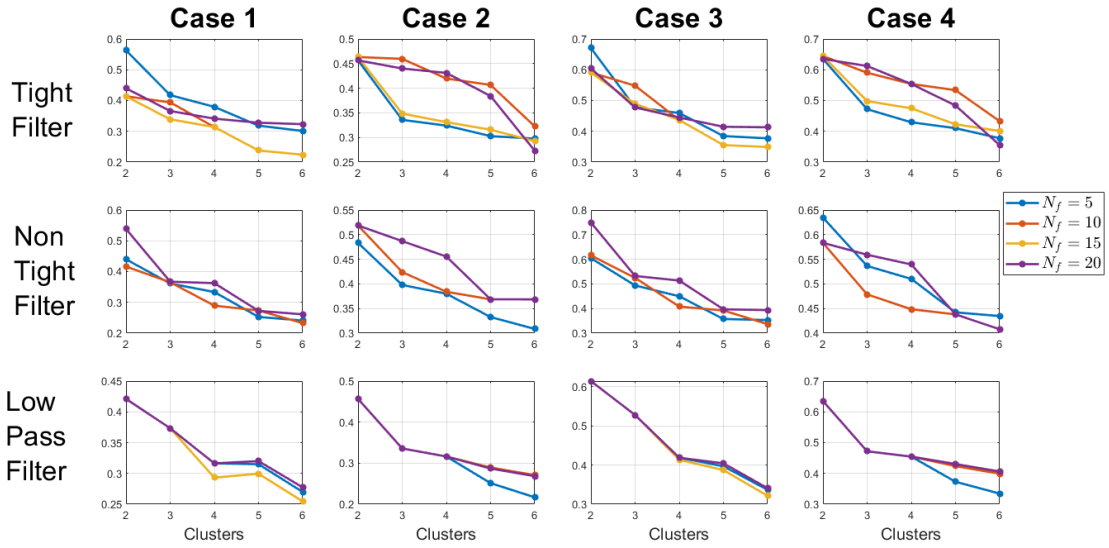

Figure 5-29: The variation of the Fowlkes Mallows Score for different cases with variation in the community size for tight, non-tight and low pass heat kernel filters for IEEE 30-bus power network. The highest value is obtained for non-tight filter with tangent vector $\left(dV/d\lambda\right)$ as the graph signal

The scores obtained by comparing A_{hc} with A_{cat} is much lower when compared with A_{crit}. It suggests that the nodes obtained from hierarchical clusters have a better overlap with the critical and non-critical nodes than categorical nodes. A

higher value of B_k also confirms the fact that the critical nodes form a natural hierarchy with the non-critical nodes [297]. Moreover, a higher score is attributed to the non-zero elements in the matrix $\mathbf{M}$ formed from A_{hc} with A_{crit} rather than A_{cat}.

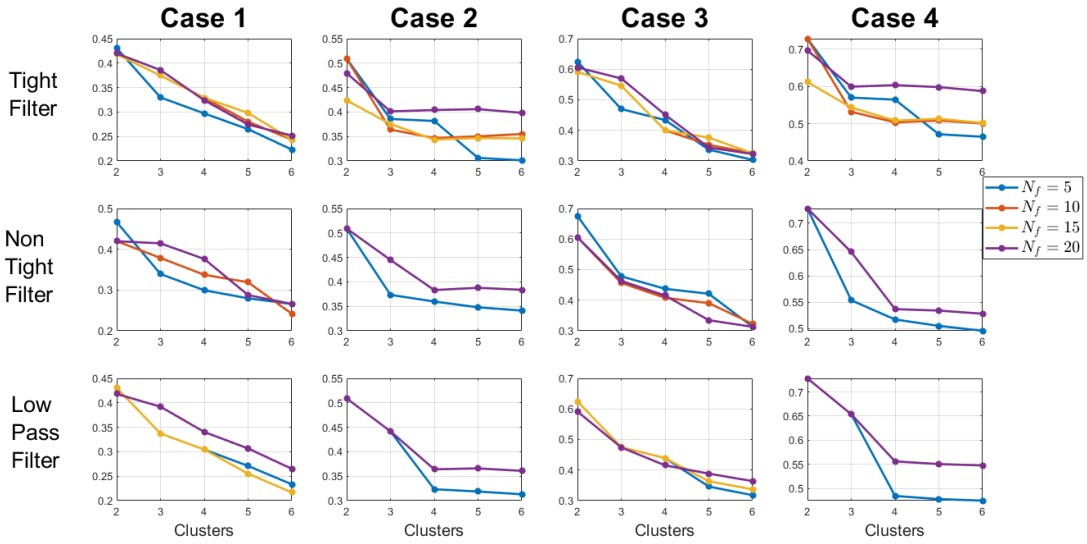

Figure 5-30: The variation of the Fowlkes Mallows Score for different cases with variation in the community size for tight, non-tight and low pass heat kernel filters for GB reduced power network. The highest value is obtained for non-tight filter with p-index as the graph signal, as it incorporates the critical nodes within the large cluster.

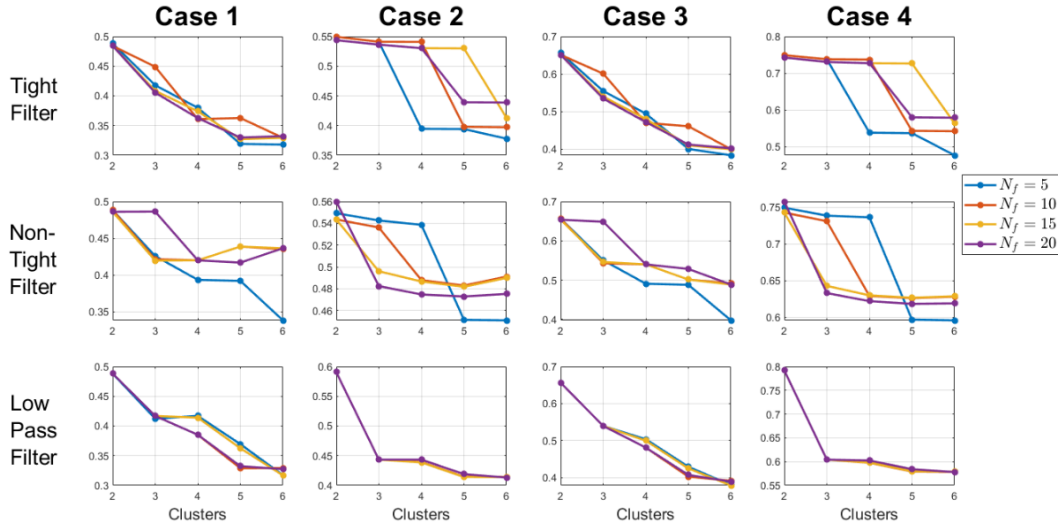

Figure 5-31: The variation of the Fowlkes Mallows Score for different cases with variation in the community size for tight, non-tight and low pass heat kernel filters IEEE 118-bus power network. The highest value across communities is obtained for tight filter with p-index as the graph signal, as it incorporates the critical nodes within the large cluster.

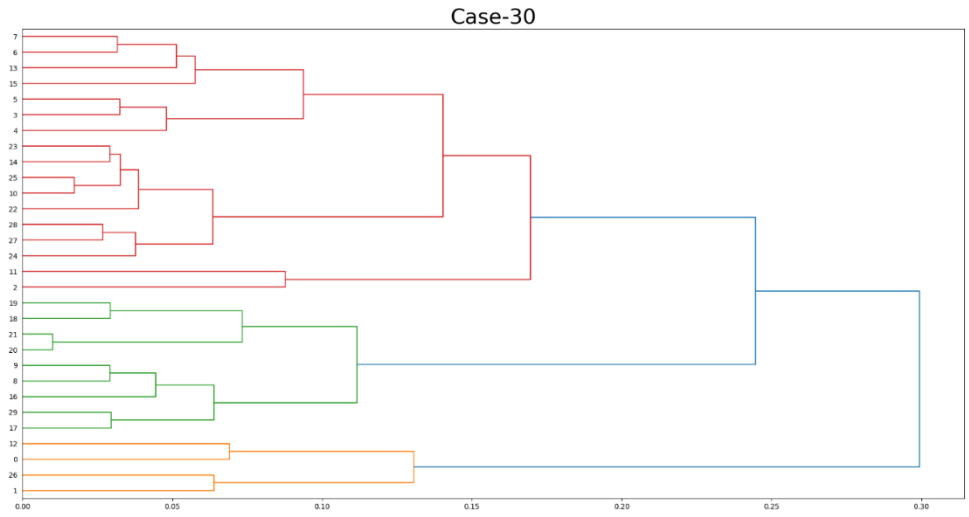

Figure 5-32: The dendogram depicting the agglomerative hierarchy of the nodes for the features obtained from non-tight filter and with tangent vector $\left(dV/d\lambda\right)$ as the graph signal. Node 26 does not fall under the same category if the dendogram is broadly divided into two categories

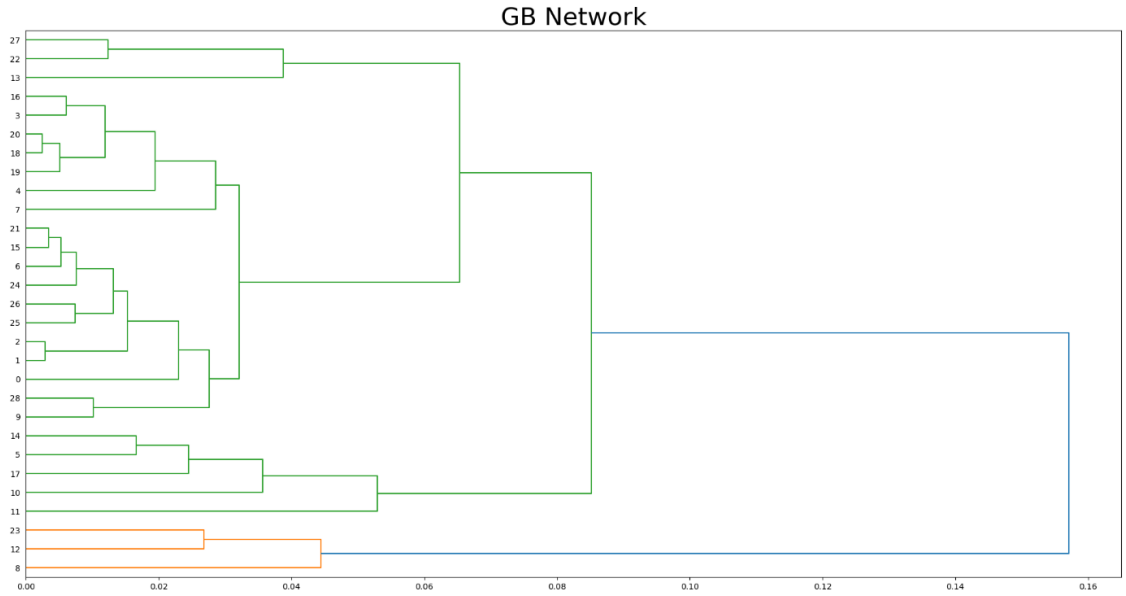

Figure 5-33: The dendogram depicting the agglomerative hierarchy of the nodes for the features obtained from non-tight filter with p-index as the graph signal, where the critical nodes are fall in the same broad category of classification.

We observe the cluster based on the score B_k between A_{crit} and the features obtained from different graph signals as presented in Figure 5-24 and Figure *5-25*. From Figure 5-29, Figure *5-30* and Figure *5-31*, a higher Fowlkes Mallows score, when the overlap between two clusters of A_{hc} is compared with A_{crit}. The score

B_k decreases in most cases when the number of communities increases, as it is a typical pattern for sub-optimal clusters [306].

We find that the optimal cluster, generated by the *p*-index, contain the critical nodes as a part of the large cluster. However, the optimal clusters in the case of features generated from tangent vector contain critical nodes as a part of diverse communities, as evident from the dendrogram plot in Figure 5-32, Figure *5-33* and Figure 5-34. The critical nodes are divided into two classes within the same cluster. However, we find an exception for the IEEE 30 bus network, where one critical node belongs to a different cluster. Hence clusters obtained from the tangent vector $dV_i/d\lambda$ has the best overlap with A_{crit}.

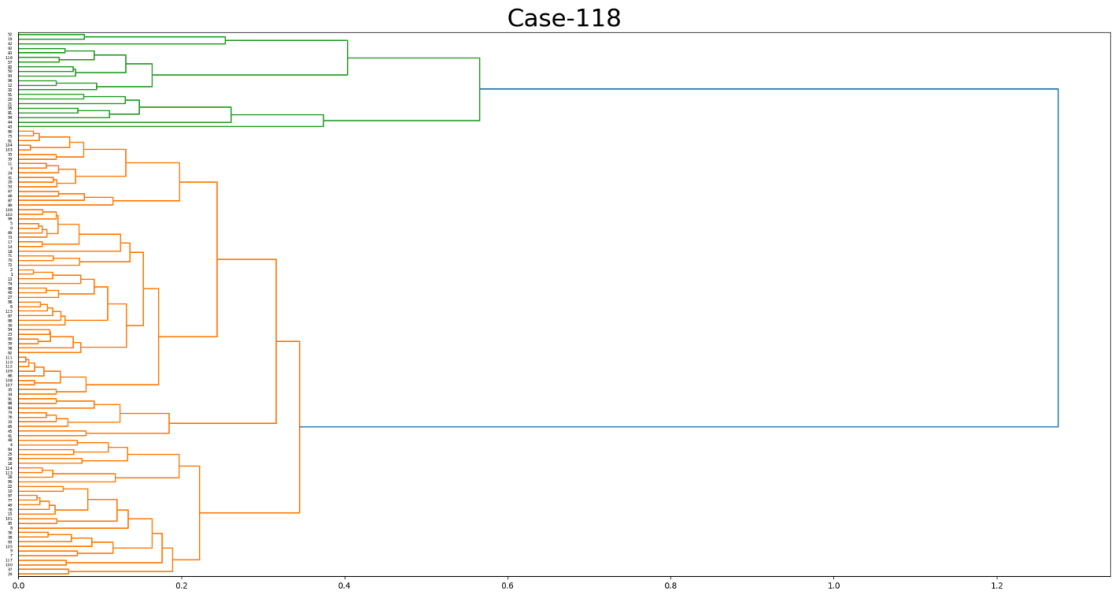

Figure 5-34: The dendogram depicting the agglomerative hierarchy of the nodes for the features obtained from tight filter with *p*-index as the graph signal for IEEE 118-bus power network, where the critical nodes are fall in the same broad category of classification.

The clusters obtained from the tangent vector are similar to those obtained from spectral clustering, which focuses on partitioning the network with a minimal number of edges between the communities [307]. Overall we observed that the optimal clusters obtained from the *p*-index have better overlap with the A_{crit} as evident from the higher B_k. As we increase the number of filters or the low-pass eigen filter characteristics of the heat kernel filter, we hardly observe any improvement in B_k when analyzing the optimal cluster. However, an exception

exists where the value is higher for 2 clusters for reduced GB network in the case of 20 non-tight filters compared with the lower numbers. The change in $(B_k)_{\text{opt}}$ is small in the case of tight and non-tight filter and negligible in case of heat kernel filter with change in the filter properties. We observe that the value B_k falls rapidly for most cases with increased communities. The observed is steeper when the number of filters is less, i.e. $N_f = 5$ which can be attributed to higher variance in the features [306]. Consequently, the features generated from the larger number of filters have lower variance; hence the fall with an increase in communities is lower. Moreover, the network also becomes disassortative with the increase in clusters [290]. The critical nodes are more likely to stay within the same clusters if more filters generate the features. However, in some cases, the characteristics are similar and close for $N_f = 5$ and $N_f = 20$, mainly when the features are generated from the tangent vector. The similarity suggests that the membership of the critical nodes in the clusters will likely be similar for $N_f = 5$ and $N_f = 20$ due to the lower variance features generated by the tangent vector. Moreover, the community structure of the nodes in the clusters generated by the tangent vector also explains lower variance. However, the clusters A_{hc} generated by the *p*-index has a better GM score than the one generated by the tangent vector. We do observe an exception for the case of IEEE 118 bus network, where the features are generated by *p*-index, and the score remains relatively similar even with the increase in clusters, suggesting that the critical nodes remain within the same cluster, even though the network is divided into several pockets of nodes. We also observe that the optimal overlap between the clusters is obtained for the non-tight filter compared to the tight filter or the heat kernel, which suggests that the weighting of different eigenmodes has to be asymmetrical, with more focus eigenvectors on the fewer but higher eigenmodes.

Thus the community of non-critical and critical nodes can be utilized to improve the resiliency of the power network [299]. However, centralized planning is more beneficial to decentralized planning, evident from the high FM score obtained from two clusters rather than a higher number of clusters. A single large cluster of critical and non-critical nodes can improve the network resiliency to nodal attack, especially for reduced GB network and IEEE 118 bus network. The

proactive measures [302] include substation relocation and transmission line rerouting, selectively converting the overhead lines to underground lines and upgrading the transmission lines. In the case of the reduced GB network, these corrective measures can be implemented in the nodes belonging in the rural regions, which belong to the same cluster of the critical nodes placed primarily in urban England and Scotland [299].

In case of prioritized investment and resilience improvement in a specific region, decentralized measures like distributed generation, demand-side management and energy storage [308] can be implemented in specific regions based on the nodes obtained from a higher number of clusters. In cases where higher FM scores are obtained and critical nodes are in different clusters like in the IEEE 30 bus network, the corrective measures can [309] be focus on strengthening a specific region prone to extreme climate conditions. However, this will not improve the overall network resiliency compared to the planned strategy on a larger cluster of nodes.

5.2.10 Conclusion

Our solution helps find the weak/critical community of nodes in a power network exploiting the eigen spectrum of the weighted Laplacian and considering the nodal influence. It shows that if we divide the network into two clusters, with the help of nodal and edge properties, we are more likely to obtain the critical nodes, along with another set of nodes (category 3 and 4 as described earlier), which can be used to improve the resilience of the network to intentional attacks.

Chapter 6 Conclusion and Future Works

6.1 Major Contribution and Results from the Thesis

6.1.1 Chapter 3

PSO serves as an efficient optimizer for maintaining control performance of the LFC loops with interrupted packet transmission as DoS cyberattacks and random delays. The response of the LFC in the smart grid is more similar to real data in case of nonstationary profiles than the stationary profiles.

Design of state feedback controller and observer gain obtained after solving the LMI can ensure stable operation under bounded load disturbance and FDI attack. The combination of decentralized EV in the LFC loop leads to stable operation at higher sampling time, utilizing lower communication bandwidth. However, the system with decentralized EV configuration is susceptible to parametric variations like the demand response time delay or increase in packet drop rate as it can cause higher frequency fluctuations and instability.

The data used for the analysis consists of the response of heterogeneous consumers for different price fluctuations based on the power balance of the grid. The statistical and machine learning methods such as feature selection and regression analysis are performed to find relationship between the input parameters with the eigenvalue and system stability conditions.

6.1.2 Chapter 4

Sensitivity of energy storage device energy storage operations to trips as it is located near the controlled generation source, it works in extreme modes with lower sensitivity to individual line trips and higher sensitivity to the tripping of generators, especially with high ramping capacity. When the energy storage device is located near the load bus, it is less sensitive to the generator trips and highly sensitive to the tripping of lines connecting the load bus to the generators. When the energy storage device is located near the stochastic renewable energy source, the operation is uniform with more similarity due to the generator trips and is recommended for placement. The energy storage operation is invariant to

the trips of the lines, not connecting to the loads irrespective of its position in the grid.

6.1.3 Chapter 5

Statistical model obtained from the smaller power network indicate that the nodes which are in the path of shortest power flow within the network along with the nodes which are in the higher end of the eigenvalue spectrum play a significant role in deteriorating the VSI of the network. However, the loading margin of the network improves if the network closeness and centrality decrease after nodal attack. This suggests that the community structure of the network is robust to nodal attacks.

Degree centrality primarily influences the VSM of the power network only when the latter has a unimodal structure. The mean prediction of non-critical nodes is under-estimated while the critical nodes are overestimated. The networks having primarily HV transmission nodes, there is a significant difference in the mean prediction between the LV and HV nodes.

The weak/critical community of nodes are obtained in a power network utilizing the eigen spectrum of the weighted Laplacian and considering the nodal influence. It shows that if we divide the network into two clusters, with the help of nodal and edge properties, we are more likely to obtain the critical nodes, along with non-critical nodes, which can be used to improve the resilience of the network to intentional attacks.

6.2 Future Works

6.2.1 Networked and Stochastic Control System

System state and disturbance vectors can be approximated and the integral term of the Ito stochastic noise can be eliminated while designing the controller. Stability criterion can be derived by considering different noises like Levy noise. The parameters of stochastic differential equation representing RES data in 0 can be obtained. The stability of the networked control system for smart grid can be derived by considering model based event triggered control with DoS attacks and stochastic deception attacks. Security conditions are derived under nonlinear

smart grid models. The control of the smart grid can be extended to multiple areas while considering cyber physical constraints as considered for the control of autonomous vehicles while deriving the stability criteria for the distributed controllers or multi agent reinforcement learning algorithms. Detailed microgrid and inverter models can be incorporated to design controllers.

6.2.2 Voltage and Frequency Stability in Complex Network

The concept of voltage stability in static networks can be extended to dynamic networks, where the nodes will have dynamics. Hence, the concept of voltage and frequency stability of the power networks can be considered. As we have seen in Section 3.3.3 the power grid can be analyzed using a Kuramoto oscillator which can be extended on a network scale by considering a Kron reduced model. The Kuramoto model and stability criterion can derived for the voltage and frequency stability. The dynamics of the inverters can be incorporated for analyzing the voltage and frequency stability. The uncertainty analysis can be considered while considering the mix of low inertia inverters and high inertia components and incorporating the communication aspects in the smart grid networks. The concept of digital twin utilizing the dynamic and the spectral features of the power network can also be used for stability and resiliency analysis.

6.2.3 Uncertainty Quantification in Dynamic Complex Power Network

The role of internal dynamics of the nonlinear systems, network topology, and uncertainty statistics can be extended in the work. Similarly, it is difficult to understand the uncertainty of the operations of the network while considering all the nodes. However, certain nodes can be selected to predict the system configuration with lower uncertainty. Similarly, the nonlinear dynamics of the generators and the economic or communication network can also be combined to understand the vulnerability of the overall system. The risk can be quantified using uncertainty. The uncertainty models of link failures can be utilized for quantifying its effect on the resilience of the network.

Chapter 7 Bibliography

[1] H. Farhangi, “The path of the smart grid,” *IEEE Power and Energy Magazine*, vol. 8, no. 1, pp. 18–28, 2009.

[2] C. Zhang, J. Wu, M. Cheng, Y. Zhou, and C. Long, “A bidding system for peer-to-peer energy trading in a grid-connected microgrid,” *Energy Procedia*, vol. 103, pp. 147–152, 2016.

[3] M. McGranaghan, D. Houseman, L. Schmitt, F. Cleveland, and E. Lambert, “Enabling the integrated grid: leveraging data to integrate distributed resources and customers,” *IEEE Power and Energy Magazine*, vol. 14, no. 1, pp. 83–93, 2016.

[4] M. H. Syed, E. Guillo-Sansano, S. M. Blair, G. M. Burt, H. Brunner, O. Gehrke, J. E. Rodriguez-Seco, and others, “Laboratory infrastructure driven key performance indicator development using the smart grid architecture model,” *CIRED-Open Access Proceedings Journal*, vol. 2017, no. 1, pp. 1866–1870, 2017.

[5] G. Schuh, J. Fluhr, M. Birkmeier, and M. Sund, “Information system architecture for the interaction of electric vehicles with the power grid,” in *Networking, Sensing and Control (ICNSC), 2013 10th IEEE International Conference on*, 2013, pp. 821–825.

[6] M. Kammerstetter, L. Langer, F. Skopik, and W. Kastner, “Architecture-driven smart grid security management,” in *Proceedings of the 2nd ACM Workshop on Information Hiding and Multimedia Security*, 2014, pp. 153–158.

[7] A. Angioni, S. Lu, H. Hooshyar, I. Cairo, S. Repo, F. Ponci, D. Della Giustina, A. Kulmala, A. Dedè, A. Monti, and others, “A distributed automation architecture for distribution networks, from design to implementation,” *Sustainable Energy, Grids and Networks*, 2017.

[8] C. Dänekas and J. M. González, “Requirements Engineering for Smart Grids,” in *Standardization in Smart Grids*, Springer, 2013, pp. 15–37.

[9] S. Khayyam, F. Ponci, J. Goikoetxea, V. Recagno, V. Bagliano, and A. Monti, “Railway energy management system: Centralized-decentralized automation architecture,” *IEEE Transactions on Smart Grid*, vol. 7, no. 2, pp. 1164–1175, 2016.

[10] N. Etherden, V. Vyatkin, and M. H. Bollen, “Virtual power plant for grid services using IEC 61850,” *IEEE Transactions on Industrial Informatics*, vol. 12, no. 1, pp. 437–447, 2016.

[11] A. Leonardi, K. Mathioudakis, A. Wiesmaier, and F. Zeiger, “Towards the smart grid: substation automation architecture and technologies,” *Advances in Electrical Engineering*, vol. 2014, 2014.

[12] G. López, P. Moura, J. I. Moreno, and J. M. Camacho, “Multi-faceted assessment of a wireless communications infrastructure for the green neighborhoods of the smart grid,” *Energies*, vol. 7, no. 5, pp. 3453–3483, 2014.

[13] E. Molina, E. Jacob, J. Matias, N. Moreira, and A. Astarloa, “Using software defined networking to manage and control IEC 61850-based systems,” *Computers & Electrical Engineering*, vol. 43, pp. 142–154, 2015.

[14] Z. Ma, A. Hudic, A. Shaaban, and S. Plosz, “Security viewpoint in a reference architecture model for cyber-physical production systems,” in *Security and Privacy Workshops (EuroS&PW), 2017 IEEE European Symposium on*, 2017, pp. 153–159.

[15] A. Srivastava, T. Morris, T. Ernster, C. Vellaithurai, S. Pan, and U. Adhikari, “Modeling cyber-physical vulnerability of the smart grid with incomplete information,” *IEEE Transactions on Smart Grid*, vol. 4, no. 1, pp. 235–244, 2013.

[16] A. Gopstein, C. Nguyen, C. O’Fallon, N. Hastings, D. Wollman, and others, *NIST framework and roadmap for smart grid interoperability standards, release 4.0*. Department of Commerce. National Institute of Standards and Technology, 2021.

[17] D. Von Dollen, “Report to NIST on the smart grid interoperability standards roadmap,” *Electric Power Research Institute (EPRI) and National Institute of Standards and Technology*, 2009.

[18] N. Framework, “Roadmap for smart grid interoperability standards,” 2010.

[19] “IEEE Smart Grid Vision for Computing: 2030 and Beyond,” *IEEE Standards*, pp. 1–133, 2013.

[20] G. Simard, “IEEE Grid Vision 2050,” *IEEE Standards*, pp. 1–93, 2013.

[21] M. A. van Amelsvoort, “SG-rating-Putting values on smart grid architectures,” *Information Technology*, vol. 58, no. 1, pp. 29–36, 2016.

[22] M. Albano, L. L. Ferreira, and L. M. Pinho, “Convergence of Smart Grid ICT architectures for the last mile,” *IEEE Transactions on Industrial Informatics*, vol. 11, no. 1, pp. 187–197, 2015.

[23] C.-C.-E. S. G. C. Group, “Smart grid reference architecture,” 2012.

[24] C. Dänekas, C. Neureiter, S. Rohjans, M. Uslar, and D. Engel, “Towards a model-driven-architecture process for smart grid projects,” in *Digital Enterprise Design & Management*, Springer, 2014, pp. 47–58.

[25] B. Huang, X. Bai, Z. Zhou, Q. Cui, D. Zhu, and R. Hu, “Energy informatics: Fundamentals and standardization,” *ICT Express*, vol. 3, no. 2, pp. 76–80, 2017.

[26] M. Faschang, S. Cejka, M. Stefan, A. Frischenschlager, A. Einfalt, K. Diwold, F. P. Andrén, T. Strasser, and F. Kupzog, “Provisioning, deployment, and operation of smart grid applications on substation level,” *Computer Science-Research and Development*, vol. 32, no. 1–2, pp. 117–130, 2017.

[27] I. G. Mason, S. Page, and A. Williamson, “A 100% renewable electricity generation system for New Zealand utilising hydro, wind, geothermal and biomass resources,” *Energy Policy*, vol. 38, no. 8, pp. 3973–3984, 2010.

[28] E. Pursiheimo, H. Holttinen, and T. Koljonen, “Path toward 100\% renewable energy future and feasibility of power-to-gas technology in Nordic countries,” *IET Renewable Power Generation*, vol. 11, no. 13, pp. 1695–1706, 2017.

[29] B. Römer, K. Aldonza, Y. Julliard, and O. Lewis, “Planning 100% renewable energy islands: The case of the Caribbean island of Montserrat,” *CIRED-Open Access Proceedings Journal*, vol. 2017, no. 1, pp. 2488–2492, 2017.

[30] B. Cosic, G. Krajavcic, and N. Duic, “A 100% renewable energy system in the year 2050: The case of Macedonia,” *Energy*, vol. 48, no. 1, pp. 80–87, 2012.

[31] D. Connolly and B. V. Mathiesen, “A technical and economic analysis of one potential pathway to a 100% renewable energy system,” *International Journal of Sustainable Energy Planning and Management*, vol. 1, pp. 7–28, 2014.

[32] H. Lund and B. V. Mathiesen, “Energy system analysis of 100% renewable energy systems—The case of Denmark in years 2030 and 2050,” *Energy*, vol. 34, no. 5, pp. 524–531, 2009.

[33] D. Connolly, H. Lund, B. V. Mathiesen, and M. Leahy, “The first step towards a 100% renewable energy-system for Ireland,” *Applied Energy*, vol. 88, no. 2, pp. 502–507, 2011.

[34] M. Esteban, Q. Zhang, and A. Utama, “Estimation of the energy storage requirement of a future 100% renewable energy system in Japan,” *Energy Policy*, vol. 47, pp. 22–31, 2012.

[35] M. Z. Jacobson, M. A. Delucchi, G. Bazouin, Z. A. Bauer, C. C. Heavey, E. Fisher, S. B. Morris, D. J. Piekutowski, T. A. Vencill, and T. W. Yeskoo, “100% clean and renewable wind, water, and sunlight (WWS) all-sector energy roadmaps for the 50 United States,” *Energy & Environmental Science*, vol. 8, no. 7, pp. 2093–2117, 2015.

[36] M. J. Alexander, P. James, and N. Richardson, “Energy storage against interconnection as a balancing mechanism for a 100% renewable UK electricity grid,” *IET Renewable Power Generation*, vol. 9, no. 2, pp. 131–141, 2014.

[37] J. Matevosyan, J. MacDowell, N. Miller, B. Badrzadeh, D. Ramasubramanian, A. Isaacs, R. Quint, E. Quitmann, R. Pfeiffer, H. Urdal, and others, “A future with inverter-based resources: Finding strength from traditional weakness,” *IEEE Power and Energy Magazine*, vol. 19, no. 6, pp. 18–28, 2021.

[38] N. Grid, “Non-BM balancing services and volumes reports,” 2017. [Online]. Available: https://www.nationalgrideso.com/document/107511/download. [Accessed: Sep-2020].

[39] S.-C. Chan, K. M. Tsui, H. Wu, Y. Hou, Y.-C. Wu, and F. F. Wu, “Load/price forecasting and managing demand response for smart grids: Methodologies and challenges,” *IEEE Signal Processing Magazine*, vol. 29, no. 5, pp. 68–85, 2012.

[40] B. Schäfer, M. Matthiae, M. Timme, and D. Witthaut, “Decentral smart grid control,” *New Journal of Physics*, vol. 17, no. 1, p. 015002, 2015.

[41] W. F. Pickard and D. Abbott, “Addressing the intermittency challenge: Massive energy storage in a sustainable future,” *Proceedings of the IEEE*, vol. 100, no. 2, p. 317, 2012.

[42] D. H. Doughty, P. C. Butler, A. A. Akhil, N. H. Clark, and J. D. Boyes, “Batteries for large-scale stationary electrical energy storage,” *The Electrochemical Society Interface*, vol. 19, no. 3, pp. 49–53, 2010.

[43] C. E. Murillo-Sánchez, R. D. Zimmerman, C. L. Anderson, and R. J. Thomas, “Secure planning and operations of systems with stochastic sources, energy storage, and active demand,” *IEEE Transactions on Smart Grid*, vol. 4, no. 4, pp. 2220–2229, 2013.

[44] D. Pozo, J. Contreras, and E. E. Sauma, “Unit commitment with ideal and generic energy storage units,” *IEEE Transactions on Power Systems*, vol. 29, no. 6, pp. 2974–2984, 2014.

[45] P. Denholm, E. Ela, B. Kirby, and M. Milligan, “Role of energy storage with renewable electricity generation,” 2010.

[46] M. Aneke and M. Wang, “Energy storage technologies and real life applications-A state of the art review,” *Applied Energy*, vol. 179, pp. 350–377, 2016.

[47] S. Chu and A. Majumdar, “Opportunities and challenges for a sustainable energy future,” *Nature*, vol. 488, no. 7411, pp. 294–303, 2012.

[48] Z. Lin, F. Wen, and Y. Xue, “A restorative self-healing algorithm for transmission systems based on complex network theory,” *IEEE Transactions on Smart Grid*, vol. 7, no. 4, pp. 2154–2162, 2016.

[49] M. Aunedi, K. Wills, T. Green, and G. Strbac, “Net-Zero GB electricity: cost-optimal generation and storage mix,” 2021.

[50] N. Grid, “Connecting to a Net Zero Future,” 2021. [Online]. Available: https://www.nationalgrid.com/document/141856/download.

[51] “Networks Options Assessment.” [Online]. Available: https://www.nationalgrideso.com/document/233081/download.

[52] P. Pourbeik, P. S. Kundur, and C. W. Taylor, “The anatomy of a power grid blackout-root causes and dynamics of recent major blackouts,” *IEEE Power and Energy Magazine*, vol. 4, no. 5, pp. 22–29, 2006.

[53] P. Kundur, J. Paserba, V. Ajjarapu, G. Andersson, A. Bose, C. Canizares, N. Hatziargyriou, D. Hill, A. Stankovic, C. Taylor, and others, “Definition and classification of power system stability IEEE/CIGRE joint task force on stability terms and definitions,” *IEEE Transactions on Power Systems*, vol. 19, no. 3, pp. 1387–1401, 2004.

[54] R. M. M. Pereira, C. M. M. Ferreira, and F. M. Barbosa, “Comparative study of STATCOM and SVC performance on dynamic voltage collapse of an electric power system with wind generation,” *IEEE Latin America Transactions*, vol. 12, no. 2, pp. 138–145, 2014.

[55] Y. Amrane, M. Boudour, and M. Belazzoug, “A new optimal reactive power planning based on differential search algorithm,” *International Journal of Electrical Power & Energy Systems*, vol. 64, pp. 551–561, 2015.

[56] I. Musirin and T. A. Rahman, “Estimating maximum loadability for weak bus identification using FVSI,” *IEEE Power Engineering Review*, vol. 22, no. 11, pp. 50–52, 2002.

[57] I. Pan and S. Das, “Fractional-order load-frequency control of interconnected power systems using chaotic multi-objective optimization,” *Applied Soft Computing*, vol. 29, pp. 328–344, 2015.

[58] I. Pan and S. Das, “Fractional order fuzzy control of hybrid power system with renewable generation using chaotic PSO,” *ISA Transactions*, vol. 62, pp. 19–29, 2016.

[59] I. Pan and S. Das, “Fractional order AGC for distributed energy resources using robust optimization,” *IEEE Transactions on Smart Grid*, vol. 7, no. 5, pp. 2175–2186, 2015.

[60] J. Pahasa and I. Ngamroo, “Coordinated control of wind turbine blade pitch angle and PHEVs using MPCs for load frequency control of microgrid,” *IEEE Systems Journal*, vol. 10, no. 1, pp. 97–105, 2014.

[61] X. Qi, Y. Bai, H. Luo, Y. Zhang, G. Zhou, and Z. Wei, “Fully-distributed Load Frequency Control Strategy in an Islanded Microgrid Considering Plug-In Electric Vehicles,” *Energies*, vol. 11, no. 6, p. 1613, 2018.

[62] A. Safari, F. Babaei, and M. Farrokhifar, “A load frequency control using a PSO-based ANN for micro-grids in the presence of electric vehicles,” *International Journal of Ambient Energy*, pp. 1–13, 2019.

[63] T. Masuta and A. Yokoyama, “Supplementary load frequency control by use of a number of both electric vehicles and heat pump water heaters,” *IEEE Transactions on Smart Grid*, vol. 3, no. 3, pp. 1253–1262, 2012.

[64] M.-H. Khooban, “Secondary load frequency control of time-delay stand-alone microgrids with electric vehicles,” *IEEE Transactions on Industrial Electronics*, vol. 65, no. 9, pp. 7416–7422, 2017.

[65] X. Zhou, Z. Gu, and F. Yang, “Resilient event-triggered output feedback control for load frequency control systems subject to cyber attacks,” *IEEE Access*, vol. 7, pp. 58951–58958, 2019.

[66] J. Liu, Y. Gu, L. Zha, Y. Liu, and J. Cao, “Event-Triggered $ H_$\backslash$infty $ Load Frequency Control for Multiarea Power Systems Under Hybrid Cyber Attacks,” *IEEE Transactions on Systems, Man, and Cybernetics: Systems*, vol. 49, no. 8, pp. 1665–1678, 2019.

[67] C. Peng, J. Li, and M. Fei, “Resilient Event-Triggering H_∞ Load Frequency Control for Multi-Area Power Systems With Energy-Limited DoS Attacks,” *IEEE Transactions on Power Systems*, vol. 32, no. 5, pp. 4110–4118, 2016.

[68] D. K. Panda, S. Das, and S. Townley, “Toward a More Renewable Energy-Based LFC Under Random Packet Transmissions and Delays With Stochastic Generation and Demand,” *IEEE Transactions on Automation Science and Engineering*, 2020.

[69] H. Yuan, Y. Xia, H. Yang, and Y. Yuan, “Resilient control for wireless networked control systems under DoS attack via a hierarchical game,” *International Journal of Robust and Nonlinear Control*, vol. 28, no. 15, pp. 4604–4623, 2018.

[70] A. Ameli, A. Hooshyar, E. F. El-Saadany, and A. M. Youssef, “Attack detection and identification for automatic generation control systems,” *IEEE Transactions on Power Systems*, vol. 33, no. 5, pp. 4760–4774, 2018.

[71] A. Sargolzaei, K. K. Yen, M. N. Abdelghani, S. Sargolzaei, and B. Carbunar, “Resilient design of networked control systems under time delay switch attacks, application in smart grid,” *IEEE Access*, vol. 5, pp. 15901–15912, 2017.

[72] Z. Cheng, D. Yue, S. Hu, C. Huang, C. Dou, and L. Chen, “Resilient load frequency control design: DoS attacks against additional control loop,”

International Journal of Electrical Power & Energy Systems, vol. 115, p. 105496, 2020.

[73] M. Olsson, M. Perninge, and L. Söder, “Modeling real-time balancing power demands in wind power systems using stochastic differential equations,” *Electric Power Systems Research*, vol. 80, no. 8, pp. 966–974, 2010.

[74] M.-H. Khooban, T. Dragicevic, F. Blaabjerg, and M. Delimar, “Shipboard microgrids: A novel approach to load frequency control,” *IEEE Transactions on Sustainable Energy*, vol. 9, no. 2, pp. 843–852, 2017.

[75] D. Photovoltaics and E. Storage, “IEEE standard for interconnection and interoperability of distributed energy resources with associated electric power systems interfaces,” *IEEE Std*, pp. 1547–2018, 2018.

[76] M. I. Alomoush, “Load frequency control and automatic generation control using fractional-order controllers,” *Electrical Engineering*, vol. 91, no. 7, pp. 357–368, 2010.

[77] K. Sabahi, M. Teshnehlab, and others, “Recurrent fuzzy neural network by using feedback error learning approaches for LFC in interconnected power system,” *Energy Conversion and Management*, vol. 50, no. 4, pp. 938–946, 2009.

[78] K. Sudha and R. V. Santhi, “Robust decentralized load frequency control of interconnected power system with generation rate constraint using type-2 fuzzy approach,” *International Journal of Electrical Power & Energy Systems*, vol. 33, no. 3, pp. 699–707, 2011.

[79] T. Mohamed, H. Bevrani, A. Hassan, and T. Hiyama, “Decentralized model predictive based load frequency control in an interconnected power system,” *Energy Conversion and Management*, vol. 52, no. 2, pp. 1208–1214, 2011.

[80] S. A. Taher, M. H. Fini, and S. F. Aliabadi, “Fractional order PID controller design for LFC in electric power systems using imperialist competitive algorithm,” *Ain Shams Engineering Journal*, vol. 5, no. 1, pp. 121–135, 2014.

[81] J. Leithon, S. Sun, and T. J. Lim, “Demand response and renewable energy management using continuous-time optimization,” *IEEE Transactions on Sustainable Energy*, vol. 9, no. 2, pp. 991–1000, 2017.

[82] H. Li, X. Wang, and J. Xiao, “Differential evolution-based load frequency robust control for micro-grids with energy storage systems,” *Energies*, vol. 11, no. 7, p. 1686, 2018.

[83] I. Pan and S. Das, “Kriging based surrogate modeling for fractional order control of microgrids,” *IEEE Transactions on Smart grid*, vol. 6, no. 1, pp. 36–44, 2014.

[84] W. Zhang, M. S. Branicky, and S. M. Phillips, “Stability of networked control systems,” *IEEE Control Systems Magazine*, vol. 21, no. 1, pp. 84–99, 2001.

[85] F. F. Wu, K. Moslehi, and A. Bose, “Power system control centers: Past, present, and future,” *Proceedings of the IEEE*, vol. 93, no. 11, pp. 1890–1908, 2005.

[86] Y. Xie and S.-Z. Yu, “Monitoring the application-layer DDoS attacks for popular websites,” *IEEE/ACM Transactions on networking*, vol. 17, no. 1, pp. 15–25, 2008.

[87] I. Pan, S. Das, and A. Gupta, “Handling packet dropouts and random delays for unstable delayed processes in NCS by optimal tuning of PIλDμ controllers with evolutionary algorithms,” *ISA Transactions*, vol. 50, no. 4, pp. 557–572, 2011.

[88] I. Pan, S. Das, and A. Gupta, “Tuning of an optimal fuzzy PID controller with stochastic algorithms for networked control systems with random time delay,” *ISA Transactions*, vol. 50, no. 1, pp. 28–36, 2011.

[89] W.-D. Chang and S.-P. Shih, “PID controller design of nonlinear systems using an improved particle swarm optimization approach,” *Communications in Nonlinear Science and Numerical Simulation*, vol. 15, no. 11, pp. 3632–3639, 2010.

[90] T.-H. Kim, I. Maruta, and T. Sugie, “Robust PID controller tuning based on the constrained particle swarm optimization,” *Automatica*, vol. 44, no. 4, pp. 1104–1110, 2008.

[91] Z.-L. Gaing, “A particle swarm optimization approach for optimum design of PID controller in AVR system,” *IEEE Transactions on Energy Conversion*, vol. 19, no. 2, pp. 384–391, 2004.

[92] C. Yin, S. Wu, S. Zhou, J. Cao, X. Huang, and Y. Cheng, “Design and stability analysis of multivariate extremum seeking with Newton method,” *Journal of the Franklin Institute*, vol. 355, no. 4, pp. 1559–1578, 2018.

[93] C. Yin, S. Dadras, X. Huang, Y. Chen, and S. Zhong, “Optimizing Energy Consumption for Lighting Control System via Multivariate Extremum Seeking Control With Diminishing Dither Signal,” *IEEE Transactions on Automation Science and Engineering*, vol. 16, no. 4, pp. 1848–1859, 2019.

[94] I. Pan and S. Das, “Design of hybrid regrouping PSO-GA based sub-optimal networked control system with random packet losses,” *Memetic Computing*, vol. 5, no. 2, pp. 141–153, 2013.

[95] S. Das, S. Das, and I. Pan, “Multi-objective optimization framework for networked predictive controller design,” *ISA transactions*, vol. 52, no. 1, pp. 56–77, 2013.

[96] R. Eberhart and J. Kennedy, “Particle swarm optimization,” in *Proceedings of the IEEE International Conference on Neural Networks*, 1995, vol. 4, pp. 1942–1948.

[97] H. Bevrani, F. Habibi, P. Babahajyani, M. Watanabe, and Y. Mitani, “Intelligent frequency control in an AC microgrid: Online PSO-based fuzzy tuning approach,” *IEEE Transactions on Smart Grid*, vol. 3, no. 4, pp. 1935–1944, 2012.

[98] J. L. T. Garcia, E. C. Calderón, E. R. Heras, and C. M. Ontiveros, “Generating electrical demand time series applying SRA technique to complement NAR and sARIMA models,” *Energy Efficiency*, pp. 1–19, 2019.

[99] M. Rypdal and K. Rypdal, “Is there long-range memory in solar activity on timescales shorter than the sunspot period?,” *Journal of Geophysical Research: Space Physics*, vol. 117, no. A4, 2012.

[100] R. Calif and F. G. Schmitt, “Modeling of atmospheric wind speed sequence using a lognormal continuous stochastic equation,” *Journal of Wind Engineering and Industrial Aerodynamics*, vol. 109, pp. 1–8, 2012.

[101] A. Loukatou, S. Howell, P. Johnson, and P. Duck, “Stochastic wind speed modelling for estimation of expected wind power output,” *Applied Energy*, vol. 228, pp. 1328–1340, 2018.

[102] M. Perninge, V. Knazkins, M. Amelin, and L. Söder, “Modeling the electric power consumption in a multi-area system,” *European Transactions on Electrical Power*, vol. 21, no. 1, pp. 413–423, 2011.

[103] S. S. Hamlen, W. A. Hamlen Jr, and J. T. Tschirhart, “Geometric Brownian distribution of solar radiation with an economic application,” *Solar Energy*, vol. 21, no. 6, pp. 469–475, 1978.

[104] E. Bossanyi, T. Burton, D. Sharpe, and N. Jenkins, “Wind energy handbook,” 2000.

[105] D.-J. Lee and L. Wang, “Small-signal stability analysis of an autonomous hybrid renewable energy power generation/energy storage system part I: Time-domain simulations,” *IEEE Transactions on Energy Conversion*, vol. 23, no. 1, pp. 311–320, 2008.

[106] I. Karatzas and S. E. Shreve, “Brownian motion,” in *Brownian Motion and Stochastic Calculus*, Springer, 1998, pp. 47–127.

[107] B. B. Mandelbrot and J. W. Van Ness, “Fractional Brownian motions, fractional noises and applications,” *SIAM review*, vol. 10, no. 4, pp. 422–437, 1968.

[108] I. M. Gelfand and G. E. Shilov, *Generalized functions, Vol. 4: Applications of Harmonic Analysis*. Academic Press, 1964.

[109] “Wavelet Toolbox .” [Online]. Available: https://uk.mathworks.com/products/wavelet.html.

[110] D. Dufresne, “The integral of geometric Brownian motion,” *Advances in Applied Probability*, vol. 33, no. 1, pp. 223–241, 2001.

[111] “Financial Toolbox.” [Online]. Available: https://www.mathworks.com/products/finance.html.

[112] D. T. Gillespie, “Exact numerical simulation of the Ornstein-Uhlenbeck process and its integral,” *Physical Review E*, vol. 54, no. 2, p. 2084, 1996.

[113] “DALRYMPLE ESCRI-SA BATTERY PROJECT.” [Online]. Available: https://www.escri-sa.com.au/. [Accessed: 17-May-2019].

[114] J. Fried and S. Zietz, “Curve fitting by Spline and Akima methods: possibility of interpolation error and its suppression,” *Physics in Medicine & Biology*, vol. 18, no. 4, p. 550, 1973.

[115] M. E. H. Pedersen, “Good parameters for particle swarm optimization,” *Hvass Lab., Copenhagen, Denmark, Tech. Rep. HL1001*, pp. 1551–3203, 2010.

[116] “Global Optimization Toolbox Matlab.” [Online]. Available: https://uk.mathworks.com/products/global-optimization.html.

[117] S. Das, K. Halder, and A. Gupta, “Delay Handling Method in Dominant Pole Placement based PID Controller Design,” *IEEE Transactions on Industrial Informatics*, 2019.

[118] J. Nanda, S. Mishra, and L. C. Saikia, “Maiden application of bacterial foraging-based optimization technique in multiarea automatic generation control,” *IEEE Transactions on Power Systems*, vol. 24, no. 2, pp. 602–609, 2009.

[119] J. Sharma, Y. V. Hote, and R. Prasad, “PID controller design for interval load frequency control system with communication time delay,” *Control Engineering Practice*, vol. 89, pp. 154–168, 2019.

[120] C. J. Ramlal, A. Singh, S. Rocke, and M. Sutherland, “Decentralized Fuzzy H_∞ -Iterative Learning LFC With Time-Varying Communication Delays and Parametric Uncertainties,” *IEEE Transactions on Power Systems*, vol. 34, no. 6, pp. 4718–4727, 2019.

[121] A. Azarbahram, A. Amini, and M. Sojoodi, “Resilient fixed-order distributed dynamic output feedback load frequency control design for interconnected multi-area power systems,” *IEEE/CAA Journal of Automatica Sinica*, vol. 6, no. 5, pp. 1139–1151, 2019.

[122] A. D. Rosaline and U. Somarajan, “Structured H_∞ Controller for an Uncertain Deregulated Power System,” *IEEE Transactions on Industry Applications*, vol. 55, no. 1, pp. 892–906, 2018.

[123] Y. Li, P. Zhang, and L. Ma, “Denial of service attack and defense method on load frequency control system,” *Journal of the Franklin Institute*, vol. 356, no. 15, pp. 8625–8645, 2019.

[124] M. Heshmati, R. Noroozian, S. Jalilzadeh, and H. Shayeghi, “Optimal design of CDM controller to frequency control of a realistic power system equipped with storage devices using grasshopper optimization algorithm,” *ISA Transactions*, 2019.

[125] Z. Li, X. Li, and B. Cui, “Planar clouds based load frequency control in interconnected power system with renewable energy,” *IEEE Access*, vol. 6, pp. 36459–36468, 2018.

[126] Z. Yan and Y. Xu, “Data-driven load frequency control for stochastic power systems: A deep reinforcement learning method with continuous action search,” *IEEE Transactions on Power Systems*, vol. 34, no. 2, pp. 1653–1656, 2018.

[127] D. Ganger, J. Zhang, and V. Vittal, “Forecast-based anticipatory frequency control in power systems,” *IEEE Transactions on Power Systems*, vol. 33, no. 1, pp. 1004–1012, 2017.

[128] A. M. Prostejovsky, M. Marinelli, M. Rezkalla, M. H. Syed, and E. Guillo-Sansano, “Tuningless load frequency control through active engagement of distributed resources,” *IEEE Transactions on Power Systems*, vol. 33, no. 3, pp. 2929–2939, 2017.

[129] F. J. Massey Jr, “The Kolmogorov-Smirnov test for goodness of fit,” *Journal of the American Statistical Association*, vol. 46, no. 253, pp. 68–78, 1951.

[130] H. Abdi and P. Molin, “Lilliefors/Van Soest’s test of normality,” *Encyclopedia of Measurement and Statistics*, pp. 540–544, 2007.

[131] P. E. McKight and J. Najab, “Kruskal-wallis test,” *The Corsini Encyclopedia of Psychology*, pp. 1–1, 2010.

[132] S. A. Pourmousavi and M. H. Nehrir, “Introducing dynamic demand response in the LFC model,” *IEEE Transactions on Power Systems*, vol. 29, no. 4, pp. 1562–1572, 2014.

[133] M. R. V. Moghadam, R. T. Ma, and R. Zhang, “Distributed frequency control in smart grids via randomized demand response,” *IEEE Transactions on Smart Grid*, vol. 5, no. 6, pp. 2798–2809, 2014.

[134] P. Babahajiani, Q. Shafiee, and H. Bevrani, “Intelligent demand response contribution in frequency control of multi-area power systems,” *IEEE Transactions on Smart Grid*, vol. 9, no. 2, pp. 1282–1291, 2016.

[135] G. Benysek, J. Bojarski, M. Jarnut, and R. Smolenski, “Decentralized Active Demand Response (DADR) system for improvement of frequency stability in distribution network,” *Electric Power Systems Research*, vol. 134, pp. 80–87, 2016.

[136] T. Yang, Y. Zhang, W. Li, and A. Y. Zomaya, “Decentralized networked load frequency control in interconnected power systems based on stochastic jump system theory,” *IEEE Transactions on Smart Grid*, vol. 11, no. 5, pp. 4427–4439, 2020.

[137] C. Hua and Y. Wang, “Delay-Dependent Stability for Load Frequency Control System via Linear Operator Inequality,” *IEEE Transactions on Cybernetics*, 2020.

[138] S. Saxena and E. Fridman, “Event-triggered load frequency control via switching approach,” *IEEE Transactions on Power Systems*, vol. 35, no. 6, pp. 4484–4494, 2020.

[139] Z. Wang, F. Yang, D. W. Ho, and X. Liu, “Robust H_∞ Control for Networked Systems With Random Packet Losses,” *IEEE Transactions on Systems, Man, and Cybernetics, Part B (Cybernetics)*, vol. 37, no. 4, pp. 916–924, 2007.

[140] H. Zhang, Y. Shi, and A. S. Mehr, “Robust static output feedback control and remote PID design for networked motor systems,” *IEEE Transactions on Industrial Electronics*, vol. 58, no. 12, pp. 5396–5405, 2011.

[141] C.-Z. Liu, L. Li, J.-W. Yong, F. Muhammad, S. Cheng, and Q. Wu, “An Innovative Adaptive Cruise Control Method With Packet Dropout,” *IEEE Transactions on Intelligent Transportation Systems*, 2020.

[142] K. Halder, S. Das, S. Dasgupta, S. Banerjee, and A. Gupta, “Controller design for Networked Control Systems—An approach based on L2 induced norm,” *Nonlinear Analysis: Hybrid Systems*, vol. 19, pp. 134–145, 2016.

[143] W.-A. Zhang and L. Yu, “Output feedback stabilization of networked control systems with packet dropouts,” *IEEE Transactions on Automatic Control*, vol. 52, no. 9, pp. 1705–1710, 2007.

[144] Y. Shi and B. Yu, “Output feedback stabilization of networked control systems with random delays modeled by Markov chains,” *IEEE Transactions on Automatic Control*, vol. 54, no. 7, pp. 1668–1674, 2009.

[145] Y. Shi, J. Huang, and B. Yu, “Robust tracking control of networked control systems: application to a networked DC motor,” *IEEE Transactions on Industrial Electronics*, vol. 60, no. 12, pp. 5864–5874, 2012.

[146] J. Zhang, C. Peng, X. Xie, and D. Yue, “Output feedback stabilization of networked control systems under a stochastic scheduling protocol,” *IEEE Transactions on Cybernetics*, vol. 50, no. 6, pp. 2851–2860, 2019.

[147] K. Halder, S. Das, D. K. Panda, S. Das, and A. Gupta, “QoS aware joint observer and networked PI/PID controller design using LMIs under

specified rate of packet dropouts," *Applied Mathematics and Computation*, vol. 401, p. 126125, 2021.

[148] A. K. Singh, R. Singh, and B. C. Pal, "Stability analysis of networked control in smart grids," *IEEE Transactions on Smart Grid*, vol. 6, no. 1, pp. 381–390, 2014.

[149] R. Santodomingo, M. Uslar, A. Göring, M. Gottschalk, L. Nordström, A. Saleem, and M. Chenine, "SGAM-based methodology to analyse Smart Grid solutions in DISCERN European research project," in *2014 IEEE International Energy Conference (ENERGYCON)*, 2014, pp. 751–758.

[150] J. Trefke, S. Rohjans, M. Uslar, S. Lehnhoff, L. Nordström, and A. Saleem, "Smart Grid Architecture Model use case management in a large European Smart Grid project," in *IEEE PES ISGT Europe 2013*, 2013, pp. 1–5.

[151] S. Dasgupta, K. Halder, S. Banerjee, and A. Gupta, "Stability of Networked Control System (NCS) with discrete time-driven PID controllers," *Control Engineering Practice*, vol. 42, pp. 41–49, 2015.

[152] K. Liao and Y. Xu, "A robust load frequency control scheme for power systems based on second-order sliding mode and extended disturbance observer," *IEEE Transactions on Industrial Informatics*, vol. 14, no. 7, pp. 3076–3086, 2017.

[153] I.-S. S. Board, "IEEE Guide for the Benefit Evaluation of Electric Power Grid Customer Demand Response," *IEEE Std 2030.6™-2016*, 2016.

[154] G. H. Golub and others, "CF vanLoan, Matrix Computations," *The Johns Hopkins*, 1996.

[155] K. Ogata and others, *Discrete-Time Control Systems*, vol. 2. Prentice Hall Englewood Cliffs, NJ, 1995.

[156] H. Lin and P. J. Antsaklis, "Stability and persistent disturbance attenuation properties for a class of networked control systems: switched system approach," *International Journal of Control*, vol. 78, no. 18, pp. 1447–1458, 2005.

[157] A. Hassibi, S. P. Boyd, and J. P. How, "Control of asynchronous dynamical systems with rate constraints on events," in *Proceedings of the 38th IEEE Conference on Decision and Control (Cat. No. 99CH36304)*, 1999, vol. 2, pp. 1345–1351.

[158] D. Liberzon and A. S. Morse, “Basic problems in stability and design of switched systems,” *IEEE Control Systems Magazine*, vol. 19, no. 5, pp. 59–70, 1999.

[159] R. A. DeCarlo, M. S. Branicky, S. Pettersson, and B. Lennartson, “Perspectives and results on the stability and stabilizability of hybrid systems,” *Proceedings of the IEEE*, vol. 88, no. 7, pp. 1069–1082, 2000.

[160] M. Yu, L. Wang, T. Chu, and G. Xie, “Stabilization of networked control systems with data packet dropout and network delays via switching system approach,” in *2004 43rd IEEE Conference on Decision and Control (CDC)(IEEE Cat. No. 04CH37601)*, 2004, vol. 4, pp. 3539–3544.

[161] I. S. Association and others, “IEEE standard for electric power systems communications-distributed network protocol (dnp3),” 2012.

[162] A. Alessandri, M. Baglietto, and G. Battistelli, “Luenberger observers for switching discrete-time linear systems,” *International Journal of Control*, vol. 80, no. 12, pp. 1931–1943, 2007.

[163] A. Alessandri and P. Coletta, “Switching observers for continuous-time and discrete-time linear systems,” in *Proceedings of the 2001 American Control Conference.(Cat. No. 01CH37148)*, 2001, vol. 3, pp. 2516–2521.

[164] F. Yang, Z. Wang, Y. Hung, and M. Gani, “H/sub/spl infin//control for networked systems with random communication delays,” *IEEE Transactions on Automatic Control*, vol. 51, no. 3, pp. 511–518, 2006.

[165] M. Farhadi and O. A. Mohammed, “Performance enhancement of actively controlled hybrid DC microgrid incorporating pulsed load,” *IEEE Transactions on Industry Applications*, vol. 51, no. 5, pp. 3570–3578, 2015.

[166] J. Zhu, H. Wu, J. Huang, M. Hua, L. Li, and Y. Xing, “A Dual-DC Output Three-Phase Three-level AC-DC Converter for Low Frequency Pulsed Power Decoupling Applications,” *IEEE Transactions on Industrial Electronics*, 2021.

[167] A. Abbaspour, A. Sargolzaei, P. Forouzannezhad, K. K. Yen, and A. I. Sarwat, “Resilient control design for load frequency control system under false data injection attacks,” *IEEE Transactions on Industrial Electronics*, vol. 67, no. 9, pp. 7951–7962, 2019.

[168] M. Fu and Z.-Q. Luo, “Computational complexity of a problem arising in fixed order output feedback design,” *Systems & Control Letters*, vol. 30, no. 5, pp. 209–215, 1997.

[169] L. El Ghaoui, F. Oustry, and M. AitRami, “A cone complementarity linearization algorithm for static output-feedback and related problems,” *IEEE Transactions on Automatic Control*, vol. 42, no. 8, pp. 1171–1176, 1997.

[170] H. Gao, T. Chen, and J. Lam, “A new delay system approach to network-based control,” *Automatica*, vol. 44, no. 1, pp. 39–52, 2008.

[171] J. Lofberg, “YALMIP: A toolbox for modeling and optimization in MATLAB,” in *2004 IEEE International Conference on Robotics and Automation (IEEE Cat. No. 04CH37508)*, 2004, pp. 284–289.

[172] J. F. Sturm, “Using SeDuMi 1.02, a MATLAB toolbox for optimization over symmetric cones,” *Optimization Methods and Software*, vol. 11, no. 1–4, pp. 625–653, 1999.

[173] D. Yue, Q.-L. Han, and C. Peng, “State feedback controller design of networked control systems,” in *Proceedings of the 2004 IEEE International Conference on Control Applications, 2004.*, 2004, vol. 1, pp. 242–247.

[174] D. Liberzon, *Switching in systems and control*. Springer Science \& Business Media, 2003.

[175] H. Lin and P. J. Antsaklis, “Stability and stabilizability of switched linear systems: a survey of recent results,” *IEEE Transactions on Automatic control*, vol. 54, no. 2, pp. 308–322, 2009.

[176] J. P. Hespanha and A. S. Morse, “Stability of switched systems with average dwell-time,” in *Proceedings of the 38th IEEE Conference on Decision and Control (Cat. No. 99CH36304)*, 1999, vol. 3, pp. 2655–2660.

[177] J. P. Hespanha, “Uniform stability of switched linear systems: Extensions of LaSalle’s invariance principle,” *IEEE Transactions on Automatic Control*, vol. 49, no. 4, pp. 470–482, 2004.

[178] G. Zhai, B. Hu, K. Yasuda, and A. N. Michel, “Stability analysis of switched systems with stable and unstable subsystems: an average dwell time approach,” *International Journal of Systems Science*, vol. 32, no. 8, pp. 1055–1061, 2001.

[179] D. K. Panda and S. Das, “Economic operational analytics for energy storage placement at different grid locations and contingency scenarios with stochastic wind profiles,” *Renewable and Sustainable Energy Reviews*, p. 110474, 2020.

[180] T. D. Fletcher and M. T. D. Fletcher, “Package ‘QuantPsyc,’” 2010.

[181] W. W. Burchett, A. R. Ellis, S. W. Harrar, and A. C. Bathke, “Nonparametric inference for multivariate data: the R package npmv,” *Journal of Statistical Software*, vol. 76, no. 1, pp. 1–18, 2017.

[182] K. Sajan, V. Kumar, and B. Tyagi, “Genetic algorithm based support vector machine for on-line voltage stability monitoring,” *International Journal of Electrical Power & Energy Systems*, vol. 73, pp. 200–208, 2015.

[183] V. Malbasa, C. Zheng, P.-C. Chen, T. Popovic, and M. Kezunovic, “Voltage stability prediction using active machine learning,” *IEEE Transactions on Smart Grid*, vol. 8, no. 6, pp. 3117–3124, 2017.

[184] J. Hazra, R. K. Reddi, K. Das, D. P. Seetharam, and A. K. Sinha, “Power grid transient stability prediction using wide area synchrophasor measurements,” in *2012 3rd IEEE PES Innovative Smart Grid Technologies Europe (ISGT Europe)*, 2012, pp. 1–8.

[185] B. Wang, B. Fang, Y. Wang, H. Liu, and Y. Liu, “Power system transient stability assessment based on big data and the core vector machine,” *IEEE Transactions on Smart Grid*, vol. 7, no. 5, pp. 2561–2570, 2016.

[186] L. Moulin, A. A. Da Silva, M. El-Sharkawi, and R. J. Marks, “Support vector machines for transient stability analysis of large-scale power systems,” *IEEE Transactions on Power Systems*, vol. 19, no. 2, pp. 818–825, 2004.

[187] B. Jayasekara and U. D. Annakkage, “Derivation of an accurate polynomial representation of the transient stability boundary,” *IEEE Transactions on Power Systems*, vol. 21, no. 4, pp. 1856–1863, 2006.

[188] T. Amraee and S. Ranjbar, “Transient instability prediction using decision tree technique,” *IEEE Transactions on Power Systems*, vol. 28, no. 3, pp. 3028–3037, 2013.

[189] Y. Xu, Z. Dong, K. Meng, R. Zhang, and K. Wong, “Real-time transient stability assessment model using extreme learning machine,” *IET Generation, Transmission & Distribution*, vol. 5, no. 3, pp. 314–322, 2011.

[190] N. Bassamzadeh and R. Ghanem, “Multiscale stochastic prediction of electricity demand in smart grids using Bayesian networks,” *Applied Energy*, vol. 193, pp. 369–380, 2017.

[191] D. Yang, L. Xu, S. Gong, H. Li, G. D. Peterson, and Z. Zhang, “Joint electrical load modeling and forecasting based on sparse bayesian learning for the smart grid,” in *2011 45th Annual Conference on Information Sciences and Systems*, 2011, pp. 1–6.

[192] G. Filatrella, A. H. Nielsen, and N. F. Pedersen, “Analysis of a power grid using a Kuramoto-like model,” *The European Physical Journal B*, vol. 61, no. 4, pp. 485–491, 2008.

[193] B. Schäfer, C. Grabow, S. Auer, J. Kurths, D. Witthaut, and M. Timme, “Taming instabilities in power grid networks by decentralized control,” *The European Physical Journal Special Topics*, vol. 225, no. 3, pp. 569–582, 2016.

[194] V. Arzamasov, K. Böhm, and P. Jochem, “Towards Concise Models of Grid Stability,” in *2018 IEEE International Conference on Communications, Control, and Computing Technologies for Smart Grids (SmartGridComm)*, 2018, pp. 1–6.

[195] G. James, D. Witten, T. Hastie, and R. Tibshirani, *An Introduction to Statistical Learning*, vol. 112. Springer, 2013.

[196] M. L. Bermingham, R. Pong-Wong, A. Spiliopoulou, C. Hayward, I. Rudan, H. Campbell, A. F. Wright, J. F. Wilson, F. Agakov, P. Navarro, and others, “Application of high-dimensional feature selection: evaluation for genomic prediction in man,” *Scientific Reports*, vol. 5, p. 10312, 2015.

[197] Q. Gu, Z. Li, and J. Han, “Generalized fisher score for feature selection,” *arXiv preprint arXiv:1202.3725*, 2012.

[198] H. L. Seal, *The historical development of the Gauss linear model*. Yale University New Haven, 1968.

[199] J. Neter, M. H. Kutner, C. J. Nachtsheim, and W. Wasserman, *Applied linear statistical models*, vol. 4. Irwin Chicago, 1996.

[200] J. J. Faraway, *Linear models with R*. Chapman and Hall/CRC, 2016.

[201] M. C. Wang and B. J. Bushman, “Using the normal quantile plot to explore meta-analytic data sets.,” *Psychological Methods*, vol. 3, no. 1, p. 46, 1998.

[202] J. J. Filliben, “The probability plot correlation coefficient test for normality,” *Technometrics*, vol. 17, no. 1, pp. 111–117, 1975.

[203] A. Monticelli, M. Pereira, and S. Granville, “Security-constrained optimal power flow with post-contingency corrective rescheduling,” *IEEE Transactions on Power Systems*, vol. 2, no. 1, pp. 175–180, 1987.

[204] Y. Fu, M. Shahidehpour, and Z. Li, “AC contingency dispatch based on security-constrained unit commitment,” *IEEE Transactions on Power Systems*, vol. 21, no. 2, pp. 897–908, 2006.

[205] L. Wu, M. Shahidehpour, and T. Li, “Stochastic security-constrained unit commitment,” *IEEE Transactions on Power Systems*, vol. 22, no. 2, pp. 800–811, 2007.

[206] S. Naghdalian, T. Amraee, S. Kamali, and F. Capitanescu, “Stochastic Network-Constrained Unit Commitment to Determine Flexible Ramp Reserve for Handling Wind Power and Demand Uncertainties,” *IEEE Transactions on Industrial Informatics*, vol. 16, no. 7, pp. 4580–4591, 2019.

[207] A. Ahmadi, A. E. Nezhad, and B. Hredzak, “Security-constrained unit commitment in presence of lithium-ion battery storage units using information-gap decision theory,” *IEEE Transactions on Industrial Informatics*, vol. 15, no. 1, pp. 148–157, 2018.

[208] Z. Zhang, Y. Chen, X. Liu, and W. Wang, “Two-stage robust security-constrained unit commitment model considering time autocorrelation of wind/load prediction error and outage contingency probability of units,” *IEEE Access*, vol. 7, pp. 25398–25408, 2019.

[209] Y. Wen, C. Guo, H. Pandvzic, and D. S. Kirschen, “Enhanced security-constrained unit commitment with emerging utility-scale energy storage,” *IEEE Transactions on Power Systems*, vol. 31, no. 1, pp. 652–662, 2015.

[210] H. Daneshi and A. Srivastava, “Security-constrained unit commitment with wind generation and compressed air energy storage,” *IET Generation, Transmission & Distribution*, vol. 6, no. 2, pp. 167–175, 2012.

[211] A. A. Salimi, A. Karimi, and Y. Noorizadeh, “Simultaneous operation of wind and pumped storage hydropower plants in a linearized security-constrained unit commitment model for high wind energy penetration,” *Journal of Energy Storage*, vol. 22, pp. 318–330, 2019.

[212] W. Gan, X. Ai, J. Fang, M. Yan, W. Yao, W. Zuo, and J. Wen, “Security constrained co-planning of transmission expansion and energy storage,” *Applied Energy*, vol. 239, pp. 383–394, 2019.

[213] V. Guerrero-Mestre, Y. Dvorkin, R. Fernández-Blanco, M. A. Ortega-Vazquez, and J. Contreras, “Incorporating energy storage into probabilistic security-constrained unit commitment,” *IET Generation, Transmission & Distribution*, vol. 12, no. 18, pp. 4206–4215, 2018.

[214] L. A. Wong, V. K. Ramachandaramurthy, P. Taylor, J. Ekanayake, S. L. Walker, and S. Padmanaban, “Review on the optimal placement, sizing and control of an energy storage system in the distribution network,” *Journal of Energy Storage*, vol. 21, pp. 489–504, 2019.

[215] P. Fortenbacher, A. Ulbig, and G. Andersson, “Optimal placement and sizing of distributed battery storage in low voltage grids using receding horizon control strategies,” *IEEE Transactions on Power Systems*, vol. 33, no. 3, pp. 2383–2394, 2017.

[216] M. Bucciarelli, S. Paoletti, and A. Vicino, “Optimal sizing of energy storage systems under uncertain demand and generation,” *Applied Energy*, vol. 225, pp. 611–621, 2018.

[217] R. D. Zimmerman and C. E. Murillo-Sanchez, “Matpower 4.1 user’s manual,” *Power Systems Engineering Research Center, Cornell University, Ithaca, NY*, 2011.

[218] A. R. Ellis, W. W. Burchett, S. W. Harrar, and A. C. Bathke, “Nonparametric inference for multivariate data: the R package npmv,” *Journal of Statistical Software*, vol. 76, no. 4, pp. 1–18, 2017.

[219] T. Anderson, “An introduction to multivariate statistical analysis,” 1984.

[220] M. H. DeGroot, *Probability and Statistics (2nd Ed)*. Addison-Wesley., 1986.

[221] C. Liu, A. C. Bathke, and S. W. Harrar, “A nonparametric version of Wilks’ lambda—Asymptotic results and small sample approximations,” *Statistics & Probability Letters*, vol. 81, no. 10, pp. 1502–1506, 2011.

[222] J. Cao, W. Du, and H. Wang, “An improved corrective security constrained OPF with distributed energy storage,” *IEEE Transactions on Power Systems*, vol. 31, no. 2, pp. 1537–1545, 2015.

[223] R. D. Zimmerman and C. E. Murillo-Sánchez, “Matpower Optimal Scheduling Tool MOST 1.0 User’s Manual,” *Power Systems Engineering Research Center (PSerc)*, 2016.

[224] K. Divya and J. Ostergaard, “Battery energy storage technology for power systems—An overview,” *Electric Power Systems Research*, vol. 79, no. 4, pp. 511–520, 2009.

[225] V. Latora and M. Marchiori, “A measure of centrality based on network efficiency,” *New Journal of Physics*, vol. 9, no. 6, p. 188, 2007.

[226] G. A. Pagani and M. Aiello, “The power grid as a complex network: a survey,” *Physica A: Statistical Mechanics and its Applications*, vol. 392, no. 11, pp. 2688–2700, 2013.

[227] P. Hines and S. Blumsack, “A centrality measure for electrical networks,” in *Proceedings of the 41st Annual Hawaii International Conference on System Sciences (HICSS 2008)*, 2008, pp. 185–185.

[228] Z. Lin, F. Wen, H. Wang, G. Lin, T. Mo, and X. Ye, “CRITIC-based node importance evaluation in skeleton-network reconfiguration of power grids,” *IEEE Transactions on Circuits and Systems II: Express Briefs*, vol. 65, no. 2, pp. 206–210, 2017.

[229] R. Espejo, S. Lumbreras, and A. Ramos, “Analysis of transmission-power-grid topology and scalability, the European case study,” *Physica A: Statistical Mechanics and its Applications*, vol. 509, pp. 383–395, 2018.

[230] S. Wang, W. Lv, J. Zhang, S. Luan, C. Chen, and X. Gu, “Method of power network critical nodes identification and robustness enhancement based on a cooperative framework,” *Reliability Engineering & System Safety*, vol. 207, p. 107313, 2021.

[231] A. Albarakati and M. Bikdash, “Empirical electrical-based framework to judge the ability of centrality measures in predicting grid vulnerability,” *Journal of Electrical Engineering & Technology*, pp. 1–11, 2021.

[232] B. Liu, Z. Li, X. Chen, Y. Huang, and X. Liu, “Recognition and vulnerability analysis of key nodes in power grid based on complex network centrality,” *IEEE Transactions on Circuits and Systems II: Express Briefs*, vol. 65, no. 3, pp. 346–350, 2017.

[233] A. Nasiruzzaman, H. Pota, and M. Mahmud, “Application of centrality measures of complex network framework in power grid,” in *IECON 2011-*

37th Annual Conference of the IEEE Industrial Electronics Society, 2011, pp. 4660–4665.

[234] H. Cetinay, K. Devriendt, and P. Van Mieghem, “Nodal vulnerability to targeted attacks in power grids,” *Applied Network Science*, vol. 3, no. 1, p. 34, 2018.

[235] C. Chen, X. Zhou, Z. Li, Z. He, Z. Li, and X. Lin, “Novel complex network model and its application in identifying critical components of power grid,” *Physica A: Statistical Mechanics and Its Applications*, vol. 512, pp. 316–329, 2018.

[236] D. Wu, F. Ma, M. Javadi, K. Thulasiraman, E. Bompard, and J. N. Jiang, “A study of the impacts of flow direction and electrical constraints on vulnerability assessment of power grid using electrical betweenness measures,” *Physica A: Statistical Mechanics and its Applications*, vol. 466, pp. 295–309, 2017.

[237] G. A. Pagani and M. Aiello, “Power grid complex network evolutions for the smart grid,” *Physica A: Statistical Mechanics and its Applications*, vol. 396, pp. 248–266, 2014.

[238] S. J. Young, Y. Makarov, R. Diao, M. Halappanavar, M. Vallem, R. Fan, R. Huang, J. O’Brien, and Z. H. Huang, “Topological Power Grid Statistics from a Network-of-Networks Perspective,” in *2018 IEEE Power & Energy Society General Meeting (PESGM)*, 2018, pp. 1–5.

[239] S. Wang, J. Zhang, M. Zhao, and X. Min, “Vulnerability analysis and critical areas identification of the power systems under terrorist attacks,” *Physica A: Statistical Mechanics and Its Applications*, vol. 473, pp. 156–165, 2017.

[240] Y. Wang, W. Li, and J. Lu, “A new node voltage stability index based on local voltage phasors,” *Electric Power Systems Research*, vol. 79, no. 1, pp. 265–271, 2009.

[241] I. Smon, G. Verbic, and F. Gubina, “Local voltage-stability index using Tellegen’s theorem,” *IEEE Transactions on Power Systems*, vol. 21, no. 3, pp. 1267–1275, 2006.

[242] J. Modarresi, E. Gholipour, and A. Khodabakhshian, “A comprehensive review of the voltage stability indices,” *Renewable and Sustainable Energy Reviews*, vol. 63, pp. 1–12, 2016.

[243] P. Kessel and H. Glavitsch, “Estimating the voltage stability of a power system,” *IEEE Transactions on Power Delivery*, vol. 1, no. 3, pp. 346–354, 1986.

[244] P.-A. Lof, G. Andersson, and D. Hill, “Voltage stability indices for stressed power systems,” *IEEE Transactions on Power Systems*, vol. 8, no. 1, pp. 326–335, 1993.

[245] W. Huang, D. J. Hill, and X. Zhang, “Small-disturbance voltage stability of power systems: Dependence on network structure,” *IEEE Transactions on Power Systems*, vol. 35, no. 4, pp. 2609–2618, 2019.

[246] F. Yang, Z. Ling, M. Wei, T. Mi, H. Yang, and R. C. Qiu, “Real-time static voltage stability assessment in large-scale power systems based on spectrum estimation of phasor measurement unit data,” *International Journal of Electrical Power & Energy Systems*, vol. 124, p. 106196, 2021.

[247] W. Huang and D. J. Hill, “Network-based analysis of long-term voltage stability considering loads with recovery dynamics,” *International Journal of Electrical Power & Energy Systems*, vol. 119, p. 105891, 2020.

[248] J. W. Simpson-Porco, F. Dörfler, and F. Bullo, “Voltage collapse in complex power grids,” *Nature Communications*, vol. 7, no. 1, pp. 1–8, 2016.

[249] C. Caro-Ruiz and E. Mojica-Nava, “Centrality measures for voltage instability analysis in power networks,” in *2015 IEEE 2nd Colombian Conference on Automatic Control (CCAC)*, 2015, pp. 1–6.

[250] H.-Y. Su and T.-Y. Liu, “Enhanced-online-random-forest model for static voltage stability assessment using wide area measurements,” *IEEE Transactions on Power Systems*, vol. 33, no. 6, pp. 6696–6704, 2018.

[251] G. Wang, Z. Zhang, Z. Bian, and Z. Xu, “A short-term voltage stability online prediction method based on graph convolutional networks and long short-term memory networks,” *International Journal of Electrical Power & Energy Systems*, vol. 127, p. 106647, 2021.

[252] H.-Y. Su and H.-H. Hong, “An Intelligent Data-Driven Learning Approach to Enhance Online Probabilistic Voltage Stability Margin Prediction,” *IEEE Transactions on Power Systems*, 2021.

[253] D. P. Kothari and I. Nagrath, *Modern power system analysis*. Tata McGraw-Hill Education, 1989.

[254] A. B. Birchfield, T. Xu, K. M. Gegner, K. S. Shetye, and T. J. Overbye, “Grid structural characteristics as validation criteria for synthetic networks,” *IEEE Transactions on Power Systems*, vol. 32, no. 4, pp. 3258–3265, 2016.

[255] S. Fliscounakis, P. Panciatici, F. Capitanescu, and L. Wehenkel, “Contingency ranking with respect to overloads in very large power systems taking into account uncertainty, preventive, and corrective actions,” *IEEE Transactions on Power Systems*, vol. 28, no. 4, pp. 4909–4917, 2013.

[256] “Security and Quality Supply Standards.” [Online]. Available: https://www.nationalgrideso.com/industry-information/codes/security-and-quality-supply-standards.

[257] “Power Systems Test Case Archive.” [Online]. Available: https://www.maths.ed.ac.uk/optenergy/NetworkData/howtouse.html.

[258] G. M. R. M. S. Fortunato and V. Nicosia, *Complex Networks*. New York, NY, USA: Springer, 2009.

[259] Y. Liu and X. Gu, “Skeleton-network reconfiguration based on topological characteristics of scale-free networks and discrete particle swarm optimization,” *IEEE Transactions on Power Systems*, vol. 22, no. 3, pp. 1267–1274, 2007.

[260] F. Wenli, H. Ping, and L. Zhigang, “Multi-attribute node importance evaluation method based on Gini-coefficient in complex power grids,” *IET Generation, Transmission & Distribution*, vol. 10, no. 9, pp. 2027–2034, 2016.

[261] P. Hagmann, L. Cammoun, X. Gigandet, R. Meuli, C. J. Honey, V. J. Wedeen, and O. Sporns, “Mapping the structural core of human cerebral cortex,” *PLoS Biology*, vol. 6, no. 7, p. e159, 2008.

[262] C. J. Honey, R. Kötter, M. Breakspear, and O. Sporns, “Network structure of cerebral cortex shapes functional connectivity on multiple time scales,” *Proceedings of the National Academy of Sciences*, vol. 104, no. 24, pp. 10240–10245, 2007.

[263] J. R. F. Ronqui and G. Travieso, “Analyzing complex networks through correlations in centrality measurements,” *Journal of Statistical Mechanics: Theory and Experiment*, vol. 2015, no. 5, p. P05030, 2015.

[264] C. Li, Q. Li, P. Van Mieghem, H. E. Stanley, and H. Wang, “Correlation between centrality metrics and their application to the opinion model,” *The European Physical Journal B*, vol. 88, no. 3, pp. 1–13, 2015.

[265] V. Ajjarapu and C. Christy, “The continuation power flow: a tool for steady state voltage stability analysis,” *IEEE Transactions on Power Systems*, vol. 7, no. 1, pp. 416–423, 1992.

[266] H. Mori and S. Yamada, “Continuation power flow with the nonlinear predictor of the Lagrange’s polynomial interpolation formula,” in *IEEE/PES Transmission and Distribution Conference and Exhibition*, 2002, vol. 2, pp. 1133–1138.

[267] R. D. Zimmerman, C. E. Murillo-Sánchez, and D. Gan, “MATPOWER: A MATLAB power system simulation package,” *Manual, Power Systems Engineering Research Center, Ithaca NY*, vol. 1, 1997.

[268] R. Kaye and F. Wu, “Analysis of linearized decoupled power flow approximations for steady-state security assessment,” *IEEE Transactions on Circuits and Systems*, vol. 31, no. 7, pp. 623–636, 1984.

[269] J. Thorp, D. Schulz, and M. Ili’c-Spong, “Reactive power-voltage problem: conditions for the existence of solution and localized disturbance propagation,” *International Journal of Electrical Power & Energy Systems*, vol. 8, no. 2, pp. 66–74, 1986.

[270] C. R. Johnson and R. A. Horn, *Matrix analysis*. Cambridge university press Cambridge, 1985.

[271] K. L. Lange, R. J. Little, and J. M. Taylor, “Robust statistical modeling using the t distribution,” *Journal of the American Statistical Association*, vol. 84, no. 408, pp. 881–896, 1989.

[272] H. Tak, J. A. Ellis, and S. K. Ghosh, “Robust and Accurate Inference via a Mixture of Gaussian and Student’st Errors,” *Journal of Computational and Graphical Statistics*, vol. 28, no. 2, pp. 415–426, 2019.

[273] M. Vallisneri and R. van Haasteren, “Taming outliers in pulsar-timing data sets with hierarchical likelihoods and Hamiltonian sampling,” *Monthly Notices of the Royal Astronomical Society*, vol. 466, no. 4, pp. 4954–4959, 2017.

[274] M. D. Hoffman and A. Gelman, “The No-U-Turn sampler: adaptively setting path lengths in Hamiltonian Monte Carlo.,” *Journal of Machine Learning Research*, vol. 15, no. 1, pp. 1593–1623, 2014.

[275] E. I. George and R. E. McCulloch, “Variable selection via Gibbs sampling,” *Journal of the American Statistical Association*, vol. 88, no. 423, pp. 881–889, 1993.

[276] C. E. Rasmussen, “Gaussian processes in machine learning,” in *Summer School on Machine Learning*, 2003, pp. 63–71.

[277] J. Snoek, H. Larochelle, and R. P. Adams, “Practical bayesian optimization of machine learning algorithms,” *Advances in Neural Information Processing Systems*, vol. 25, 2012.

[278] “Brain Connectivity Toolbox.” [Online]. Available: https://sites.google.com/site/bctnet/.

[279] M. Waskom and the seaborn development team, “mwaskom/seaborn,” *Zenodo*. [Online]. Available: https://doi.org/10.5281/zenodo.592845.

[280] J. Salvatier, T. V. Wiecki, and C. Fonnesbeck, “Probabilistic programming in Python using PyMC3,” *PeerJ Computer Science*, vol. 2, p. e55, 2016.

[281] A. Gelman, “Scaling regression inputs by dividing by two standard deviations,” *Statistics in Medicine*, vol. 27, no. 15, pp. 2865–2873, 2008.

[282] B. P. Carlin and T. A. Louis, *Bayesian Methods for Data Analysis, Third Edition.* . Chapman and Hall/CRC, 2008.

[283] A. Gelman, J. B. Carlin, H. S. Stern, D. B. Dunson, A. Vehtari, and D. B. Rubin, *Bayesian Data Analysis*. CRC press, 2013.

[284] “Econometric Toolbox Matlab.” [Online]. Available: https://www.mathworks.com/help/econ/.

[285] M. MATLAB, “Statistics and Machine Learning Toolbox: 2016a-Ensemble Methods,” *The MathWorks Inc., Natick, Massachusetts, United States*, 2016.

[286] I. M. Dudurych, “The Impact of Renewables on Operational Security: Operating Power Systems That Have Extremely High Penetrations of Nonsynchronous Renewable Sources,” *IEEE Power and Energy Magazine*, vol. 19, no. 2, pp. 37–45, 2021.

[287] P. Crucitti, V. Latora, and M. Marchiori, “Model for cascading failures in complex networks,” *Physical Review E*, vol. 69, no. 4, p. 045104, 2004.

[288] D. De Martino, L. Dall'Asta, G. Bianconi, and M. Marsili, "Congestion phenomena on complex networks," *Physical Review E*, vol. 79, no. 1, p. 015101, 2009.

[289] M. Li, R.-R. Liu, L. Lü, M.-B. Hu, S. Xu, and Y.-C. Zhang, "Percolation on complex networks: Theory and application," *Physics Reports*, 2021.

[290] F. Krzakala, C. Moore, E. Mossel, J. Neeman, A. Sly, L. Zdeborová, and P. Zhang, "Spectral redemption in clustering sparse networks," *Proceedings of the National Academy of Sciences*, vol. 110, no. 52, pp. 20935–20940, 2013.

[291] F. Radicchi, "Predicting percolation thresholds in networks," *Physical Review E*, vol. 91, no. 1, p. 010801, 2015.

[292] A. Vespignani, "Modelling dynamical processes in complex socio-technical systems," *Nature Physics*, vol. 8, no. 1, pp. 32–39, 2012.

[293] P. N. McGraw and M. Menzinger, "Laplacian spectra as a diagnostic tool for network structure and dynamics," *Physical Review E*, vol. 77, no. 3, p. 031102, 2008.

[294] H.-T. Wai, S. Segarra, A. E. Ozdaglar, A. Scaglione, and A. Jadbabaie, "Blind community detection from low-rank excitations of a graph filter," *IEEE Transactions on Signal Processing*, vol. 68, pp. 436–451, 2019.

[295] Z. Wang and K. Y. Szeto, "Comparing the reliability of networks by spectral analysis," *The European Physical Journal B*, vol. 87, no. 10, pp. 1–6, 2014.

[296] M. E. Newman, "Finding community structure in networks using the eigenvectors of matrices," *Physical Review E*, vol. 74, no. 3, p. 036104, 2006.

[297] F. Morone and H. A. Makse, "Influence maximization in complex networks through optimal percolation," *Nature*, vol. 524, no. 7563, pp. 65–68, 2015.

[298] A. J. Alvarez, C. E. Sanz-Rodriguez, and J. L. Cabrera, "Weighting dissimilarities to detect communities in networks," *Philosophical Transactions of the Royal Society A: Mathematical, Physical and Engineering Sciences*, vol. 373, no. 2056, p. 20150108, 2015.

[299] M. Panteli, D. N. Trakas, P. Mancarella, and N. D. Hatziargyriou, "Power systems resilience assessment: Hardening and smart operational enhancement strategies," *Proceedings of the IEEE*, vol. 105, no. 7, pp. 1202–1213, 2017.

[300] K. Kopsidas and S. Liu, “Power network reliability framework for integrating cable design and ageing,” *IEEE Transactions on Power Systems*, vol. 33, no. 2, pp. 1521–1532, 2017.

[301] S. A. Zareei, M. Hosseini, and M. Ghafory-Ashtiany, “Seismic failure probability of a 400 kV power transformer using analytical fragility curves,” *Engineering Failure Analysis*, vol. 70, pp. 273–289, 2016.

[302] M. A. Mohamed, T. Chen, W. Su, and T. Jin, “Proactive resilience of power systems against natural disasters: A literature review,” *IEEE Access*, vol. 7, pp. 163778–163795, 2019.

[303] M. Kamel, A. A. Karrar, and A. H. Eltom, “Development and application of a new voltage stability index for on-line monitoring and shedding,” *IEEE Transactions on Power Systems*, vol. 33, no. 2, pp. 1231–1241, 2017.

[304] A. Z. De Souza, C. A. Canizares, and V. H. Quintana, “New techniques to speed up voltage collapse computations using tangent vectors,” *IEEE Transactions on Power Systems*, vol. 12, no. 3, pp. 1380–1387, 1997.

[305] R. J. Sánchez-Garcia, M. Fennelly, S. Norris, N. Wright, G. Niblo, J. Brodzki, and J. W. Bialek, “Hierarchical spectral clustering of power grids,” *IEEE Transactions on Power Systems*, vol. 29, no. 5, pp. 2229–2237, 2014.

[306] E. B. Fowlkes and C. L. Mallows, “A method for comparing two hierarchical clusterings,” *Journal of the American Statistical Association*, vol. 78, no. 383, pp. 553–569, 1983.

[307] T. Michoel and B. Nachtergaele, “Alignment and integration of complex networks by hypergraph-based spectral clustering,” *Physical Review E*, vol. 86, no. 5, p. 056111, 2012.

[308] X. Liu, M. Shahidehpour, Z. Li, X. Liu, Y. Cao, and Z. Bie, “Microgrids for enhancing the power grid resilience in extreme conditions,” *IEEE Transactions on Smart Grid*, vol. 8, no. 2, pp. 589–597, 2016.

[309] M. Panteli, P. A. Crossley, D. S. Kirschen, and D. J. Sobajic, “Assessing the impact of insufficient situation awareness on power system operation,” *IEEE Transactions on Power Systems*, vol. 28, no. 3, pp. 2967–2977, 2013.

Appendix A Stochastic Unit Commitment Cost Function and Constraints

A.1 Objective Function

The total objective function for optimization can be written as:

$$\min f(x) = f_p(p, p_+, p_-) + f_{1f}(\delta_+, \delta_-) + f_{uc}(u, v, w) + f_s(s_0, p_{sc}, p_{sd}). \quad (1)$$

The components of the objective functions can be defined as follows:

- **Generation Costs**: The generation costs are considered as a quadratic polynomial of the generation quantity, which is modelled using the stochastic variables as:

$$f_p(p, p_+, p_-) = \sum_{t \in T} \sum_{j \in J^t} \sum_{k \in K^{tj}} \psi_\alpha^{tjk} \sum_{i \in I^{tjk}} C_P^{ti}(p^{tijk}) . \quad (2)$$

- **Load Following Reserve Costs:** The costs involved in maintaining the balance between the total generation and demand by scheduling the storage and the generator reserves during the given time interval can be written as:

$$f_{\text{lf}}(\delta_+, \delta_-) = \sum_{t \in T} \gamma^t \sum_{i \in I^t} \left[C_{\delta+}^{ti}(\delta_+^{ti}) + C_{\delta-}^{ti}(\delta_-^{ti}) \right] . \quad (3)$$

- **Unit Commitment Costs:** The costs due to the startup and shutdown of the generation units can be written as:

$$f_{\text{uc}}(u, v, w) = \sum_{t \in T} \gamma^t \sum_{i \in I^t} \left(C_P^{ti}(0) u^{ti} + C_v^{ti}(0) v^{ti} + C_w^{ti}(0) w^{ti} \right). \quad (4)$$

- **Storage Operations Costs:** The cost of the initial, terminal stored energy and leftover energy in the terminal states is:

$$f_s(s_0, p_{sc}, p_{sd}) = \sum_{i \in I^{tjk}} C_{s0}^T s_0^{\,i} - \sum_{t \in T} \left(C_{s0}^T s_{0t}^{\,i} + \sum_{j \in J^t} \sum_{k \in K^{tj}} C_{sc}^T p_{sc}^{\,tijk} + C_{sd}^T p_{sd}^{\,tijk} \right). \quad (5)$$

A.2 Contingency Constraints Formulation

The following equations define the operational constraints on the storage that act as reserves during contingency like generator trips or transmission line failure. The total limit on the reserve, redispatch and contract variables are:

$$0 \le p_{+}^{tijk} \le r_{+}^{ti} \le R_{max+}^{ti} ,$$
$$0 \le p_{-}^{tijk} \le r_{-}^{ti} \le R_{max-}^{ti} . \quad (6)$$

Ramping limits due to the contingency operations can be defined as:

$$-\Delta_{\max-}^{i} \le p^{tijk} - p^{tij0} \le \Delta_{\max+}^{i}, \quad k \ne 0. \quad (7)$$

A.3 Unit Commitment Constraints

The unit commitment constraints can be imposed based on the injection limits that can be described as:

$$u^{ti} P_{min}^{tijk} \le p^{tijk} \le u^{ti} P_{max}^{tijk}. \quad (8)$$

The constraints are setup based on the start-up and shutdown events as:

$$u^{ti} - u^{(t-1)i} = v^{ti} - w^{ti}. \quad (9)$$

The up and downtime of the generators for different time horizons can be written as:

$$\sum_{y=t-\tau_i^{+}}^{t} v^{yi} \le u^{ti}, \quad \sum_{y=t-\tau_i^{-}}^{t} w^{yi} \le 1 - u^{ti}. \quad (10)$$

The binary variables are represented as the following constraints:

$$u^{ti} \in \{0,1\}, v^{ti} \in \{0,1\}, w^{ti} \in \{0,1\}. \quad (11)$$

The cost coefficients along with the generator ramping capacity values are considered as the default values from the MATPOWER MOST manual [1].

Appendix B Multivariate Hypothesis Tests

B.1 Multivariate Normality Test

It is essential to check the assumptions regarding the underlying distributions of the data. Multivariate Analysis of Variance (MANOVA) is used in [2] for testing the multivariate samples. In the test, it is assumed that the underlying distribution is normal. Multivariate skewness and kurtosis measures are used to find the underlying normality as shown in [3].

Let us consider the random variables $y_1,\ldots,y_m$. For any general multivariate distribution, the following terms can be defined for a sample size of n:

$$\hat{\beta}_{1m} = \frac{1}{n^2} \sum_{i=1}^{n} \sum_{j=1}^{n} g_{ij}^3, \hat{\beta}_{2m} = \frac{1}{n^2} \sum_{i=1}^{n} g_{ii}^2 = \frac{1}{n^2} \sum_{i=1}^{n} d_i^4 , \quad (12)$$

where, $g_{ij} = (y_i - \bar{y})' \mathbf{S}_n^{-1} (y_j - \bar{y})$ and $d_i^4 = \sqrt{g_{ii}}$. Here $\mathbf{S}_n$ and $\bar{y}$ denotes the covariance matrix and sample mean, respectively. The quantities $\hat{\beta}_{1m}$ and $\hat{\beta}_{2m}$ are the skewness and kurtosis coefficients. When there is a departure from the spherical symmetry, $\hat{\beta}_{1m}$ tends to be close to zero and $\hat{\beta}_{2m}$ tends to be significant for the multivariate normal data as shown in [4]. The hypothesis test is conducted based on Mahalanobis distance g_{ii} and the critical value (κ_1), which is defined by:

$$\kappa_1 = n\hat{\beta}_{1m}/6 , \tag{13}$$

with $m(m+1)(m+2)/6$ being the degrees of freedom and the critical significance level specified in the test. The above test is performed using the function `mult.norm()` in the *QuantPsyc* package in R [5]. If the hypothesis is accepted within the significance level, then the multivariate extension of ANOVA test (MANOVA) has been performed. Otherwise, non-parametric multivariate testing is performed, which is explained in the next subsection.

B.2 General Non-Parametric Multivariate Test

Non-parametric inference for testing the hypothesis of multivariate samples has been performed, as described in [6]–[8]. The multivariate samples used are of the form $X_{ij} = \left[x_{ij}^{(1)}, \ldots, x_{ij}^{(m)} \right]^T$ where $i = 1, \ldots, a$ represent the samples to be tested and $j = 1, \ldots, n_i$ represent the results from the Monte Carlo samples, $k = 1, \ldots, m$ denote the multi-period intervals for optimization. The random vectors are assumed independent with the dependent distribution given as $X_{ij} = \left[x_{ij}^{(1)}, \ldots, x_{ij}^{(m)} \right]^T \sim F_i$. F_i can be represented as a degenerate distribution defined as:

$$F_i^{(k)}(x) = \frac{1}{2}\left[P\left(x_{ij}^{(k)} \le x\right) + P\left(x_{ij}^{(k)} \le x\right) \right], \tag{14}$$

where, $P(.)$ represents the probability of the variable *x*. The null hypothesis in terms of distribution functions considering the multivariate hypothesis is given as:

$$H_0 : F_1^{(k)} = \cdots = F_A^{(k)} . \tag{15}$$

The alternative hypothesis is that the *F* statistic is unequal between different samples.The non-parametric statistics generally deals with the rankings of m different variables. The column vector $\mathbf{R}_{ij} = \left(\mathbf{r}_{ij}^{(1)},...,\mathbf{r}_{ij}^{(m)}\right)^{T}$ consists of the rank of multivariate observations X_{ij}, and the matrix $\mathbf{R} = \left(\mathbf{R}_{11},\cdots,\mathbf{R}_{1n_i},\mathbf{R}_{21},\cdots,\mathbf{R}_{n_a}\right)$ has the ranks for all observations among the variable. The Wilks' Lambda statistic is the commonly used measure for statistical significance due to its flexibility and robustness [8]. The asymptotic results state that either the number of samples A is quite large while the sample size n is fixed or vice versa. $\mathbf{G_1}$ and $\mathbf{H_1}$ are defined as a multivariate version of the residual sum of squares within groups and between groups, respectively [6]. It is defined as:

$$\begin{aligned}\mathbf{G_1} &= \frac{1}{N-A}\sum_{i=1}^{A}\sum_{j=1}^{n_j}\left(\mathbf{R}_{ij}-\bar{\mathbf{R}}_{i\cdot}\right)\left(\mathbf{R}_{ij}-\bar{\mathbf{R}}_{i\cdot}\right)^{T},\\ \mathbf{H_1} &= \frac{1}{A-1}\sum_{i=1}^{A} n_i\left(\bar{\mathbf{R}}_{i\cdot}-\bar{\mathbf{R}}_{\cdot\cdot}\right)\left(\bar{\mathbf{R}}_{i\cdot}-\bar{\mathbf{R}}_{\cdot\cdot}\right)^{T},\end{aligned} \tag{16}$$

where, $\bar{\mathbf{R}}_{i\cdot}$ represents the mean rank of i^{th} group while $\bar{\mathbf{R}}_{\cdot\cdot}$ represents the overall rank of the groups. The Wilk's Lambda statistic derived for the asymptotic approximations can be defined using (16) as:

$$T_1 = -\log\frac{\det\left[(N-A)\mathbf{G_1}\right]}{\det\left[(N-A)\mathbf{G_1}+(A-1)\mathbf{H_1}\right]}, \tag{17}$$

where, $N = \sum_{i=1}^{A} n_i$.

Appendix C Description of the Spectral Filters

C.1 Tight Filters

In order to exploit the full eigenvalue spectrum of the Laplacians, dictionaries have been constructed [9] by translation of the smooth graph spectral filters centred at different graph vertices. The smoothness of the filters ensures that the translated atoms are localized around their vertices [10].

However, tight graph wavelet kernels are adapted to the maximum eigenvalue of the graph Laplacian matrix. Hence graphs with irregularly spaced Laplacian eigenvalues causes the spectral graph wavelets to be highly correlated to the wavelets centred at nearby vertices and scales. They lose the power for

discriminating the graph signals. Spectral graph kernels are adapted to the entire graph Laplacian spectrum, and the dictionaries are obtained from the translation of the kernels across the vertices of the graph resulting in a tight frame [9]. Here, the warping function approximates the cumulative spectral density of the graph Laplacian, adapting the kernels to the entire spectrum. The dictionaries considered is characterized by a sequence of graph spectral filters $\{\hat{g}_m(\cdot)\}_{m=1,2,\ldots,M}$. It consists of $M \cdot N$ atoms.

$$\begin{aligned} g_{i,m} := T_i g_m &= \sqrt{N}\delta_i * g_m, \\ &= \sqrt{N}\hat{g}_m(\mathcal{L})\delta_i, \\ &= \sqrt{N}\sum_{l=0}^{B-1} g(\lambda_l)\chi_l^*(n)\chi_l(m). \end{aligned} \tag{18}$$

Thus we can consider,

$$\hat{g}_m(\mathcal{L}) = \mathbf{U}\begin{bmatrix} g_m(\lambda_0) & \cdots & 0 \\ \vdots & \ddots & \vdots \\ 0 & \cdots & g_m(\lambda_{N-1}) \end{bmatrix}\mathbf{U}^*. \tag{19}$$

The bandpass kernel is given by $\hat{g}_m(\lambda_l) = \hat{g}_m(\hat{t}_m\lambda_l)$ equivalent to dilation factors $\hat{t}_m$.

Lemma 1: Let us consider $\mathbb{D} = \{g_{i,m}\}_{i=1,2,\ldots,N;m=1,2,\ldots,M}$ be a dictionary of atoms with $g_{i,m} = T_i g_m$ and define:

$$G(\lambda) := \sum_{m=1}^{M}\left[\hat{g}_m(\lambda)\right]^2. \tag{20}$$

If $G(\lambda) > 0$ for all, $\lambda \in \sigma(\mathcal{L})$ then for all $f \in \mathbb{R}$,

$$A\|f\|_2^2 \le \sum_{i=1}^{N}\sum_{m=1}^{M}\left|\langle f, g_{i,m}\rangle\right|^2 \le B\|f\|_2^2, \tag{21}$$

where, $A = N \cdot \min_{\lambda\in\sigma(\mathcal{L})} G(\lambda)$ and $B = N \cdot \min_{\lambda\in\sigma(\mathcal{L})} G(\lambda)$. y uniform translation, $M \cdot N$ dictionary atoms are created by applying a generalized translation operator T_i to each filter to form a tight frame. The job is to find the kernel $\hat{g}^U(\cdot)$ and the constants *a* and *A* such that:

$$G(\lambda)=\sum_{m=1}^{M}\left[\hat{g}^{U}(\lambda-ma)\right]^{2}=A,\forall\lambda\in\left[0,\lambda_{\max}\right] \tag{22}$$

The properties of the uniformly translated filters, which spans across the entire eigenvalue spectrum, based on the translation of smooth functions

Theorem 1: *Let* $K\in\mathbb{N}$ *and* $a_k\in\mathbb{R}$ *for* $k\in\{0,1,\ldots,K\}$. *Let us define*

$$q(t)=\sum_{k=0}^{K}a_k\cos(2\pi kt)\mathbf{1}_{\left\{-\frac{1}{2}\le t<\frac{1}{2}\right\}}, \tag{23}$$

Then for any $R\in\mathbb{N}$ *satisfying* $R>2K$,

$$\sum_{m\in\mathbb{Z}}q^{2}\left(t-\frac{m}{R}\right)=Ra_0^2+\frac{R}{2}\sum_{k=1}^{K}a_k^2,\forall t\in\mathbb{R}. \tag{24}$$

Squares of a system of regular translation sum up to a constant function. Theorem 1 can be generalized for the *M* spectral filters as:

Corollary 1: Let us consider a number of filters M, let R and K be considered as any integers which satisfy $2<R\le M$ and $K<\frac{R}{2}$. Defining the kernel,

$$\hat{h}(\breve{y})=\sum_{k=0}^{K}a_k\cos\left[2\pi k\left(\breve{y}-\frac{1}{2}\right)\right]\mathbf{1}_{\{0\le\breve{y}<1\}}, \tag{25}$$

where $\{a_k\}_{k=0,1,\ldots,K}$ be the real sequence of coefficients which satisfies the relation

$$\sum_{k=0}^{K}(-1)^{k}a_k=0. \tag{26}$$

Then we can write,

$$H(\breve{y})=\sum_{m=1-R}^{M-R}\left[\hat{h}\left(\breve{y}-\frac{m}{R}\right)\right]^{2}=Ra_0^2+\frac{R}{2}\sum_{k=1}^{K}a_k^2,\forall\breve{y}\in\left[0,\frac{M+1-R}{R}\right]. \tag{27}$$

The kernel relation $\hat{h}(\cdot)$ (25) specified that it has to be continuous. If we define the filters as:

$$\hat{g}^{U}(\lambda)=\sum_{k=0}^{K}a_k\cos\left[2\pi k\left(\frac{M+1-R}{R\gamma}\lambda+\frac{1}{2}\right)\right]\mathbf{1}_{\left\{-\frac{R\gamma}{M+1-R}\le\lambda<0\right\}}, \tag{28}$$

Then

$$G(\lambda) := \sum_{m=1}^{M}\left[\hat{g}_m(\lambda)\right]^2 = Ra_0^2 + \frac{R}{2}\sum_{k=1}^{K} a_k^2, \forall\lambda \in [0,\gamma]. \tag{29}$$

Where $\hat{g}^U(\lambda) = \hat{g}^U\left(\lambda - m\frac{\gamma}{M+1-R}\right)$. Tight frames conserve the energies in the wavelet domain. If we consider $A = B = 1$, then the family of wavelet coefficients forms a Parseval frame that preserves signal energy given by $\forall f \in l_2(V)$ where V represents the vertices of a graph and $\|f\|^2 = \sum_t\sum_n \left|\langle f, \psi_{t,n}\rangle\right|^2$. The eigenvalues are generally unevenly distributed, which depends on the graph. Rational wavelet generating kernels $g(.)$ and scaling functions $h(\cdot)$ have been used with a dilation factor M [11] which is defined as $M = \frac{r+1}{r}$, $r \in \mathbb{Z}$. It is defined on Meyer wavelet as follows:

$$g(\lambda) = \begin{cases} \sin\left(\frac{\pi}{2}\nu\left(r\left(\frac{\lambda}{a}-1\right)\right)\right), \forall\lambda \in \left]a, Ma\right] \\ \cos\left(\frac{\pi}{2}\nu\left(r\left(\frac{\lambda}{a}-1\right)\right)\right), \forall\lambda \in \left]Ma, M^2a\right] \\ 0 \qquad\qquad\qquad\qquad , \text{elsewhere} \end{cases} \tag{30}$$

$$h(\lambda) = \begin{cases} 1 \qquad\qquad\qquad\qquad , \forall\lambda \in [0,a] \\ \cos\left(\frac{\pi}{2}\nu\left(r\left(\frac{\lambda}{a}-1\right)\right)\right), \forall\lambda \in \left]a, Ma\right] \\ 0 \qquad\qquad\qquad\qquad , \text{elsewhere} \end{cases} \tag{31}$$

Here $a = (q-\varepsilon)b$ where $\varepsilon = \left]0,(1+M)^{-1}\right]$ and $a, b \in \mathbb{R}^+$. The dilation which leads to Parseval wavelet frames are given by $M = 2$, which are J wavelet frames are defined on the scales $t_j = \frac{a}{\lambda_{\max}}M^j$ for $j = 1,\ldots,J$.

C.2 Non-Tight Filters

Heat kernel signature is a temporal descriptor that is an exponentially weighted combination of Laplace-Beltrami operator [12] for shape signatures eigenfunctions. Wave kernel signature is used to extract high-frequency information. Mexican hat wavelet is generally used for shape analysis, as it

considers essential frequencies equally opposed to cubic spline kernel [13]. Let consider the heat kernel $\underset{\frown}{h}_t(x,y)$ defined on a manifold $\Delta_{\mathbb{M}}$. It is obtained by solving the following PDE [14]

$$\frac{\partial \underset{\frown}{h}(x,t)}{\partial t} - \Delta_{\mathbb{M}} \underset{\frown}{h}(x,t) = 0 \quad , \tag{32}$$

Where $\Delta_{\mathbb{M}}$ represents Laplace-Beltrami operator given by,

$$\Delta_{\mathbb{M}} \varphi_k(x) = -\lambda_k \varphi_k(x). \tag{33}$$

where $\varphi_k(x)$ represents eigenfunctions on the manifold $\Delta_{\mathbb{M}}$ and λ_k represents eigenvalue of the Laplacian. Mexican hat kernel in Fourier domain is obtained by the product of Laplace-Beltrami operator $\Delta_{\mathbb{M}}$ with the heat kernel . If we define Mexican can kernel as $\underset{\frown}{\psi}_t(x,y) : \mathbb{R}^+ \times \mathbb{M} \times \mathbb{M}$ we write that in the given space as

$$\underset{\frown}{\psi}_t(x,y) = \sum_{k=0}^{\infty} \lambda_k e^{-\lambda_k t} \phi_k(x) \phi_k(y) \ . \tag{34}$$

The concept is *g* and *h* is similar to the previous sections, where *h* is defined as,

$$h(x) = \lambda \exp\left[-\left(\frac{x}{0.6\lambda_{\min}} \right)^4 \right] \tag{35}$$

Where $\lambda_{\min} = \lambda_{\max}/20$. γ is set such that for the scales $t_i = 2/\lambda_{\min}$ and $t_L = 2/\lambda_{\max}$ .The area under the curve on the energy extracted from the graph signal is given by,

$$G(\lambda) = h(\lambda)^2 + \sum_k g(t_k \lambda)^2 \ . \tag{36}$$

It represents the energy contributed by the eigenvalue λ of the graph, and the importance of all frequencies are taken, and discriminative ability is based on detecting a certain shape [13]. Spline filters can optimize the response based on high and low pass responses. The spline filter bank [15] satisfies perfect construction, critical sampling, capturing the localized properties of graph signals, localized reconstruction, orthogonality condition, graph structure invariance, and diagonalizable by the eigenvectors. The $g(\cdot)$ is defined by [16],

$$g(h)=\begin{cases}(h/h_1)^{\hat{\alpha}}, \text{for } h<h_1\\ s(h), h_1\le h<h_2\\ (h_2/h)^{\hat{\beta}}, \text{for } h>h_2\end{cases} \quad (37)$$

Here $s(h)$ is a unique cubic spline where it follows the curvature of g. Here $\hat{\alpha}=\hat{\beta}=1$, $h_1=1$ and $h_2=1$.

C.3 Low pass Heat Kernel

Simple low pass heat kernel is defined as,

$$g(\lambda)=\exp\left[-N_f\frac{\lambda}{\lambda_{max}}\right]. \quad (38)$$

Here, λ_{max} it represents the maximum eigenvalue of the Laplacian Matrix. λ represents the eigen mode of the Laplacian. N_f represents a scaling parameter. Low-pass filter property increases with an increase in N_f.

Appendix D Power Network Cluster Visualisation

D.1 Power Network Visualisation with change in number of spectral filters

D.1.1 IEEE 30 Bus Network

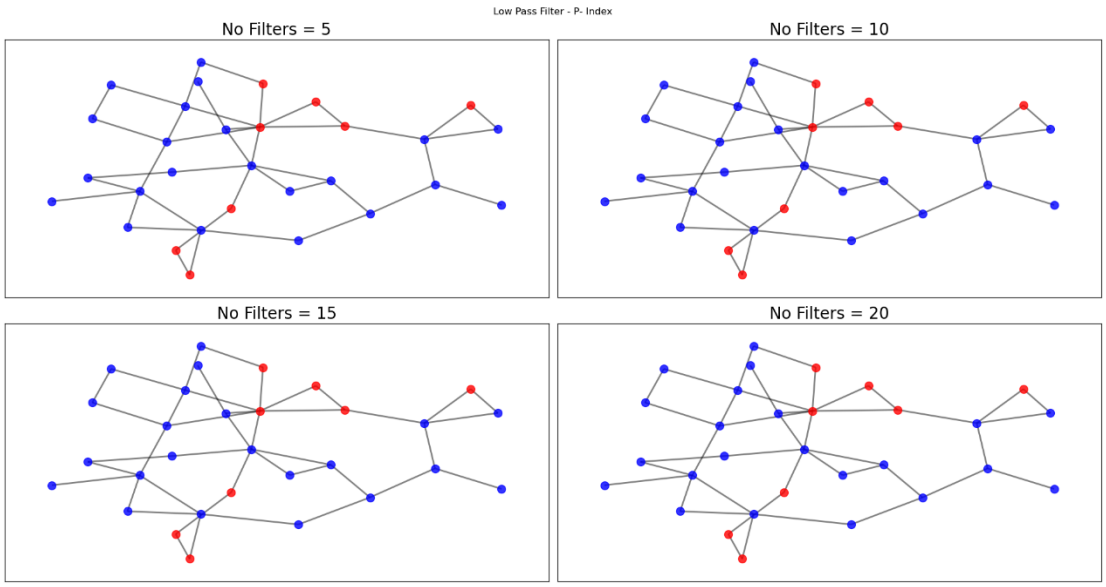

(a)

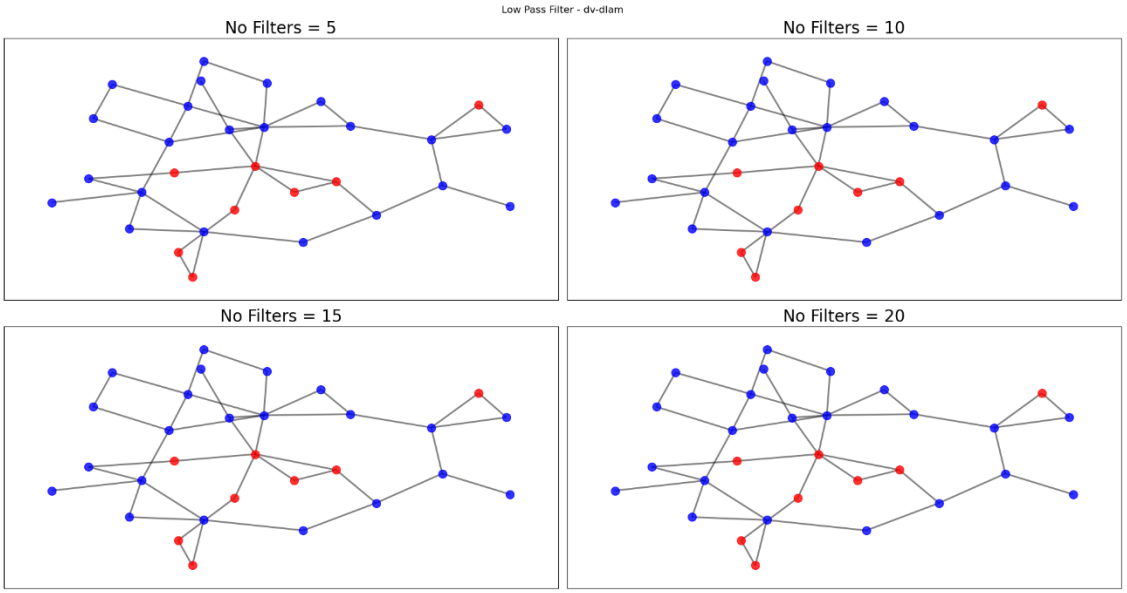
Low Pass Filter - dv-dlam
No Filters = 5
No Filters = 10
No Filters = 15
No Filters = 20

(b)

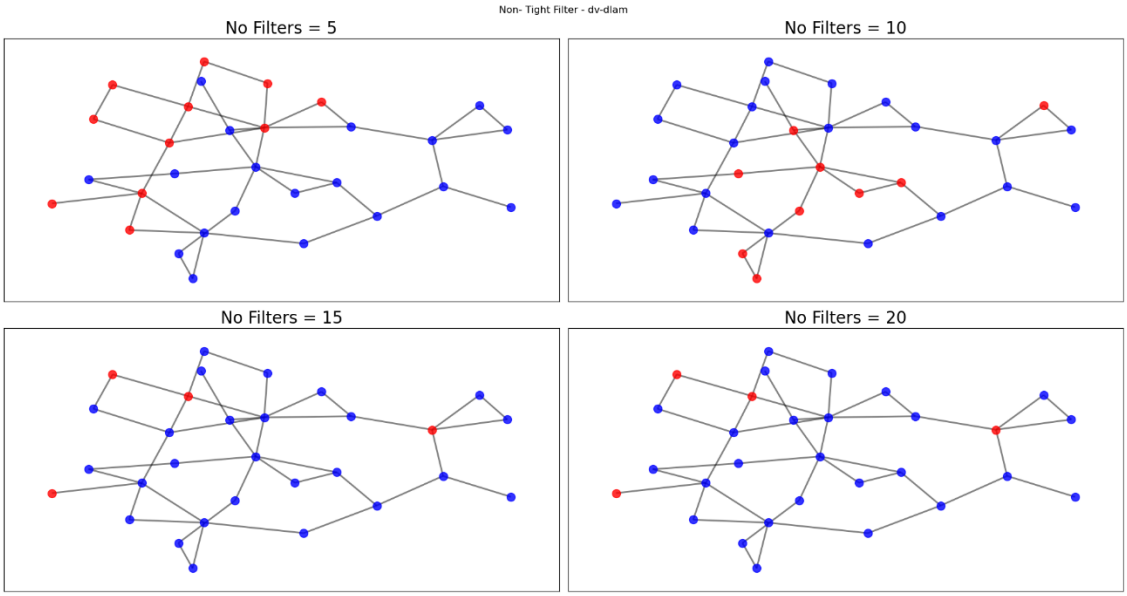
Non- Tight Filter - dv-dlam
No Filters = 5
No Filters = 10
No Filters = 15
No Filters = 20

(c)

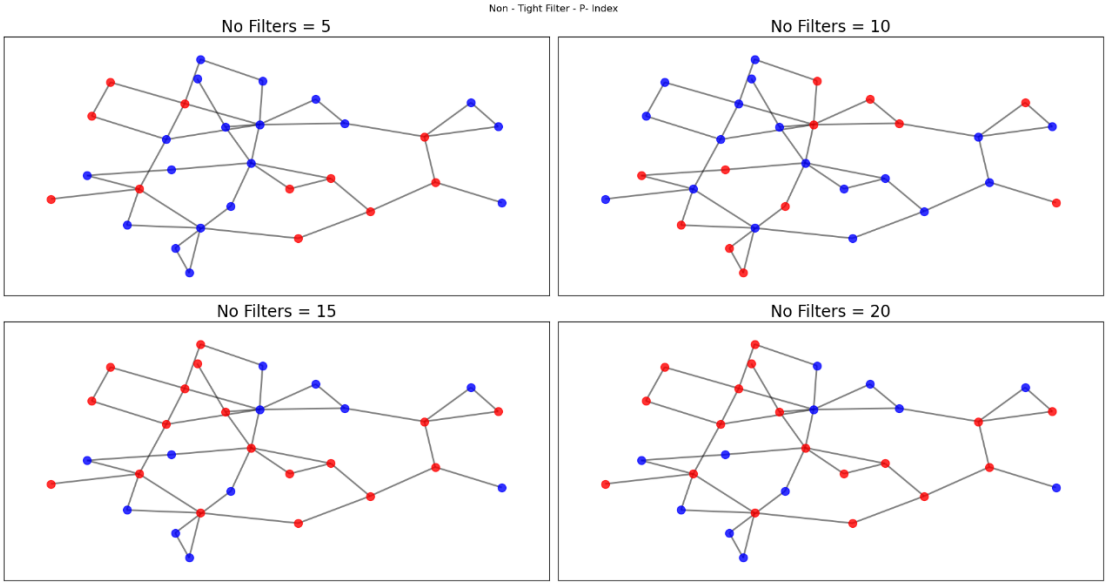
Non - Tight Filter - P- Index
No Filters = 5
No Filters = 10
No Filters = 15
No Filters = 20

(d)

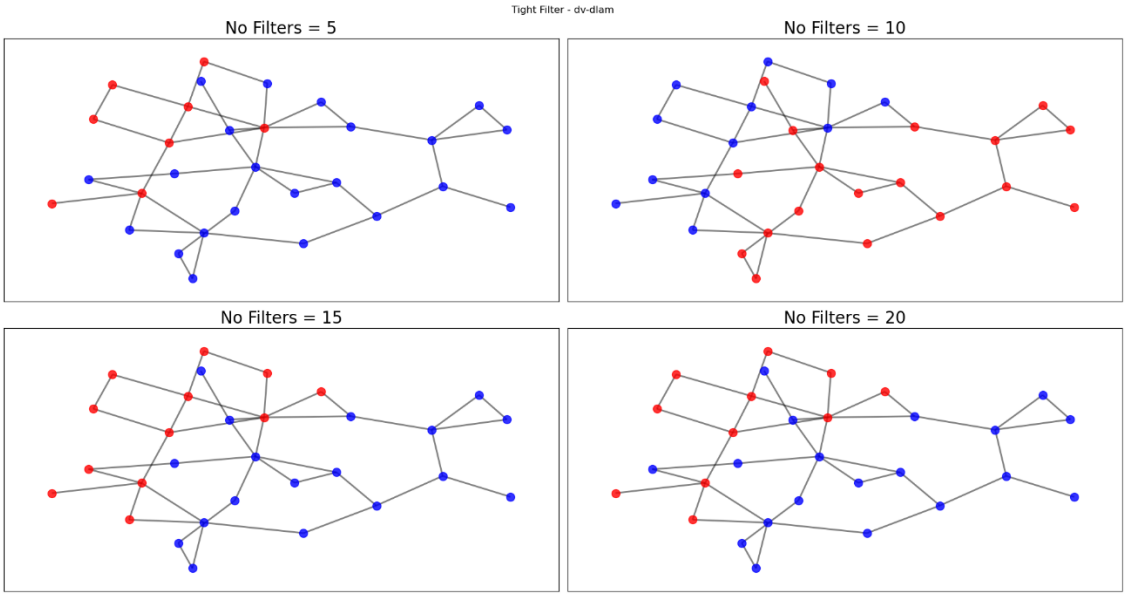
Tight Filter - dv-dlam
No Filters = 5
No Filters = 10
No Filters = 15
No Filters = 20

(e)

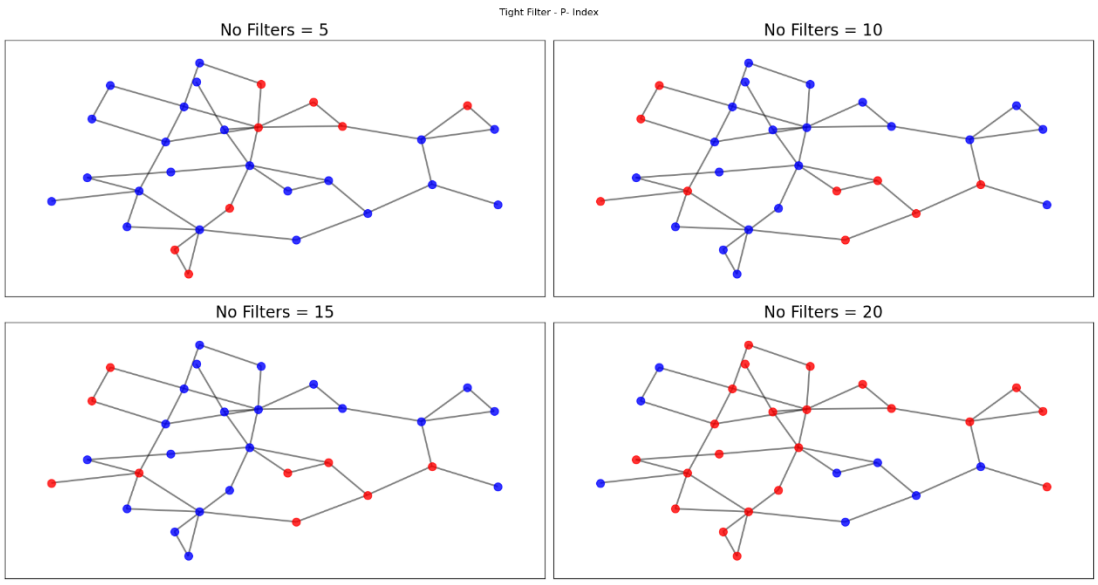

(f)

Figure 0-1: The two level clusters obtained for different graph signals for IEEE 30 bus network with increase in the number of spectral filters (a,b) Low Pass Filter (c,d) Non-Tight Filter (e,f) Tight Filter.

D.1.2 GB Reduced Network

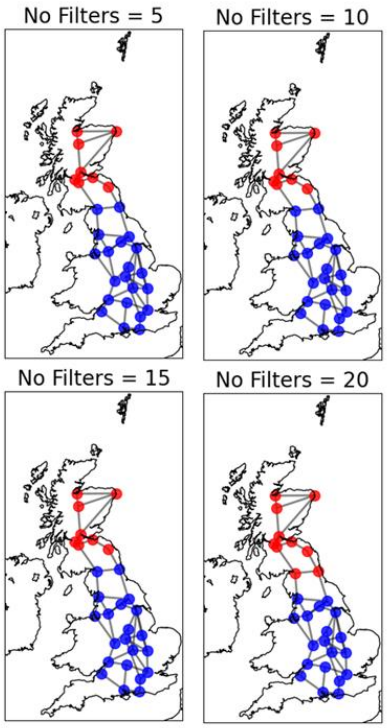

(a)

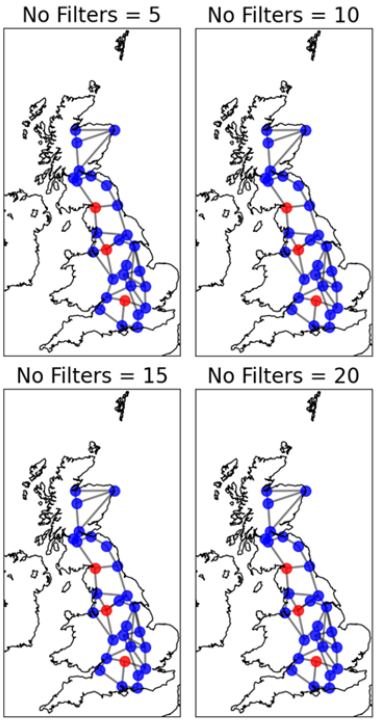

(b)

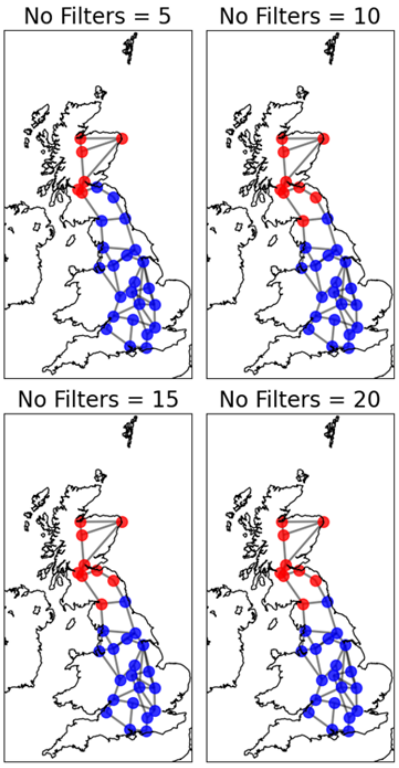

(c)

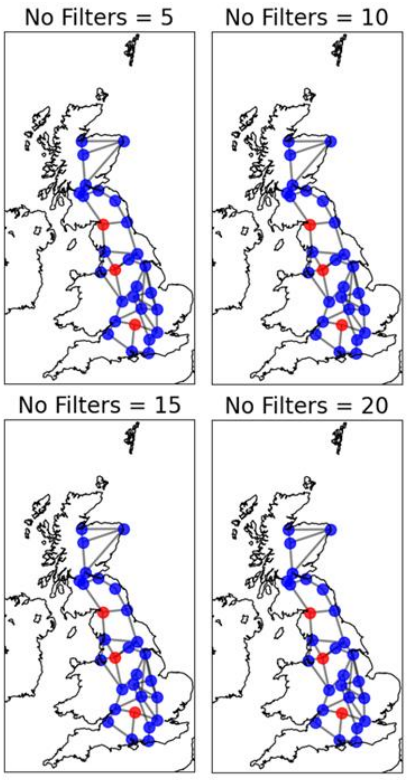

(d)

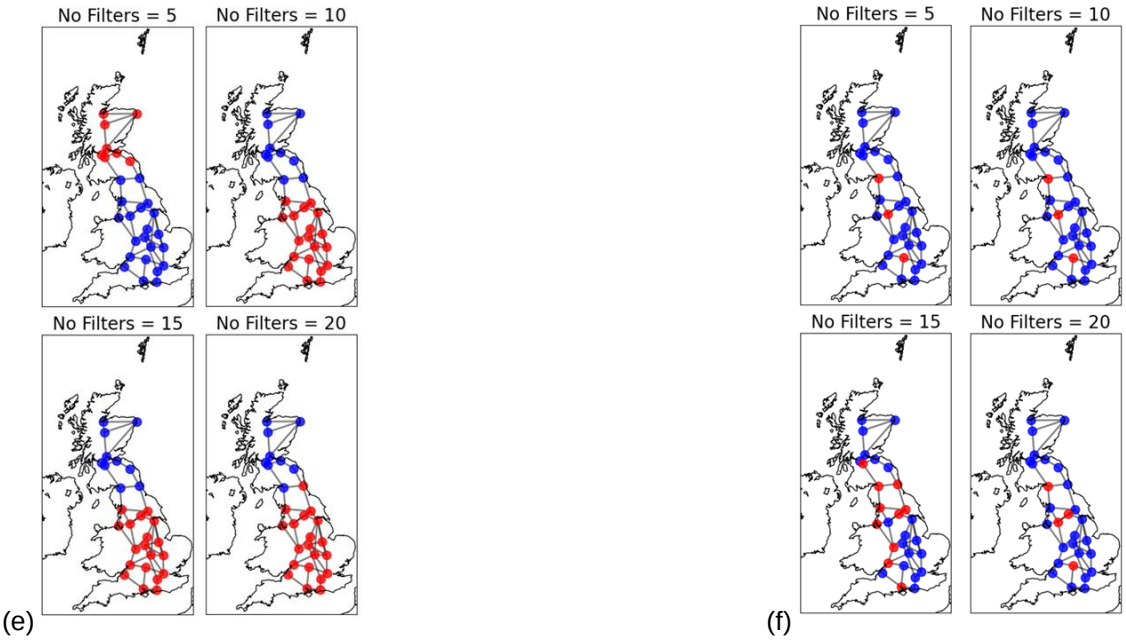

(e) (f)

Figure 0-2: The two level clusters obtained for different graph signals for GB reduced network with increase in the number of spectral filters (a,b) Low Pass Filter (c,d) Non-Tight Filter (e,f) Tight Filter

D.1.3 IEEE 118 Bus Network

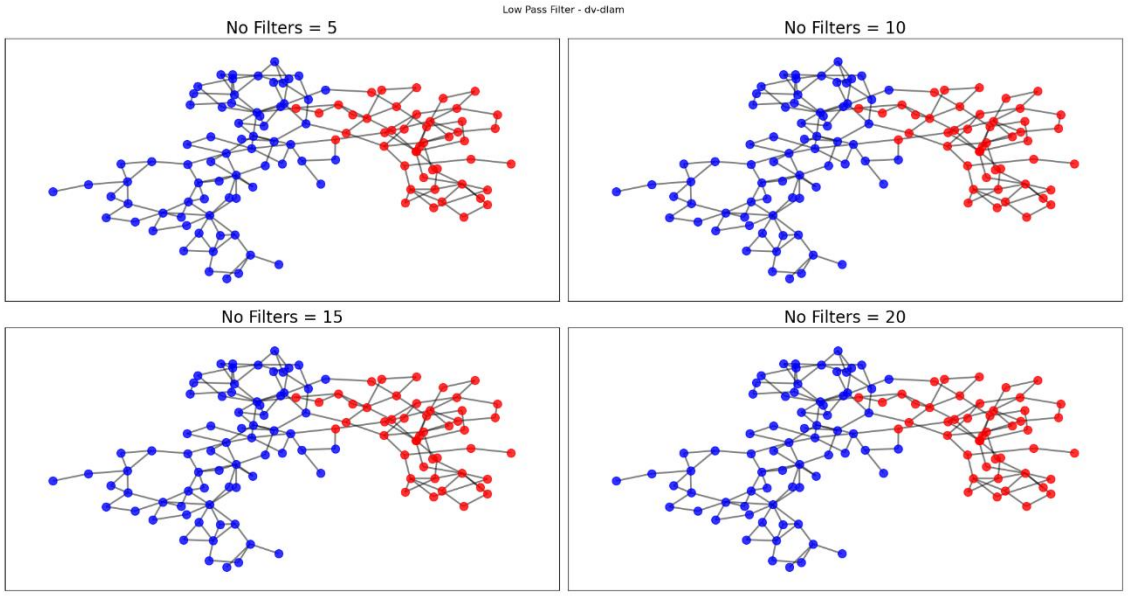

(a)

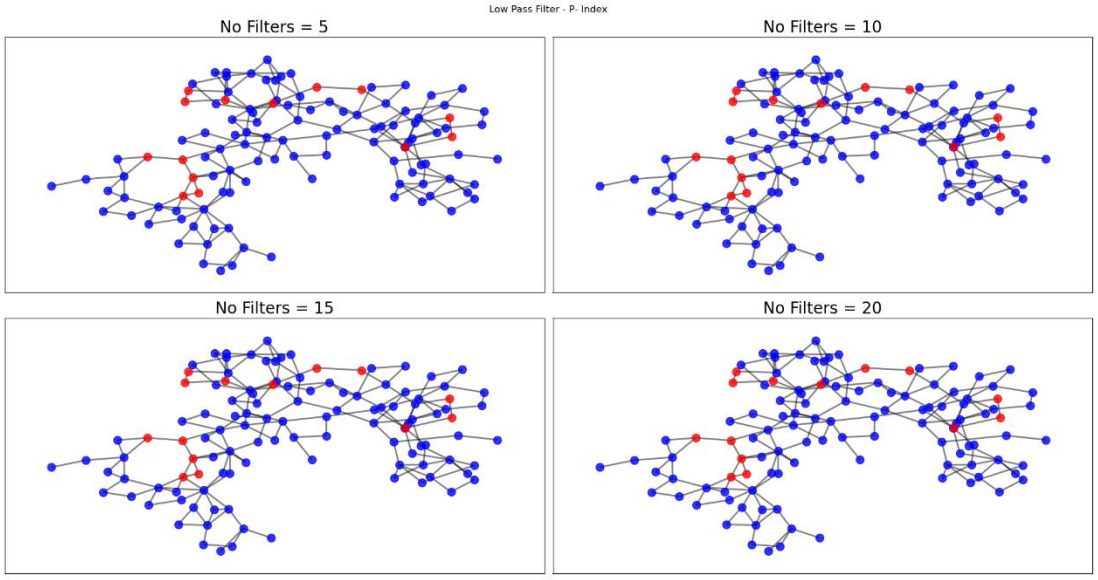
Low Pass Filter - P- Index
No Filters = 5
No Filters = 10
No Filters = 15
No Filters = 20

(b)

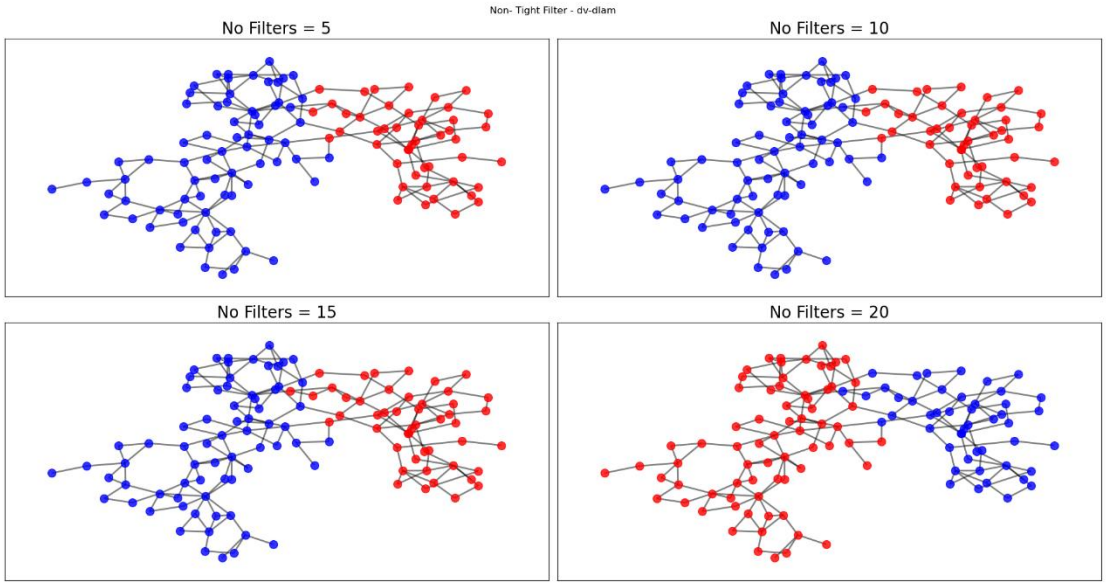
Non- Tight Filter - dv-dlam
No Filters = 5
No Filters = 10
No Filters = 15
No Filters = 20

(c)

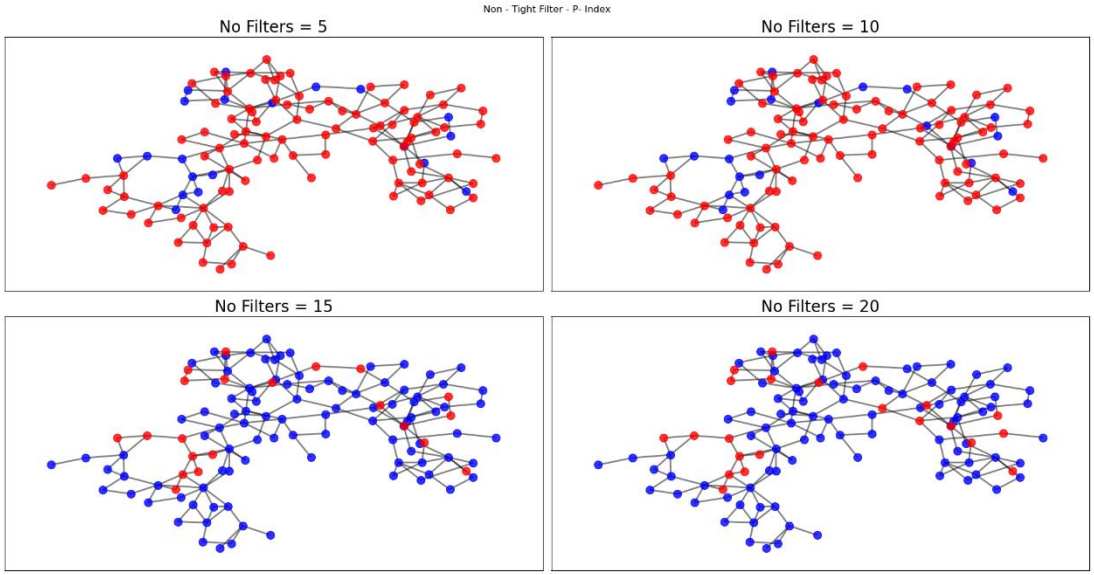
Non - Tight Filter - P- Index
No Filters = 5
No Filters = 10
No Filters = 15
No Filters = 20

(d)

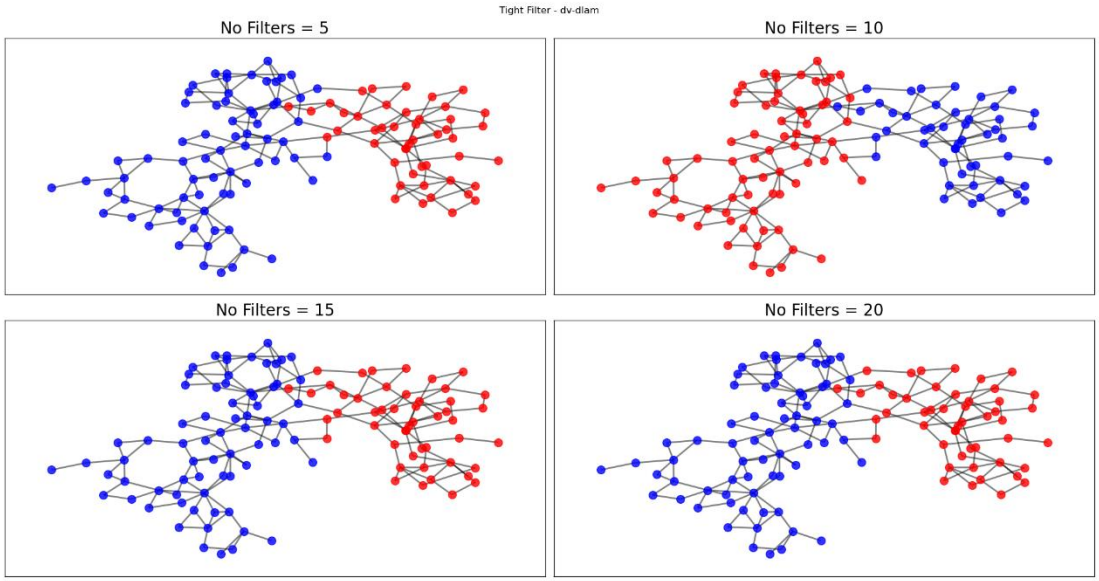
Tight Filter - dv-diam
No Filters = 5
No Filters = 10
No Filters = 15
No Filters = 20

(e)

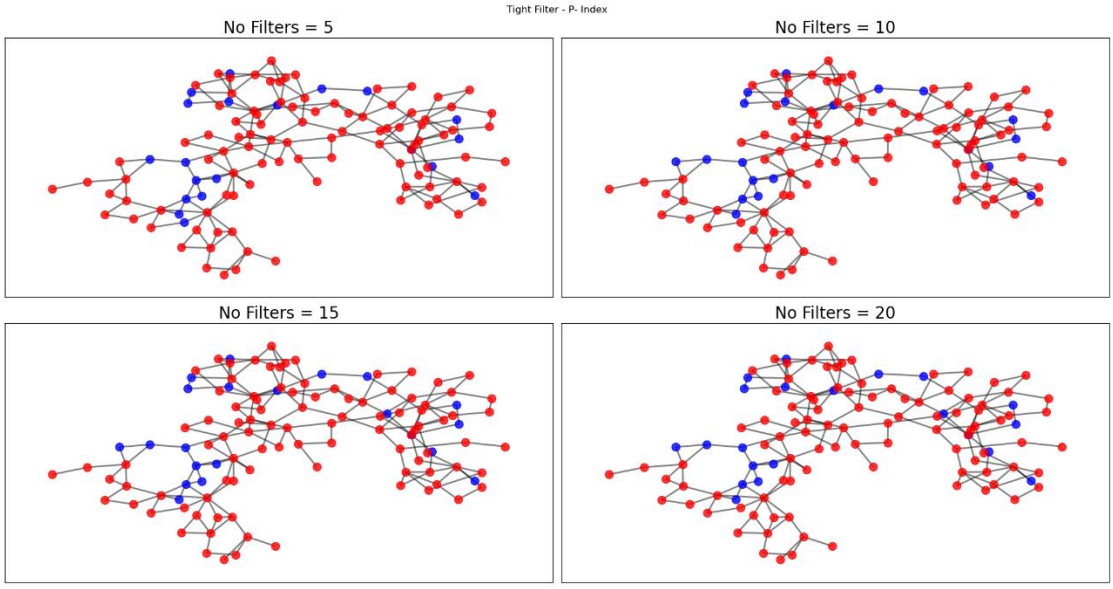

(f)

Figure 0-3: The two level clusters obtained for different graph signals for IEEE 118 bus network with increase in the number of spectral filters (a,b) Low Pass Filter (c,d) Non-Tight Filter (e,f) Tight Filter

D.2 Power Network Visualization with the Change in Clusters

D.2.1 IEEE 30 Bus Network

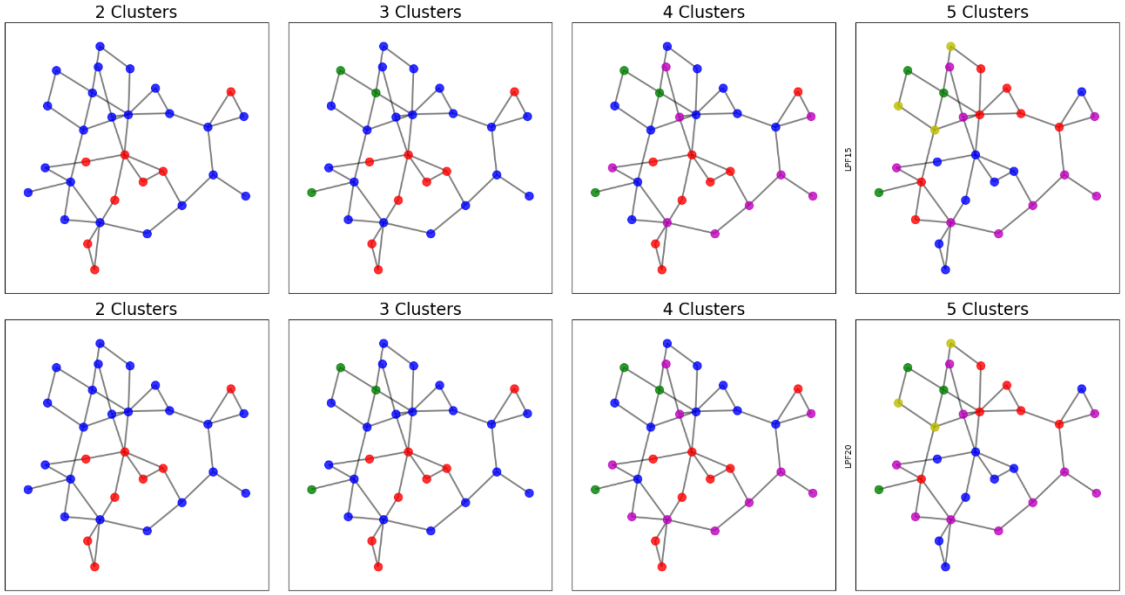

(a)

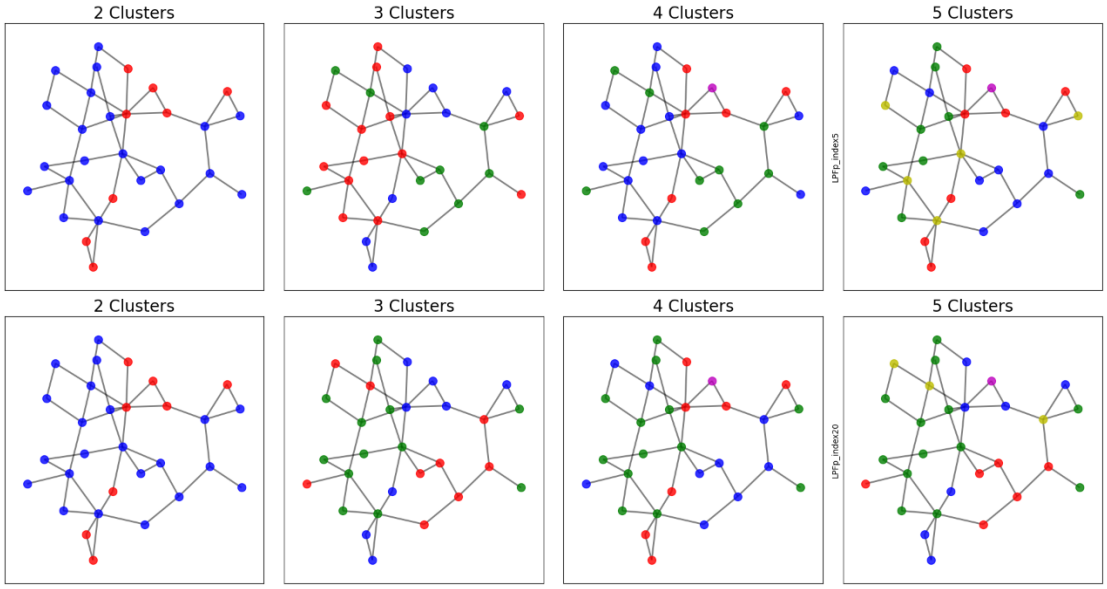
2 Clusters
3 Clusters
4 Clusters
5 Clusters
LPI[p_index5
2 Clusters
3 Clusters
4 Clusters
5 Clusters
LPI[p_index20

(b)

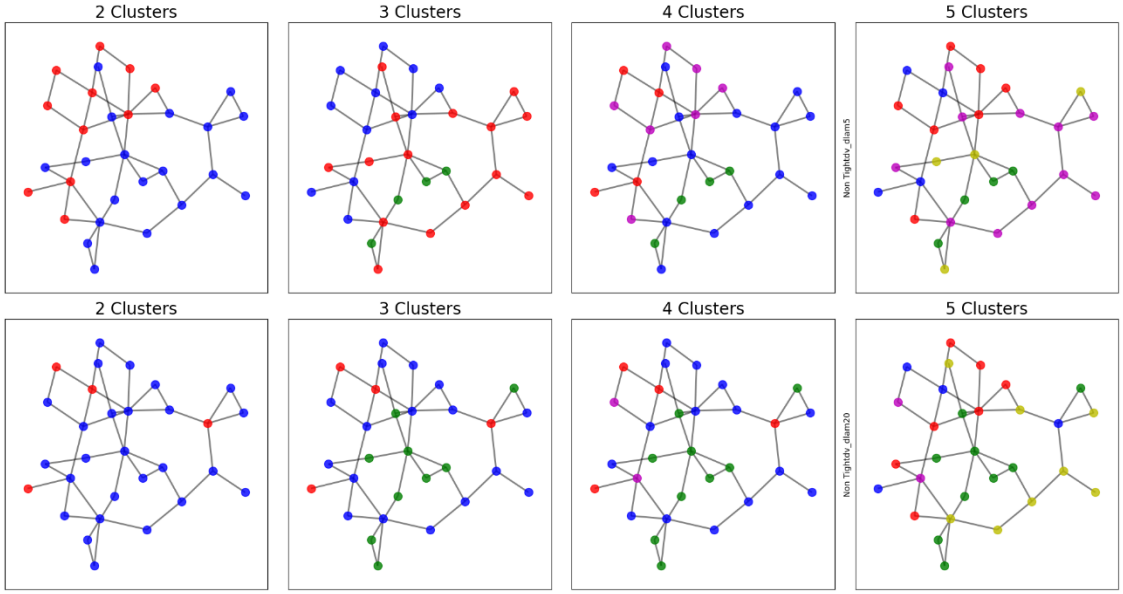
2 Clusters
3 Clusters
4 Clusters
5 Clusters
Non Tightdv_diam5
2 Clusters
3 Clusters
4 Clusters
5 Clusters
Non Tightdv_diam20

(c)

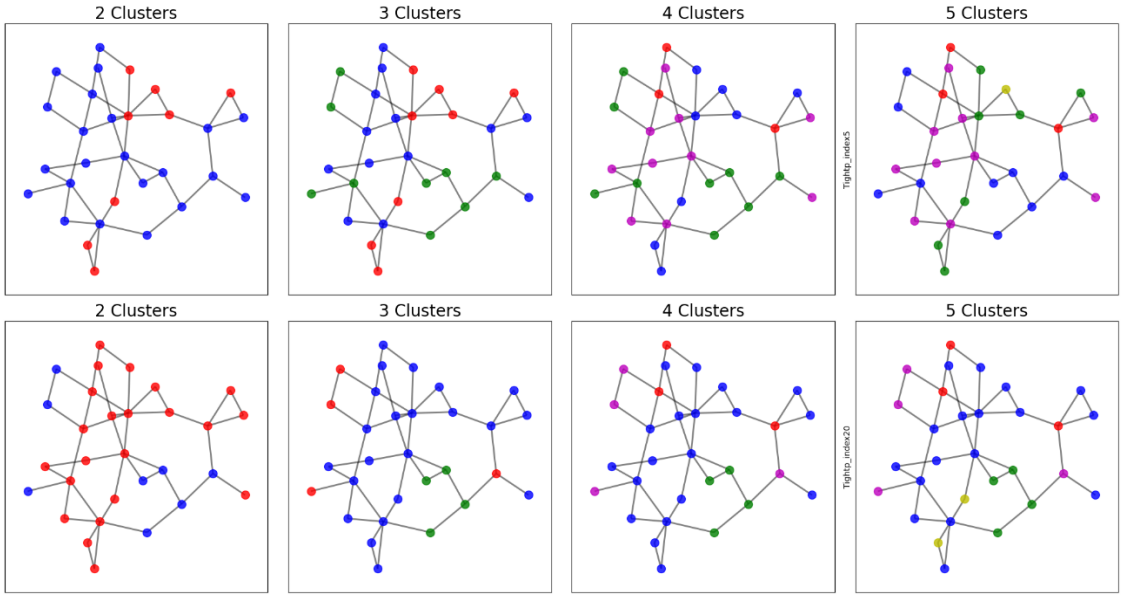

(d)

Figure 0-4: The clusters obtained in IEEE 30 bus power network with change for various graph signal and spectral filters. Various clusters obtained for IEEE 30 bus power network considering (a) The heat kernel $\tau = 15$ (first row) and $\tau = 20$ (second row) considering tangent vector as graph signal. (b) The heat kernel $\tau = 5$ (first row) and $\tau = 20$ (second row) considering p-index as graph signal. (c) 5 (first row) and 20 (second row) non-tight spectral filters considering tangent vector as graph signal. (d) the 5 (first row) and 20 (second row) tight spectral filters considering p-index as graph signal.

D.2.2 GB Reduced Network

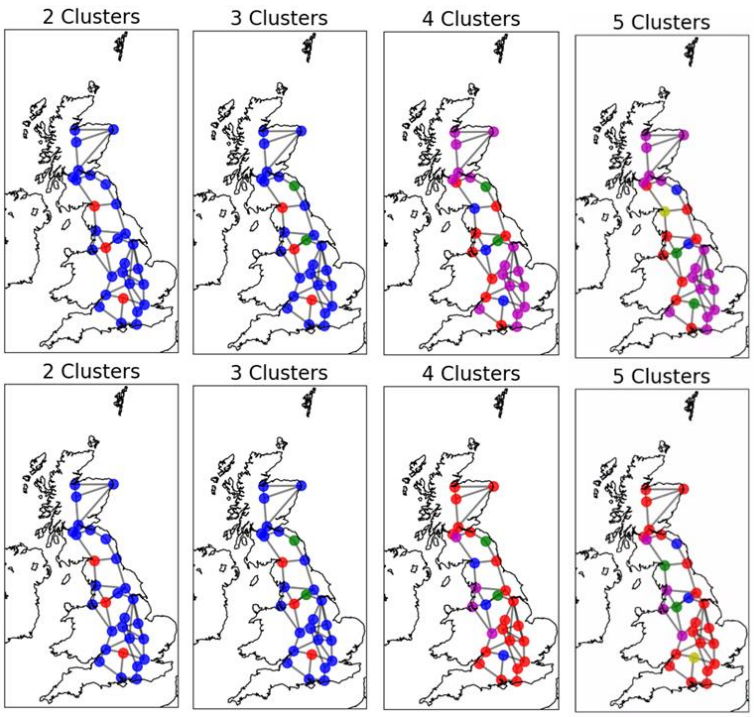

(a)

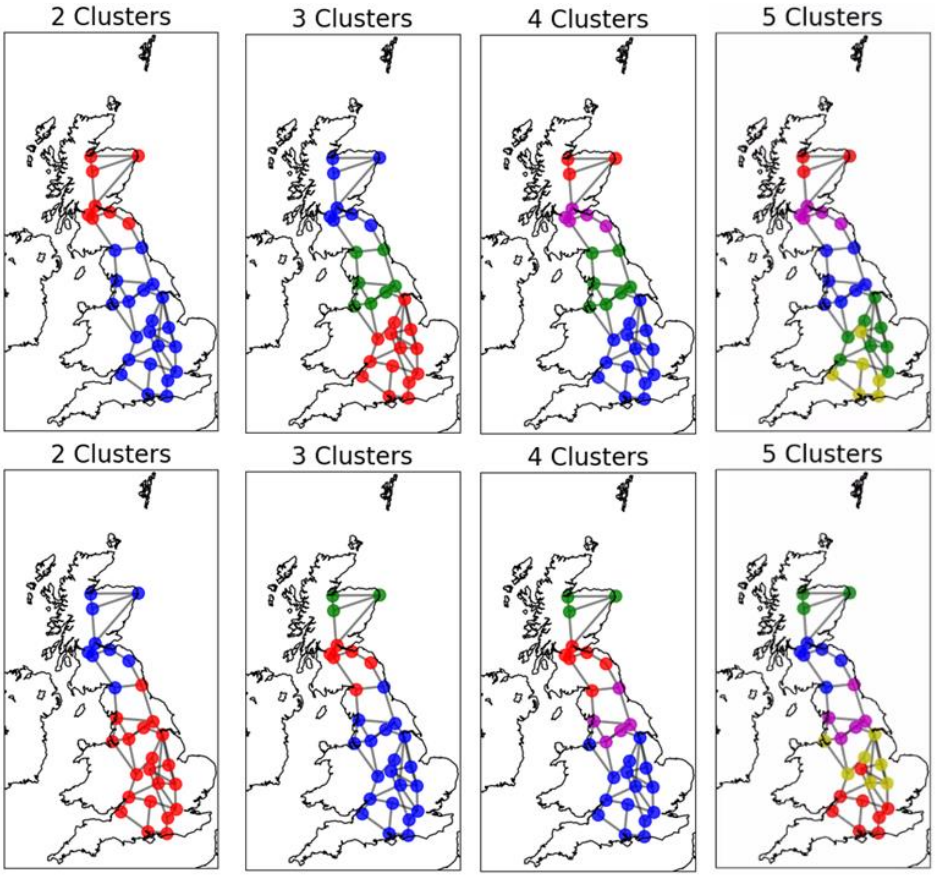
2 Clusters
3 Clusters
4 Clusters
5 Clusters
2 Clusters
3 Clusters
4 Clusters
5 Clusters

(b)

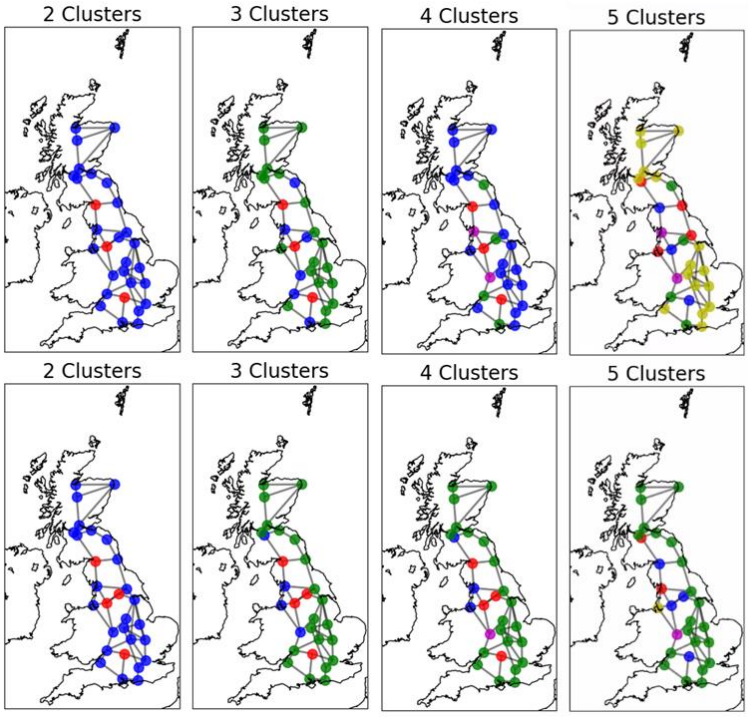

(c)

Figure 0-5: The clusters obtained in GB reduced power network with change for various graph signal and spectral filters. (a) Various clusters obtained for reduced Great Britain power network considering the heat kernel $\tau = 5$ (first row) and $\tau = 20$ (second row) with p-index as graph signal. (b) Various clusters obtained for reduced Great Britain power network considering the 5 (first row) and 20 (second row) tight spectral filters considering tangent vector as graph signal. (c) Various clusters obtained for reduced Great Britain bus power network considering the 5 (first row) and 20 (second row) tight spectral filters considering p-index as graph signal.

D.2.3 IEEE 118 Bus Network

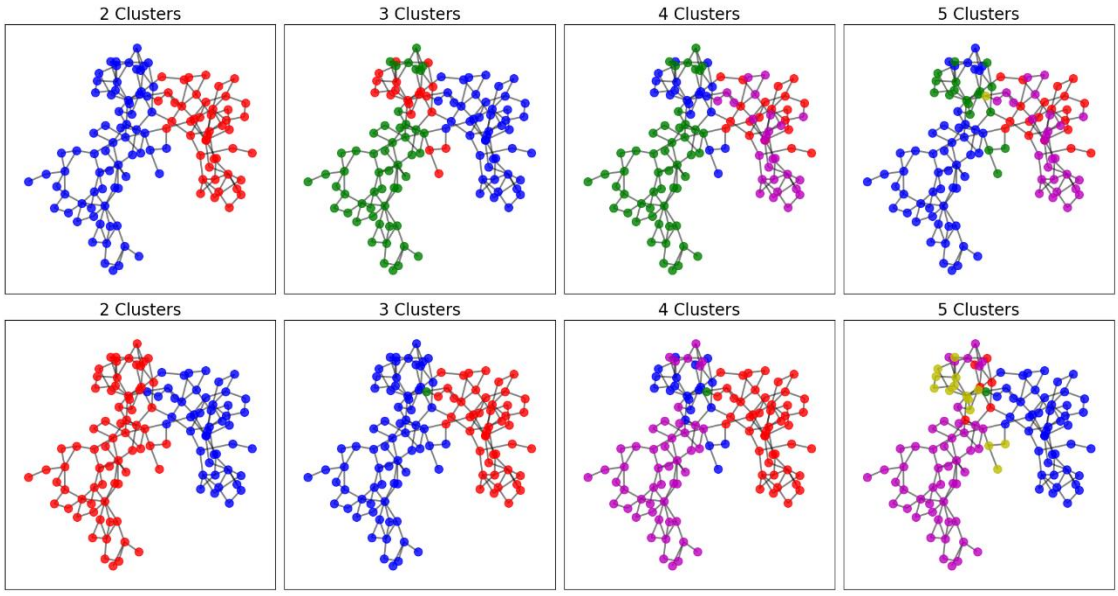

(a)

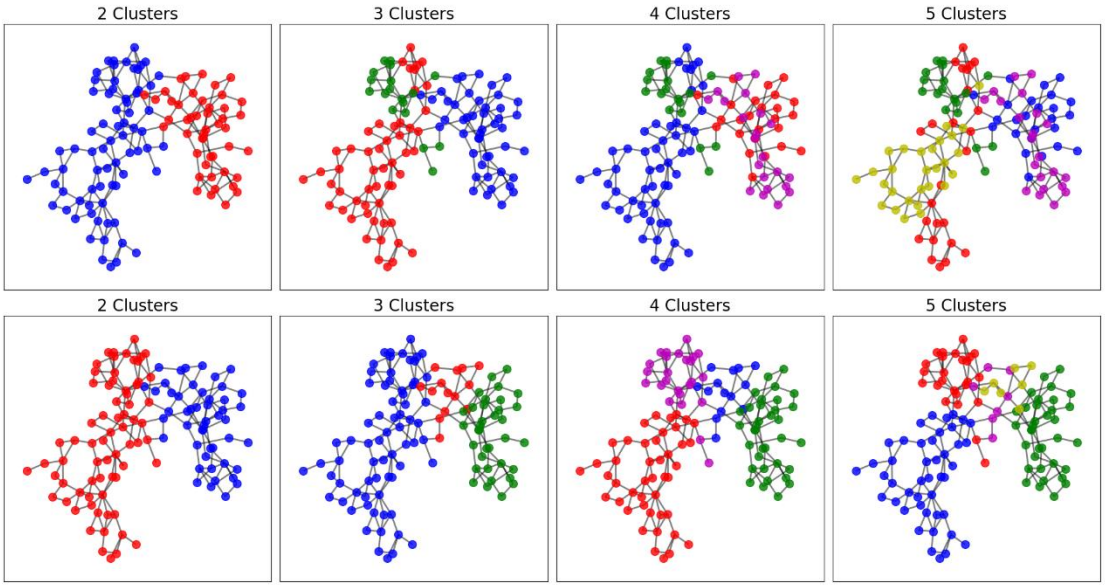

(b)

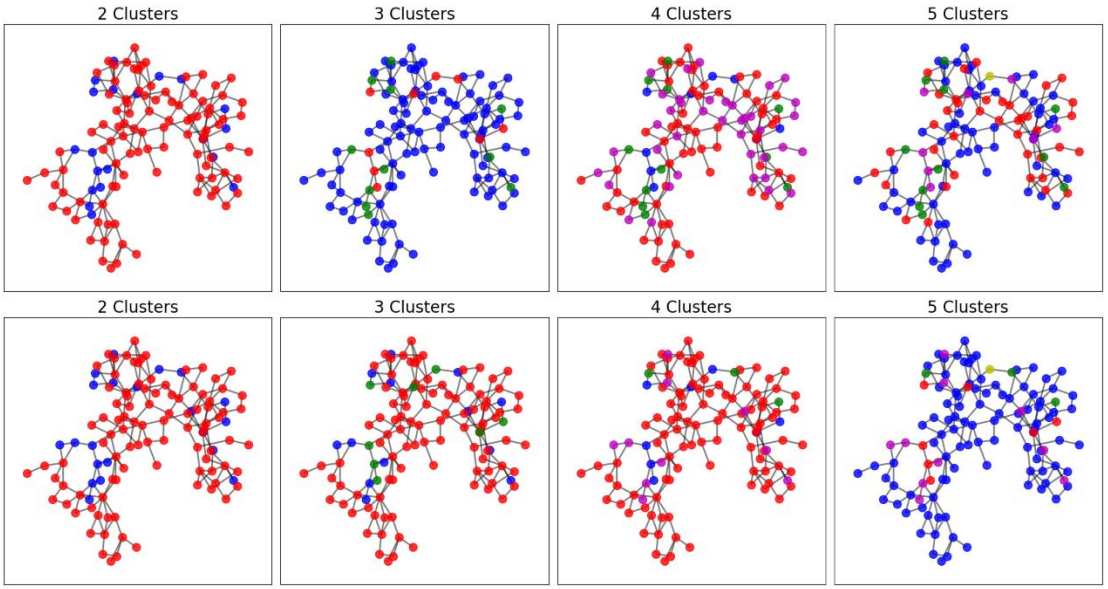

(c)

Figure 0-6: The clusters obtained in IEEE 118 bus power network with change for various graph signal and spectral filters (a) Various clusters obtained for IEEE 118 bus power network considering the 5 (first row) and 20 (second row) non-tight spectral filters considering tangent vector as graph signal. (b) Various clusters obtained for IEEE 118 bus power network considering the the 5 (first row) and 20 (second row) tight spectral filters considering tangent vector as graph signal. (c) Various clusters obtained for IEEE 118 bus power network considering the the 5 (first row) and 20 (second row) tight spectral filters considering p-index as graph signal

References

[1] R. D. Zimmerman and C. E. Murillo-Sánchez, “Matpower Optimal Scheduling Tool MOST 1.0 User’s Manual,” *Power Systems Engineering Research Center (PSerc)*, 2016.

[2] C. J. Huberty and S. Olejnik, *Applied MANOVA and discriminant analysis*, vol. 498. John Wiley & Sons, 2006.

[3] K. V. Mardia, “Measures of multivariate skewness and kurtosis with applications,” *Biometrika*, vol. 57, no. 3, pp. 519–530, 1970.

[4] R. Khattree and D. N. Naik, *Applied multivariate statistics with SAS software*. SAS Institute Inc., 2018.

[5] T. D. Fletcher, “QuantPsyc: Quantitative Psychology Tools. R package version 1.3, 2008.” [Online]. Available: https://cran.r-project.org/web/packages/QuantPsyc/QuantPsyc.pdf.

[6] C. Liu, A. C. Bathke, and S. W. Harrar, “A nonparametric version of Wilks’ lambda—Asymptotic results and small sample approximations,” *Statistics & Probability Letters*, vol. 81, no. 10, pp. 1502–1506, 2011.

[7] A. C. Bathke, S. W. Harrar, and L. V. Madden, “How to compare small multivariate samples using nonparametric tests,” *Computational Statistics & Data Analysis*, vol. 52, no. 11, pp. 4951–4965, 2008.

[8] A. R. Ellis, W. W. Burchett, S. W. Harrar, and A. C. Bathke, “Nonparametric inference for multivariate data: the R package npmv,” *Journal of Statistical Software*, vol. 76, no. 4, pp. 1–18, 2017.

[9] D. I. Shuman, C. Wiesmeyr, N. Holighaus, and P. Vandergheynst, “Spectrum-adapted tight graph wavelet and vertex-frequency frames,” *IEEE Transactions on Signal Processing*, vol. 63, no. 16, pp. 4223–4235, 2015.

[10] D. K. Hammond, P. Vandergheynst, and R. Gribonval, “Wavelets on graphs via spectral graph theory,” *Applied and Computational Harmonic Analysis*, vol. 30, no. 2, pp. 129–150, 2011.

[11] N. Leonardi and D. Van De Ville, “Tight wavelet frames on multislice graphs,” *IEEE Transactions on Signal Processing*, vol. 61, no. 13, pp. 3357–3367, 2013.

[12] V. Y. Ivrii, “Second term of the spectral asymptotic expansion of the Laplace-Beltrami operator on manifolds with boundary,” *Functional Analysis and Its Applications*, vol. 14, no. 2, pp. 98–106, 1980.

[13] C. Li and A. B. Hamza, “A multiresolution descriptor for deformable 3D shape retrieval,” *The Visual Computer*, vol. 29, no. 6, pp. 513–524, 2013.

[14] T. Hou and H. Qin, “Continuous and discrete Mexican hat wavelet transforms on manifolds,” *Graphical Models*, vol. 74, no. 4, pp. 221–232, 2012.

[15] V. N. Ekambaram, G. C. Fanti, B. Ayazifar, and K. Ramchandran, “Spline-like wavelet filterbanks for multiresolution analysis of graph-structured data,” *IEEE Transactions on Signal and Information Processing over Networks*, vol. 1, no. 4, pp. 268–278, 2015.

[16] H. K. Meena, K. K. Sharma, and S. D. Joshi, “Facial expression recognition using the spectral graph wavelet,” *IET Signal Processing*, vol. 13, no. 2, pp. 224–229, 2019.

.